

University of Nottingham



Faculty of Engineering

Non-invasive Photoplethysmography and Contact Pressure Optical Fibre Sensor

Chong Liu

Student ID: 4222693

A thesis submitted to the University of Nottingham for the degree of
DOCTOR OF PHILOSOPHY

June 2020

Abstract

In healthcare, measurement of the photoplethysmogram (PPG) can be used for diagnosing diseases (e.g. hypoxaemia, vascular and heart diseases) and measuring a patient's physiological parameters (blood oxygen saturation and heart rate). For measuring PPG signals, the contact force between the skin and the sensor plays an important role since both insufficient and too high contact pressure will distort the PPG signal. It would therefore be advantageous to develop a sensor that could measure contact pressure and PPG simultaneously.

In this research, a novel optical fibre based pulse oximeter probe was developed that combines the measurements of heart rate (HR), blood oxygen saturation (S_{pO_2}) and capillary refill time (CRT) whilst recording the contact pressure under ambient conditions. The probe consists of three 45° angle-tipped plastic optical fibres (POFs) used to deliver and collect light for pulse oximetry and CRT measurement along with dual fibre Bragg gratings (FBGs) inscribed in silica fibre to measure the applied contact pressure. Compared to previous studies of using numerous POFs to measure S_{pO_2} values, this research has reduced the number of fibres applied by increasing the coupling efficiency in order to avoid challenges of manufacturing difficulties associated with large numbers of optical fibres. The coupling efficiency increase of POFs applied in the developed probe was achieved via cleaving the optical fibre tip at 45° . All optical fibres were housed in a biocompatible epoxy patch that reduces motion artefacts in the PPG and transduces transverse loading into an axial strain in the FBG. Meanwhile, the sensitivity of the pressure sensing FBG was increased according to the surrounding material's low Young's modulus. A reference FBG written on the silica fibre was protected by a stainless steel tube which was applied to compensate the effects of temperature on the pressure sensing FBG.

It was found that the designed non-invasive sensor could continuously detect the PPG signals for S_{pO_2} measurement from a subject's finger during repeatable 5 minute recording sessions. The recorded PPG signals were assessed by utilising suitable signal quality indices (SQIs) applied in this research, and then the qualifying PPG signals were used to calculate S_{pO_2} . This S_{pO_2} test result was validated against the output of the commercial pulse oximeter (Masimo Radical-7), which demonstrated the S_{pO_2} measurement capability of the designed sensor. By comparing the S_{pO_2} data of 10

volunteers obtained from the sensor under different contact pressures (2 to 45kPa), it was found that a contact pressure ranging from 5 to 15kPa generated the optimal PPG signal, and provided the best $S_{\text{P}}\text{O}_2$ measurement performance. Data recorded by the sensor also demonstrated the ability of the sensor to detect changes in contact pressure and blood volume in the finger.

Since the designed sensing probe is capable of detecting the reflected light intensity and the contact pressure from a subject, the probe was applied to measure 10 volunteers' CRTs from their index fingers. The CRT was calculated from the detected light intensity and contact pressure data via signal processing (i.e. refilling signal extraction, normalisation and exponential curve fitting process) whilst poor quality capillary refill signals were rejected if they had a positive gradient for the blood refilling region or had an excessive gradient for the baseline region. By comparing the calculated CRT and the indices of exponential fitting curves, an exponential-like relationship was found between them. Further investigation on using indices of exponential fitting curves to assess the reliability of calculated CRT is highly recommended.

Acknowledgement

I would like to express my thanks to Professor Barrie R. Hayes-Gill, Professor Stephen P. Morgan, Dr Serhiy Korposh and Dr Ricardo Correia for their enthusiastic and committed supervision, guidance and support throughout this work. Thanks also go to Dr Shen Sun for his design in the opto-electronic unit for walking CRT measurement.

Further acknowledgement goes to EPSRC and HERMES for their financial support; to Footfalls & Heartbeats (UK) for supporting conductive yarn based textiles; the subjects who participated in the study; to Hattan Ballaji for his contribution to the study. Finally, for their invaluable support and advice, I would like to thank friends and members of the Optics and Photonics Research Group of the University of Nottingham.

Contents

Abstract	i
Acknowledgement.....	iii
Contents	iv
Chapter 1 Introduction	1
1.1 Motivation	1
1.2 Background	2
1.2.1 Blood Oxygen Saturation Measurement	2
1.2.1.1 Oxygen Transportation	2
1.2.1.2 Photoplethysmography	5
1.2.1.3 Pulse Oximeter Design	6
1.2.2 Capillary Refill Time Measurement	8
1.3 Aims and Objectives	9
1.4 Thesis Construction	10
Chapter 2 Literature Review	12
2.1 Pulse Oximetry Equations for Blood Oxygen Saturation Measurement.....	12
2.2 Optical Reflectance Pulse Oximeter Design	19
2.2.1 Reflectance Mode Pulse Oximeter.....	19
2.2.2 Optical Fibre Sensor Configuration	20
2.3 Fibre Bragg Grating Contact Force Sensing	26
2.4 Capillary Refill Time (CRT) Measurement	31
2.5 The Novelty of the Thesis	33
2.6 Conclusion.....	36
Chapter 3 Fibre Bragg Grating (FBG) Pressure Sensor.....	38
3.1 Fibre Bragg Grating (FBG) Patch Configuration.....	38
3.1.1 Dual FBG Configuration.....	38
3.1.2 Epoxy Resin Cuboid Patch.....	43
3.2 Fibre Bragg Grating (FBG) Patch Temperature Compensation.....	46
3.2.1 Temperature Response of the Dual FBGs Silica Fibre	48
3.2.2 Temperature Response of the Dual FBG Silica Fibre Epoxy Patch	53
3.3 Fibre Bragg Grating (FBG) Patch Pressure Measurement	56
3.3.1 Pressure Response of the Pressure Sensing Epoxy Patch	57
3.3.2 Pressure Response of the Integrated Pulse Oximeter.....	60

3.4	Discussion and Conclusion	63
Chapter 4 Non-invasive Pulse Oximetry Measurement Using the POF Patch		65
4.1	Design of the Pulse Oximetry Sensor.....	65
4.1.1	Probe Design	66
4.1.2	Opto-electronic System Design.....	69
4.1.2.1	Light Source and LED Drivers	71
4.1.2.2	Photodiode and Trans-impedance Amplifier	71
4.1.2.3	Data Acquisition System	73
4.1.2.4	FBG Interrogator.....	75
4.1.3	Gain and Noise Measurement	76
4.1.3.1	Analogue Front-end Gain	77
4.1.3.2	Analogue Front-end Noise.....	78
4.2	Pulse Oximetry Sensor Characteristics	83
4.2.1	Time Division Multiplexing.....	83
4.2.2	Stray Light Immunity	84
4.2.3	Analogue Front-end Noise	86
4.3	PPG Signals Processing.....	88
4.3.1	TDMA Demodulation	88
4.3.2	PPG Signal Digital Filtering and Interpolation	90
4.3.3	Signal Quality Index of PPG Signals	94
4.3.3.1	Signal to Noise Ratio (SNR) Index.....	95
4.3.3.2	Perfusion Index (PI).....	96
4.3.3.3	Skewness Index (SKI)	98
4.4	S _p O ₂ Measurement Results	102
4.4.1	Preliminary S _p O ₂ Measurements.....	103
4.4.2	The Impact of Skin Temperature on S _p O ₂ Measurements	108
4.4.3	The Impact of Contact Pressure on S _p O ₂ Measurements.....	115
4.5	Discussion and Conclusion	121
Chapter 5 Capillary Refill Time Measurement		124
5.1	Capillary Refilling Signal Processing	124
5.1.1	Refilling Signal Extraction.....	124
5.1.2	Refilling Signal Normalisation	126
5.1.3	Refilling Signal Fitting Process	127

5.1.4	Capillary Refill Time Estimation.....	129
5.2	Finger Capillary Refill Time Measurement Using the Sensing Patch	132
5.2.1	Finger CRT Measurement Setup.....	132
5.2.2	Finger CRT Measurement Results.....	134
5.3	Discussion and Conclusion	138
Chapter 6 Summary and Further Work.....		139
6.1	Discussion	139
6.2	Conclusion.....	143
6.3	Future Work	144
6.3.1	Axial Loading Strain Interference Compensation Error! Bookmark not defined.	
6.3.2	Temperature Caused Low Perfusion Signals Detection Error! Bookmark not defined.	
6.3.3	Estimation of Breathing Rate Using Reflectance PPG Signals	Error! Bookmark not defined.
6.3.4	Motion Artefact Detection	Error! Bookmark not defined.
6.3.5	Plethysmography Using an FBG Pressure Sensor Error! Bookmark not defined.	
6.3.6	Lock-in detection with quadrature demodulation Error! Bookmark not defined.	
6.3.7	CRT Simulation System.....	Error! Bookmark not defined.
6.3.8	The Photonic Sensing Sock.....	Error! Bookmark not defined.
References.....		146
Appendix A.....		159
A.1	Temperature Response of the FBG sensor	159
A.2	Pressure Response of the FBG Sensor	164
Appendix B		169
Appendix C		171
C.1	Pulse Oximetry Sensor Calibration	171
C.2	12 Experiment Results of S_{pO_2} Measurements under Different Skin Temperature Situations	184
C.3	30 Experimental Results of S_{pO_2} Measurements under Different Contact Pressures.....	197
C.4	10 CRT Experiments Results	217
Appendix D.....		Error! Bookmark not defined.
D.1	Photonic Sensing Sock.....	Error! Bookmark not defined.

D.2 Walking CRT Measurement Results..... **Error! Bookmark not defined.**

Chapter 1 Introduction

1.1 Motivation

This thesis is focused on improving the accuracy of peripheral blood oxygen saturation (S_{pO_2}) and capillary refill time (CRT) measurement by combining photoplethysmography with contact pressure measurement.

S_{pO_2} shows the percentage of oxygen saturated haemoglobin over the total haemoglobin in our body. For medical use, S_{pO_2} is used as an indicator for diagnosing for example breathing and circulation problems. Patients with acute respiratory failure (ARF) commonly have arterial hypoxaemia problems which cause low blood oxygen saturation levels [1]. Another example is during anaesthesia, where it is required to continuously measure the S_{pO_2} of patients for safety purposes [2]. In terms of maintaining a healthy lifestyle, there is growing interest to measure S_{pO_2} continuously in daily life. For example, pulse oximetry has been applied in detecting the deoxygenation caused by snoring-apnoea during sleep [3].

The traditional type of pulse oximetry (transmission mode, finger clip device) which is widely used to detect S_{pO_2} and heart rate is obtrusive, uncomfortable and inconvenient for long-term measuring during activities of daily life. Furthermore, motion artefacts can mean that obtaining reliable signals is difficult.

CRT measurement is a simple means of cardiovascular assessment that is widely applied in clinical care. CRT was applied as a clinical indicator to detect dehydration of patients as early as 1910 [4]. Nowadays, CRT measurement is commonly performed using a manually applied force to assess the perfusion, dehydration and septic shock of subjects. Specifically for diabetic foot ulcers, tissue perfusion is an important indicator [5]. As a result, CRT measurement may offer the potential of detecting ulcers at an early stage reducing subsequent healthcare costs.

Both S_{pO_2} and CRT can be calculated from photoplethysmography (PPG) signals but it is known that motion artefacts and contact pressure can affect the measured signals. The motivation of this research is to develop a method to improve the measurement accuracy and interpretation of PPG signals through simultaneous pressure measurement. Compared to other biomedical measurement devices, optical fibre

sensors are low cost, thin, flexible, and can be functionalised in order to measure a range of parameters [6, 7]. For PPG measurements, optical fibres can be used to deliver light to and from remote locations on or within the body, for example the oesophagus [8, 9], the trachea [10] or under the foot [11, 12]. What's more, as the optical fibre is insensitive to the electromagnetic radiation and not susceptible to electrical discharges, the optical fibre could be applied in conjunction with other bio-medical devices (e.g. insulin pumps and pace makers) [13] or in some environments such as an MRI scanner [13, 14]. Consequently, sensors in this research have been designed based on optical fibres which have the potential to fulfil long-term S_{pO_2} and CRT measurement requirements in the future.

1.2 Background

1.2.1 Blood Oxygen Saturation Measurement

1.2.1.1 Oxygen Transportation

Oxygen is vital to the human body as cells will finally die if they are deprived of oxygen [15, 16], brain cells are particularly sensitive and begin to die within five minutes after cutting off oxygen supply [17]. For oxygen delivery, the respiratory and circulatory system are required. First, air moves into and out of the lungs where gas exchange occurs via inspiration and expiration – see Figure 1.1. Here, oxygen in the lungs is diffused into the blood and transferred throughout the body using the circulatory system. Figure 1.2 shows the circulation process. During this period, the blood reaches the oxygen depleted areas and diffuses oxygen to cells while transferring carbon dioxide back to the lungs [18].

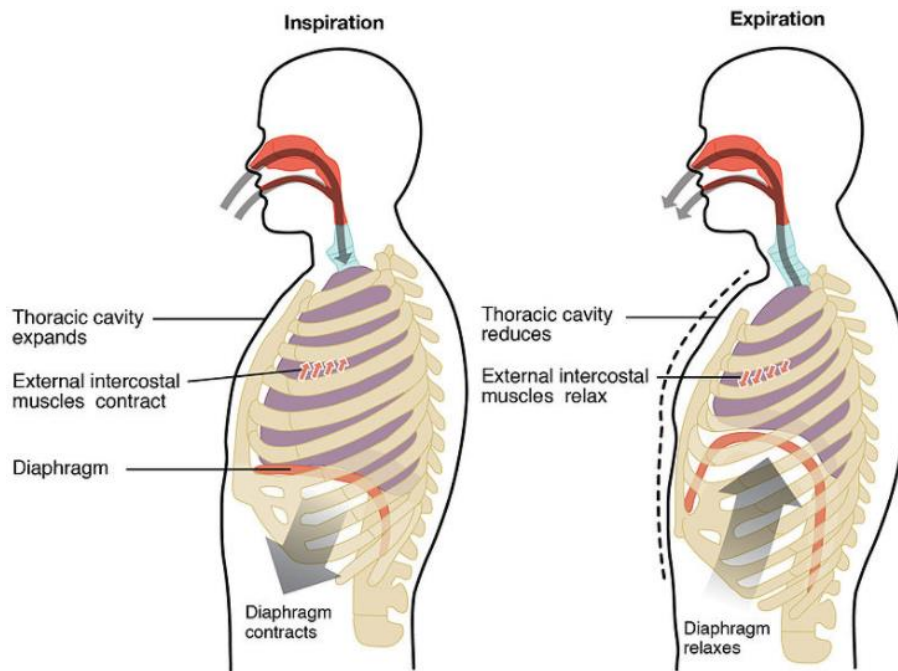


Figure 1.1. Inspiration and Expiration. Pulmonary ventilation contains two major steps – inspiration and expiration. The inspiration is the process to inhale the air into the lungs whilst the expiration is the process to exhale the CO₂-rich out of the lungs (source: [18]).

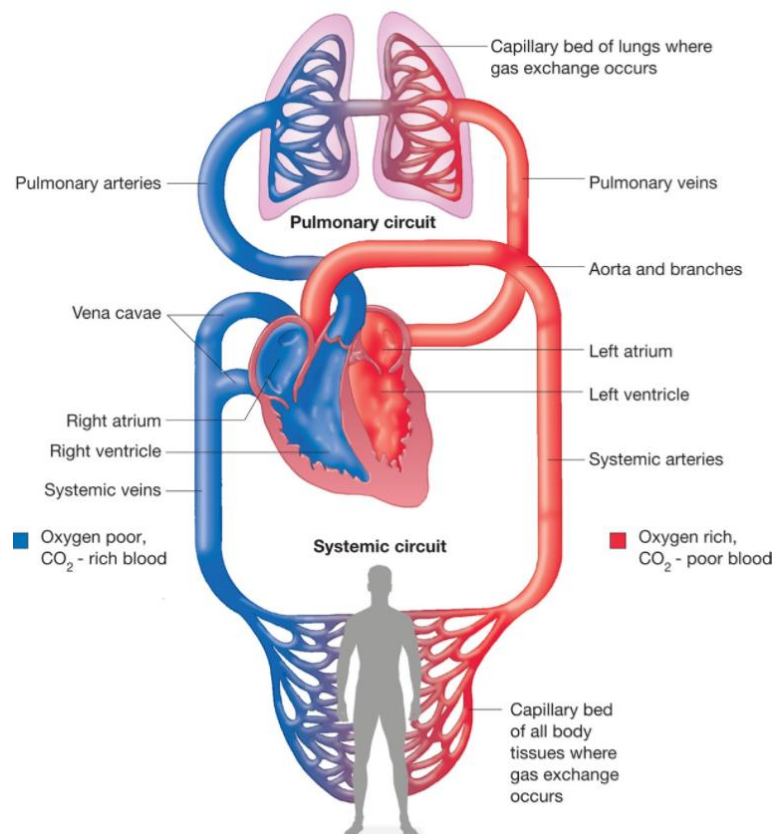
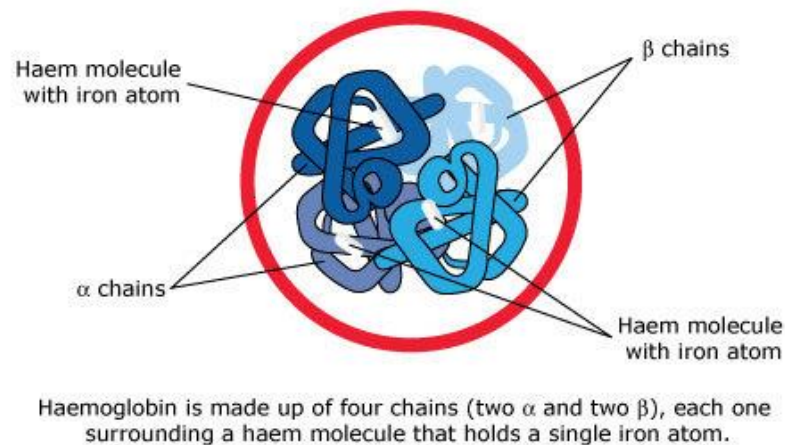


Figure 1.2. The circulation system is composed of two separate systems – the cardiovascular system and the lymphatic system. In this diagram only the cardiovascular system is shown which distributes the blood. First of all, oxygen in the lungs is diffused into the blood through the lung capillary bed to the pulmonary veins. The heart then pumps oxygenated blood from the Aorta and branches arteries to the body and deoxygenated blood to the lungs through the pulmonary arteries. The blood is transferred from the arteries to the veins through capillaries (source: [19]).

In the blood, an oxygen-carrying protein called haemoglobin plays the most important role in the oxygen delivery process. Oxygen is a nonpolar molecule which cannot dissolve easily in an aqueous environment. With haemoglobin, it will significantly increase O₂ solubility in blood by nearly a hundredfold. The reason of haemoglobin's ability to increase the O₂ solubility in blood is its structure. In order to significantly increase the oxygen-binding ability, the haemoglobin contains four polypeptide chains all with an attached additional iron-containing group (haeme). The central iron ion (Fe²⁺) in the haeme group reversibly binds O₂ to the haemoglobin [20].



© 2007 – 2009 The University of Waikato | www.sciencelearn.org.nz

Figure 1.3. The construction of haemoglobin. It clearly shows that one single haemoglobin has four polypeptide chains (2 alpha-chains and 2 beta-chains). The iron is an essential trace element part of haeme that can bind oxygen to itself (source: [15]).

Max Perutz found that haemoglobin can be identified into two different forms by using X-ray diffraction. Figure 1.3 shows the structure of haemoglobin. Since two different shapes of haemoglobin depend on whether oxygen was saturated or not, he named the two different forms “oxy-haemoglobin” and “deoxy-haemoglobin” respectively. The relationship between two forms can be written as follows:



Blood oxygen saturation (SO₂) shows the percentage of haemoglobin saturated with oxygen (oxy-haemoglobin) which is a very important indicator showing the subject's cardio-respiratory status. Peripheral capillary oxygen saturation (S_PO₂) is an estimation of the percentage of oxy-haemoglobin which can be calculated using pulse

oximetry, which is a common and non-invasive method applied in clinical environment, by using two different wavelengths [21].

1.2.1.2 Photoplethysmography

It may seem that the human body is opaque, however, visible and near-infrared wavelength light is capable of penetrating the soft tissue and is then scattered by the flowing blood under the skin. Photoplethysmography (PPG) is a non-invasive method to measure the time varying optical signal intensity variations due to the blood changes under the skin. This is illustrated in figure 1.4 [16].

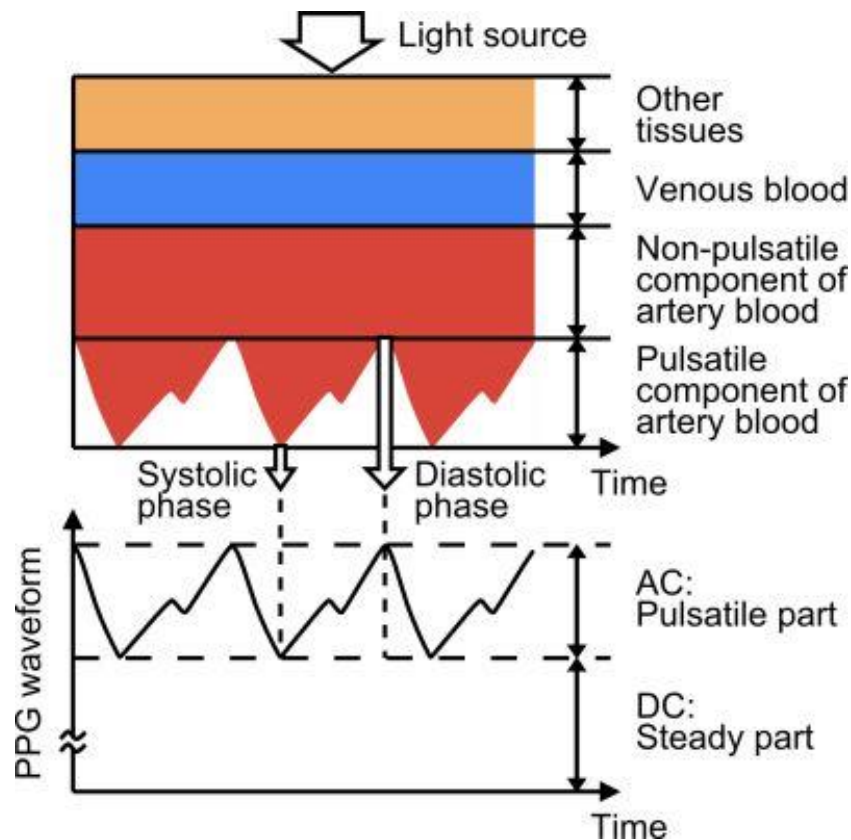


Figure 1.4. In this figure, two diagrams show the various components of the PPG. The PPG signal is the light (reflected/transmitted) intensity variations caused by the blood volume changes. The upper diagram shows the path of light illuminated in the body from the light source. The lower diagram shows the PPG signal which is composed of two parts namely the pulsatile and DC or steady parts (source: [22]).

PPG signals are composed of two parts which are the slowly varying DC component (shown constant in Figure 1.4) and the AC component. The slowly varying DC component mainly reflects the optical property of constant tissue, non-pulsatile blood (vasoconstrictor, thermoregulation and Mayer waves [23]) and bone whilst the PPG AC component arises from time varying blood volume changes [16].

A typical PPG sensor contains a light source and a photo detector. In terms of the method of collecting optical signals, there are two different modes of PPG sensors. One is called *transmission* mode where the photo diode is sited on one side of the skin and the light source is positioned on the other side of the skin. The second is called *reflectance* mode which positions the photo diode on the same side of the skin as the light source. In this case, the photo diode detects the light scattered by the blood, tissue and skin [24]. Figure 1.5 shows the construction of the two different sensor modes.

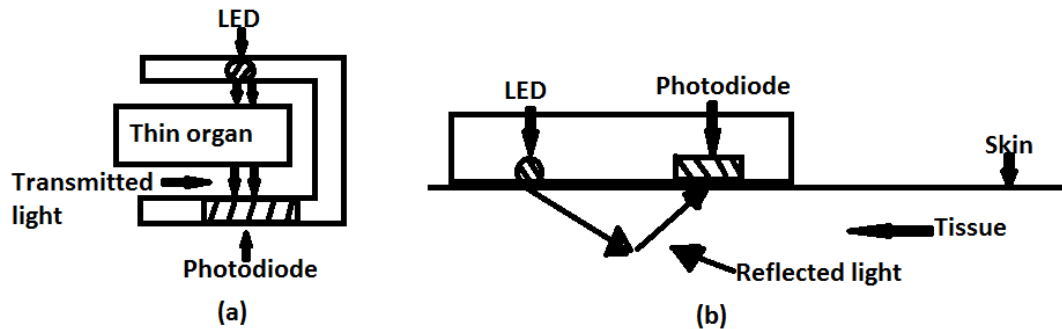


Figure 1.5. Transmission PPG sensor and Reflectance PPG sensor. (a) Transmission PPG: here the sensor collects light from the LED that penetrates the thin organ. The LED and the photodiode are sited on opposite surfaces of the organ. (b) Reflectance PPG: here the LED and the photodiode are located on the same side of the skin and hence are adjacent to each other.

For the transmission PPG, the photo-diode is located on the opposite side of the skin to the LED. In this case, the pulsatile signals (i.e. AC PPG components) are recorded from the light transmitted through the tissue [25]. Therefore, it is limited to application at peripheral areas of the body (i.e. finger, toe and earlobe) due to the thickness of the body part [26]. Moreover, when the subject has a low peripheral perfusion, pulse oximetry will be compromised at the subject's limbs [27]. For the reflectance PPG sensor, the photo-diode and light sources are sited on the same surface of the skin in this case the sensor detects the light scattered or reflected by tissues and peripheral capillaries. Thus, it has less limitation on the choice of the position of the detection area making the reflectance PPG sensor more flexible and convenient [18].

1.2.1.3 Pulse Oximeter Design

The pulse oximeter is a non-invasive medical device that indirectly monitors the oxygen saturation of subjects and changes in blood volume in the skin. Pulse oximetry is a convenient measurement method which requires measurement of two PPG signals at different wavelengths. As the light absorption of oxy-haemoglobin and deoxy-

haemoglobin are different, it is possible to calculate the ratio between these using two different wavelength PPG signals in order to obtain the S_pO_2 of subjects [28]. Figure 1.6 shows the different light absorption of oxy-haemoglobin and deoxy-haemoglobin. Typically, the pulse oximeter design uses two LEDs (red and infrared) to illuminate a subject and record the transmitted or reflected light signal from the skin using a photo diode.

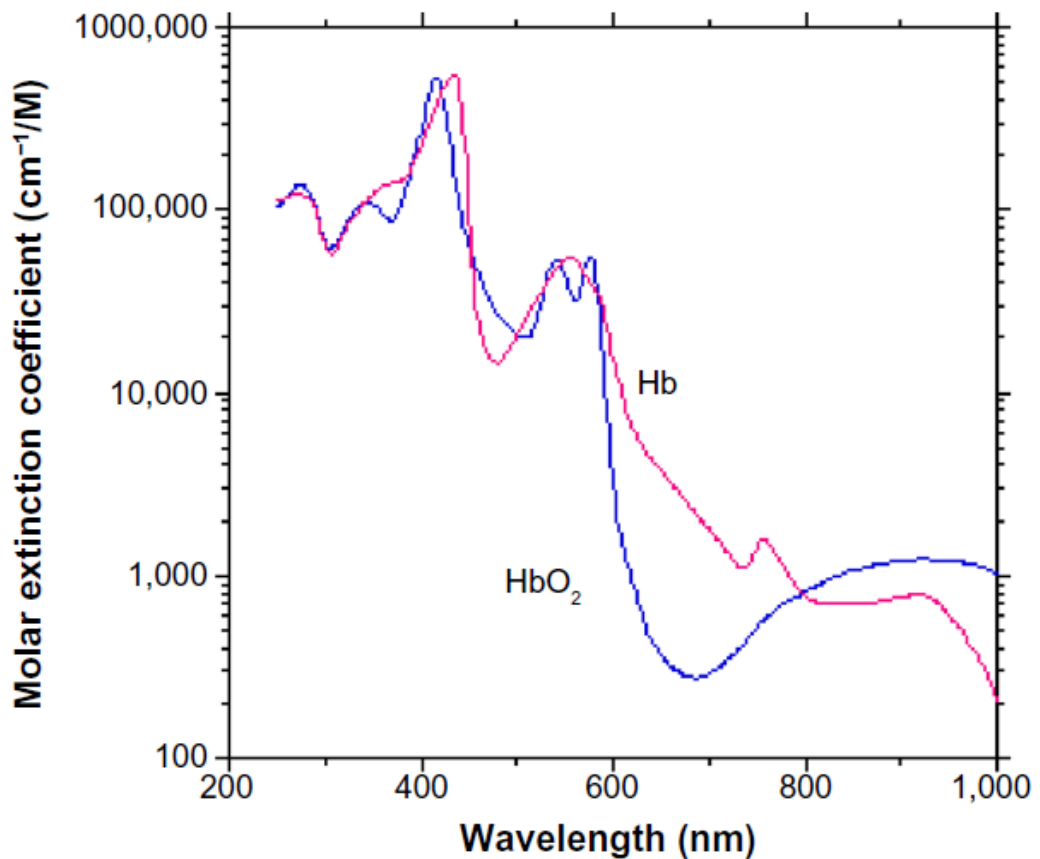


Figure 1.6. The light absorption of oxy-haemoglobin (HbO_2) and deoxy-haemoglobin (Hb) in the red and near infrared spectrum. The deoxy-haemoglobin has higher light absorption when the exposed light has wavelength less than 800nm. When the haemoglobin is exposed to the light whose wavelength is higher than 800 nm, the oxy-haemoglobin has higher light absorption (source: [28]).

From section 1.2.1.2, there are two different PPG sensors – transmission PPG sensor and reflection PPG sensor. Since the pulse oximeter design is very similar to the PPG detector, there are two different kinds of pulse oximeter as well. Figure 1.7 shows constructions of two different types of pulse oximeter.

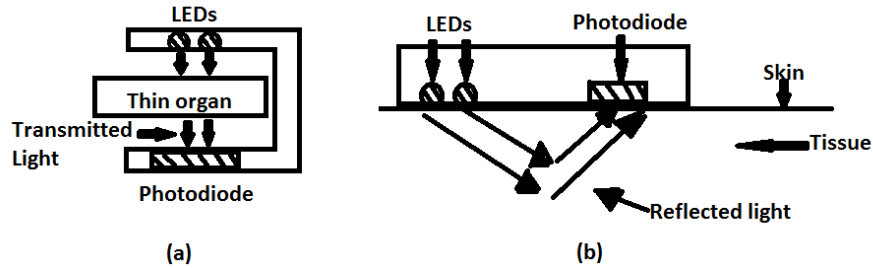


Figure 1.7. The transmission mode pulse oximeter and the reflectance pulse oximeter (a) shows the structure of the transmission pulse oximetry which is very similar to the transmission PPG sensor. The only difference is that the pulse oximetry requires two LEDs due to two different wavelength PPG signals required. (b) shows the structure of the reflectance pulse oximetry which is similar to the reflectance PPG sensor. The only difference is an additional LED.

1.2.2 Capillary Refill Time Measurement

Capillary refill time (CRT) is defined as the time taken for a distal capillary bed to regain its colour after blanching caused by pressure exerted on it. Figure 1.8 shows the CRT test process on the index finger. The physiological principle of CRT is underpinned by peripheral perfusion which is complex as it is affected by many factors such as driving pressure, arteriolar tone and the constituents of the blood all affect the capillary blood flow. CRT is used as a medical indicator to assess perfusion, dehydration and shock [29].

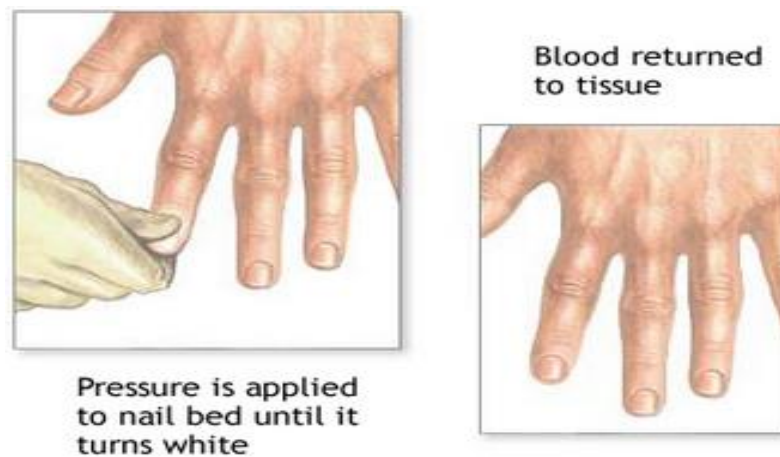


Figure 1.8. The CRT testing process on the index finger. The left diagram shows that the external pressure (applied by pinching) blanches the tested index finger. Since the external pressure has pushed the blood out, the colour of the tested area under the pressure has changed to white. The right diagram shows the blood refilled back to the tested area after releasing the pressure. The time taken for the tested area to regain its colour is called the Capillary Refill Time (CRT) (source: [21]).

In World War 2, CRT was used to estimate the degree of shock in battlefield survivors. At that time, although it was imprecisely used, it classified no/slight/severe shocks in normal/definite slowing/very sluggish groups [29]. The first record of medical use of CRT was as part of the numerical trauma score in 1981. In published literature, the

upper limit of the normal CRT is 2s and is age and temperature dependent [29, 30]. Since CRT is highly subjective and observer dependent, there is no clearly accepted process by which CRT measurement should be performed. Generally speaking, the distal finger, the nail bed and the sternum are recommended as the CRT measurement areas. The pressure is externally exerted on these areas for 3 to 5 seconds in order to cause blanching. The normal CRT for children is less than 2 seconds [31].

The predominant method of CRT measurement is through manual assessment of the time taken for colour to return to the skin. However, there is evidence to suggest that the manually assessed CRT is heavily affected by the bias from the background light conditions, a lack of standardisation of both external applied pressure and blanching time, subjectivity of normal skin colour, and observer-dependent manual assessment of time [32]. Therefore, it is hoped to overcome some shortcomings of manual CRT by standardising the test. In addition, a pressure sensing system will be useful for standardising the optimum blanching pressure and duration which are currently poorly standardised. As new methods of automating CRT measurement are in the early stages of development, it is not yet established how accurate measurements will need to be without further clinical investigation.

1.3 Aims and Objectives

According to the motivation of this research as described in the section 1.1, this research aims to develop an optical fibre based system for S_{pO_2} and CRT measurements, and to analyse the sensor performance under different contact pressure levels. The research investigates whether simultaneous pressure and PPG measurement can improve the performance of systems for S_{pO_2} and CRT measurements. The hypothesis of this research is that knowledge of the contact pressure can improve the accuracy of these measurements.

The above research aim raises the research project objectives described as follows:

- To review the literature related to the optical fibre based pulse oximeter design, and the pressure effect on the performance of PPG systems. The outcomes of this review are described in Chapter 2.
- To develop an optical fibre based pressure sensing system with high accuracy and pressure sensitivity. Details are provided in Chapter 3.

- To develop an integrated fibre based pulse oximetry system which can detect the PPG signals and skin contact pressure simultaneously, and assess the quality of obtained PPG signals using different kinds of signal quality index. Details are provided in Chapter 4.
- To analyse the performance of the integrated pulse oximetry system under different contact pressure levels in order to find the optimum contact pressure for S_{pO_2} measurement. Details are provided in Chapter 4.
- To apply the designed PPG system in CRT measurements. Details are provided in Chapter 5.

The further study of the research and improved performance of the designed system is discussed in Chapter 6.

1.4 Thesis Construction

Chapter 1 covers the introduction of this thesis. In Section 1.1, the motivation of the research is described. In Section 1.2, the background knowledge of this research is introduced.

Chapter 2 is concerned with the literature review of this thesis. In Section 2.1, the mathematic equations for blood oxygen saturation calculation are introduced. Section 2.2 discusses the previous studies for designing pulse oximeters. Section 2.3 shows the work that has been carried out using an FBG to measure loaded pressures. Section 2.4 briefly introduces the capillary refill times. Section 2.5 describes the novelty of this research. Finally, Section 2.6 draws the conclusion.

Chapter 3 reports the characterisation and calibration work of the FBG sensing patch. Section 3.1 provides the configuration of the FBG patch. Section 3.2 describes the temperature responses of the FBG sensor. Section 3.3 shows the pressure characterisation of the FBG sensor with temperature compensation. Section 3.4 gives the summary of Chapter 3.

Section 4.1 describes the design of the pulse oximetry system which consists of a POF based probe and an opto-electronic system. The characterisation of the designed sensor consisting of signal modulation, stray light immunity and the gain/noise measurement of the analogue front-end, which is discussed in section 4.2. Section 4.3 illustrates the signal processing of obtained PPG including band pass filtering and quality assessment

using three signal quality indices (i.e. signal-to-noise ratio, perfusion index and skewness index). Section 4.4 shows the S_{pO_2} test results of 10 volunteers under different temperature or contact pressure situations. Section 4.5 closes Chapter 4 with summary and suggestions for further work.

In Chapter 5, it firstly discusses how to process the intensity and pressure data recorded by the designed pulse oximetry sensor to measure the capillary refill time (CRT) (i.e. refilling signal extraction, normalisation, two-parts fitting process and thresholds calculation). Section 5.2 presents index finger CRT test results of 10 volunteers.

Chapter 6 closes with a summary and recommendation for future study. Section 6.1 provides discussion of each of the main experimental chapters, Section 6.2 concludes the whole thesis whilst section 6.3 gives suggestions for further work.

Chapter 2 Literature Review

Chapter 1 has introduced the background knowledge of pulse oximetry and capillary refill time (CRT) measurements. This chapter provides an overview of previously published research and experiments in pulse oximetry design and CRT measurement, and discusses the novelty of the research described and undertaken in this thesis.

In this chapter, the blood oxygen saturation equation will be derived and its implementation in both transmission and reflection mode settings discussed. The usage of reflectance mode deployment and subsequent rationale of using plastic optical fibres (POFs) will be justified. The importance of optimum contact pressure application and the deployment of FBGs by other workers will be reviewed along with previous research of CRT measurement. Finally, the novelty of this research consisting of using 45° cleaved end optical fibres for pulse oximetry and housing a FBG sensor in epoxy patch to record the contact pressure will be discussed.

2.1 Pulse Oximetry Equations for Blood Oxygen Saturation Measurement

As mentioned in section 1.2.1.3 Pulse oximetry (PO) is an optical, non-invasive, reliable, real time and continuous blood oxygen saturation measurement method. During the Second World War, the first practical aviation ear oximeter was designed by Millikan and has been used as an early warning sign for pilots in under-pressurised cabins [33]. The initial effort to establish pulse oximetry as a mandatory standard procedure in administering general anaesthetic originated in United States during the 1980s, and succeeded in 1987 to set pulse oximetry as standard procedure for patient measurement during anaesthesia [34]. Subsequently, PO was quickly utilised in other medical units such as emergency rooms, recovery rooms, neonatal units and intensive care units [35].

Pulse oximetry is based on the technique of using PPG signals to estimate the percentage of the oxy-haemoglobin over the total haemoglobin in the arterial blood. As introduced in section 1.2.1.1, haemoglobin was discovered in 1860 as the carrier of oxygen which is also the coloured substance in blood [36]. At the same time, it was also found that the haemoglobin solution's absorption of light (visible) varied with

different degrees of oxygenation [37]. This is because the haemoglobin has two common forms: oxy-haemoglobin and deoxy-haemoglobin. The absorption spectra of these two different types of haemoglobin is shown in figure 2.1.

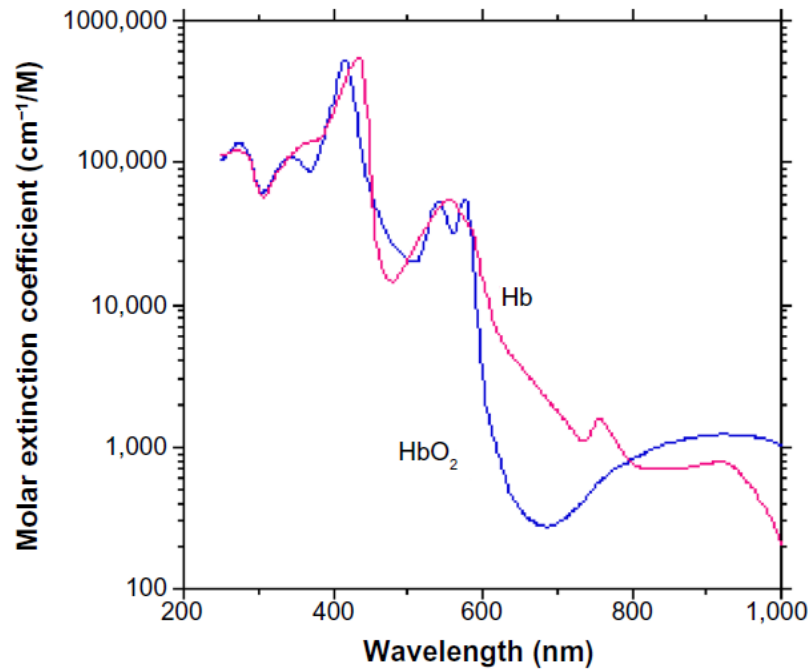


Figure 2.1. Absorption spectra of the oxygenated (blue) and deoxygenated haemoglobin (red) molecules. In the red and the near infrared (NIR) regions, the absorption is relatively low. There also exists large differences of the extinction coefficient between HbO_2 and Hb in red and NIR regions (source: [21]).

Because the arterial blood is oxygenated then a PO effectively only monitors arterial blood volume changes when measuring blood oxygen saturation. In tissues, although the majority of light in the red and near-infrared regions is absorbed by the haemoglobin, other chromophores (such as melanin and myoglobin) can also absorb light in this same region. Furthermore, venous blood, containing less oxygenated haemoglobin, also absorbs light in the same spectral region (red and near infrared) as the arterial blood [21]. Thus, pulse oximetry design focuses on measuring the blood oxygen saturation in the arterial blood, by isolating the absorption of arterial blood from the total absorption. Since only the artery has pulsatile components in the blood flow, the method of determining S_pO_2 by measuring changes in absorbance over time can exclude the influence of venous and capillary blood and other stationary tissues from S_pO_2 calculation [38].

From the previous discussion, it can be seen that the light attenuation coefficient (i.e. extinction coefficient) of the arterial blood varies with different arterial oxygenation degree. Assuming that the dominant absorbers in the blood are oxy- and deoxyhaemoglobin, the extinction coefficient of the arterial blood ϵ is a function of the

extinction coefficient of the oxy-haemoglobin ϵ_O , the extinction coefficient of the deoxy-haemoglobin ϵ_D and the arterial oxygen saturation (S_aO_2) shown in equation 2.1 [21].

$$\epsilon = \epsilon_O \times S_aO_2 + \epsilon_D \times (1 - S_aO_2) \quad (2.1)$$

From equation 2.1, it can be seen that the extinction coefficients of oxy/deoxy-haemoglobin (ϵ_O/ϵ_D) can be used to assess the S_aO_2 of subjects. Based on the different light absorption spectra for two different types of haemoglobin (Hb and HbO₂), and by analysing two different wavelengths of light one can use the corresponding pulsatile (PPG) signals to calculate the blood oxygen saturation – the technique is called pulse oximetry. The PPG is the measurement of light absorption changes according when the volume changes in the pulsing arterial blood. Its utility in calculating the blood oxygen saturation in the artery was discovered in 1970s [39]. The typical PPG signal is shown in Figure 2.2.

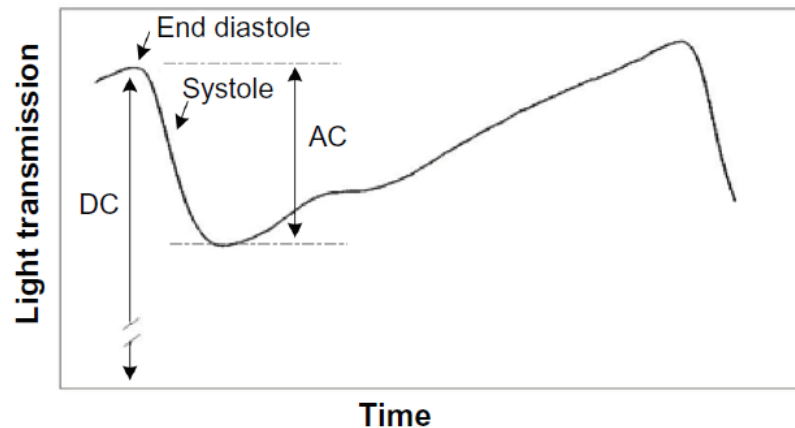


Figure 2.2. Typical photoplethysmography signal. The cardiac systole will decrease the light transmission of the PPG signal whilst the cardiac diastole will increase the light transmission. At the end of the diastole, the transmitted light reaches to the highest value (source: [44]).

Figure 2.2 illustrates that the systolic increase in arterial blood volume contributes to the decrease in the light level of transmitted PPG signals. During the systole, there is more blood flowing in the arteries than during the diastole, leading to an increase of the diameter of the arteries [40]. These diameter changes in the arteries affect the light attenuation of PPG signals, which will be discussed later. Section 1.2.1.2 described that the PPG sensor used LEDs to illuminate light into the skin, and then the transmitted/reflected light is collected by using the photo-detector. Based on the Beer – Lambert law, the PPG sensor can be simplified as a model shown in figure 2.3.

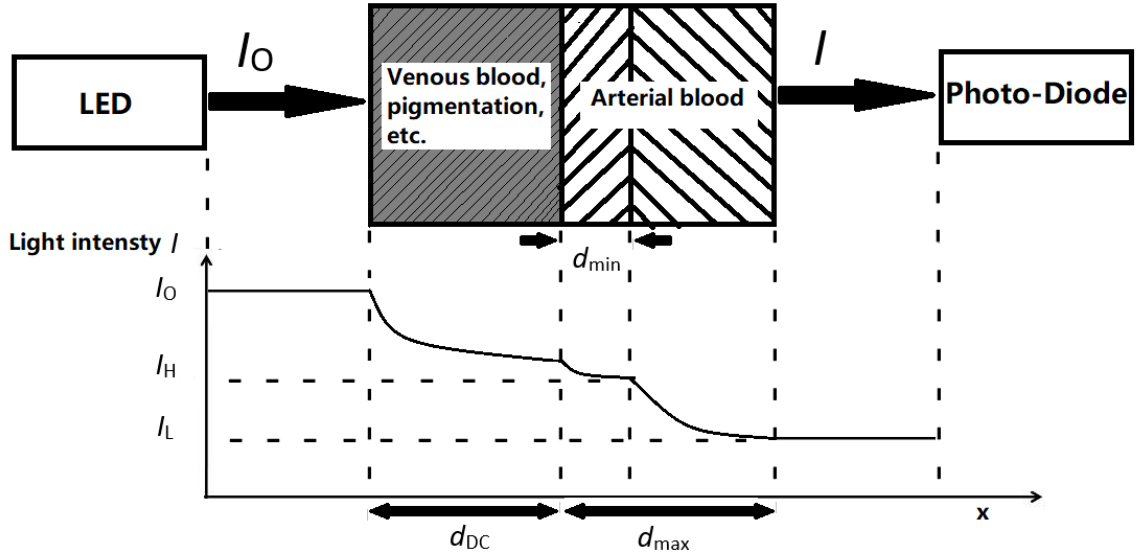


Figure 2.3. Beer-Lambert law in PPG sensor. The DC component reflects the non-pulsatile part of the tissue such as absorption of the venous blood, pigmentation, bone, skin and non-pulsatile part of arterial blood which absorb a certain amount of light from the initial light I_0 . The DC component effective optical path length is $d_{DC} + d_{min}$. At the end of the diastole, the optical path length of the arterial blood part is d_{min} . During the systole, the optical path length of the arterial blood reaches to d_{max} which is the longest (source: [21]).

The model shown in figure 2.3 illustrates that the light intensity was varied with the different amount of arterial blood flowing in the arteries. In accordance with the Beer-Lambert law, the light intensity I (at any point d) is a function of the initial light intensity I_0 and the effective optical path length d of the tissue (non-pulsatile and pulsatile parts) ranging from $d_{DC} + d_{min}$ to $d_{DC} + d_{max}$ as shown in equation 2.2 [24].

$$I = I_0 \times e^{-\varepsilon(\lambda) \times c \times d} \quad (2.2)$$

$\varepsilon(\lambda)$ is the extinction coefficient of the total absorbing substance at wavelength λ , c is the concentration of the total absorbing substance, and d is the optical path length.

The previous paragraph explains that the optical path length “ d ” was varied from $d_{DC} + d_{min}$ to $d_{DC} + d_{max}$. Since the $d_{DC} + d_{min}$ presents the optical path length of the non-pulsatile parts (stable), then the optical path length is determined by the diameter changes of the artery. At the end of the diastole, the optical path length reaches a minimum of $d_{DC} + d_{min}$. The amount of light, I , received reaches to its highest peak (I_H) as the equation 2.3 below describes. During the systolic phase, the diameter of the artery vessels continue to increase up to the maximum d_{max} . The total optical path length is at its maximum of $d_{DC} + d_{max}$. Thus, the tissue absorbs the largest amount of light (I_H) at this moment, viz:

$$I_H = I_0 \times e^{-\varepsilon_{DC}(\lambda) \times c_{DC} \times d_{DC}} \times e^{-[\varepsilon_{Hb}(\lambda) \times c_{Hb} + \varepsilon_{HbO2}(\lambda) \times c_{HbO2}] \times d_{min}} \quad (2.3)$$

In a similar manner the light intensity I reaches its lowest peak I_L depicted by equation 2.4 below:

$$I_L = I_0 * e^{-\epsilon_{DC}(\lambda) \times c_{DC} \times d_{DC}} e^{-[\epsilon_{Hb}(\lambda) \times c_{Hb} + \epsilon_{HbO2}(\lambda) \times c_{HbO2}] \times d_{max}} \quad (2.4)$$

From equation 2.3 and 2.4, it can be deduced that the light intensity, I , arriving at the photo-diode is a function of the diameter of the arteries and arterioles. In other words the only variable of the function is the diameter of the arteries and arterioles changing from d_{min} to d_{max} during the cardiac cycle. In order to deduce the function of the intensity of light I , Δd is defined as the change in diameter of the arteries and arterioles (ie. subtracting d_{min} from d_{max}). Then, the light intensity, I , can be written as:

$$I = I_H * e^{-[\epsilon_{Hb}(\lambda) \times c_{Hb} + \epsilon_{HbO2}(\lambda) \times c_{HbO2}] \times \Delta d} \quad (2.5)$$

Before proceeding to calculate the blood oxygen saturation, the light intensity I obtained at the photo-diode is required to be normalised. As already described, pulse oximetry detects and analyses two different wavelength light signals to calculate the blood oxygen saturation. The problem is that the two light sources may emit different light intensity levels. In addition the photo-diode utilised will have different sensitivity for different wavelengths of light (responsivity). Further, the tissue absorption and effective path length will vary widely from patient to patient along with the probe site. Due to these issues, in 1991, Kock and Tarassenko proposed to normalise different PPG signals, which were detected by the same probe, before comparing them [41]. The normalised equation 2.6 derived from equation 2.5 is:

$$I_n = I/I_H = e^{-[\epsilon_{Hb}(\lambda) \times c_{Hb} + \epsilon_{HbO2}(\lambda) \times c_{HbO2}] \times \Delta d} \quad (2.6)$$

Equation 2.6 has expressed that the light intensity I is changing with the changes in the diameter of the arteries and arterioles (Δd). As described in section 1.2.1.2, the light intensity changes in I is the PPG signal. Thus PPG measurement in each wavelength is available to assess the contribution of the pulsatile arterial blood to the total tissue absorbance of light. The light absorbance can be calculated from the natural logarithm of the measured and normalised transmitted light level. The ratio R is now introduced and is used to represent light absorbance by using the normalised light absorbance at the red and the IR regions. The ratio R is defined as [21]:

$$R = \frac{At(R)}{At(IR)} = \frac{\ln\left(\frac{IL(R)}{IH(R)}\right)}{\ln\left(\frac{IL(IR)}{IH(IR)}\right)} \quad (2.7)$$

Where, “At” = $\varepsilon(\lambda) * c * d$ and represents the attenuation of the absorbers in the arterial blood. As equation 2.7 shows, R is a ratio of red and IR reflected light ratios which will help compensate for variations in the light source and detector efficiency. If equations 2.3 and 2.4 are substituted into equation 2.7, the equation 2.8 is acquired as follows:

$$R = \frac{[\varepsilon_{Hb}(\lambda_R) \times c_{Hb} + \varepsilon_{HbO_2}(\lambda_R) \times c_{HbO_2}] \times \Delta d_R}{[\varepsilon_{Hb}(\lambda_{IR}) \times c_{Hb} + \varepsilon_{HbO_2}(\lambda_{IR}) \times c_{HbO_2}] \times \Delta d_{IR}} \quad (2.8)$$

As presented by Chatterjee et.al [42], the mean optical path lengths of red (660nm) and infrared (940nm) for the reflectance pulse oximeter are nearly the same when the source-detector separation is less than 2.5mm. In this research, the distances between the photodetector and two light sources (red and infrared) are 2mm and 2.5mm respectively. As a result, the optical path length for these two different wavelengths (red and infrared) are assumed to be equal in this research. What’s more, as the direction of light propagation after one transport mean free path (about 0.5mm) is random due to multiple scattering, the propagation angle of the light is usually neglected. Using equation 2.1, the ratio R can be defined as:

$$R = \frac{[\varepsilon_{Hb}(\lambda_R) + (\varepsilon_{HbO_2}(\lambda_R) - \varepsilon_{Hb}(\lambda_R)) \times S_aO_2]}{[\varepsilon_{Hb}(\lambda_{IR}) + (\varepsilon_{HbO_2}(\lambda_{IR}) - \varepsilon_{Hb}(\lambda_{IR})) \times S_aO_2]} \quad (2.9)$$

The theoretical equation of S_aO_2 can be deduced from equation 2.9 as equation 2.10.

$$S_aO_2 = \frac{\varepsilon_{Hb}(\lambda_{660}) - \varepsilon_{Hb}(\lambda_{850}) \times R}{[\varepsilon_{Hb}(\lambda_{660}) - \varepsilon_{HbO_2}(\lambda_{660}) + (\varepsilon_{HbO_2}(\lambda_{850}) - \varepsilon_{Hb}(\lambda_{850})) \times R]} \quad (2.10)$$

A typical empirical calibration curve for R versus S_aO_2 is shown in Figure 2.4. The figure plots the theoretical calibration curve and empirical calibration curve for transmission pulse oximeters. Another calibration curve would be required for reflectance mode SpO₂.

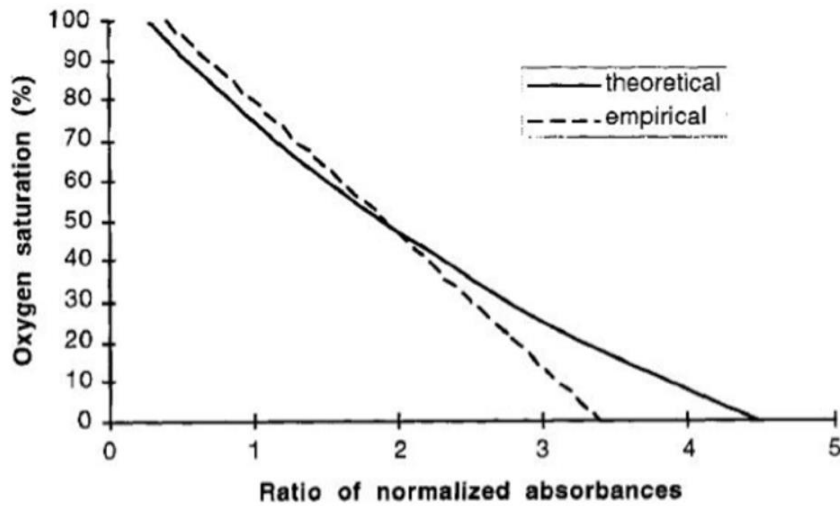


Figure 2.4 Calibration curves for pulse oximeters for transmission pulse oximeters. The solid line is the theoretical calculation curve based on Beer-Lambert law and equation 2.10. The dashed line is the empirical calibration curve. The empirical curve can be fixed to a second order polynomial (source: [21]).

In order to simplify the calculation of blood oxygen saturation, in 1989, Mendelson and Kent modified equation 2.10 of the theoretical calibration curve as follows:

$$S_{pO_2} = \frac{(k_1 - k_2 \times R)}{(k_3 + k_4 \times R)} \quad (2.11)$$

Here, in equation 2.11, the extinction coefficients in equation 2.10 were replaced by four constants (K_1 , K_2 , K_3 and K_4) which were determined from the best fit to the in-vitro measured data from clinical studies. Equation 2.11 clearly shows that the relationship between S_{pO_2} and the R ratio is non-linear. However, over a small region, a linear approximation can be applied. In 2008, Stuban and Masatsugu published work illustrating that linear regression could be used in the range of reflectance S_{pO_2} from 86 to 100% with a relatively good accuracy (2.76% average error) [41, 43]. Equation 2.12 below represents the linear regression of the S_{pO_2} calculation over this range of S_{pO_2} percentage. Since the designed pulse oximeter in this research is based also on a reflectance mode device then equation 2.12 is applied to calculate S_{pO_2} in this thesis:

$$S_{pO_2} = K_1 \times R + K_2 \quad (2.12)$$

K_1 and K_2 are constants determined from the best linear fit to the in-vitro measured data from this study.

Although the conventional design of the pulse oximetry system introduced above is widely applied in medical and health care aspects, it has some limitations. First of all,

the relationship between R ratio and blood oxygen saturation is determined experimentally but not directly from the consideration of light absorption in HbO₂ and Hb based on the Beer-Lambert law. This is due to the reason that light scattering in tissue and blood affects the path length and attenuation of light in tissue. In this case, empirical calibration between R ratio and the blood oxygen saturation for the pulse oximeter is required [44]. Secondly, the conventional pulse oximeter design is based on the assumption that only HbO₂ and Hb in the blood absorb light. However, adult blood contains other dysaemoglobins apart from HbO₂ and Hb such as methaemoglobin (MetHb) and carboxyhaemoglobin (COHb) which absorb and scatter light in the wavelengths applied in pulse oximetry. In this case, it will cause an error in S_PO₂ measurement [45, 46] Thirdly, the low perfusion caused by vasoconstriction will result in decreased PPG signals which reduces the accuracy of the pulse oximeter. The final limitation is that the accuracy and reliability of the conventional pulse oximeter could be reduced by motion-artefact noise.

Some research has attempted to use temporal, frequency and spatial domains to take into account the scattering effects but estimating the path length of the scattered light. One of the most applied methods is to directly measure the mean time of flight of the temporal point spread function (TPSF) [47]. However, this method requires high speed detectors which are expensive [48]. Other researchers have also applied spatial domain methods using multiple detectors but this adds complexity to the system [49]. In this thesis, this research is focused on measuring the light intensity at a single position which follows the conventional established pulse oximetry.

2.2 Optical Reflectance Pulse Oximeter Design

2.2.1 Reflectance Mode Pulse Oximeter

Section 2.1 described that the pulse oximetry technique uses PPG signals in two different wavelength to estimate the ratio of the oxy-haemoglobin over the total haemoglobin. Acquisition of these PPG signals can be divided into two different types, namely reflectance and transmission modes simply because of the different physical configuration in each setting.

Transmission systems are usually limited to measure at fingertips and earlobes which makes the transmission mode pulse oximeter less versatile. For reflectance systems, they are theoretically able to detect the PPG on any surface of the body by arranging the LEDs and the photo-diode to be sited on the same side of the skin. By comparison with the transmission mode pulse oximeter, the reflectance pulse device offers more flexibility.

The dependence of the pulse oximeter probe on body site location will not only cause inconvenience for measurement but also compromises the sensor under low peripheral perfusion conditions. The decreasing blood volume in arteries and changes in vasoactivity can limit the function of pulse oximeters. For example, in the late 1980s, Paulus and Monroe [50], Mihm and Halperin [51] and Alexander et al [52] all reported that poor peripheral perfusion due to hypovolemia, hypothermia and vasoactive medications causes either failing or false display of pulse oximeters. Under normal conditions, the fingertip and earlobe can provide good PPG signals with a high signal-to-noise ratio [22]. However, under low surrounding temperature or low perfusion situations, the arteries will be constricted in order to decrease the heat dissipation and guarantee the blood supply to other critical organs such as the heart, kidneys and the most important organ the brain [53]. This is the intensive regulation which is controlled by the autonomic nervous system. Hence with a poor peripheral perfusion, the accuracy of the pulse oximeter is poor and potentially unreliable [54].

The reflectance pulse oximeter can be used on the forearm, forehead and chest, which enables the oxygen measurement in areas close to critical organs. In this case, the reflectance pulse oximeter is less affected under low peripheral perfusion situations than its transmission counterpart. Due to the advantages of the reflectance mode pulse oximeter being able to be placed on any site of the body then optical fibre sensor design based on a reflectance mode pulse oximetry setting was chosen.

2.2.2 Optical Fibre Sensor Configuration

A pulse oximeter (both transmission and reflectance mode) is composed of two parts – light sources and photo detectors. Normally, the light sources are two high intensity LEDs (red and NIR) whilst the photo detector is a photo-diode that has a typical silicon wavelength response. A transmission pulse oximeter uses a gentle clamp clipped to the finger or earlobe. Two LEDs are located on the upper part of the clip whilst the

photo-diode is embedded on the lower part of the clip directly opposite the LEDs (figure 1.5). For the reflectance mode pulse oximeter, the probe is made flat and is attached to the skin position using typically adhesive tape. Two LEDs are mounted on one end of the probe whilst at the other end in the same plane is a photo-diode (figure 1.7).

As described in section 1.3, this research aims to design an optical fibre based reflectance pulse oximetry system. Compared to conventional reflectance pulse oximetry systems, the optical fibre based pulse oximetry design has some drawbacks. Firstly, many previous optical fibre based reflectance PPG sensors applied a large number of optical fibres due to the relatively low coupling efficiency of fibres [13, 55-57]. What's more, the optical fibre based PPG sensor design requires additional consideration about the optical fibre configuration in order to reduce the bending loss [58-60].

However, the optical fibres can still be useful in healthcare applications because of four reasons listed as follows:

1. As the optical probes of conventional pulse oximeters consist of metallic parts and electrical wires, the optical fibre based design makes the sensor more comfortable and convenient for the daily use.
2. In some specific applications exposed to strong electromagnetic radiation like MRI setting, the conventional sensor is not appropriate and can damage skin [33]. However, the optical fibre can be applied as it is insensitive to electromagnetic radiation.
3. The optical fibre enables PPG measurement within a small area and isolates the tested tissue from the light source electrically and thermally. In this case, the optical fibre based PPG system has been applied in brain issue, splanchnic organ and oesophageal pulse oximetry design [61-63].
4. The optical fibre PPG system can also work with the optical fibre Bragg grating sensor, in case the integrated system could measure the other physiological factors such as temperature, humidity and contact pressure simultaneously [64-66].

The utilisation of the optical fibre to transmit light was first demonstrated over 150 years ago [67]. More recently, in 1967, Derick and Synder [68] published a patent on the use of polymeric optical fibres (POF) in textile structures for light coupling. Although glass fibres have significantly lower light attenuation and a higher transmission frequency bandwidth, the POF still became popular in the late 1990s due to the demand of the short range digital transmission system. Compared to inorganic glass fibres, POFs are cheaper and easier to process making it more popular in short-range applications. In 2005, Koncar [69] processed optical fibres in a textile to build a data communication device [56]. In 2006, Boczkowska and Leonowicz [70] developed sensors by using polymeric optical fibre fabrics (POFFs) to transfer signals to processor units for the measurement of temperature, strain, and the sensing of gases, biological spices and odour. In 2008, Rothmaier et al [55] produced a plastic optical fibre based sensor to measure pressure. POFFs enriches the range of illuminating products due to its flat and flexible structure in 2D design. In 2006, a European Union funded research project deployed silica fibres and POFs to develop a wearable measurement system - called 'Optical fibre sensors embedded into technical textile for healthcare' (OFSETH FP6-IST-2005-027869). In consideration of the advantages of POFs, this research consider POFs that could in future be used photonic textiles to measure the blood volume changes.

In 2006, Phillips et al. [71] built a reflectance optical fibre oximetry system which obtained red (660nm) and near infrared (850nm) PPG signals from the dura of spinal cords of rats. In the system developed, optical signals propagated through optical fibres from/to the opto-electronic system. The schematic of the system is shown in figure 2.5 [71].

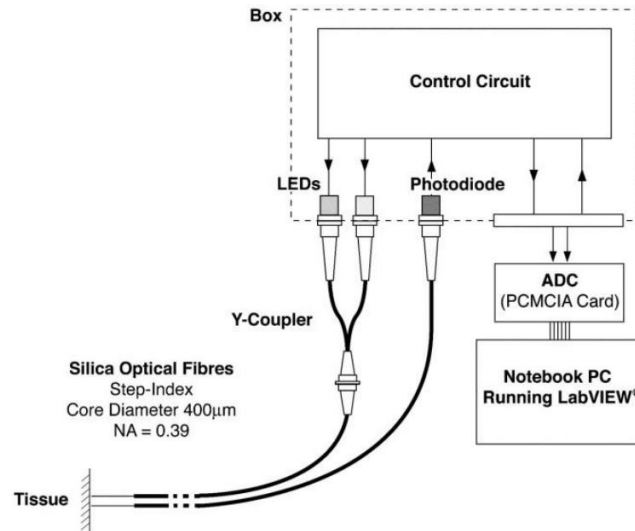


Figure 2.5 Reflectance optical fibre based oximetry system. The electrical system drives two different wavelength LEDs (660nm and 850nm). For each fibre, one end is cut flat and polished, the other end is terminated with an SMA connector. The Y-coupler in the figure couples two light sources into one fibre whilst the other one fibre transferred reflected light from tissue to the photodiode (source: [71]).

The probe of the sensor shown in figure 2.5 consists of two silica optical fibres (SpecTran Speciality Optics, Avon, CT, USA) to transfer light from LEDs or to the photodiode. The schematic of the probe positioned vertical to the skin is shown in figure 2.6. Although this proves the possibility of using optical fibres to transfer the light for pulse oximeters to measure S_pO_2 of subjects, the configuration of this sensor is not convenient in the design of 2D photonic textiles or flat sensors.

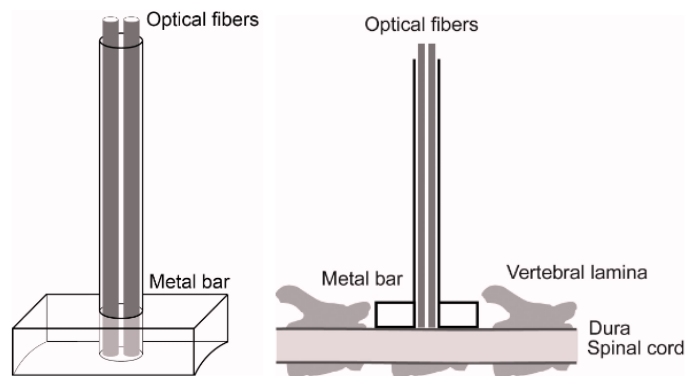


Figure 2.6 Apparatus for rat spine core PPG measurement. Two different wavelength lights are coupled into one optical fibre by using a Y-coupler. The other optical fibre is applied to receive the backscattered PPG signals (source: [71]).

In 2014, Markus et al [72] designed a luminous photonic textile for reflective pulse oximetry measurements. The schematic of the photonic textile is shown in figure 2.7(a) and has embroidered POFs (Zeonor 1020R core and THVP 2030GX cladding). The POFs applied in this design were produced using a melt-spinning process [73]. These

optical yarns were then embroidered on the fabric using an ERA TM 0625 embroidery machine. During the embroidering process, the underlying carrier fabric textile was set perpendicularly to a set of needles equipped with a monofilament optical fibre. Consequently, the shuttle stitched POFs on the surface of the textile. In this research by Markus, two patterns ('M' and 'V') of layered POFs were sewn on the fabric surface and this is illustrated in figure 2.7(b). By testing and characterising both patterns, it was found that the 'V' pattern stitched fabric was superior due to its 35% higher coupling-in light efficiency and less rigidity than the 'M' pattern fabric. Figure 2.7 (c) is a photograph of the designed luminous textile. The light coupling efficiency of this textile was high enough to obtain good PPG signals since dozens of POFs are embroidered to carry out the light in/out coupling process in a small area of the textile [74].

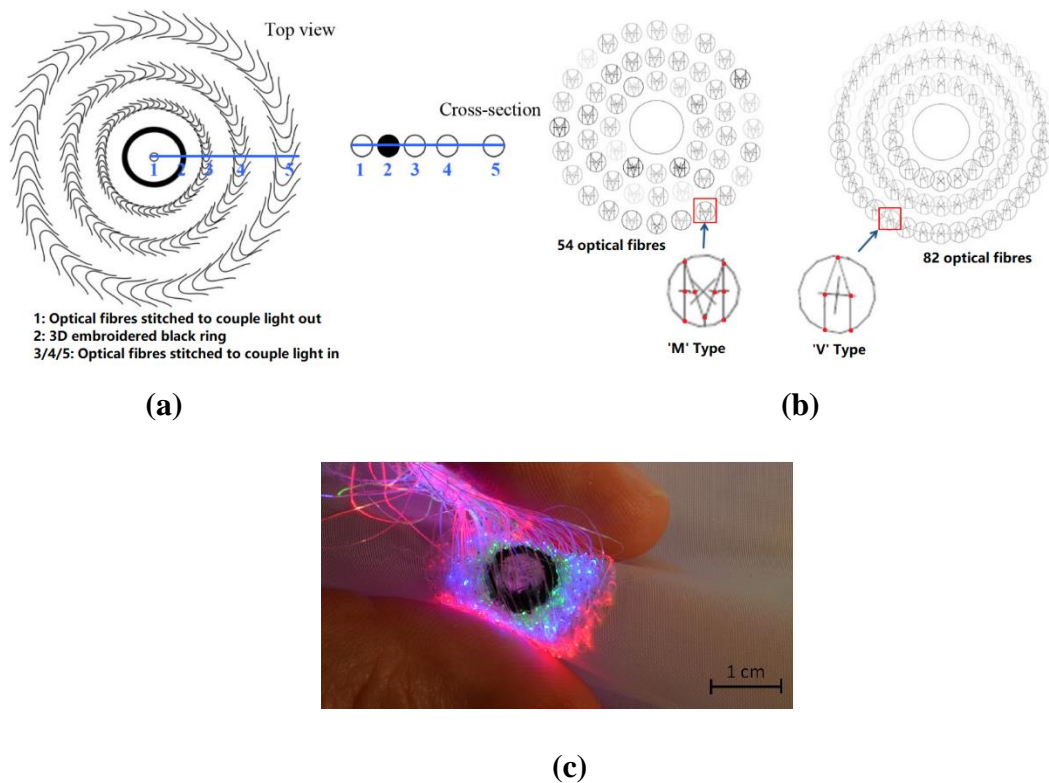


Figure 2.7 Photonic textile reflectance pulse oximeter. (a) Schematic of the top view. Point 1 is the POF stitched for illumination. Point 2 is a black ring to block the light to avoid light coupling directly from the source to the detector. Points 3,4 and 5 represents three rings of stitched POFs to detect light. Each "V" – shaped line in the rings represents a portion of one POF. (b) Illustrates two types of embroidery patterns for stitching the POFs. Red dots in the zoomed-in regions indicate the fixation points with the underlying textile carrier. For the 'M' type pattern (left diagram), 54 POFs are used whilst 82 POFs are used in the 'V' type (right diagram). (c) Photograph of the photonic textile. The fibre bundles of each ring (3,4 and 5) were connected to LEDs (source: [74]).

In 2017, Quandt et al [57] also built a photonic textile based heart rate measure detecting different wavelength (600 to 1000 nm) PPG signals. Figure 2.8(a) shows a schematic of the designed sensor. A continuous melt-spinning process was again required to produce the POFs applied in this design [75]. They used a melt-spinning manufacturer (Fourné Polymertechnik) to spin two polymers to create the core-cladding-structure (Zeonor 1020R core and THVP 2030G sheath polymer). These POFs are then embroidered into moisture-wicking fabrics, and light sources are coupled as shown in figure 2.8(b). Figure 2.8(c) shows a photograph of the designed photonic textile.

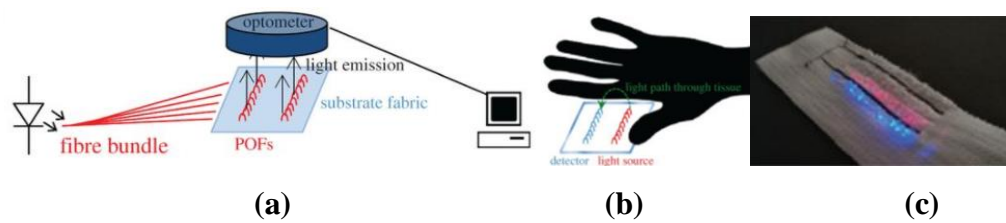


Figure 2.8 Schematic of photonic sensing textile. (a) Test-bench used to check the light coupling efficiency of the photonic sensing textile. Each POF stitched was bended to a certain degree. (b) Schematic of the photonic textile. (c) Photograph of the actual photonic textile (source: [57]).

The above previously published studies have shown that these photonic textiles can obtain clear PPG signals using embroidered POFs. However, this method required dozens of POFs over a small area. The increasing number of POFs used increases the possibility of the fibres intertwining which will deform the POF and reduce the light transmission efficiency. Moreover, the difficulty of stitching or embroidering the photonic textile will be increased if a large number of POFs are deployed. In order to reduce the number of optical fibres used in the textile, it is necessary to increase the optical coupling efficiency of the optical fibres. The research in this thesis has applied fibre end-cleavage methods to increase the light coupling efficiency of the POFs. Here, the designed 2D pulse oximeter which will be described later in this thesis, only requires three POFs to measure the S_{pO_2} .

2.3 Fibre Bragg Grating Contact Force Sensing

As described previously, pulse oximeters are sensitive to the peripheral perfusion condition of subjects. One factor that will affect the peripheral perfusion around the oxygen saturation measurement zone is the external force applied by the pulse oximeter probe. In 2006, Russel and Yitzhak [76] built a forehead reflectance pulse oximeter, and found that the contact force between the sensor and the forehead skin affects the forehead reflected pulse oximeter performance. They demonstrated that the absolute S_{pO_2} error under different contact forces, was a minimum over the 8-12kPa pressure range. This is because the forehead sensor obtained on average the largest PPG amplitudes over the contact force in this pressure range [76]. Dresler [77], describes the minimisation of motion and pressure artefacts on wearable forehead pulse oximetry probes. According to Russell, the contact pressure of 60mmHg (~8kPa), provided in this case by an elastic band, can reduce PPG and S_{pO_2} measurement errors [77]. In 2012, Pedro Filipe demonstrated how contact pressure has a significant effect on PPG and S_{pO_2} measurement accuracy [78]. In summary many studies have previously illustrated that the applied probe contact force will affect the S_{pO_2} measurement accuracy. Although a mathematical relationship between contact pressure and is not yet established, it nonetheless may be beneficial to measure pressure and the resultant oxygen saturation simultaneously.

In previous studies, several types of pressure sensors have been applied for measuring contact force, which are piezoelectric, piezoresistive, resistive and capacitive sensors [79, 80]. Piezoelectric sensor outputs a voltage (electric field) signal in response to the external applied pressure [80]. A piezoresistive sensor is made of semiconductor material of which the electrical resistivity is changes with the force applied [79]. For resistive and capacitive sensors, the external force applied will deform their constructions which result in resistive or capacitive changes [81, 82]. However, all of these pressure sensors have electrical wire connection configurations, and provide electrical signal outputs (either voltage or current) [80]. As described in section 2.2.2, the electrical wire connection configuration makes the sensor inconvenient and uncomfortable in daily life, and comparatively sensitive to electromagnetic radiation. In order to solve these problems, this research has utilised a FBG fibre sensor in the design.

Although extensive researches have been carried out on measuring PPG signals and pressure signals simultaneously, no single study exists which combine a fibre optic pulse oximeter with a parallel fibre Bragg grating sensor. As a result this thesis demonstrates the deployment of an integrated POF pulse oximeter and an FBG sensor into the same sensor. The designed sensor will record both oximetry and pressure signals concurrently. It was also found that the designed sensor is capable of measuring capillary refill time – see section 2.4.

A fibre Bragg grating (FBG) consists of a periodic variation of the core refractive index over a short length of an optical fibre. At a particular grating period, light is reflected by the grating at a specific wavelength (the Bragg wavelength). The effective refractive index and the grating period of the FBG determine the reflected light wavelength (Bragg wavelength - λ_B) [83]. The equation of the Bragg wavelength is given is:

$$\lambda_B = 2 \times n_{\text{eff}} \times \Lambda \quad (2.13)$$

Where n_{eff} and Λ are the effective refractive index of the FBG fibre core and the period of the index of refraction variation of the FBG respectively.

Figure 2.9 shows the effect of strain on the FBG where the grating parameter changes shifts the Bragg wavelength by $\Delta\lambda_B$. These changes can be caused by the effect of hydrostatic pressure, temperature and strain on the fibre. Equation 2.14 shown below defines the Bragg wavelength shift $\Delta\lambda_B$ in the FBG [84].

$$\Delta\lambda_B = K_T \times \Delta T + K_{\sigma_z} \times \sigma_z + K_P \times P \quad (2.14)$$

Where K_T is the sensitivity coefficient for the environment temperature, K_{σ_z} is the sensitivity coefficient for strain along the axis and K_P is the sensitivity coefficient for transversely loaded pressure which is vertical to the axial. K_T , K_{σ_z} and K_P are material dependent, but for the silica optical fibre used in this work they are typically 19pm/°C (K_T), 1.21pm/ $\mu\epsilon$ (K_{σ_z}) and 0.022pm/psi (K_P). [85] [86] [87] ΔT , σ_z and P are the variance of temperature, the axial strain and the loaded pressure respectively.

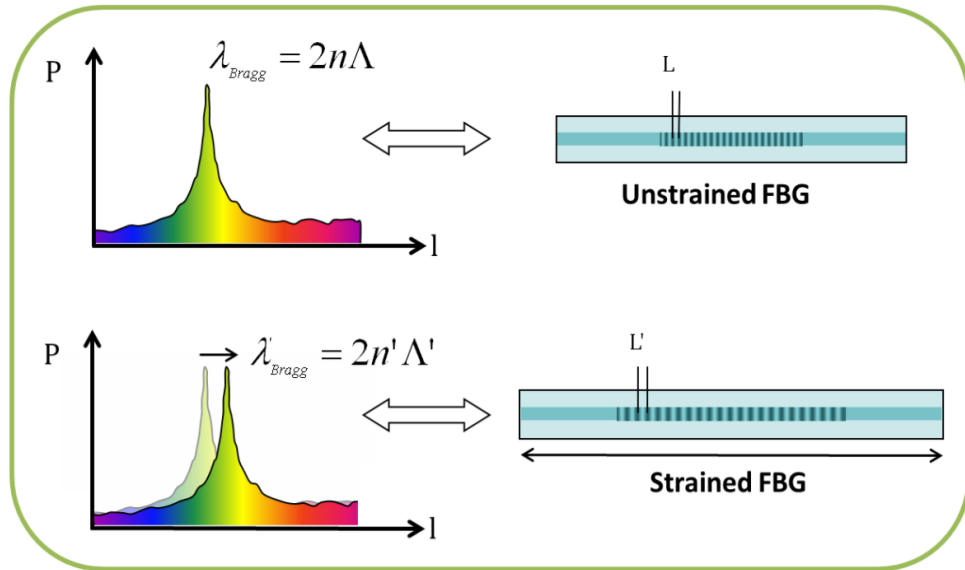


Figure 2.9 FBG response as function of strain. Here, n and n' are the unstrained/strained refractive indices, and Λ is the period of the index of refraction variation of the FBG equal to the grating period L . When the FBG is strained, the grating period L is increased as well as Λ . Thus the Bragg wavelength is increased as well (source: [77]).

The main weakness of using an FBG to measure the contact force is its low sensitivity to downward and upward applied pressure to the FBG [88]. Originally, FBGs were applied to large scale industrial uses experiencing very high pressure load tests in settings such as geo-technical tests. Here the pressures are usually higher than 50 GPa [89, 90] but in the research of this thesis the pressures are considerably lower at 5-25 kPa and hence it is necessary to increase the pressure sensitivity of the FBG sensor. In 1996, Xu et al [88] used a glass-bubble housing to enhance the pressure sensitivity of the FBG. Figure 2.10 illustrates: (a) the schematic of the system set up, and (b) X-section of the fibre Bragg grating in a glass-bubble pressure housing [88].

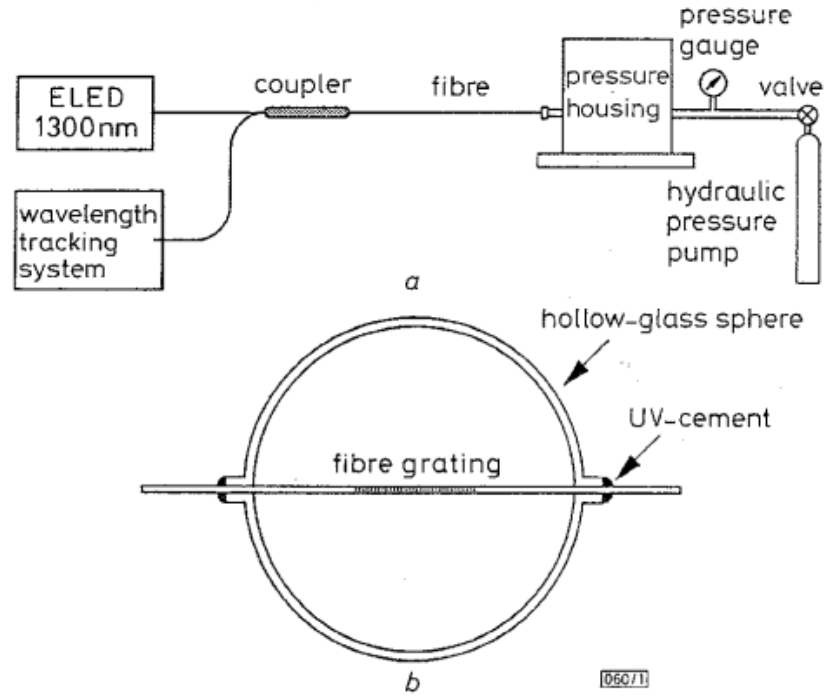


Figure 2.10 FBG pressure sensor using glass-bubble housing. (a) Schematic diagram of experimental setup; (b) Sensing element: fibre Bragg grating in glass-bubble pressure housing (source: [88]).

The glass-bubble housing in figure 2.10 has a greater mechanical compliance which results in an enhancement of pressure sensitivity of the FBG. When the glass housing is pressurised by the hydraulic pressure pump uniformly (as shown in figure 2.10a), the fractional change in the diameter of the housing can be calculated based on the equation as follows [88]:

$$\frac{\Delta d}{d} = \frac{-d \times (1-\mu) \times \Delta P}{(4 \times E \times t)} \quad (2.15)$$

Where $\left(\frac{\Delta d}{d}\right)$, μ , ΔP , E and t are the diameter of the glass-bubble housing, the fractional change in the diameter of the housing, the pressure change, the Poisson ratio, Young's modulus and the wall thickness.

If the bonding between the housing and the fibre is strong, then the fractional change in the diameter of the housing ($\Delta d/d$) results in an axial pressure-induced strain in the fibre grating. As a result a change in the Bragg wavelength (λ_B) occurs. If $\Delta \lambda_B / \lambda_B$ is defined as the fractional change in Bragg wavelength which is also the pressure sensitivity, then the pressure sensitivity can be calculated based on equation 2.16 below [88]. From equation 2.15, it can be seen that the pressure sensitivity of FBG

housing in the glass-bubble can be enhanced by choosing a low Young's modulus material and thin wall thickness housing.

$$\frac{\Delta \lambda_B}{\lambda_B} = (1-p_e) \times \frac{\Delta d}{d} = 0.17 \times \frac{-d \times (1-\mu) \times \Delta P}{(4 \times E \times t)} \quad (2.16)$$

Where p_e is the effective photo-elastic constant for silica which is 0.22.

In 2010, Correia et al [91] described a method of increasing the FBG axial strain sensitivity to downward force (i.e. pressure) by encasing the bare FBG sensor in an epoxy based UV-cured “patch” [91]. As the lower Young's modulus material is more easily deformed under the pressure which generates a strain force along the fibre, the transversely (i.e. axial) loaded pressure sensitivity of the FBG can be significantly increased by covering the FBG with a lower Young's modulus material (such as Epoxy). The schematic of the sensor is shown in figure 2.11. This patch arrangement makes itself potentially useful for contact force measurements of tissue and hence will be deployed in the research of this thesis.

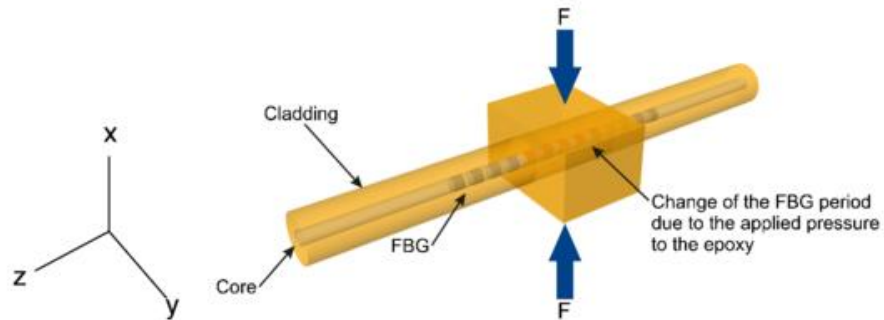


Figure 2.11 FBG embedded within epoxy material. F is applied upward or downward force. When force is applied, the epoxy patch is deformed, and the force is transferred to the fibre as an axial strain. This changes the physical period (the grating period) of the FBG and the refractive index of the fibre over the embedded region (source: [91]).

In addition to the loaded pressure changes any environmental temperature change around the FBG will also result in a Bragg wavelength shift [92]. Therefore, the temperature confounding influence on the FBG sensor needs to be removed. There are various methods of removing this thermal interference which includes: using a second grating in a different material to compensate for the temperature effect [93]; measuring strain and temperature using two super-imposed fibre gratings [94]; cancelling the thermal response through locating surface mounted fibre gratings [92]; and applying a tapered fibre to make a chirped FBG [95]. In the research in this thesis, a pressure-

independent FBG was applied close to the pressure sensing FBG to compensate the ambient temperature effects since this method has been successfully applied in previous research[96, 97]. Detailed information is described in Chapter 3.

2.4 Capillary Refill Time (CRT) Measurement

According to the description in section 1.2.3, the measurement of CRT is based on counting the time for a blanched area of skin to regain its colour after releasing the external pressure. When the external pressure applied pushes the blood out, the large amount of haemoglobin which is the main source of the light absorption is forced out with the blood flow. Thus, the colour of the skin becomes lighter as less light absorbers are present during the blanching. After releasing the pressure, the blood flows back, which returns the light absorbers such as haemoglobin back to the capillary bed. Usually this process is not automated and relies on manual application of an unknown pressure (squeeze until tissue blanches) and use a watch to count the time taken for the blood to return to the tissue. The inter and intra observability is therefore quite large [98]. In this research, the designed sensor measures CRT using the light intensity changes and the applied pressure recording data, which is less dependent on manual operations compared to the method of using a stopwatch to count CRT.

There are various methods to calculate the CRT. As early as 1999, Tibby et al [99] presented their research about the effect of ambient temperature on capillary refill in healthy children. Here, the method applied to calculate the CRT was to press for 5s and then release and use a stopwatch to record the time for the skin to return to its previous colour [99]. In addition to Tibby many previous studies have used this method to count CRT time such as Aasuri et al. (1999), Osborn et al (2004) and Anderson et al. (2008) [99-102]. However, the method of assessing the colour return point by eye is highly subjective and recording the time using a stopwatch will cause further deviations in the CRT results. Therefore, a more reliable and accurate method is required which is presented in the research of this thesis. For example, in 2009, Kviesis-Kipge et al. [103] presented a new methodology for temporal analysis of the capillary refill process by using PPG signals in the blue spectral region. This work demonstrated the possibility of using PPG signals to measure the CRT of subjects. The limitation of this work was lack of the blanching pressure recording. Figure 2.12 illustrates the work of Bezzerides et al [104] in 2017 who presented a new CRT

diagnostic method which set two pre-defined limits (maximum and minimum) as indicators to count the CRT between – namely points 640 (pre-defined first limit) and 650 (pre-defined second limit).

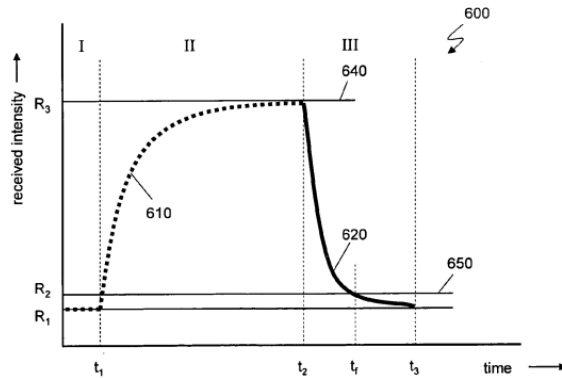


Figure 2.12 Signal representative of blanching of a measurement region and capillary refill within the measurement region. 600 is considered to be an ‘ideal case’ without noise. 610 is the rising curve of light intensity caused by blanching pressure. 620 represents the process of blood refilling back to capillaries. 640 is the pre-defined limit (maximum). 650 is the second pre-defined limit (minimum) (source: [104]).

The blanching pressure applied can also affect the CRT measurement. For example in 2015, Blaxter et al [32] presented a method to calculate CRT with consideration of the applied pressure. In this work, a pump and diaphragm was deployed to blanch the skin. When the air pressure decreased lower than 3.1 kPa, the system will check whether the system has previously pumped the air pressure higher than 3.5 kPa for more than 1s. If this was the case then the system records the data of reflected light intensity from the skin testing area in the following 6s for further analysis. The 6s data record is then signal processed (i.e. normalised, straight line fit and second order polynomial fit), and then used for CRT calculation [32]. In the research of this thesis, within Chapter 5, the pump and diaphragm (and Photodiode/LED) is replaced with a combined FBG pressure sensor and POF pulse oximeter.

The light wavelength chosen to undertake automated CRT measurement is often green (typically 530nm) as this provides the highest contrast while still providing a detectable signal. Cui [105] observed that green wavelength light gave the PPG signal with the best SNR as it was shielded from the random movement of tissue and blood that is present in the deeper layers. This is attributed to lower penetration depth of green light [39]. Ugnell and Oberg [106] also suggested that the PPG signal at 560nm (green) reflects the blood volume in the ascending arterioles that supply the horizontal layer of capillaries, small arterioles and venues which form the vascular bed near the

surface of the skin [17]. This means that the green light PPG signal can reflect more capillary refilling activities than other longer wavelength optical signals. Apart from green light, red and infrared light have also been used as the light source in CRT measurement. For example in 2016, Blaxter et al. successfully detected CRT using three different wavelengths namely 520nm, 640nm and 950nm [32].

2.5 The Novelty of the Thesis

As described above in this section, the accuracy and reliability of the pulse oximeter and the CRT sensor can be increased by recording the contact pressure simultaneously. In this case, this research has developed a probe which combined the POF sensor and the FBG sensor together in order to detect the reflected light signal and the contact pressure at the same time. Although some research has been carried out on integrating FBG and PPG sensors to measure a subject's physiological parameters (e.g. heart rate, body temperature, level of consciousness, blood pressure and respiratory status) [64, 107, 108], no single study exists which combines the FBG contact pressure sensor and the pulse oximeter.

The novelty of this research is therefore to design an optical fibre based pulse oximeter with an FBG pressure sensor placed beneath so as to continuously measure applied pressure. With such a design it is proposed that the performance of the POF pulse oximeter under different contact forces between the sensor and the index finger can be ascertained. By calculating the absolute S_{pO_2} error, the optimum contact force range for the POF oximeter is demonstrated. Further, by analysing the data, this research has developed a suitable signal quality index (SQI) to judge the signal quality under different contact forces. Furthermore the same sensor can also be utilised to measure CRT as a novel measurement method.

In the previous studies of using POF sensors to measure S_{pO_2} values, many optical fibres are used to fulfil the light in/out coupling for pulse oximetry design. In order to avoid the manufacturing difficulty and the fibre intertwining caused by the large number of optical fibres applied, it is required to reduce the number of fibres applied by increasing the light coupling efficiency. In 2011, Phillips et al [109] designed a reflectance PPG sensor (shown in figure 2.13) which attached 45° prisms to ends of optical fibres to increase light coupling efficiency. With higher light coupling

efficiency, only two prism attached optical fibres (i.e. one coupling-out optical fibre and one light coupling-in optical fibre) were applied in this reflectance PPG sensor.

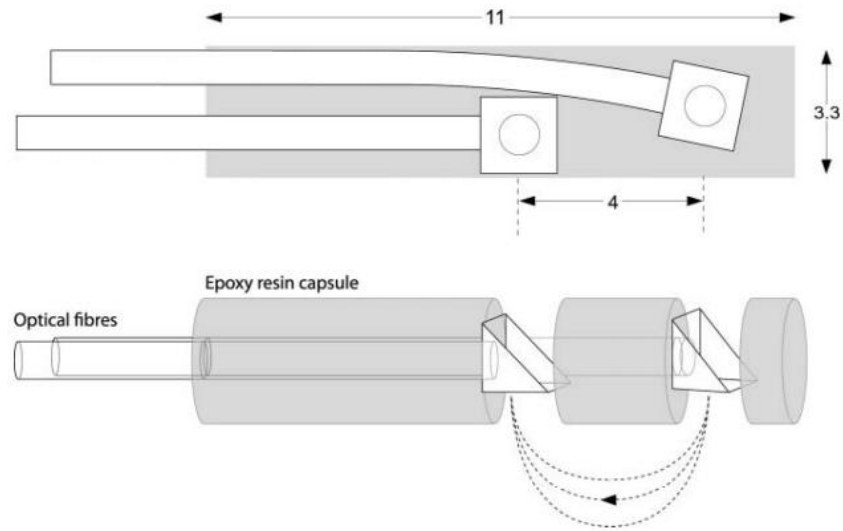


Figure 2.13 Simplified diagram of the fibre optic oesophageal oximetry sensor. The top of each optical fibre is attached to the 45 degree angled glass prisms. The dimensions are shown in millimetres (source : [109]).

In 2016, Davenport et al [72] have published a paper which shows the variation of output intensity with angle for the angle-tipped optical fibre with a 0.48 numerical aperture. In this paper, it placed a power meter 120 mm from the distal tip of the optical fibres (the flat tipped and the 45° angle-tipped optical fibres), and moved around to measure the output intensity at a range of angles. According to the test results, the output intensity of the flat tipped optical fibre was centred on the axis of the fibre, and decreased to 0 at about 30°. For the 45° angle-tipped optical fibre, the output intensity has a peak diffracted out from the tip of the fibre (shifted to about 30°), and a peak reflected from the tip centred around 90° with an average reflectivity of 58%. Figure 2.14 shows that the light is diffracted from the tip of the angle-tipped fibre, and reflected from the tip surface. [72]. In this case, the 45° angle-tipped optical fibre increases the coupling efficiency in the reflection direction (i.e. perpendicular to the axis of the optical fibre) compared to the flat tipped optical fibre. Therefore, in this research, the designed pulse oximeter contains three integrated POFs with 45° cleaved ends embedded in an epoxy resin patch to deliver/collect optical signals from/to the system. Compared to photonic textile based pulse oximeters, this pulse oximetry design reduces the number of optical fibres applied without external attachments.

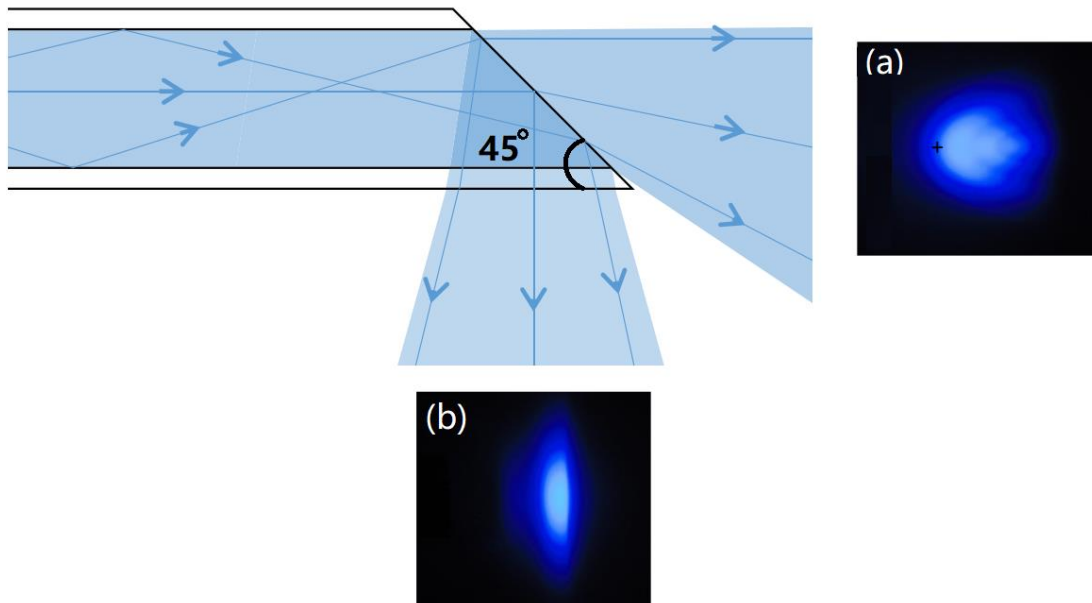


Figure 2.14 Diagram of light reflecting from the side of the 45° end optical fibre as well as diffracting from the tip. The photo of diffracted light (470 nm) from the front of the 45° end optical fibre is shown in black block (a) whilst the reflected light from the side of the 45° end optical fibre is shown in black block (b).(source: [72]).

In this research, two FBGs (pressure sensing and temperature sensing) are written on the same silica fibre to reduce the temperature influence on the pressure sensing FBG. Before encasing the two FBGs into the epoxy (NOA 65, Norland Products, USA) patch, a metal tube is used to cover the temperature sensing FBG, and the end of the metal tube close to the other FBG is sealed – see Figure 2.15. Therefore, the temperature sensing FBG in the tube is free of the pressure load influence due to the metal tube. The Bragg wavelength shift of the FBG in the metal tube is now only related to temperature changes. Thus, this FBG can be applied to measure the temperature changes inside the epoxy patch. Since two FBGs are very close to each other, the surrounding temperature of the two FBGs are assumed to be equal. By adding the compensation (inverted) from the temperature sensing FBG output, the temperature influence on the pressure sensing FBG can be removed.

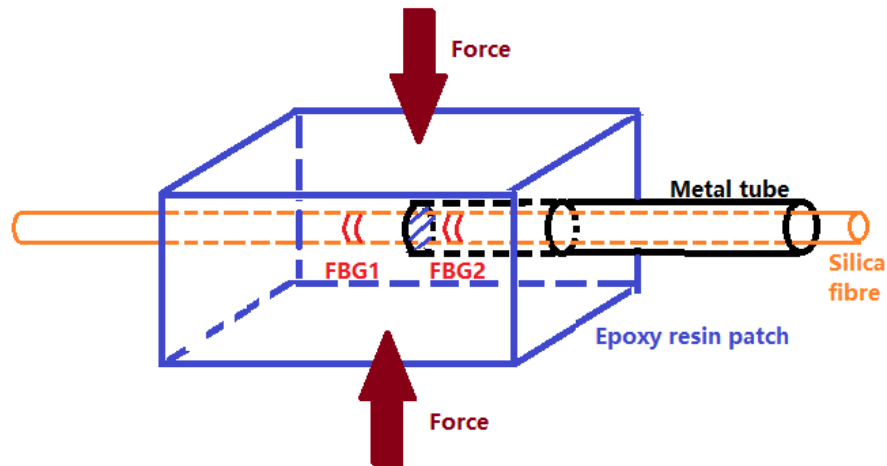


Figure 2.15 Schematic of the FBG pressure sensor. In the diagram, half embedded region of the silica fibre is protected by the metal tube. The end of the metal tube between two FBGs is sealed. Therefore, when the force is loaded on the epoxy patch, only half embedded region of the silica fibre is strained. Thus, the output from FBG1 is influenced by the force whilst the performance FBG2 is unrelated to the force applied on the epoxy patch. Since FBG1 and FBG2 are very close, it assumes that the surrounding temperatures of FBG1 and FBG2 are equal. In this case, FBG1 and FBG2 are influenced by the same temperature changes. Thus by analysing the output of FBG2, the temperature changes can be deduced to compensate the FBG1 output.

2.6 Conclusion

Pulse oximeters using optical fibres have been presented before, however, most of them applied numerous fibres. In this research, only three POFs are used in the pulse oximeter patch with a 45 degree cleavage at one end. A second novelty of the design in this research is to combine the POF pulse oximeter and the FBG pressure sensor into the same patch. Since the pressure is a very important factor for S_{pO_2} and CRT measurement, the designed sensor is available to record the pressure profile simultaneously during oximetry and CRT measurements and remove temperature effects.

For the pulse oximeter function, the design of the pulse oximeter is based on reflectance mode pulse oximetry due to its high flexibility and better performance under the discolouration and poor peripheral perfusion conditions. The POF sensor integrates three 500 μm diameter POFs in an epoxy patch. For each light wavelength (red and IR), only one POF is used to illuminate whilst only one POF is connected to the photo-diode to transfer the reflected light. For future textile applications, fewer POFs required in the textile makes the photonic textile structure more economical and

easier to produce and also reduces the possibility of the POFs intertwining. Beneath the POF sensor, a temperature compensated FBG pressure sensor is used to record the contact force between the finger and the sensor. In this research the effect of contact force on S_{pO_2} measurement can therefore be investigated using this approach.

For the CRT sensing function, this research uses an optical method to measure the optical attenuation changes of the skin. Thus, the designed sensor is able to record the reflected light intensity for CRT measurement. The FBG sensor continuously records the pressure changes during testing which therefore improves the interpretation of the measured signals.

The following chapter 3 discusses the calibration of the FBG temperature and pressure. Chapters 4 and 5 demonstrate the performance of the combined POF sensor and FBG sensor for measuring both S_{pO_2} and CRT in-vivo respectively.

Chapter 3 Fibre Bragg Grating (FBG) Pressure Sensor

Chapter 2 described the previous research in optical reflectance pulse oximetry designs, FBG contact force sensing and CRT measurements and also discussed the novelty of this project in these areas. In section 2.3, it was mentioned that using a lower Young's modulus material to coat the bare FBG can increase the FBG's pressure sensitivity in the transverse direction. In the same section, it also expressed the necessity of compensating the Bragg wavelength changes caused by temperature changes. This Chapter presents and discusses the design and performance of the fabricated FBG patch.

The configuration of the FBG sensing patch which consists of two FBGs (the pressure sensing FBG and the temperature reference FBG) and a cured epoxy resin cuboid surrounding will be presented. The sensor's temperature response and pressure response of both FBGs enclosed in the FBG patch is shown and discussed. Finally, the temperature compensation equation of the pressure sensing FBG using the temperature reference FBG will be derived.

3.1 Fibre Bragg Grating (FBG) Patch Configuration

This section introduces the configuration of the fabricated FBG patch for contact pressure measurement. The designed patch consists of two FBGs (dual FBG) which are fabricated in the core of the same silica fibre (PS1250 from Fibercore) using a phase mask to provide Bragg wavelengths of 1540 nm and 1546 nm, respectively [110]. To increase the pressure sensitivity of the FBG, the pressure sensing FBG was incorporated into a UV cured epoxy cuboid patch. Section 3.1.1 introduces the configuration of the dual FBG fibre, and the stainless steel protector which protects the temperature sensing FBG against the loaded pressure. Section 3.1.2 discusses the configuration of the epoxy cuboid patch, and the mould for shaping the patch.

3.1.1 Dual FBG Configuration

The working principle of the FBG sensor is to detect the Bragg wavelength shifts as a result of the environmental variations such as temperature, pressure and external strain.

Equation 3.1, illustrates that the Bragg wavelength λ_B shifts by an amount, $\Delta\lambda_B$, in response to strain ε and temperature change ΔT [111] :

$$\frac{\Delta\lambda_B}{\lambda_B} = \left(\left\{ 1 - \left(\frac{n^2}{2} \right) \times [P_{12} - \nu \times (P_{11} + P_{12})] \right\} \right) \times \varepsilon + \left[a + \frac{dn}{dT} \right] \times \Delta T \quad (3.1)$$

Where n is the refractive index of the grating, P_{11} and P_{12} are the Pockels (piezo) coefficients of the stress-optic tensor, ν is the Poisson's ratio and a is the coefficient of thermal expansion (CTE) of the fibre material.

If the fibre bonding material used to increase the FBG pressure sensitivity is taken into consideration, the equation 3.2 can be rewritten and simplified as follows [112]:

$$\frac{\Delta\lambda_B}{\lambda_B} = P_e \times \varepsilon + [P_e \times (a_s - a_f) + \zeta] \times \Delta T \quad (3.2)$$

Where P_e is the strain-optic coefficient, a_s and a_f are the thermal expansion coefficients of any fibre bonding material and of the fibre itself, respectively and ζ is the thermo-optic coefficient.

As described in section 2.3, when pressure is applied on the FBG sensor, it will cause a deformation of the FBG sensor which results in an axial strain on the fibre. According to Equation 3.1, it is possible to obtain the loaded pressure by relating the Bragg wavelength shift to the pressure induced axial strain. However, in Equation 3.2, it is also shown that temperature changes will cause Bragg wavelength shifts as well. Therefore, it is necessary to remove this temperature interference effect [113].

In section 2.3, a few methods were described to compensate the temperature effect, one of them is to add an additional FBG to measure the temperature. In 2015, Ahmed et al. [114] presented a silica fibre based FBG thermometer consisting of three FBGs with Bragg resonance set at 1540nm, 1550nm and 1560nm. They demonstrated that FBG sensors can be used to make accurate temperature measurement over the range of 233 K (-40.15 °C) to 393 K (119.85 °C) with only 500 mK uncertainty. In this thesis, the FBG was fabricated in the University of Nottingham's Optics and Photonics Research laboratory using the method described in a paper published by Correia et al [110]. The FBG is used to measure the contact pressure between the skin and the applied fibre PPG sensor. A second FBG (not placed under strain) is located near the strain measurement FBG and measures the temperature.

Figure 3.1a shows a schematic of the configuration of the resulting dual FBG silica fibre arrangement. The distance between the pressure sensor FBG1 and the thermometer FBG2 is 6mm. The short gap between both FBGs ensures that the thermal environment of both FBGs are similar. Figure 3.1b is a photograph of the dual FBG silica fibre.

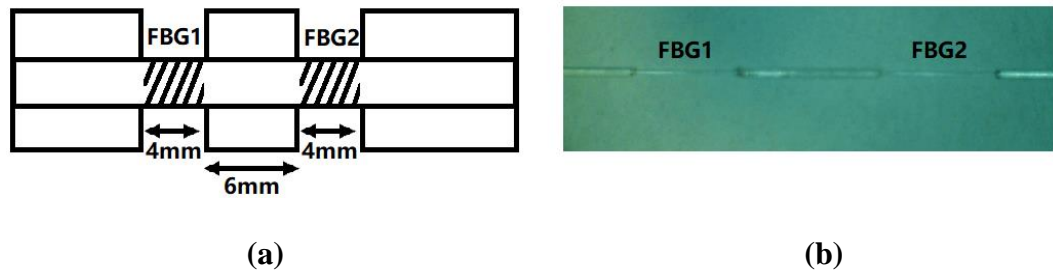


Figure 3.1. Dual FBG configuration. (a) The schematic of the dual FBG silica fibre. Since two FBGs are very close to each other, the temperature detected around FBG2 is almost equal to the temperature around the FBG1. (b) The photograph of the dual FBG silica fibre.

Figure 3.2 illustrates the effect of downward loading pressure on the FBGs. In order to measure the downward pressure, the pressure sensor FBG1 should be set perpendicular to the applied pressure. As the thermometer FBG2 is designed close to the FBG1, the loaded pressure is likely to generate the unexpected strain on the FBG2 covered in the red dotted frame in figure 3.2.

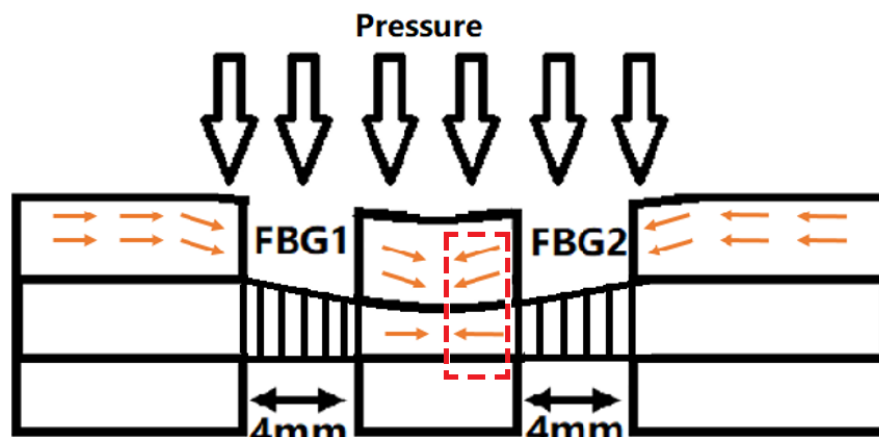


Figure 3.2. Loading pressure on both FBGs. The diagram shows how the transversely loaded (black arrows) pressure generates strain (orange arrows) that affects both FBGs. The red dotted frame shows the unexpected strain on the FBG2 caused by the loaded pressure.

As the FBG2 is designed to measure only the temperature, it is necessary to isolate the FBG2 from the downward pressure. In order to achieve this a stainless steel tube (outer

diameter: 0.56mm, inner diameter: 0.305mm, Gauge 24* Cooper Needle Works L., UK) is placed around FBG2. Figure 3.3a illustrates a side view of the FBG2 protected by the metal tube, and figure 3.3b is the x-sectional view of the fibre looking down the centre of the metal tube.

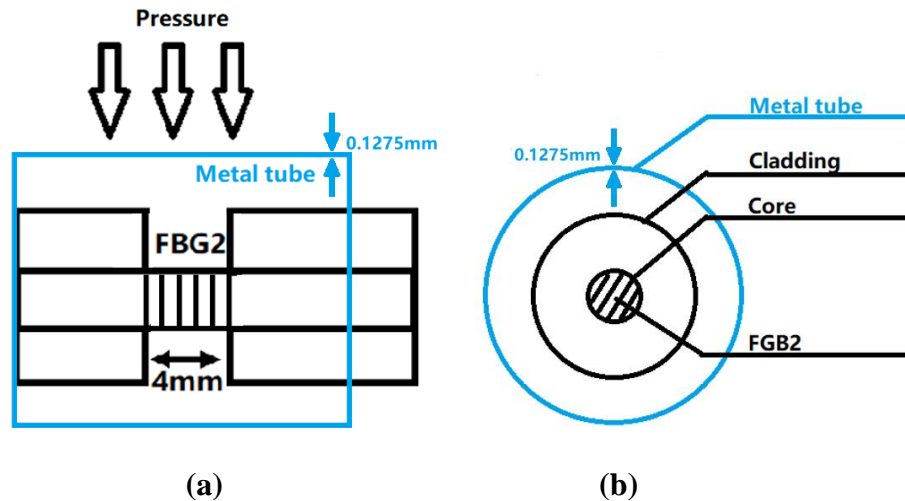


Figure 3.3. The metal tube protector of FBG2 (thermal measurement). (a) Side view of the fibre protected in the tube. In the diagram, the blue frame presents the outline of the tube. The tube resists the pressure perpendicular to the FBG2. (b) X-Sectional view of the fibre viewed down the centre of the metal pipe in blue.

Although the design shown in figure 3.3 can resist the load applied directly onto FBG2, it cannot remove the strain induced from the other points on the silica fibre due to the pressure. As the FBG1 & 2 are fabricated in the core of the same fibre, the strain generated due to the pressure at FBG1 will always affect FBG2. Moreover, the pressure strain created at the other points of the silica fibre will affect FBG2 as well. In figure 3.4, although the pressure loaded directly to the FBG2 is isolated, the pressures applied outside of the metal tube will influence the FBG2 ultimately.

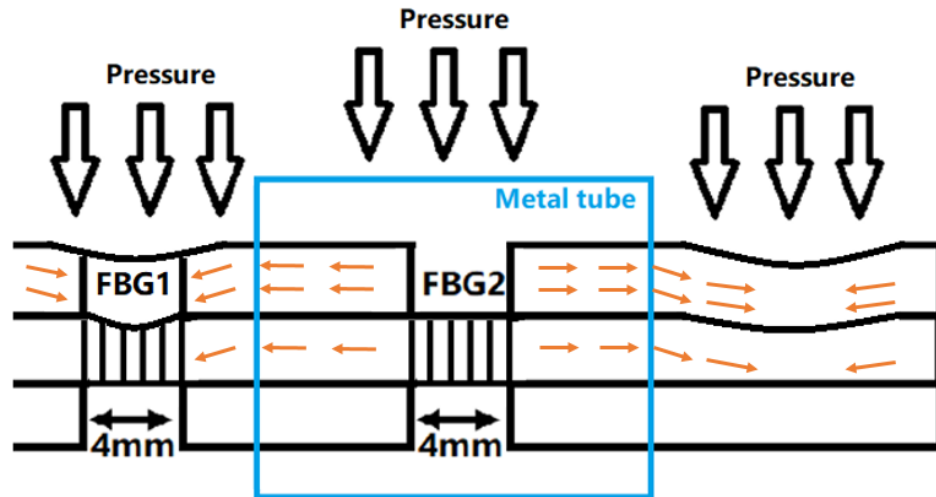


Figure 3.4. Dual FBGs silica fibre with the metal tube protector. The diagram shows that the strain (orange arrows) caused by pressure added on FBG1 or right side of the FBG2 will penetrate to the FBG2 and change its period length as well.

As discussed above, the protector of FBG2 is required to block the strain induced from the other parts of the silica fibre. In order to achieve this, two different approaches are carried out. Firstly, the metal tube is extended long enough to cover the end of the silica fibre on the right hand side of FBG2 as shown in figure 3.5a. The extended metal tube is capable of withstanding the pressure loaded on the right side of the FBG2. The second approach is to seal the end of the metal tube between two FBGs by cured epoxy resin, and leave the right end free to move as shown in figure 3.5(b). Since the sealing material (epoxy resin) filled between the fibre and inner side of the tube holds the silica fibre tight enough, the strains induced from the left side are largely attenuated.

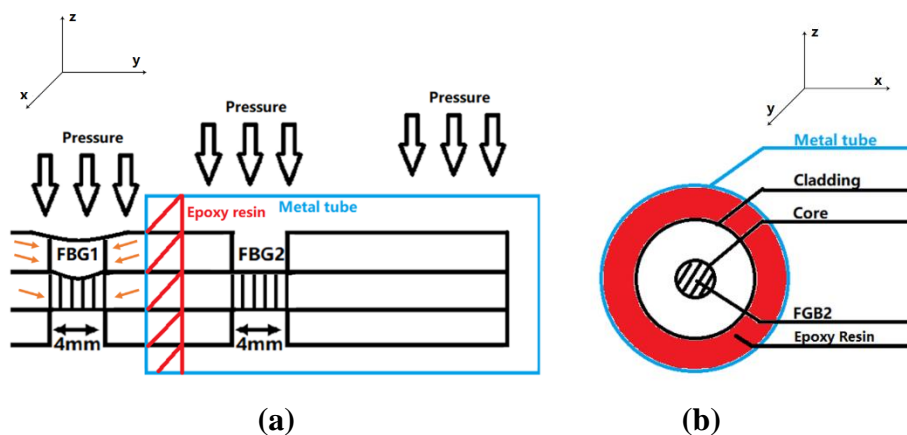


Figure 3.5. Dual FBG fibre with the modified metal tube protector. (a) Side view of the dual FBG fibre with extended metal tube protector, and sealing with cured epoxy resin. The blue frame is the metal tube. The red slash lines presents the cured epoxy resin seal. (b) Section view of the dual FBG fibre. Blue circle presents the metal tube. The red colour represents the cured epoxy resin filling between two FBGs.

In this application, the pressure required to be monitored is less than 200 kPa, the stainless steel tube (Gauge 24*, Cooper Needle Works LTD., UK) chosen for protecting FBG2 is thus rigid enough to protect the FBG against the pressure. Figure 3.6 presents a photograph of the dual FBGs silica fibre applied in this project.

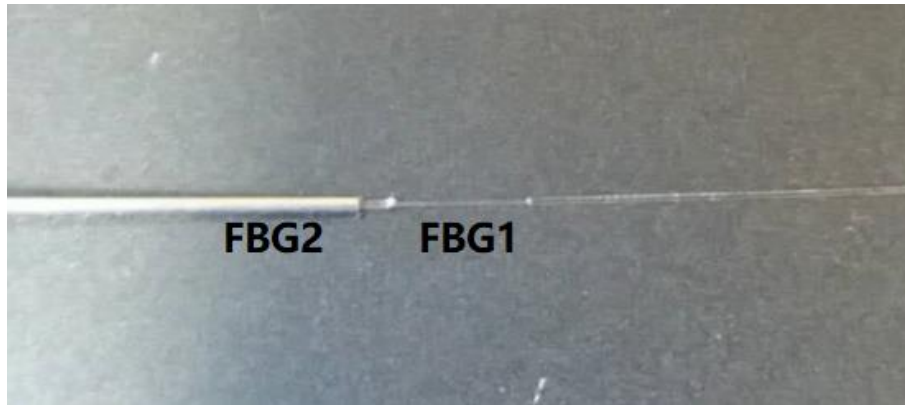


Figure 3.6. Photograph of the dual FBGs silica fibre with the stainless steel protector.

This section has presented the construction of the dual FBG (low pressure sensitivity sensor and thermometer) silica fibre with a stainless steel tube protector for FBG temperature compensation. Before one can use this fibre set-up for recording the contact pressure between the sensor and skin, it is necessary to increase the pressure sensitivity. This is achieved by using a lower Young's modulus material to coat the bare FBGs to greatly increase its pressure sensitivity. The next section introduces the material and construction of the epoxy cuboid patch.

3.1.2 Epoxy Resin Cuboid Patch

As described in section 2.3, the bare FBG written in the core of the silica fibre is not suitable for measuring the low level pressure due to the relatively high Young's modulus of the fibre. In the application of this thesis, the FBG sensor is applied to measure the contact pressure between the sensor and the skin where the loaded pressure is less than 200 kPa. In order to increase the pressure sensitivity of the FBG sensor, the pressure sensing FBG is embedded into an epoxy resin (NOA 65, Edmund Optics Ltd.) patch. In accordance with the method used by Xu et al in 1996 [88], the NOA 65 epoxy patch has a lower Young's modulus material housing to increase the FBG's pressure sensitivity. Since the Young's modulus of NOA-65 epoxy resin is 138 MPa which is much lower than the silica fibre (73 GPa), the epoxy resin patch enhances the FBG's pressure sensitivity significantly.

After confirming the material used to make the housing patch, the next step is to consider the patch configuration. In this application, the designed sensor (POF patch and FBG patch) is located under the fingertip in order to detect a subject's S_pO_2 and CRT. Thus the size of the patch has been designed to match the applied testing area. In 2009, Peters et al [115] published a paper to show that the area of the index finger of a male is around 425 mm^2 (50 male participants) whilst the area of index finger of a female is around 350 mm^2 (50 female participants). In 2008, Voracek et al [116] also published their work on the measurement of the fingertip size of 40 male and 40 female participants. They demonstrated that the relationship between the fingertip area (FTA) and the fingertip length (FTL) by using a fingertip index (FTI). The FTI is calculated as $FTI = (FTA/FTL^2) \times 100$ which is shown in figure 3.7. As a result and according to the size of the index finger, the length and width of the FBG patch were 20mm and 10mm respectively as shown in figure 3.8. The thickness chosen for the FBG patch design was 3mm, which was not too thin to be worn tightly or too thick to be worn comfortably during experiments. For the future study, it is recommended to research the relationship between the pressure sensitivity and the thickness of the FBG patch.

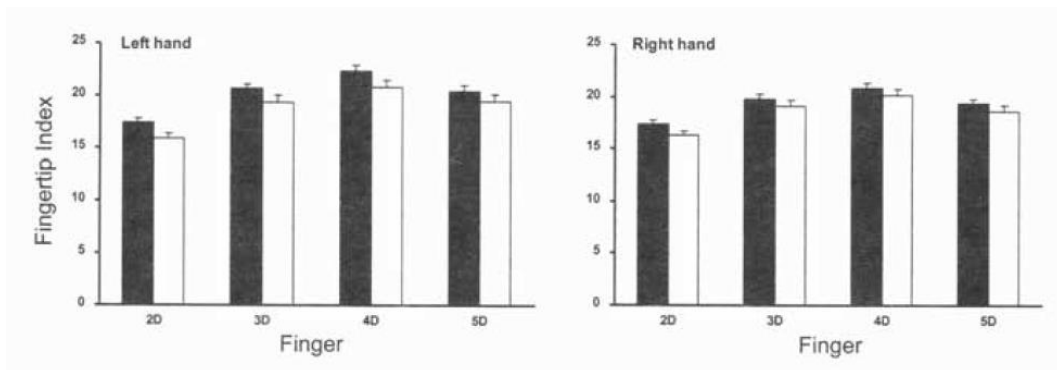


Figure 3.7. Fingertip index (men ■ , women □). 2D, 3D, 4D and 5D represents index finger, middle finger, ring finger and little finger. Bars represent means whilst the error bars represent standard errors of the mean.

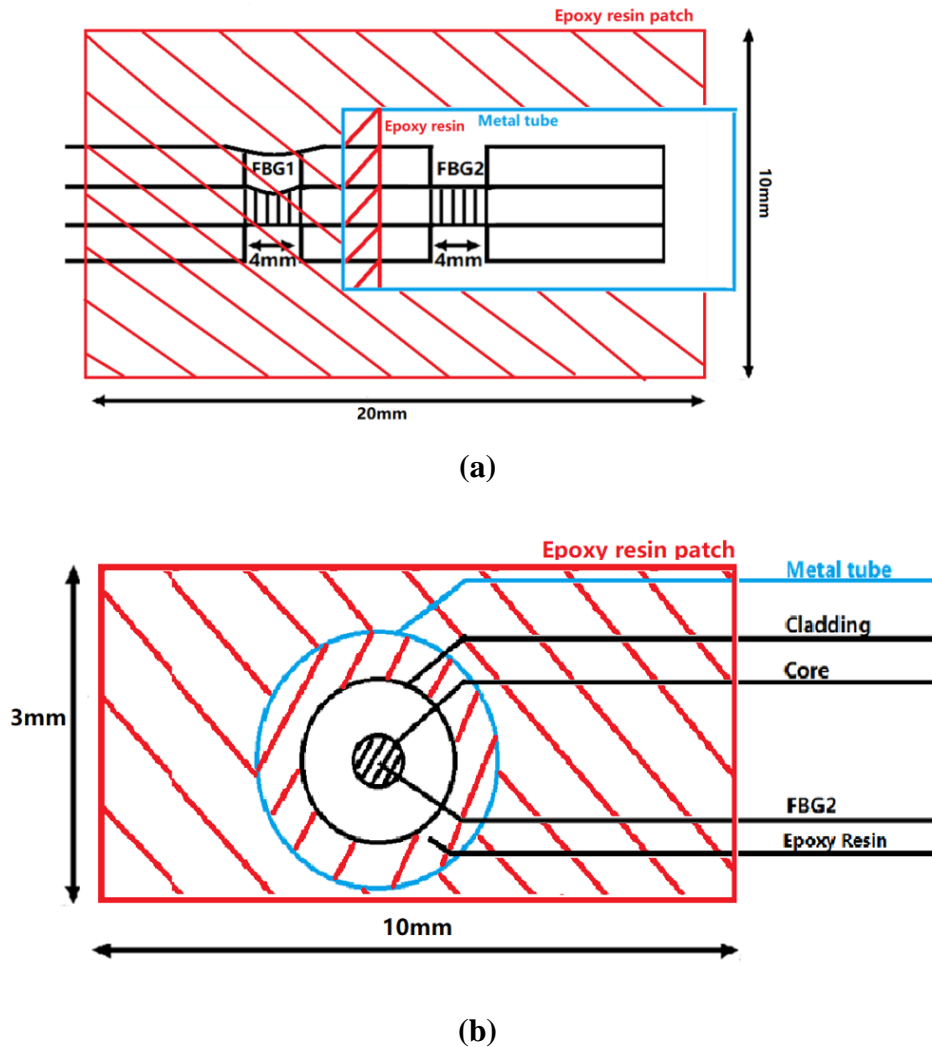


Figure 3.8. The schematic of the epoxy resin patch. (a) Top view of the epoxy resin patch. The red frame is the top surface (20mm×10mm) of the patch which is made of NOA-65 epoxy resin. There is no epoxy filling in the metal tube due to the sealing. (b) X-Sectional view of the patch. The red frame represents the side surface (10mm×3mm) of the patch.

Section 2.5 briefly introduced the uncured epoxy resins which have poor mechanical, chemical and heat resistance properties but obtains good properties after curing or gelation process. The curative process of the NOA 65 epoxy resin is to expose the uncured liquid epoxy resin to ultraviolet light with a maximum absorption within the range of 350 – 380 nano-meters for few minutes. The UV lamp (UV365nm, Sidiou Group) illuminates the epoxy resin patch for 15 minutes until the patch is fully cured. However, as described before, the uncured epoxy resin NOA 65 is fluid (1200cps viscosity at 25 °C), and needs a mould to maintain the uncured epoxy resin in the required shape. The schematic of the mould is shown in figure 3.9a, and 3D printed using an Ultimaker-2 3D printer. Figure 3.9(b) shows the fibre set into the slots on two sides of the mould into which the uncured NOA 65 epoxy resin fluid is poured. After

curing is completed the patch, is removed from the mould and this is illustrated in figure 3.9(c).

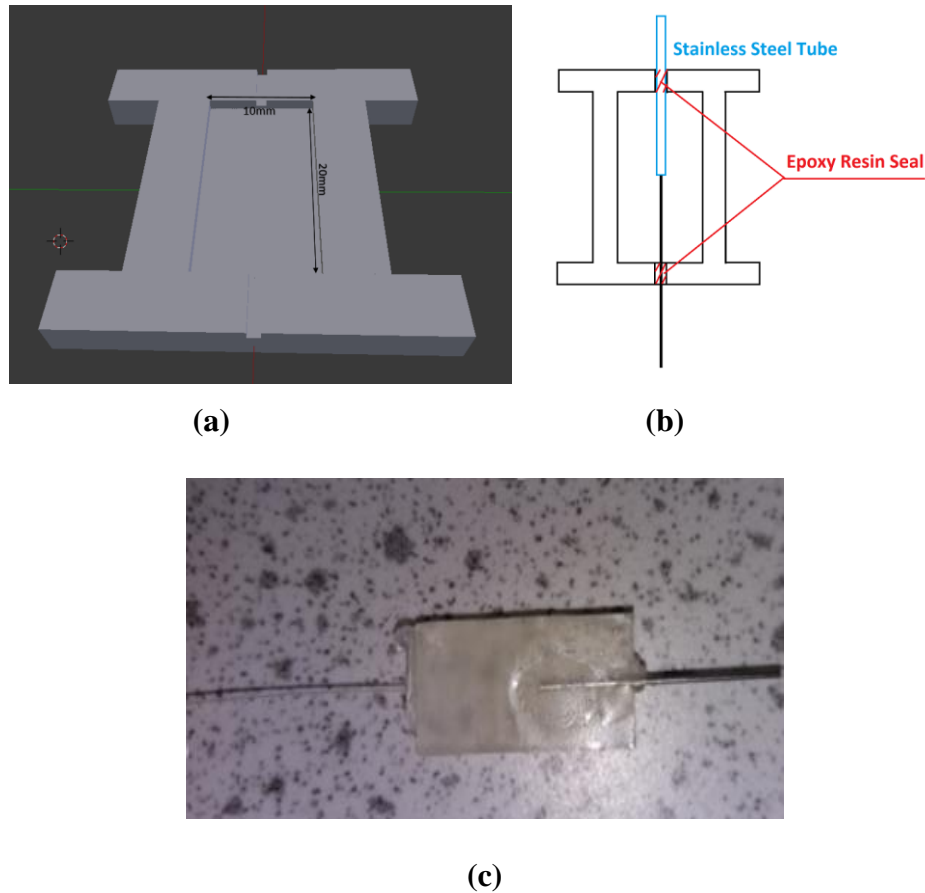


Figure 3.9. Epoxy resin patch manufacturing. (a) The schematic of the 20mm×10mm×3mm mould. (b) Schematic of FBG location. Fix the tube into one slot, and seal the slot using the epoxy patch. Then fix the fibre into the other slot, and fill the slot with epoxy resin. (c) Photograph of the epoxy patch with the embedded dual FBGs.

3.2 Fibre Bragg Grating (FBG) Patch Temperature Compensation

Section 3.1 has presented the configuration of the FBG patch which consists of one pressure sensing FBG, one temperature reference FBG and the epoxy resin coating cuboid patch. This section analyses the temperature response of both FBGs written in the same silica fibre, and describes how to determine the pressure FBG's temperature calibration from the temperature reference FBG.

Section 3.2.1 illustrates the performance of the bare dual FBGs silica fibre, and investigates the capability of using one FBG to estimate the temperature response over 30 °C to 50 °C. Section 3.2.2 presents the temperature response of the dual FBG silica

fibre embedded in the epoxy resin patch, and demonstrates the relationship between the two FBGs.

The setup of the temperature controlling system in this project is shown in figure 3.10. Figure 3.10a, b and c present the front view, side view and inside of an oven (Binder-En115), applied to continuously increase the environmental temperature. The hole sited on the side wall of the oven shown in figure 3.10b enables the silica fibre and thermocouple sensors to be inserted in the oven during the experiment. Figure 3.10d is a USB connected thermocouple logger (PICO TC-08) with two type K thermocouples.



Figure 3.10. Temperature controlling system. (a) Front view of the Binder ED-115 Oven (b) Side view of the oven (c) Inner side of the Binder ED-115 Oven. (d) Pico TC-08 thermocouple logger

The oven is first set to continuously increase the temperature from 30 °C to 50 °C during the test. When the temperature of the oven rises to 50 °C, the oven stops heating until the temperature cools back down to 30 °C. A SmartScope interrogator records the peak wavelength of both FBGs (resolution of 0.1 pm @ 1Hz). The recorded data is compared with the temperature changes measured by the Pico TC-08 later.

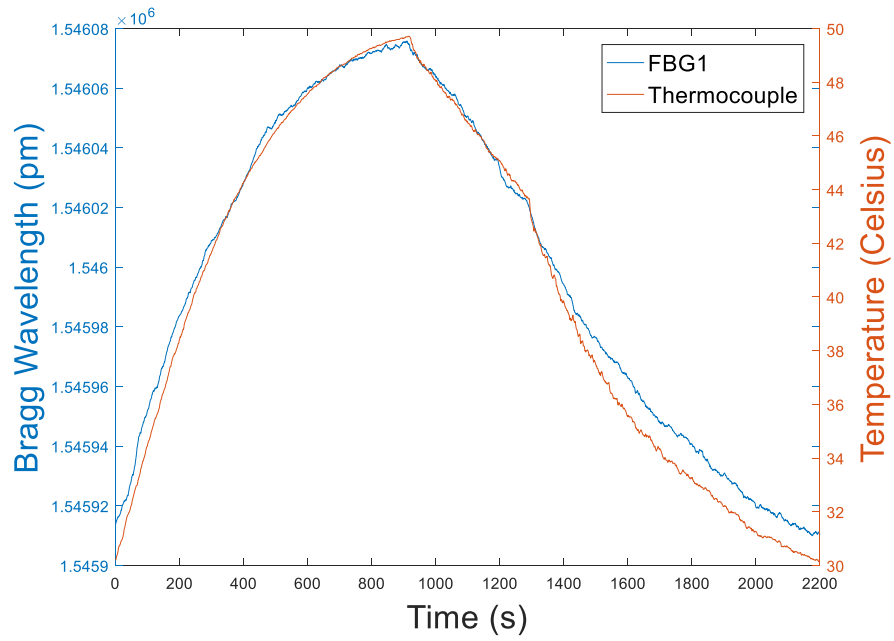
3.2.1 Temperature Response of the Dual FBGs Silica Fibre

Figure 3.11 shows the temperature response of two bare FBGs written in the core of the same silica fibre as shown in figure 3.1. The FBGs were fabricated with a 6mm separation using a phase mask to provide Bragg wavelengths of 1546nm (FBG1) and 1540nm (FBG2). The temperature response of FBG1 (bare) is 8.88 ± 0.91 pm/°C whilst the temperature response of FBG2 (bare) is 8.41 ± 0.69 pm/°C.

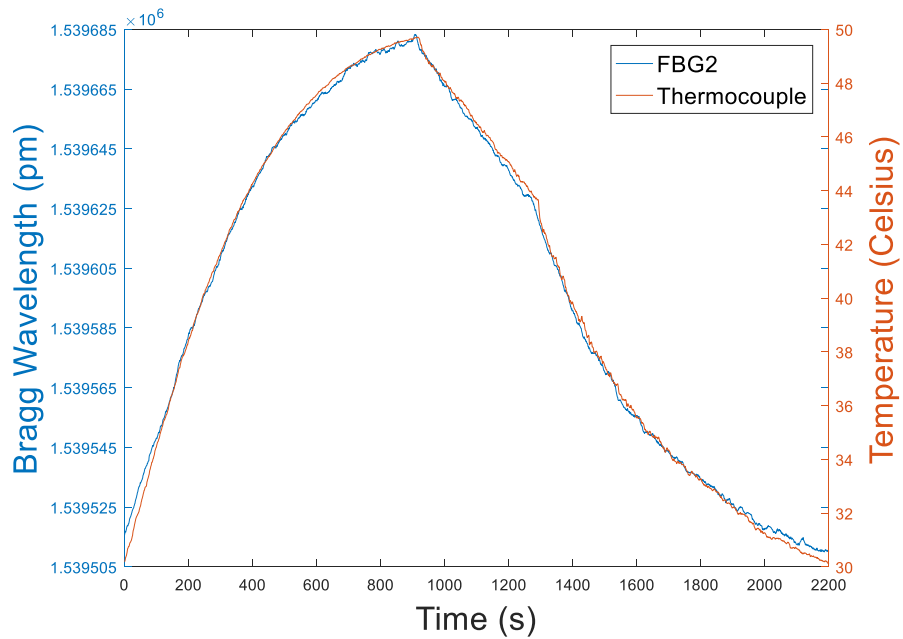
Figure 3.11 demonstrates that the Bragg shift wavelengths of both FBGs (blue curves) followed the same trend as the temperature change (red curves). Equation 3.3 shows how to calculate the Bragg wavelength shift. The baseline is the FBG output at 30 °C.

$$\Delta\lambda_{BS} = \lambda_B - \lambda_{B30} \quad (3.3)$$

$\Delta\lambda_{BS}$ is the Bragg wavelength shift. λ_B is the Bragg wavelength obtained at a certain temperature. λ_{B30} is the Bragg wavelength obtained at 30 °C.



(a)



(b)

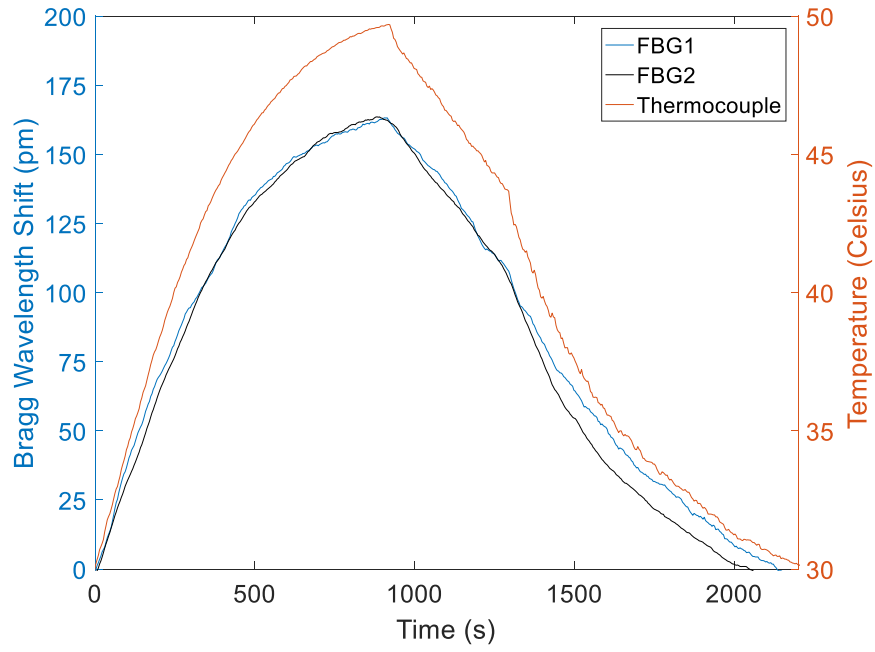
Figure 3.11. Temperature response of FBG 1&2. (a) presents the Bragg wavelength of the FBG1 which was detected by finding the peak wavelength of the reflected light from FBG1. (b) presents the Bragg wavelength of the FBG2 which was detected by finding the peak wavelength of the reflected light from FBG2.

Figure 3.12 illustrates the Bragg wavelength shifts of both FBGs in response to the temperature. In figure 3.12a, the Bragg wavelength shift curves of two FBGs (blue and black line) match the trend of the temperature changes. Figure 3.12b & 3.12c are hysteresis diagrams of Bragg wavelength shifts vs environmental temperature changes which demonstrates the linear relationship between the FBG and the temperature with negligible hysteresis. The blue traces in figure 3.12 b and c represent the Bragg wavelength of FBG sensors in heating process whereas the red lines represent the Bragg wavelength of FBG sensors in cooling process. The temperature calibration experiment has been repeated 5 times to demonstrate the repeatability of the test results which are given in Appendix A (A1 to A5). Based on the test results, empirical equations of temperature calculation of two FBGs can be deduced.

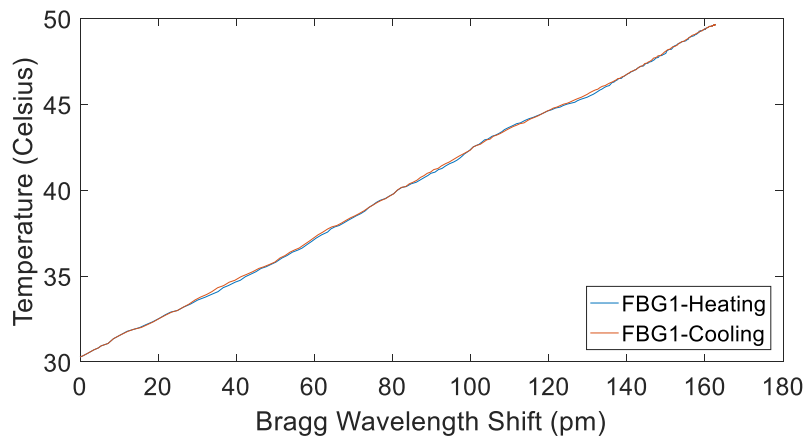
$$\text{Temperature (Celsius)} = 119.6 \times \Delta\lambda_{\text{FBG1}} + 30.13 \quad (3.4)$$

$$\text{Temperature (Celsius)} = 113.6 \times \Delta\lambda_{\text{FBG2}} + 31.13 \quad (3.5)$$

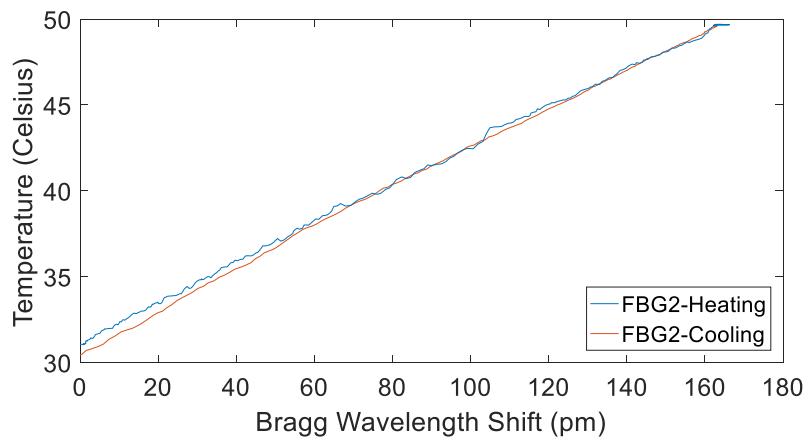
$\Delta\lambda_{\text{FBG1}}$ & $\Delta\lambda_{\text{FBG2}}$ are the Bragg wavelength shifts of FBG1&2.



(a)



(b)



(c)

Figure 3.12. Temperature response of FBG1&2. (a) Bragg wavelength shifts of two FBGs under different temperature. (b)&(c) Hysteresis diagrams of two FBGs.

As one can see, there exists a linear relationship between FBG 1&2 and temperature. The blue dots in Figure 3.13 represent the Bragg wavelength shift of FBG1 versus FBG2 during the heating period whilst the red dots in Figure 3.13 represent the Bragg wavelength shift of FBG1 versus FBG2 during the cooling period. By comparing the Bragg wavelength shifts of both FBGs at the same temperature, a linear relationship can be demonstrated which is shown in Figure 3.13. The data of the remaining experiments are provided in Appendix A (A1 to A5). Based on these test results, it is possible to deduce an empirical relationship of FBG1 temperature Bragg wavelength shift from FBG2 wavelength shift which is shown as a black dotted line in Figure 3.13. The root mean square error (RMSE) between the observed data curve and the empirical line is 3.98 pm, and the R squared value is 0.9962. Therefore, it demonstrates the empirical linear relationship between two FGBs temperature Bragg wavelength shifts. The function of the linear relationship between two FBGs temperature Bragg wavelength shift is as follows:

$$\Delta\lambda_{\text{FBG1}} = 0.9758 \times \Delta\lambda_{\text{FBG2}} + 5.0518 \quad (3.6)$$

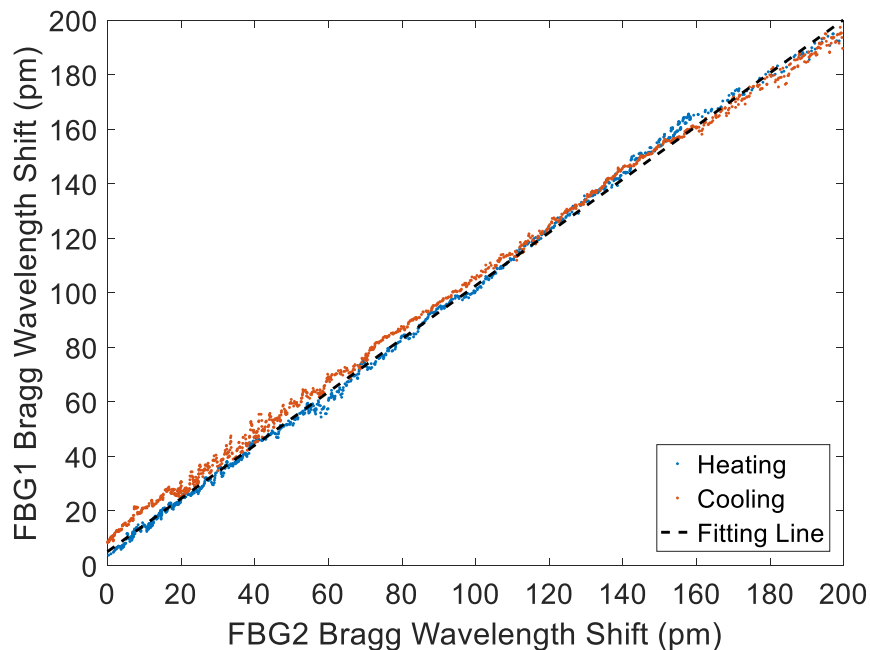


Figure 3.13. Dot plot of the Bragg wavelength shift of FBG1 VS FBG2. Blue dots presents the Bragg wavelength shifts in the heating process. Red dots presents the Bragg wavelength shifts in the cooling process.

Given the RMSE in the Bragg wavelength shift, this corresponds to an error of 0.45°C in temperature. This section has demonstrated that the designed dual FBGs silica fibre has the capability of using the output of the temperature reference FBG2 to determine and offset the effect of temperature on the pressure sensing FBG1. As mentioned in section 3.1.2, the designed dual FBGs fibre was embedded into the epoxy cuboid in this thesis. As a result the next section presents the temperature response of the epoxy cuboid patch FBG fibre, and again demonstrates the linear relationship between FBG1&2.

3.2.2 Temperature Response of the Dual FBG Silica Fibre Epoxy Patch

This section illustrates the temperature response of two FBGs written on the fibre, one of which (FBG1) is embedded inside an epoxy patch and the other embedded in a steel tube within the epoxy (FBG2) over a temperature range from 30 °C to 58 °C. Figure 3.14a shows the temperature response. The temperature response for FBG1 is 24.06 ± 1.15 pm/°C whilst the temperature response for FBG2 is 9.01 ± 0.68 pm/°C. Compared to the previous temperature responses of two FBGs, it can be observed that the temperature response of FBG1 is higher due to the surrounding material (i.e. epoxy). Figure 3.14b & c are hysteresis diagrams of the Bragg wavelength shifts of FBGs vs temperature which again demonstrates a linear relationship. Therefore, a linear relationship still exists between the temperature responses of two FBGs as shown in figure 3.15. The experiment was repeated in total 5 times which are shown in Appendix A (A6 to A10). Based on these 5 test results, the average empirical temperature equations using the Bragg wavelength shift of the FBGs was found as follows:

$$\text{Temperature (Celsius)} = 47.8243 \times \Delta\lambda_{\text{FBG1}} + 29.154 \quad (3.7)$$

$$\text{Temperature (Celsius)} = 116.0427 \times \Delta\lambda_{\text{FBG2}} + 29.6865 \quad (3.8)$$

In comparison to the temperature response between FBG1&2, it can be seen that the temperature sensitivity of FBG1 was much higher than FBG2. As Equation 3.2 shows, the thermal expansion coefficients of the fibre bonding material and of the fibre itself contribute to the temperature Bragg wavelength changes. As shown in figure 3.8c, the bare FBG2 was protected by the stainless tube whilst the FBG1 was embedded into the epoxy cuboid patch. In this case, FBG2 was immune to the surrounding material

(i.e. epoxy) in terms of temperature changes. As the housing epoxy (NOA 65) has much higher thermal expansion coefficient than the silica fibre, the temperature sensitivity of FBG1 is also much higher than FBG2.

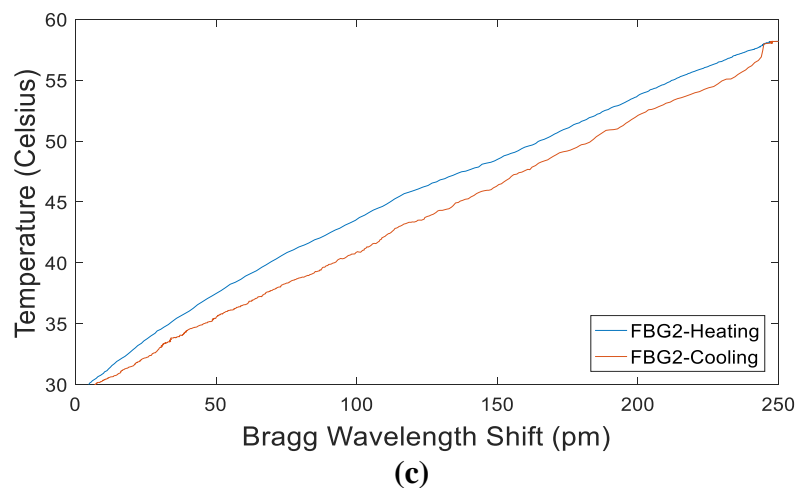
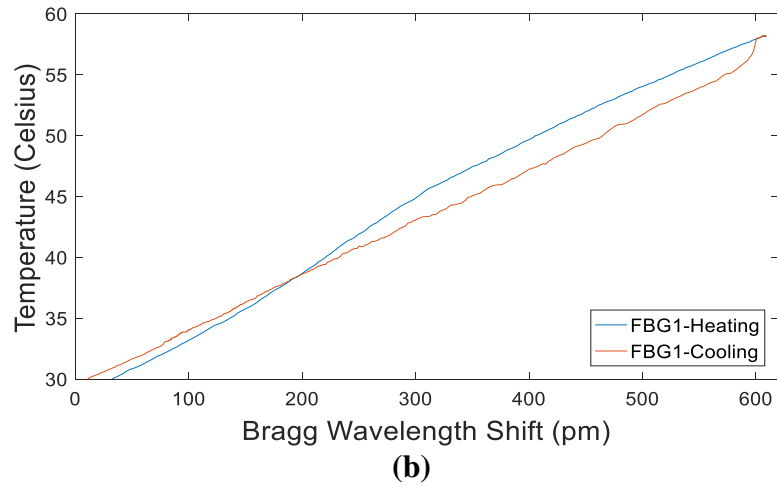
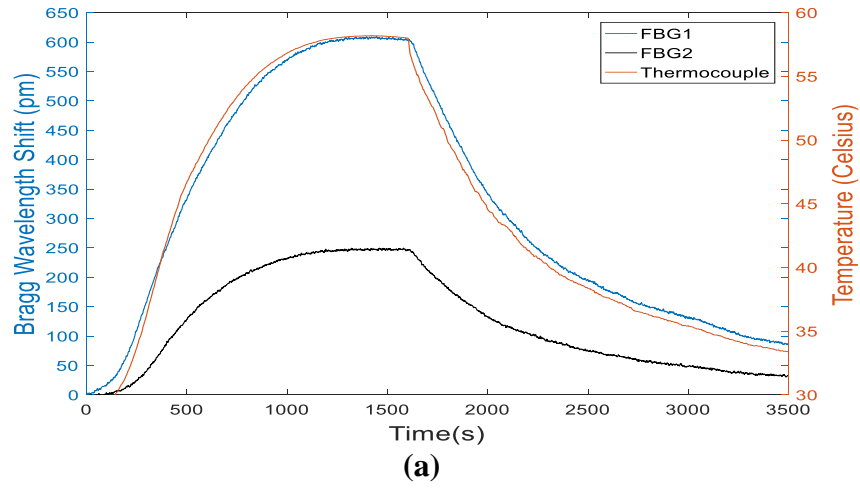


Figure 3.14. Temperature response of FBG1&2 embedded in the epoxy cubic patch. (a) Bragg wavelength shift temperature response of two FBGs. (b) Hysteresis diagrams of two FBG1. (c) Hysteresis diagrams of FBG2.

This section has demonstrated the linear relationship between Bragg wavelength shifts caused by temperature changes of two FBGs (shown in figure 3.15). Although FBG1 is more sensitive to the temperature changes, both FBGs' Bragg wavelength shifts have a linear relationship with changes in temperature. Thus, for the epoxy patch covered silica fibre, it is also possible to deduce the FBG1's Bragg wavelength shifts due to temperature changes using the Bragg wavelength shifts of FBG2. Figure 3.15 illustrates the linear relationship between the two FBGs' Bragg wavelength shifts when mounted inside the epoxy patch. The data of the remaining experiments are provided in Appendix A (A6 to A10). Based on these test results, the empirical equation of FBG1's Bragg wavelength shift from FBG2's Bragg wavelength shift can be deduced as:

$$\Delta\lambda_{\text{FBG1}} = 2.4264 \times \Delta\lambda_{\text{FBG2}} + 0.0111 \quad (3.9)$$

The RMSE value between the observed data curve and the empirical fitting line is 8.2 pm, and the R squared value is 0.9934. In this case, it demonstrates the linear relationship between two FBGs temperature Bragg wavelength shifts.

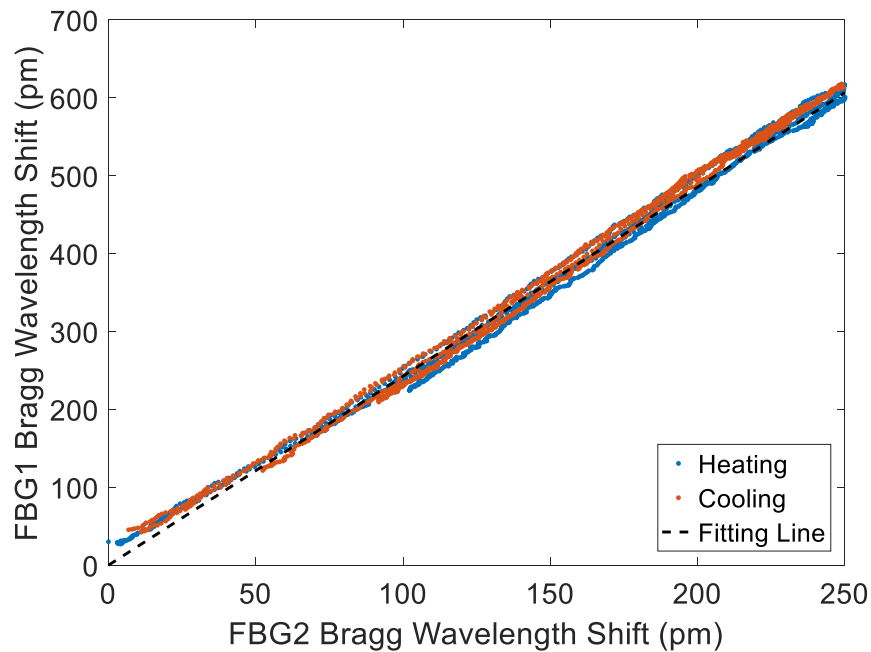


Figure 3.15. Dot plot of the Bragg wavelength shift of FBG1 vs FBG2 during heating and cooling

This section presented the temperature response of the designed epoxy patched dual FBG silica fibre, and demonstrated that the temperature Bragg wavelength shift of the embedded FBG (FBG1) can be determined from the protected FBG (FBG2).

3.3 Fibre Bragg Grating (FBG) Patch Pressure Measurement

In section 3.2, it was illustrated that it is possible to use the temperature sensing FBG (FBG2) to deduce the temperature response of the pressure sensing FBG (FBG1). In the pressure calibration, the empirical equation 3.8 can be used to compensate for temperature changes in the pressure sensing FBG. This section demonstrates the pressure response of the designed pressure sensing epoxy patch in conjunction with the temperature sensing FBG2 to compensate the FBG1's temperature crosstalk.

Section 3.3.1 presents the pressure calibration curves of the FBG patch. Since the designed pulse oximeter integrated the FBG patch and the POF patch, section 3.3.2 shows the pressure response of the designed pulse oximeter.

The pressure controlling setup is shown in figure 3.16. By screwing the manual plate to lift/lower the aluminium pole, the aluminium plate releases/loads the pressure to the testing patch (the FBG patch or the integrated pulse oximetry patch). The weighing scale (KERN PCB 6000-0) beneath records the force loaded on the testing patch and is used for characterising the pressure performance of the FBG sensor.



Figure 3.16. Pressure loading system. The manual plate is applied to lift/lower the aluminium pole and plate to load the pressure transversely. The weighing scale beneath records the pressure applied.

The testing patch (pressure patch only or with POF sensor on top) was fixed to the top plate of the weighing scale, and directly below the aluminium plate. Figure 3.17 shows the loading/releasing pressure process. In the pressure calibration experiment, the

setup increased the transversely loaded pressure step by step up to 40 kPa, which was the approximately maximum loaded pressure for pulse oximetry experiments, and then decreased the applied pressure step by step back to zero. The value of the pressure loaded is monitored by the weighing scale.

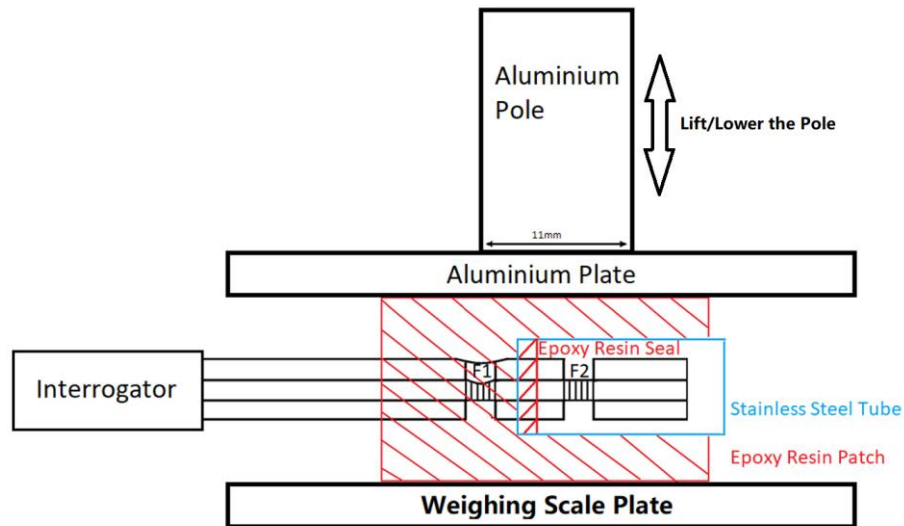
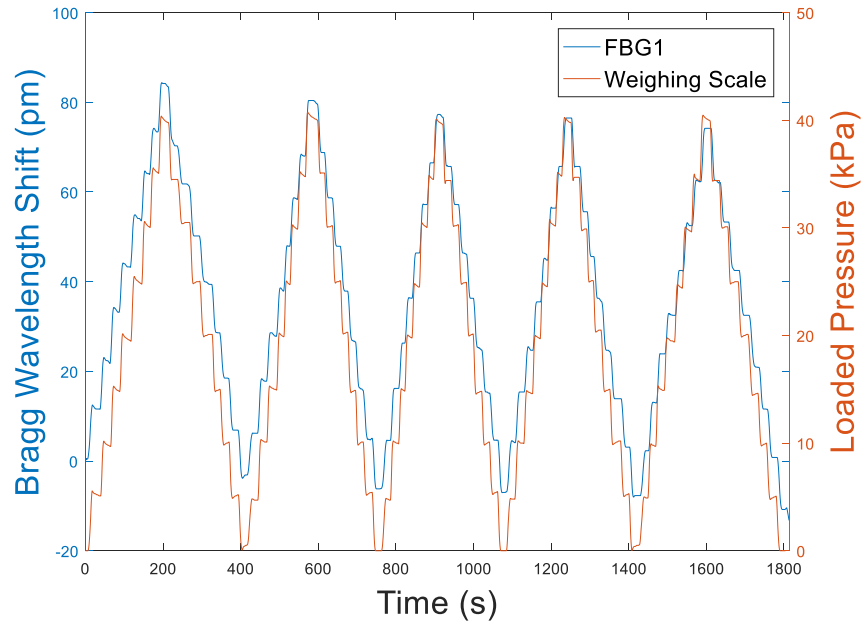


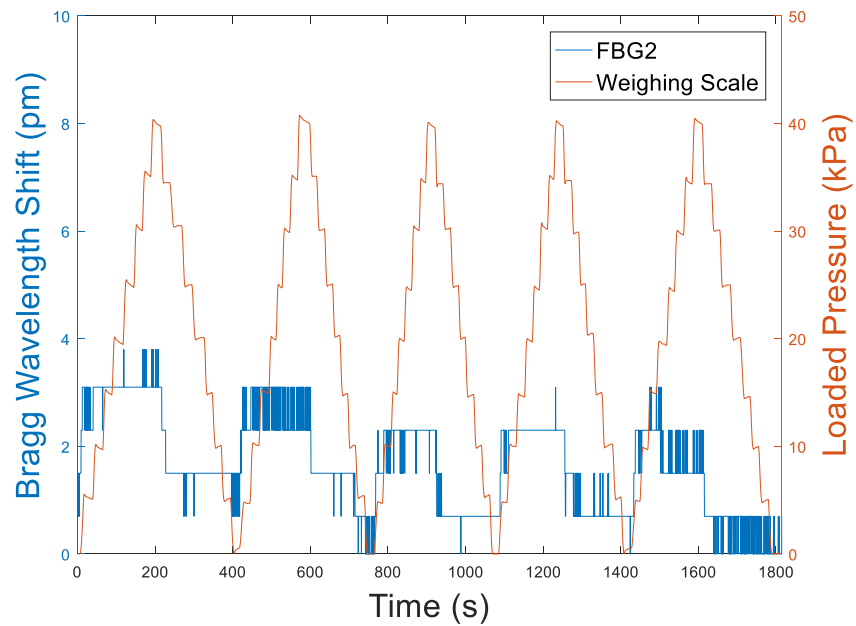
Figure 3.17. Schematic of releasing/loading pressure from Figure 3.14. The black arrow shows the movement of the stainless steel pole (lifting or lowering). When the manual plate lowers the pole, the pole presses against the aluminium plate, and passes the force to the epoxy patch uniformly. When the manual plate lifts the pole, it releases the force loaded on the epoxy patch until the aluminium plate is not in contact with the epoxy patch.

3.3.1 Pressure Response of the Pressure Sensing Epoxy Patch

This section presents the pressure response of the FBG patch only. Figure 3.18a & b are the Bragg wavelength shifts of FBG1&2 recorded by the interrogator respectively. Figure 3.18a clearly shows that the Bragg wavelength of FBG1 shifts according to the pressure changes. Figure 3.18b shows that the Bragg wavelength of FBG2 is relatively immune to the changes of the loaded force. The experiment was repeated three times in total to check the repeatability and reliability of the sensing patch. The full data set is shown in Appendix A (A11 – A13).



(a)



(b)

Figure 3.18. Step pressure increasing/decreasing experiment (a). Response of the pressure sensing FBG. The pressure sensing FBG is embedded into the cubic patch, and covered by the cured epoxy resin. The experiment increased the pressure step by step until the pressure was up to 40 kPa. Then, the loaded pressure was decreasing step by step until the pressure load was down to 0 kPa. (b). Pressure response of the temperature sensing FBG2. The temperature sensing FBG2 is set in the stainless steel tube which allows the FBG to be relatively immune (4pm out of 80 pm change) to the downward loaded pressure.

Figure 3.18a shows that the Bragg wavelength of FBG1 shifts following the trend of the loaded pressure changes. In the figure, the DC baseline value of the FBG1's Bragg wavelength shifts at the moment of no loading pressure kept decreasing, which was caused by the ambient temperature decreasing. The similar trend in FBG2's output can be applied to compensate this temperature effect. As mentioned in section 3.2.2, the Bragg wavelength shift of FBG2 can be directly subtracted from the FBG1 due to any temperature changes. Thus, based on Equation 3.9, the pressure calculation equation of FBG1 is:

$$\Delta\lambda_{P-FBG1} = \Delta\lambda_{FBG1} - 2.4264 \times \Delta\lambda_{FBG2} - 0.0111 \quad (3.10)$$

$\Delta\lambda_{P-FBG1}$ is the pressure Bragg wavelength shifts of the FBG1. $\Delta\lambda_{FBG1}$ & $\Delta\lambda_{FBG2}$ are the total Bragg wavelength shifts of FBG1&2.

Figure 3.19a shows the temperature compensated Bragg wavelength changes in FBG1 caused by pressure loading and unloading only. Figure 3.19b is the hysteresis diagram of the relationship between the FBG1's Bragg wavelength shift and the loaded pressure. This was repeated 3 times. The rest test results are given in Appendix A (A11 to A13). These results indicate that the FBG pressure patch is both reliable and repeatable for measuring pressure with negligible hysteresis. Based on the figure 3.19, the empirical equation is obtained as follows:

$$\text{Pressure (kPa)} = 0.4977 \times \Delta\lambda_{P-FBG1} - 0.0043 \quad (3.11)$$

Substituting equation 3.10 into equation 3.11, the loaded pressure is obtained by:

$$\text{Pressure (kPa)} = 0.4977 \times (\Delta\lambda_{FBG1} - 2.4264 \times \Delta\lambda_{FBG2} - 0.0111) - 0.0043 \quad (3.12)$$

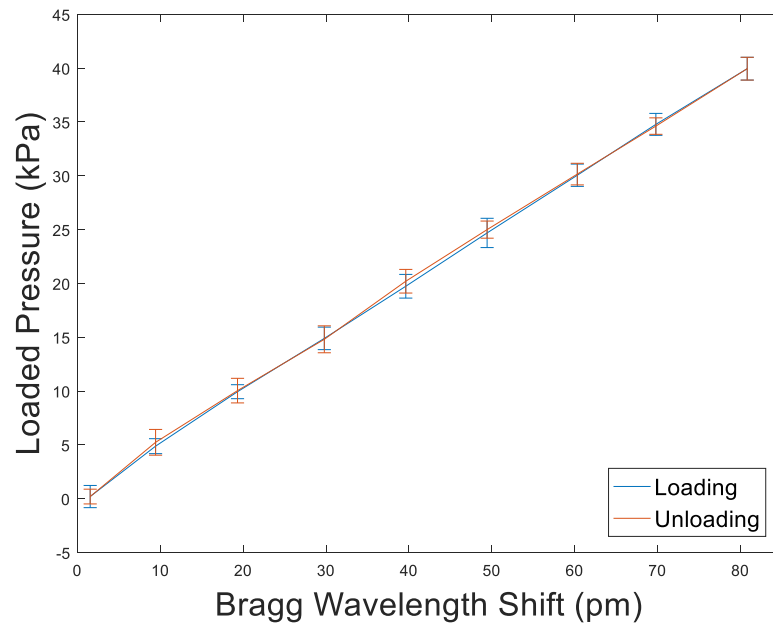
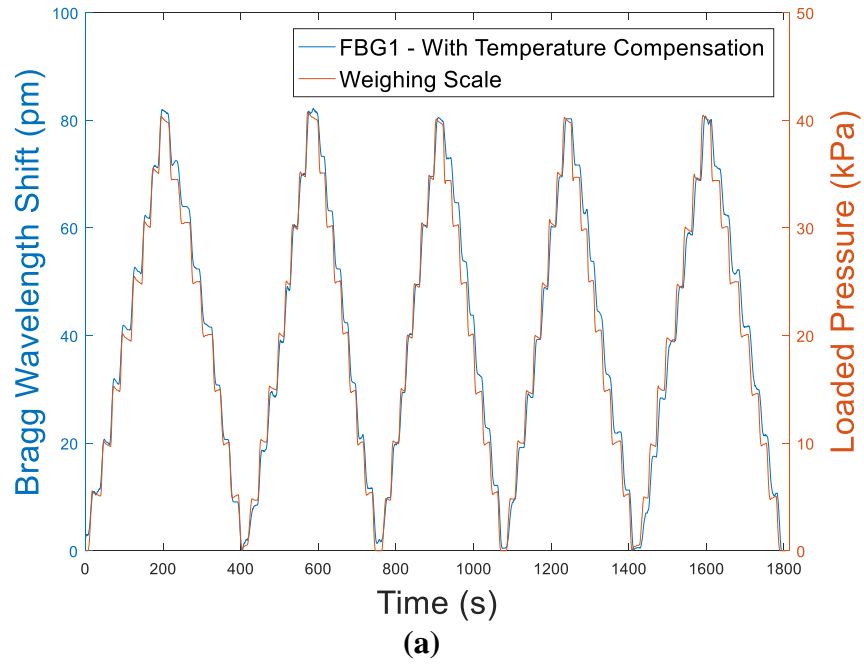
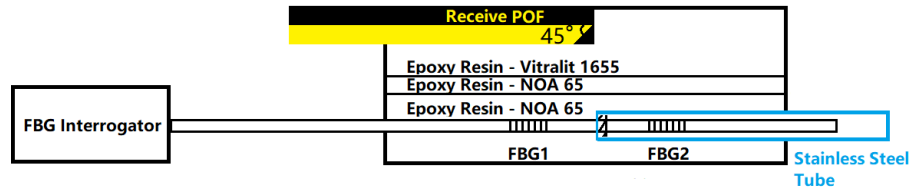


Figure 3.19. Pressure response of the epoxy patch with temperature compensation. (a) Pressure response of the FBG1 with the temperature compensation. (b) FBG Bragg wavelength shift vs loaded pressure demonstrating a linear relationship, repeatable results and negligible hysteresis.

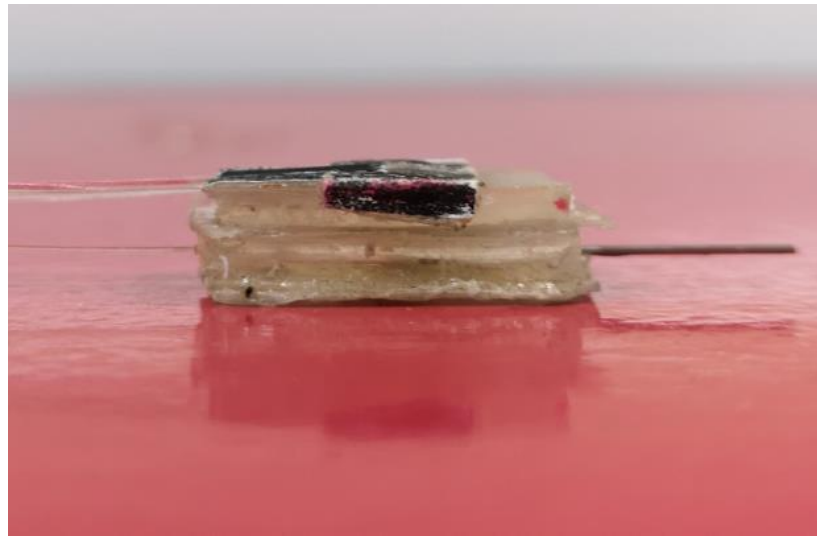
3.3.2 Pressure Response of the Integrated Pulse Oximeter

The previous section has demonstrated the pressure response of the FBG patch. In this thesis, the designed pulse oximeter was integrated into the FBG patch using NOA epoxy resin. The FBG patch was therefore used to record the contact pressure between

the skin and the sensor. The configuration of the integrated pulse oximeter is shown in figure 3.20. Details of the POF patch will be described in section 4.1.1 in Chapter 4. This section however, presents the pressure response of the integrated pulse oximeter.



(a)

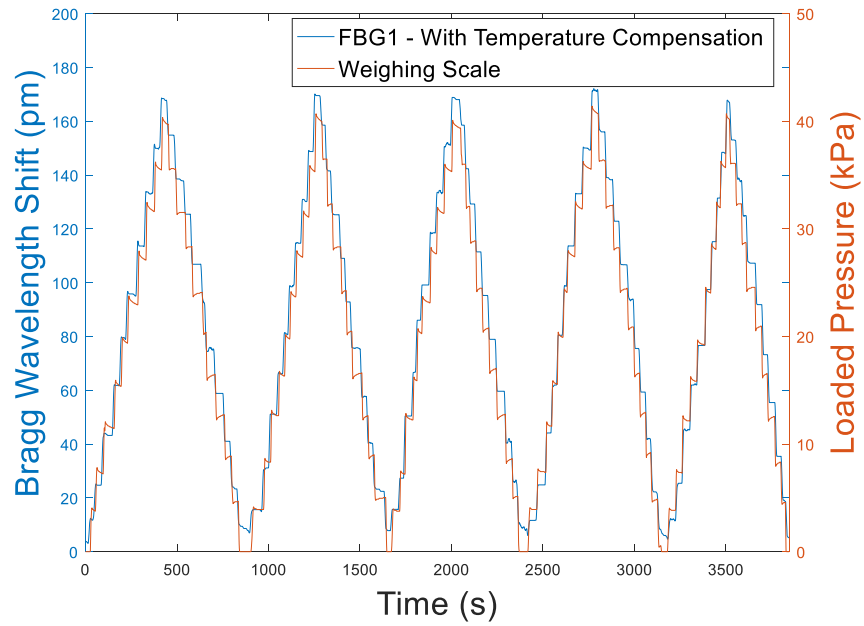


(b)

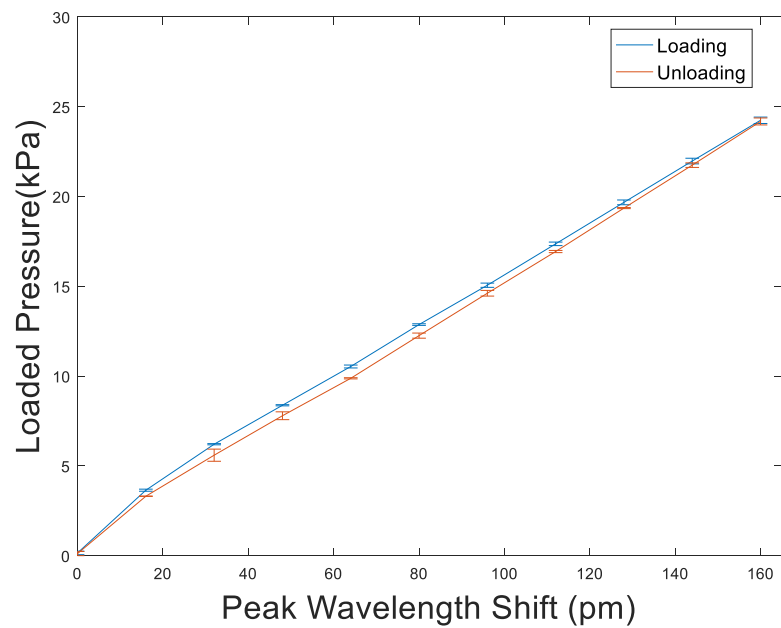
Figure 3.20. Configuration of the integrated pulse oximeter. (a). The schematic of the designed sensor. The top cuboid patch made of Vitralit 1655 enclosing POFs to couple light for measuring blood volume. Vitralit 1655 epoxy resin has EN10993 biocompatibility for skin contact. The bottom cuboid patch enclosing the dual FBGs fibre is the FBG patch discussed in section 3.3.1. Two different material patches were glued together by curing epoxy NOA 65 between them. (b) Photograph of the designed pulse oximeter.

As the pulse oximeter integrated two patches, the configuration changes will influence the pressure sensitivity of the FBG patch. As a result the calibration was repeated using this new configuration. Figure 3.21a shows the pressure response of the integrated pulse oximeter with temperature compensation. Figure 3.21b is the hysteresis diagram of the Bragg wavelength shifts vs loaded pressure. This was repeated 5 times. The further information of test results are given in Appendix A (A14 to A18). These results illustrates that the designed pulse oximeter is both reliable and repeatable for contact pressure measurement with negligible hysteresis. Based on figure 3.21b, the equation for the designed sensor to calculate pressure can be deduced:

$$\text{Pressure (kPa)} = 0.1563 \times (\Delta\lambda_{\text{FBG1}} - 2.4264 \times \Delta\lambda_{\text{FBG2}} - 0.0111) - 0.0066 \quad (3.13)$$



(a)



(b)

Figure 3.21 Pressure response of the integrated pulse oximeter (a) Pressure response of the integrate pulse oximeter (b) FBG Bragg wavelength shift vs loaded pressure.

3.4 Discussion and Conclusion

Fibre Bragg gratings are inscribed into the core of an optical fibre as intrinsic sensing elements [117]. Due to the physical characteristic of the FBG which has been introduced in section 2.3, the FBG is particularly suitable for measuring pressure, strain and temperature [118]. In this thesis, the FBG was chosen to detect the contact pressure between the skin and the pulse oximeter.

As mentioned in section 2.3, the pressure sensitivity of the FBG is inversely proportional to the Young's modulus of the fibre. Thus, for the bare fibre, the FBG is insensitive to pressure changes due to the high Young's modulus of the fibre. However, by mounting the FBG in a relatively low Young's modulus material, it can enhance the FBG's pressure sensitivity. For a Germanium doped FBG at 1550nm, which has a Young's modulus of 102.7Gpa, its pressure sensitivity was measured as -3×10^{-3} nm/MPa over a pressure range of 70MPa [5]. By housing the FBG in a hollow glass bubble, the FBG's sensitivity was increased by up to four times [88]. In this thesis, the pressure sensing FBG, therefore, was embedded into an epoxy cuboid patch with lower Young's modulus in order to increase the pressure sensitivity.

In addition to the pressure sensing FBG, another FBG was written in the core of the same silica fibre and was used as a temperature reference FBG. Using only one FBG, it is impossible to identify and separate the Bragg wavelength shifts caused by strain or temperature. But a separated, strain-free FBG can be applied as the temperature sensor of the pressure sensing FBG [92]. Thus, an extra FBG was fabricated in the same thermal environment as the pressure sensing FBG in this thesis. A stainless steel tube encased the reference FBG, and was sealed at the end of the tube to isolate the FBG from the strain.

With the separated and strain-free reference FBG, the temperature crosstalk on the pressure sensing FBG was eliminated. The next step of the study was reducing the strain effect on the pressure sensing FBG. Due to the configuration of the sensor, the pressure sensing FBG is not strain free. Thus, in this study, the silica fibre (with FBGs) was kept loose during the study to keep the FBG strain free. For future versions of the sensor it is recommended to add another FBG on the interrogator side to further compensate for temperature and strain.

Dual FBGs have been fabricated in the core of the same silica fibre, and inserted in an epoxy resin cuboid. Section 3.1 described the configuration of the FBG epoxy patch. Section 3.2 discussed the temperature responses of both FBGs (pressure sensing and reference) from 30 °C to 50 °C. A stepped temperature heating/cooling test demonstrated a linear relationship between the Bragg wavelength shifts between both FBGs and the temperature, and deduced the relationship between both FBGs. In this case, the Bragg wavelength shifts of the pressure sensing FBG caused by temperature can be deduced from the reference FBG. Section 3.3 showed the pressure response of the FBG sensing patch and the integrated pulse oximeter from 0 to 40 kPa. With temperature compensation, the FBG responses of the FBG patch followed that of the applied pressure whether the FBG patch is integrated with the POF patch or not. The experimental results indicate that the FBG patch and the integrated patch are reliable and repeatable for pressure measurement.

The combination of the FBG patch and the POF patch enables the designed sensor to measure both blood volume and contact force simultaneously. The following two chapters (Chapter 4 & 5) undertakes further more detailed studies with the deployment of this combined pressure FBG patch simultaneous with the blood volume using the POF.

Chapter 4 Non-invasive Pulse Oximetry Measurement Using the POF Patch

Chapter 3 described the configuration and performance of the FBG patch, and it was found that the pressure sensor gave the more reliable results when a temperature compensation FBG was included. This research integrates the FBG patch and the POF patch to measure the subject's PPG signals with pressure recording. This Chapter will present the design of the integrated pulse oximetry sensing patch, and will describe the performance of this patch for S_{pO_2} measurement. The following chapter describes the capillary refill time (CRT) measurement using this sensing patch.

Since the detailed information of FBG patch was already discussed in Chapter 3, this chapter will focus on the design of the POF patch and its front-end electronic part. The characterisation of the designed sensor consisting of signal modulation (Time Division Multiple Access, TDMA), stray light immunity and the gain/noise measurement of the analogue front-end will be shown. The S_{pO_2} measurement result and its signal quality assessment using three quality indices (i.e. signal-to-noise ratio, perfusion index and skewness index) will be presented.

4.1 Design of the Pulse Oximetry Sensor

According to section 1.1 and 1.3, this research aims to investigate whether simultaneous pressure and PPG measurement can improve the performance of the sensor for S_{pO_2} and CRT measurements. Therefore, the designed sensor ought to measure the S_{pO_2} /CRT and pressure at the same time whilst current commercial pulse oximetry devices only measure the subject's S_{pO_2} values. In this research, the sensor was designed based on the POF patch construction which achieved the simultaneous pressure and PPG measurement.

Section 4.1.1 describes the configuration of the designed sensor probe. Section 4.1.2 introduces the opto-electronic system design. Section 4.1.3 discusses the gain and noise measurement of the whole system.

4.1.1 Probe Design

Figure 4.1a shows the schematic diagram of the probe designed for the reflectance pulse oximeter. The photo of the real probe patch is shown in figure 4.1b. The probe embedded three 500 μm diameter POFs (Asahi Kasei DB-500) in an epoxy resin patch to deliver/receive light to/from the opto-electronic system.

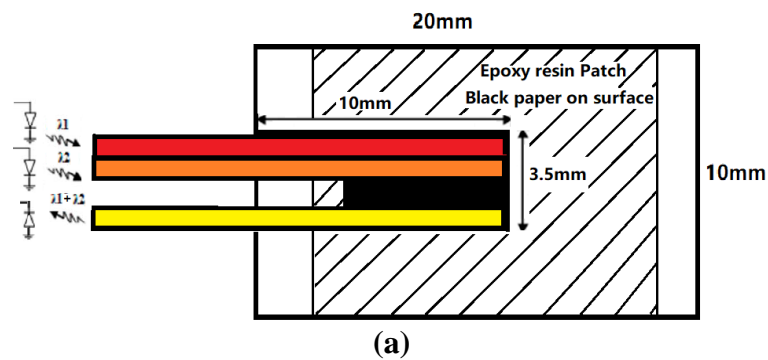


Figure 4.1. (a) The schematic of the POF patch. The patch is a $20 \times 10 \times 2 \text{ mm}^3$ cube. Three 45° cleaved end POFs are embedded in the slot. The black bar between POFs is used to block light. Red and orange bars present transmit POFs connected to two LEDs (660nm and 850nm). The yellow bar represents the receive POF connected to the photo-diode. (b) The photo of the POF patch.

The end of each POF fixed on the surface of the sensing patch is 45° cleaved to increase the light reflecting from the side of the angled optical fibre, which allows for sensing away from the axis of the fibre [72, 93]. This has been previously described in section 2.5. Figure 4.2a and b are side views of the transmit/receive POF, respectively. Both transmit and receive POFs are set parallel to the skin. Figure 4.2c is the photo of one POF with 45° cleaved end.

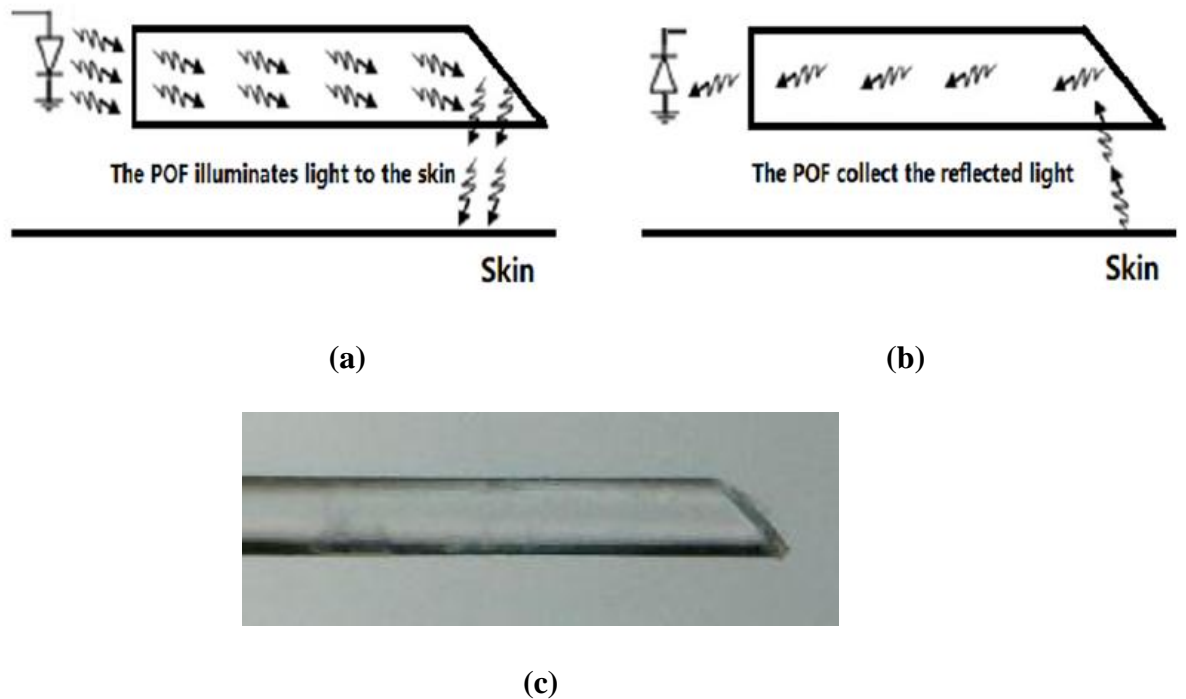


Figure 4.2. (a) Transmission POF. The transmit POF delivers light from the LED and illuminates the skin. (b) Receiving POF. The receive POF collects the light reflected by the tissue, and transfers the reflected light to the photo-diode. (c) Photo of a POF with 45° cleaved end.

The base substance of the pulse oximetry sensing patch shown in figure 4.1b is epoxy resin (Vitalit 1655) which is a bio compatible material. Exposed to UV light, the epoxy resin is cured in a mould (shown in figure 4.3). The cured patch is a 20×10×2 mm cube with a 3.5×10×1 mm slot on the top surface which is generated due to the bar protrusion in the middle of the pit of the mould. As shown in figure 4.1, three POFs with 45° cleaved ends were set into this slot, and then fixed by the epoxy resin (Vitalit 1655). As mentioned in section 3.1, the epoxy resin chosen as the substance of the FBG pressure patch was NOA 65 due to its lower Young’s modulus. The reason for choosing the different epoxy material for the POF patch was that Vitalit 1655 was bio compatible for skin contact.

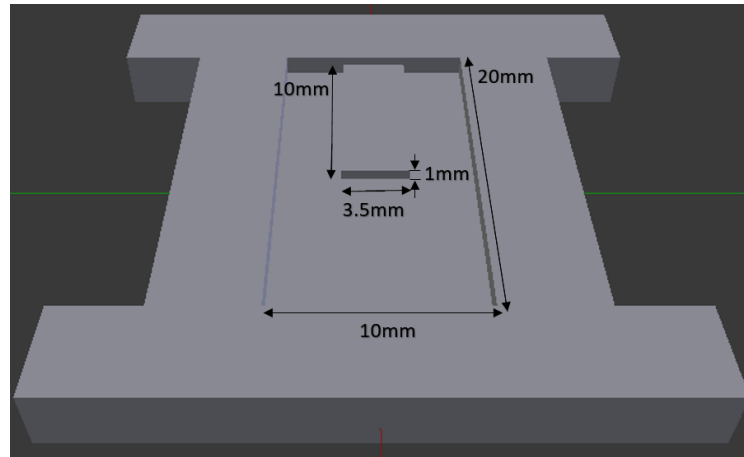
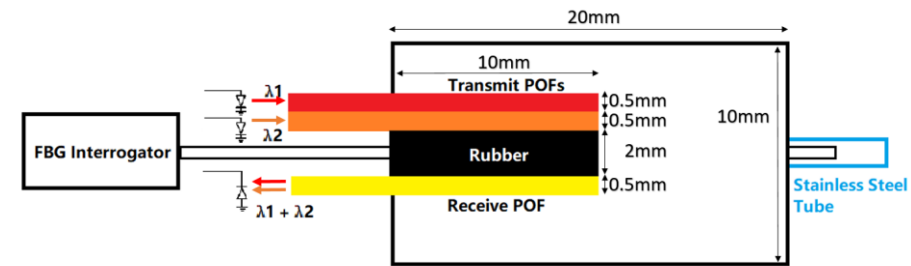


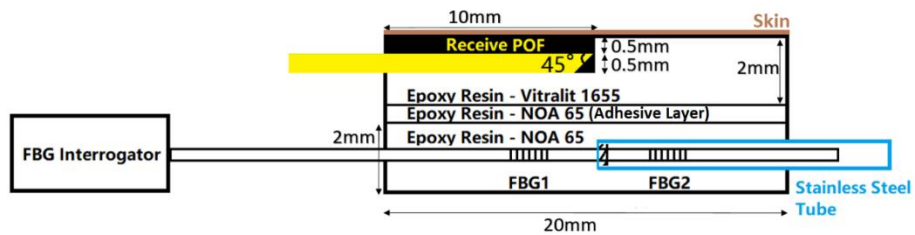
Figure 4.3. Mould for making POF epoxy patch. The bar protrusion (3.5×10×1) mm in the middle is used to generate the slot on the surface of the epoxy patch.

There was a black rubber buffer (2mm thick) set on the surface of the epoxy patch between transmit and receive POFs as shown in figure 4.1b. The black rubber is applied to prevent light passing directly from the source to the detector as this would affect the DC light level of the reflected light detected and hence the S_{PO_2} value. The immunity of the POF patch probe to stray light will be discussed later in section 4.2.2.

As mentioned in section 2.5, this research integrated the POF patch and FBG patch together. The details of the FBG patch was described in Chapter 3. Figure 4.4a and b show the final design of the integrated probe. The integrated probe is composed of two patches which are a pulse oximeter (the top POF patch) and a FBG pressure sensor (the bottom FBG patch). Two patches are glued together using epoxy resin (NOA-65).



(a)

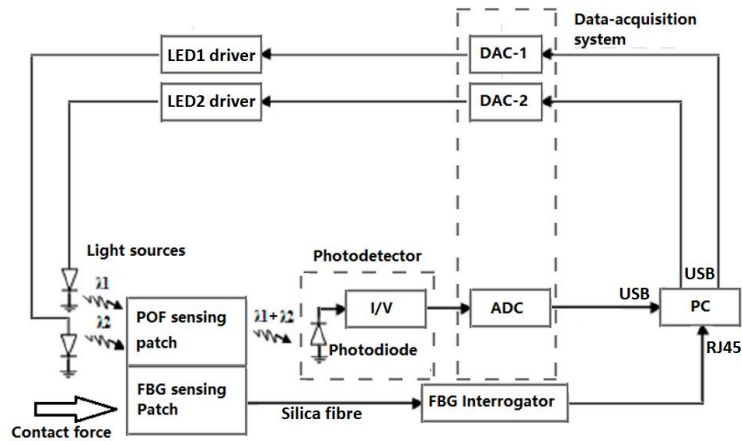


(b)

Figure 4.4. (a) The plan view of the probe. Red and orange frames present transmit POFs connected to two LEDs (660nm and 850nm). The yellow frame presents the received POF connected to the photodiode. (b) The side view of the probe. The probe consists of two epoxy rectangular patches which are glued together by using epoxy resin NOA 65. The top patch is the pulse oximeter whilst the bottom is the FBG pressure sensor. Two FBGs are fabricated in the core of the silica fibre which are connected to the FBG interrogator (see Section B). The brown line presents the skin surface where the POF patch is located.

4.1.2 Opto-electronic System Design

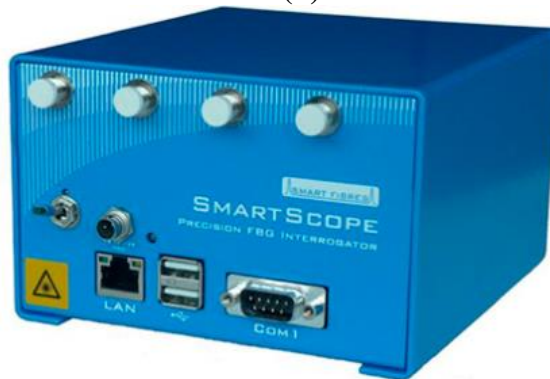
The block diagram in figure 4.5a is the design of the opto-electronic system. The design is briefly outlined in figure 4.5a, the details of each circuit block will be discussed in the following sections. Figure 4.5b is the prototype of the reflectance pulse oximetry opto-electronic system. Figure 4.5c illustrates the SmartScope FBG interrogator (Smartscope, Smartfibres, UK) for measuring the FBG patch response. The specification of all components applied are introduced in following sections.



(a)



(b)



(c)

Figure 4.5. Opto-electronics system for the designed sensor. (a) The block diagram of the designed opto-electronics system. Light sources are two different wavelength Thorlabs fibre-coupled LEDs (660nm and 850nm). The photodetector is a Thorlabs PDA36AEC. The data-acquisition system is a National Instruments myDAQ. (I/V – current to voltage converter, DAC – digital to analogue converter, ADC – analogue to digital converter and PC – personal computer). (b) The prototype of the opto-electronic system. It consists light sources which have two LEDs (red frame) and two LED drivers (yellow frame), a photodetector (blue frame) and a data acquisition card (green frame). (c) The SmartScope FBG interrogator. The resolution of the interrogator is set at 0.1pm in this research.

4.1.2.1 Light Source and LED Drivers

The reflectance pulse oximetry sensor part consists of two LEDs at different wavelength: one at $\lambda = 660$ nm (Thorlabs fibre-coupled LED. Model number M00408143); one at $\lambda = 850$ nm (Thorlabs fibre-coupled LED. Model number M00290109). The normalised intensity spectrum of both LEDs (660nm and 850nm) is shown in Appendix B. Taking the 3dB cut-off frequency into consideration, the bandwidth of both LEDs (FWHM) are 25nm (red) and 30nm (infrared). According to operator manuals of both LEDs, the typical power of 400 μ m diameter fibre coupling-out light from both LEDs are 14.5mW (Red) and 13.4mW (Infrared) [119, 120].

The light level and modulation of both LEDs were controlled by two same type Thorlabs LED drivers (yellow frame, fig 4.5b) which were switched to modulation mode. In accordance with the operator manual, the input voltage and modulation frequency ranges of the LED driver were 0 to 5V and 0 to 5 kHz [121]. Both Thorlabs LED drivers were controlled by the output of the DAC (16bit resolution). The performance of light source and LED drivers will be later discussed in section 4.2.

4.1.2.2 Photodiode and Trans-impedance Amplifier

The photodetector (PDA36-EC, Thorlabs) utilised in this study was composed of a reverse-biased PIN photo diode and a switchable gain trans-impedance amplifier packaged in a rugged housing (shown in blue frame, fig. 4.5b). The responsivity of the PIN photo diode is shown in Appendix B. According to the responsivity diagram (shown in Appendix B), the responsivity of both LEDs applied are 0.35A/W (at 660 nm) and 0.55A/W (at 850 nm), respectively [122].

Figure 4.6 is the schematic of the switchable photodetector. A blue dotted line frames the trans-impedance amplifier which converts the photo current (i_{ph}) generated by the photo-diode into the amplified output voltage. Considering the light responsivity of the photo-diode, equation 4.1 defines the light-to-voltage conversion of the photo-detector. Based on the figure 4.6, equation 4.2 is deduced from the equation 4.1 to show the output voltage of the photo-detector. The gain of the trans-impedance amplifier is switchable, and was set to 4.75×10^6 V/A in this study.

$$\text{Output [V/W]} = \text{trans-impedance gain [V/A]} \times R(\lambda)[\text{A/W}] \quad (4.1)$$

$$V_{out} (V) = - R_f (V/A) \times I_{ph} (A) \quad (4.2)$$

Where $R(\lambda)$ is the spectral responsivity of the photo-diode which is 0.35(at 660 nm) and 0.55(at 850nm) in this research, I_{ph} is the photo-current generated at the photo-diode ($I_{ph} = \text{light power} \times R(\lambda)$), R_f is the feedback resistance and V_{out} is the output voltage of the trans-impedance amplifier.

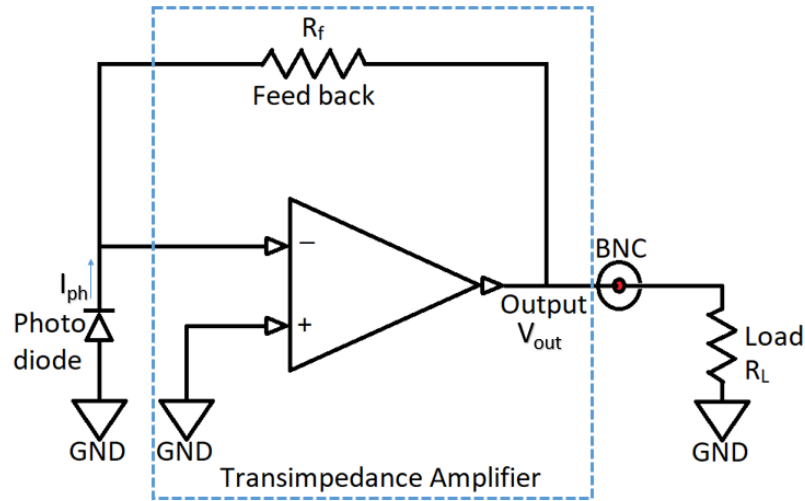


Figure 4.6 Schematic of the photodetector (photo diode and trans-impedance amplifier). I_{ph} is the photo-current, R_f is the feedback resistance and R_L is the resistance of the load. The amplifier in the diagram is the AD829J type op-amp.

As figure 4.6 shown, the output port of the photodetector is the BNC type port. The electrical resistance of the coax cable chosen in this research was very small (assumed to be 0Ω), and the terminating load was located at the end of the coax cable. The output of the trans-impedance amplifier is shown below:

$$V_{out} (V) = - R_f (V/A) \times I_{ph} (A) \times R_L \quad (4.3)$$

Figure 4.5a showed that the output of the photodetector was transferred to the data acquisition (DAQ) system. Therefore, the load impedance was the analogue input impedance of the DAQ system which was more than $10 \text{ G}\Omega \parallel 100 \text{ pF}$. The gain of the trans-impedance amplifier chosen in this research is $4.75 \times 10^6 \text{ V/A}$. Equation 4.4 is deduced from equation 4.3 by substituting the gain, and equation 4.5 inverts the output voltage back to the photonic power.

$$V_{out} (V) = 4.75 \times 10^6 (V/A) \times I_{ph} (A) \quad (4.4)$$

$$\text{Photonic power (W)} = 3.57 \times 10^{-7} (A/V) \times \frac{V_{out}(V)}{R(\lambda)} \quad (4.5)$$

Where the photonic power is the power of light transferred to the photo-detector.

As the instrument operating manual described, the maximum voltage output of the PDA36a is 10 volts for high load impedances. Therefore, in accordance with equation 4.5, the maximum photonic power detected by the PDA36a is 4.1mW. In this study, the photonic power level of PPG signals detected is around 1.79mW at 660 nm and 1.15 mW at 850 nm. The PDA36a is thus capable of detecting reflected optical signals in this research. The detailed analysis of noise will be discussed later in section 4.2.3.

4.1.2.3 Data Acquisition System

In this study, the data acquisition system (National Instruments myDAQ) consists of two parts which are analogue-to-digital converter (ADC) and digital-to-analogue converter (DAC). One ADC channel was used to read the output of the photodetector whilst two DAC channels exported two interleaved square waves to modulate LEDs. The arrangement of the NI myDAQ subsystems is depicted in Appendix B.

Figure 4.7 illustrates the differential connection between the photo-detector and the DAQ system in this study. As the DAQ system and the photodetector were not powered by the same power supplies, the negative side of the analogue signal was connected to the ground of the NI myDAQ to share the same ground reference. As figure 4.7 shown, the output impedance (50Ω) of the photodetector gives the rise to a slight imbalance in the differential signal path. Since the instrument of the DAQ system confirms that the connection shown as figure 4.7 works well with low source impedance (less than 100Ω), the imbalance in the differential signal path caused by the output impedance (50Ω) of the photodetector could be ignored.

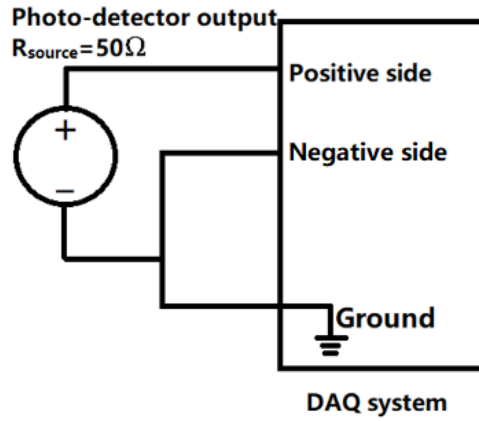


Figure 4.7. Differential connections between the photo-detector and the DAQ system. Although the source impedance ($50\ \Omega$) results in the imbalance in the differential signal path, the differential-mode noise is very tiny since the value of impedance is small. In this case, the differential noise is ignored.

Two DACs (DAC 8851, Texas Instruments) were used to control the LED drivers and therefore the modulation of the light source. Figure 4.8 shows the string resistors architecture (R-string) of the 16-bit DAC. As figure 4.8 shown, the R-string consisted of 16 same impedance (R) resistor and one voltage divider ($16 \times R$), and 17 switches followed each resistor. By closing one of the switches between the string and the followed buffer amplifier, it determines at which node on the string the voltage. In this research, the output voltage of the DAC ranged from 0 to 10 volts. Equation 4.6 describes the output of the R-string, and equation 4.7 gives the least significant bit (LSB) of the DAC.

$$V_{\text{out}} (\text{V}) = 0.5 \times V_{\text{ref}} \times \frac{\text{Number of switch closed}}{16} \quad (4.6)$$

$$\text{LSB} = \frac{0.5 \times V_{\text{ref}}}{2^{16}} \times 2 \quad (4.7)$$

Where V_{out} is the output of the R-string which is fed into the buffer amplifier and V_{ref} is the reference voltage.

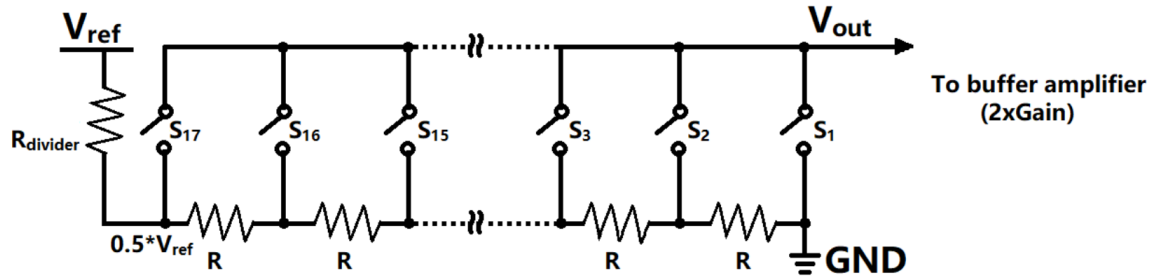


Figure 4.8. Resistor string of the 16-bit DAC. The system is composed of 16 same impedance (R) resistors and one voltage divider which is 16 times the resistor R . There is a switch set between each resistor and the output of the R -string. According to equation 4.6, the output of the string ranged from 0 to half of reference voltage. The LSB of the DAC is

The overall DAQ system is controlled by Labview (version 2015 SP1). TDMA is used to read both PPG signals using only one photodetector, which will be discussed in section 4.2.1. Two 500 Hz square wave (25% duty cycles, 180° phase difference) are used at the DAQ sampling frequency of 100 kHz.

4.1.2.4 FBG Interrogator

Figure 4.9 depicts the measurement of the FBG response using the FBG interrogator (SmartScope FBG interrogator, Smartfibres, UK). In figure 4.9, the black frame covers the FBG interrogator containing a tuneable laser which allows data rates of 25 kHz (over a narrow bandwidth or 2.5 kHz over the all 40nm range) for sequentially sampled FBGs, light splitters, communication interface, detection circuit and data processing. As figure 4.9 shows, light emitted from the tuneable laser (red arrow) is split into four couplers that in its turn is can be connected to an array of FBGs (purple bars) through FC/APC fibre connectors. For each channel, light reflected by the FBGs (blue bars) is coupled into a photodiode and transimpedance amplifier (detection circuit). By analysing the reflected light from 4 channels, the FBG interrogator processes the spectrum and tracks the FBG wavelength peak for each FBG response on each channel.

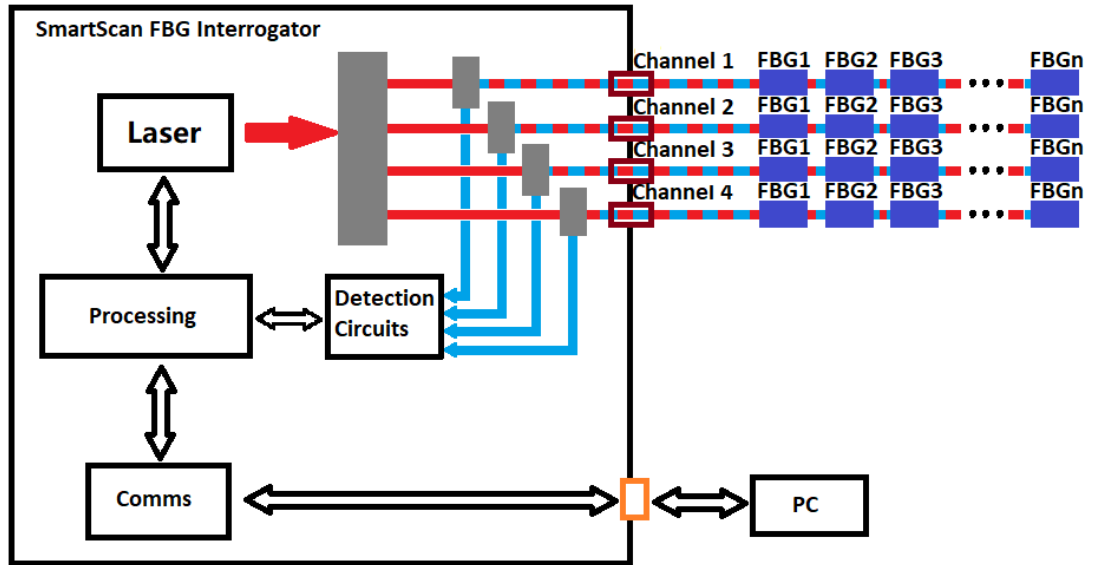


Figure 4.9. SmartScope FBG interrogator. All the components of the FBG interrogator are framed in the black rectangle. The tuneable laser allows data rates of 5 Hz (over the all 40nm range) for all sampled FBGs simultaneously. Detection circuits are used to read the spectrum value of split reflect lights. Data processor controls the laser and communications interface, and analyse the data of reflected light. Red arrow is light emitted from laser, grey bars are optical splitter, red bars are split light, blue bars are reflected light and purple bars are FBGs (Source : [115]).

The SmartScope FBG interrogator is a high resolution interrogator with 4 channels of which the wavelength resolution can achieve 0.1pm for the entire wavelength range from 1528 to 1568 nm (i.e. 40 nm with a scan frequency of 1 Hz). The maximum scan frequency of the FBG interrogator for all sensors simultaneously with reduced wavelength resolution (0.2 pm) is 5 Hz.

4.1.3 Gain and Noise Measurement

As shown in figure 4.5a, the digital reflected light intensity data processed in the PC is inverted, amplified and analogue-to-digital converted via the analogue front-end circuit. In order to investigate the original photonic signal and the input referred noise, this section summarises the gain of each block circuit (shown in figure 4.5a) and the noise of the analogue front end (shown in figure 4.5a) at the input of the ADC. The detailed information of the DAQ system can be found via the NI myDAQ Specification [123]. Section 4.1.3.1 describes the gain of each stage of the analogue front-end, and the cumulative gain as well. Section 4.1.3.2 discusses the theoretical noise at the each

stage of the analogue front-end, and inverts the noise at each stage into the photo-diode input referred noise.

4.1.3.1 Analogue Front-end Gain

Figure 4.10 is a flow chart depicting the working of the analogue front-end. In the study, the initial input signal (photonic power) was detected by the photo-diode, and then converted into the photo-current. In consequence, the trans-impedance amplifier converted the photo-current into an amplified voltage signal, and exported the signal to the ADC. Finally the ADC converted the analogue signal into the digital signal which was later processed in the PC. Table 4.1 summaries the gain of each stage of the analogue front-end, and gives the cumulative gain. For different wavelength light, the gain of the designed system is different due to the different responsivities of the photo-diode. As two different wavelength light sources were applied in this study, it was required to use two different gains in the measurement respectively.

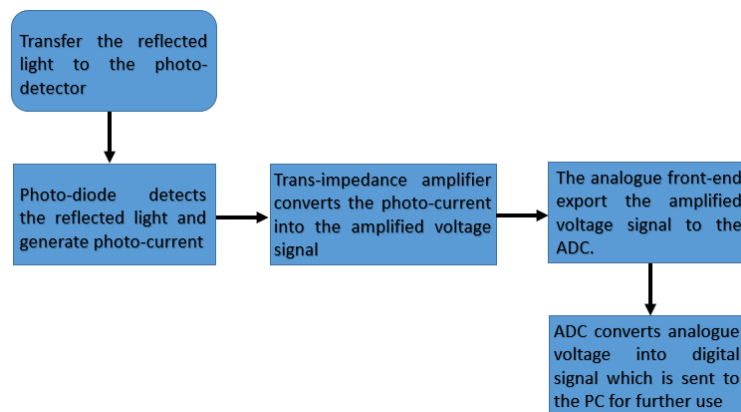


Figure 4.10. Flow chart of the working of the analogue front-end.

Function	Theoretical Gain (Red-660nm)	Cumulative Gain (Red-660nm)	Theoretical Gain (infrared-850nm)	Cumulative Gain (Infrared-850nm)
Photo-Diode Active Area (13×10 ⁻⁶ m ⁻²)	7.6923 × 10 ⁴ m ⁻²	7.6923 × 10 ⁴ m ⁻²	7.6923 × 10 ⁴ m ⁻²	7.6923 × 10 ⁴ m ⁻²
Responsivity of photo-diode	0.35 AW ⁻¹	2.6923 × 10 ⁴ AW ⁻¹ m ⁻²	0.55 AW ⁻¹	4.2308 × 10 ⁴ AW ⁻¹ m ⁻²
Transimpedance	4.75 × 10 ⁶ VA ⁻¹	1.2788 × 10 ¹¹ VW ⁻¹ m ⁻²	4.75 × 10 ⁶ VA ⁻¹	2.0096 × 10 ¹¹ VW ⁻¹ m ⁻²
Total Gain of the analogue front-end		1.2788 × 10 ¹¹ VW ⁻¹ m ⁻²		2.0096 × 10 ¹¹ VW ⁻¹ m ⁻²

Table 4.1. Gain of each stage and cumulative gain through the analogue front-end. Since the responsivity of the photo-diode is not fixed for different wavelength lights, the gain of the system is different for two LED channels.

4.1.3.2 Analogue Front-end Noise

This section summarises the noise of each stage of the analogue front-end circuit following the order of the workflow of the system (shown in Figure 4.10). The noise measured in this study consists of shot noise, thermal noise, flicker noise and quantisation noise. The brief introduction of these different kinds of noise are:

1. Shot noise: broadband noise which is caused by the random fluctuation in the motion of charge carriers. The shot noise is independent of temperature but proportional to the average current flow [124]. Equation 4.8 gives the shot noise(i_{sh}) current [125].

$$i_{sh} = \sqrt{2 \times Q \times I_{avg} \times \Delta_f} \quad (4.8)$$

Q is the electron charge (1.6×10⁻¹⁹ coulombs), I_{avg} is the average dc current (Amps) and Δ_f is the frequency bandwidth over which the noise is considered.

2. Thermal noise: broadband noise which arises from the thermally generated random distribution of electrons within a conductor. Thermal noise is independent of the current flow and is directly proportional to the temperature [126]. The thermal noise voltage (v_{th}) is shown in equation 4.9 as follows [127]:

$$v_{th} = \sqrt{4 \times k \times T \times R \times \Delta_f} \quad (4.9)$$

k is the Boltzmann's constant (1.38×10^{-23}), T is the absolute temperature (Kelvin) and R is the resistance in ohms and Δ_f is the frequency bandwidth over which the noise is considered.

3. Flicker noise: broadband noise which is present in both active and passive devices arises from not fully known reasons. Flicker noise decreases logarithmically with the frequency [128]. Equation 4.10 describes the flicker noise (v_{rms}) [126].

$$v_{rms} = K_v \times \sqrt{\ln \frac{f_{max}}{f_{min}}} \quad (4.10)$$

K_v is the proportionality constant which gives the spectral density at f_{min} , f_{max} and f_{min} are the minimum and maximum frequencies in Hz over the whole band of noise calculation.

4. Quantisation noise: Quantisation is the process of mapping a continuous input signal to the countable output. In this research study, the quantisation noise, which is broadband noise, arises from the process of using an ADC to convert the analogue input signal into digital output of finite length. Equation 4.11 show the calculation of RMS quantisation noise $e_{rms(t)}$. [126].

$$e_{rms(t)} = \frac{V_{fs}}{\sqrt{12} \times 2^N} \quad (4.11)$$

Where V_{fs} is the reference voltage of the ADC with a f_s sample rate and N is the bit number of the ADC.

If the ADC input signal is assumed to be spread over several quantisation intervals, the quantisation noise is Gaussian distributed. In this case, this noise's power spectral density is white and distributed from $-\frac{f_s}{2}$ to $\frac{f_s}{2}$.

Therefore, the spectral density of quantisation noise can be calculated by equation 4.12.

$$e_{psd(t)} = \frac{V_{fs}}{\sqrt{12} \times \sqrt{f_s} \times 2^N} \quad (4.12)$$

In addition to the four different kinds of noise mentioned above, aliasing is also an artefact to be considered in the electrical system design. This occurs when the discrete sampling rate of the system is lower than twice the Nyquist frequency. In this research, the Nyquist frequency was 10 kHz (half of the ADC sampling frequency) which is 20 times larger than the modulation frequency (500Hz) of PPG signals. Hence, aliasing did not represent a problem in this research.

Photo-diode Noise

There are two sources of noise identified in the photo-diode which are Shot noise i_{sh} and Thermal noise i_{th} . Equation 4.13 gives the total noise generated by the photo-diode. The noise of the photo-diode is often expressed as Noise Equivalent Power (NEP) which is defined as follows:

$$I_{total} = \sqrt{i_{sh}^2 + i_{th}^2} \quad (4.13)$$

$$NEP = \frac{RMS\ noise\ current(A)}{Photodiode\ sensitivity(AW^{-1})} = \frac{I_{total}}{R_{\lambda}} \quad (4.14)$$

Where R_{λ} is the responsivity of the photo-diode in AW^{-1} as described in section 4.1.2.2. For PDA36a-EC, the data sheet provided NEPs of $3.9 \times 10^{-12} W/\sqrt{Hz}$ at 660nm and $2.4818 \times 10^{-12} W/\sqrt{Hz}$ at 850nm.

Trans-impedance Amplifier Noise

Three main noise sources exist in the trans-impedance amplifier which are amplifier voltage noise v_n , amplifier current noise i_n and the thermal noise v_{th} generated by the feedback impedance. Figure 4.11a is the model of the amplifier voltage noise. A number of noise sources within the op amp (resistor noise, KT/C noise, flicker noise and current noise) are modelled externally as the voltage noise source v_N . These noise sources are effectively uncorrelated. Figure 4.11b gives the model of the amplifier current noise. Two current noises at the inverting/non-inverting inputs are uncorrelated, or do not have the same $1/f$ corner when the op amp has current feedback.

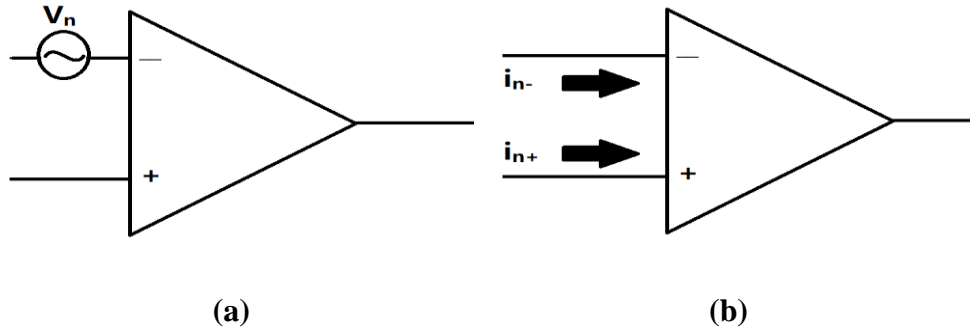


Figure 4.11 Models of amplifier noises. (a) Amplifier voltage noise model. Input voltage noise is bandwidth dependent, and normally ranged from $1\text{nV}/\sqrt{\text{Hz}}$ to $20\text{nV}/\sqrt{\text{Hz}}$. (b) Amplifier current noise model. Input current noise is also bandwidth dependent, and normally ranged from $0.1\text{fA}/\sqrt{\text{Hz}}$ to $101\text{pA}/\sqrt{\text{Hz}}$.

Figure 4.12 gives the total voltage noise v_{total} of the trans-impedance amplifier containing output referred amplifier voltage noise v_{out} , the current noise flowing through the trans-impedance v_i and the Thermal noise generated by the trans-impedance amplifier.

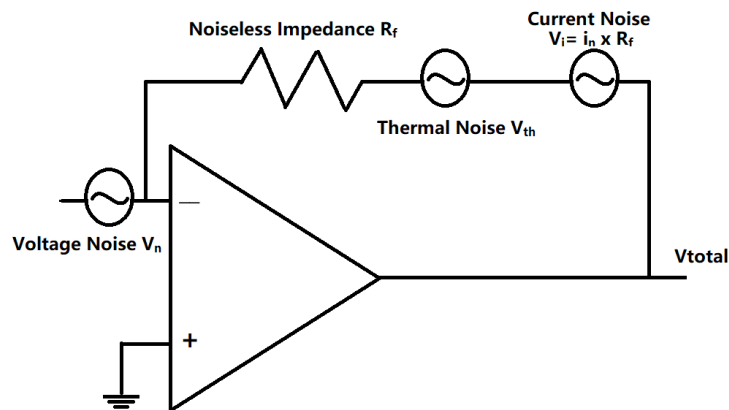


Figure 4.12. Total noise of the trans-impedance amplifier. The diagram gives the noiseless reference resistor in series with two noise-creating voltage sources. The total noise at the output of the amplifier is the rms value of the output referred voltages of three main noise sources.

The data sheet of op-amplifier AD829J provides the voltage noise, current noise and the closed-loop voltage gain [129], the calculation of noises as follows:

Voltage noise

$$V_{\text{out}} = \text{Closed-loop Voltage Gain} \times V_n \quad (4.15)$$

$$V_{\text{out}} = 10 \times 1.7\text{nV}/\sqrt{\text{Hz}} = 17\text{nV}/\sqrt{\text{Hz}}$$

Current noise

$$V_i = R_f \times i_n \quad (4.16)$$

$$V_i = 4.75\text{M}\Omega \times 1.5\text{pA}/\sqrt{\text{Hz}} = 7125 \text{ nV}/\sqrt{\text{Hz}}$$

Where R_f is the impedance of the feedback resistors.

Thermal noise

$$V_{th} = \sqrt{4 \times 1.38 \times 10^{-23} \times 298^\circ\text{K} \times 4.75\text{M}\Omega} = 279.5\text{nV}/\sqrt{\text{Hz}}$$

Total noise

$$V_{total} = \sqrt{V_{out}^2 + V_i^2 + V_{th}^2} = 7130.5 \text{ nV}/\sqrt{\text{Hz}} \quad (4.17)$$

Quantisation Noise

The data sheet of the ADC shows the full scale input, the binary output word length and sampling rate. Using equation 4.12, the quantisation noise spectral density of 16 bit ADC is as follows:

$$e_{psd} = \frac{10}{\sqrt{12} \times \sqrt{2000} \times 2^{16}} = 984.95 \text{ nV}/\sqrt{\text{Hz}}$$

In order to reduce the quantisation noise, this research interpolates the signal (oversampling). The detailed information is discussed in section 4.3.2.

Table 4.2 is the summary of the calculated output noise of each stage. In section 4.2.3, it describes the noise spectral density of the pulse oximetry sensor.

Sensor	Theoretical Noise Red	Photo-diode Input Referred - Red	Theoretical Noise Infrared	Photo-diode Input Referred - Infrared
Photo diode - NEPs	3.9×10^{-12} W Hz ^{-0.5}	5.07×10^{-17} Wm ⁻² Hz ^{-0.5}	2.5×10^{-12} W Hz ^{-0.5}	3.25×10^{-17} Wm ⁻² Hz ^{-0.5}
Transimpedance Amplifier	7130.5 nV Hz ^{-0.5}	5.58×10^{-17} Wm ⁻² Hz ^{-0.5}	7130.5 nVHz ^{-0.5}	3.55×10^{-17} Wm ⁻² Hz ^{-0.5}
Quantisation Noise	984.95 nV Hz ^{-0.5}	7.67×10^{-18} Wm ⁻² Hz ^{-0.5}	984.95 nV Hz ^{-0.5}	4.90×10^{-18} Wm ⁻² Hz ^{-0.5}
Total analogue front-end nose		7.58×10^{-17} Wm ⁻² Hz ^{-0.5}		4.84×10^{-17} Wm ⁻² Hz ^{-0.5}

Table 4.2. Summary of the output noise of each stage in the pulse oximetry sensor.

4.2 Pulse Oximetry Sensor Characteristics

Section 4.1 introduced the configuration of the designed probe and opto-electronics system. Since the characteristics of the FBG pressure sensor were described in section 3.2 and section 3.3, this section will focus on characterising the POF pulse oximeter.

4.2.1 Time Division Multiplexing

As described in section 4.1.2, the system only utilised one ADC channel to read two PPG signals using a photodiode. In order to allow the only ADC channel to read two mixed PPG signals, TDMA was used in this research.

TDMA is a type of time-division multiplexing which has multiple transmitters but only one receiver. This method divides the signal into different time slot to allow several users to share one channel [130]. Figure 4.13 shows the division of a data stream.

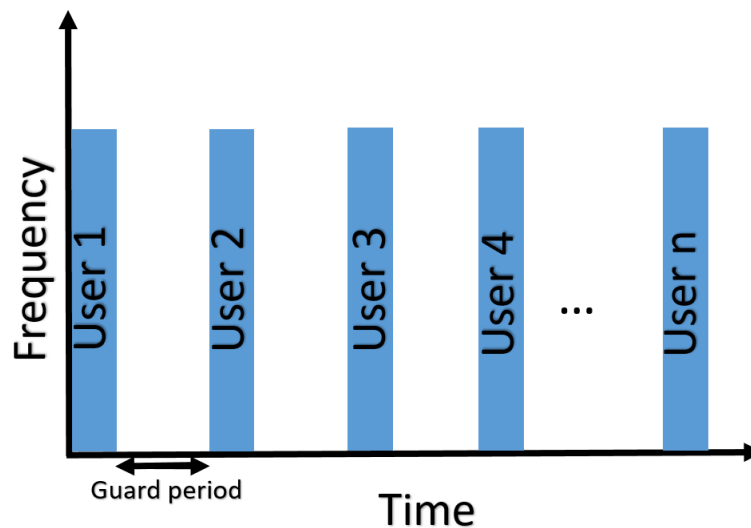


Figure 4.13. Time-division multiple access (TDMA). Each blue frame is allocated to a different user. Time slots contain data with a guard period for synchronisation and avoiding overlap problems.

In section 4.1.2, it introduced that two LEDs (red and infrared) were modulated out of phase at a 25% duty cycle with 180° phase difference. Figure 4.14a shows outputs of two DAC channels which were used to control switching-on/off of both LEDs respectively. The light from each LED is detected during its switched-on time slot whilst the other LED is turned off. Figure 4.14b shows the output of the photo-diode which contains two LEDs light. From the figure 4.14b, it is clear that two LED outputs do not overlap due to the guard period (25% duty). In accordance with the result, it verifies the capability of the system to detect dual PPG signals using one photo-diode.

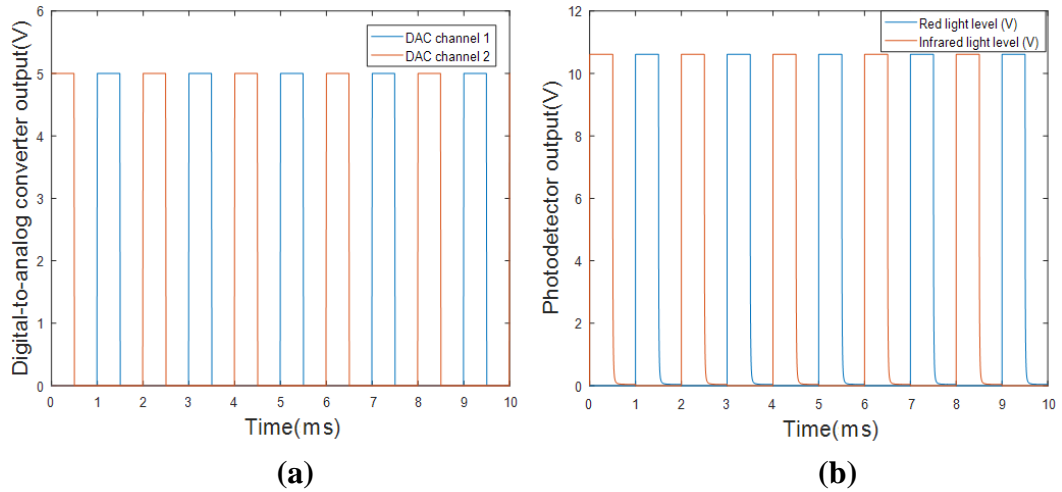


Figure 4.14. (a) TDMA system time slot. These two square waves have 180° phase difference. The red square wave controls the infrared LED and the blue square wave controls the red LED. (b) Optical signal detected by the photodetector. The photodetector detects light emitted from two LEDs directly which are transferred by POFs. The blue one is the output of the red LED controlled by DAC channel 1 and the red one is the output of the infrared LED controlled by DAC channel 2.

In this research, the ambient light measured during both LEDs switched-off slots was taken as the baseline which should be subtracted from the detected light signals. This method was applied by Asada, et al. in a PPG ring sensor design in 2003 [131]. However, this technique assumes that the ambient light is equal during the LED off and on periods. For high artificial light, the ambient light is only partially removed by the subtraction process which may cause ambient artefacts in the PPG signals [132]. Therefore, the modulation frequency is set at a suitable value (500 Hz) to ensure the ambient light does not change significant between on and off periods.

4.2.2 Stray Light Immunity

In section 4.1.2, it mentioned that the receive POF was isolated from the light transferred directly from the two transmit POFs using a 2mm thick rubber buffer. Without the rubber, the stray light detected will interfere with the DC level of the detected PPG signals. This DC crosstalk will influence the S_{PO_2} test results since the DC component of the reflected PPG signals responds to the non-pulsatile parts of the tissue.

The sensor was characterised to eliminate the ambient light interference. Figure 4.15a shows the immunity of the PPG sensor to stray light. Using the configuration shown in figure 4.4, both LEDs were both switched-off for 30s. During this period, the only light present was the ambient light in the lab. After 30s, both LEDs were switched on.

This results in a very tiny increase in the light intensity level (3 mV) caused by light directly passing from transmit to receiver fibre. Then, putting the index finger on the POF path, it resulted in a significant light level increase (to typically 0.5V), to detect the PPG signals of subjects. Figure 4.15b is the zoom-in plot during the LED switching-on period. Figure 4.16a and 4.16b show the reflected PPG signals obtained during this period with or without filtering. The PPG signals after filtering are much clearer. The details of signal filtering process will be described later in section 4.3.

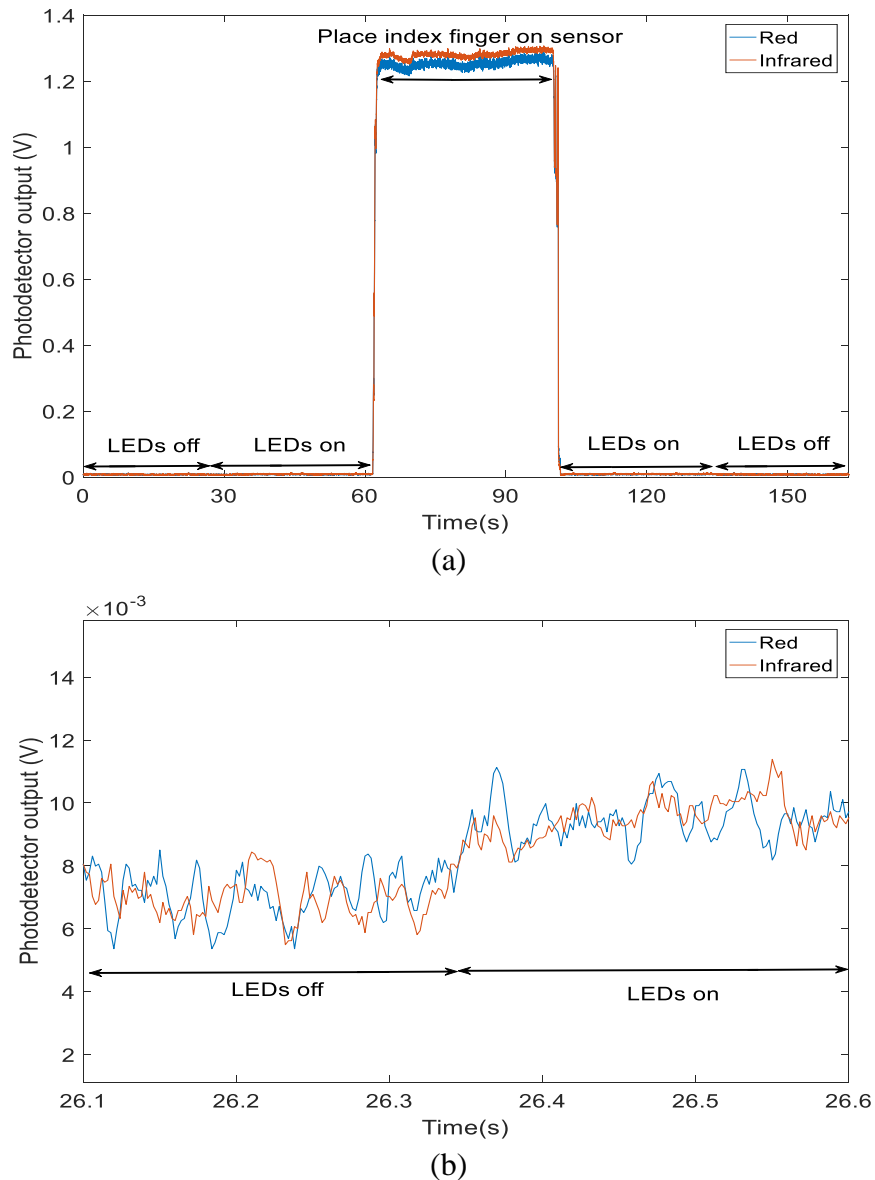


Figure 4.15. The ability of the POF patch to be immune to stray light interference. (a).According to the figure, Significant light intensity changes existed in both red and infrared channels caused by placing the index finger on. (b) The zoom-in plot shows that very tiny voltage increases (about 3mV) caused by LEDs (red and infrared) if there is no finger placed on the sensor. This demonstrates that the sensor is immune to stray light.

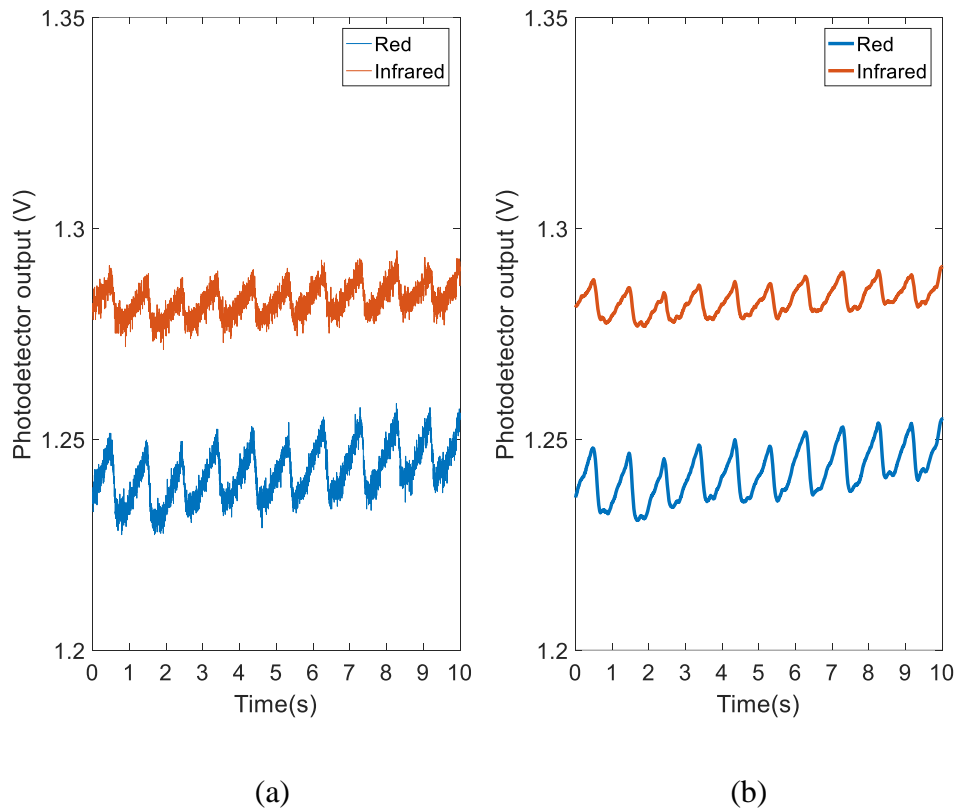
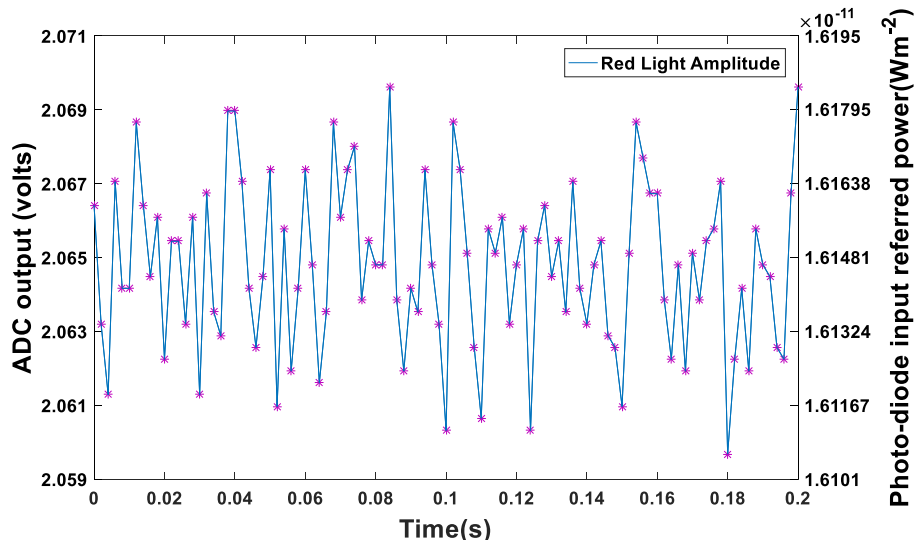


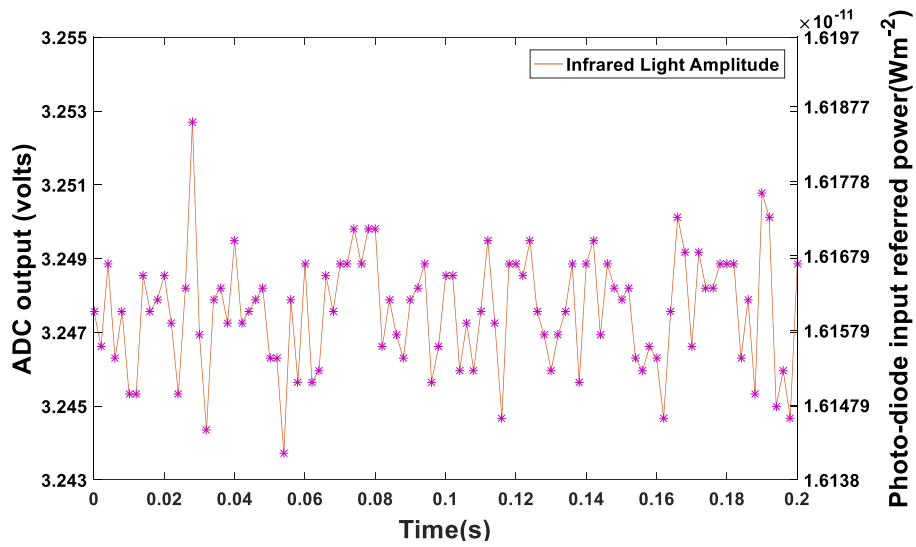
Figure 4.16. Reflectance red and infrared PPG signals obtained by the POF patch. Two different wavelength PPG signals (a). The raw PPG signals without filtering (b) The PPG signals with filtering.

4.2.3 Analogue Front-end Noise

The sensor was characterised in the dark ambient environment to measure the noise floor of the analogue front-end. Figure 4.17a and b illustrate measured time-domain signals (at 660nm and 850nm) at the output of the ADC. From figure 4.17a and b, it is clear that the DC level was set different for two different wavelength light (660nm and 850nm). In this case, the photonic power of both wavelengths detected by the photo-diode is the same. Using equation 4.5, the photonic power detected by the photo-diode is about $1.615 \times 10^{-11} \text{Wm}^{-2}$.



(a)



(b)

Figure 4.17. ADC output time domain plot of the analogue front-end noise. (a) ADC output of the light at 660nm. Individual samples are marked by a pink asterix. (b) ADC output of the light at 850nm. Individual samples are marked by a pink asterix. The DC levels of ADC output is 2.06 volts for the red light and 3.25 volts for the infrared light (photo-diode input referred magnitude is $1.62 \times 10^{-11} \text{Wm}^{-2}$).

This shows the noise of the analogue front-end when the photonic power detected by the photo-diode was $1.62 \times 10^{-11} \text{Wm}^{-2}$ (both red and infrared lights). Figure 4.18 gives the spectral density of these two different signals.

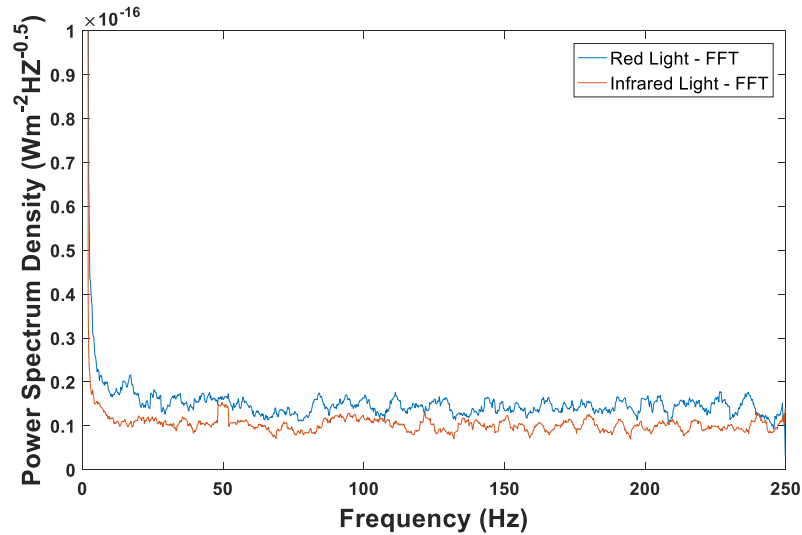


Figure 4.18. Full spectrum plot of the photo-diode input referred noise spectral density of the analogue front-end. Blue trace is the spectral density of the analogue front-end at 660 nm. Red trace is the spectral density of the analogue front-end at 850 nm. The plot is half-spectrum plot. The ADC sampling rate is set at 500 Hz for each wavelength.

Figure 4.18 gives the noise floor of the sensor which was $9.29 \times 10^{-18} \text{ Wm}^{-2}\text{Hz}^{-0.5}$ at 660 nm and $6.972 \times 10^{-18} \text{ Wm}^{-2}\text{Hz}^{-0.5}$ at 850 nm. Compared with the quantisation noise ($7.67 \times 10^{-18} \text{ Wm}^{-2}\text{Hz}^{-0.5}$ for red and $4.90 \times 10^{-18} \text{ Wm}^{-2}\text{Hz}^{-0.5}$ for infrared), the noise floor was slightly higher which probably caused by the voltage noise of the ADC reference, but was considered close enough to the theoretical value.

4.3 PPG Signals Processing

As described in section 4.2, both LEDs were driven by two mixed square waveform with 180° phase difference. Therefore, the mixed-signal obtained at the photo-detector is required to be separated (TDMA demodulation) for further process which is discussed in section 4.3.1. In section 4.3.2, it presents the digital filtering and interpolation process for noise reduction. Following, section 4.3.3 describes the signal quality indices which are used to characterise the quality of obtained PPG signals.

4.3.1 TDMA Demodulation

As described in section 4.2.1, both LEDs were controlled by using two square wave signals exported from the DAC as shown in figure 4.14a. Figure 4.19 (black line) is the 2 kHz sampling rate ADC output of two mixed PPG signals. Two 500 Hz square waves (blue and red) presented in the figure 4.19 were the LED switch controlling

signal outputted from two DACs of the DAQ system. By choosing the data in the switching-on period, figure 4.20 shows a 20 seconds long photo-diode input referred PPG signals of both light wavelength. The sampling frequency of both demodulated PPG signals decreased to 500 Hz. In order to avoid increasing the quantisation noise, the demodulated signal is required to be resampled which will be discussed in section 4.3.2. Figure 4.20 clearly shows that the raw PPG signals are very noisy, and require filtering which will be described in section 4.3.2.

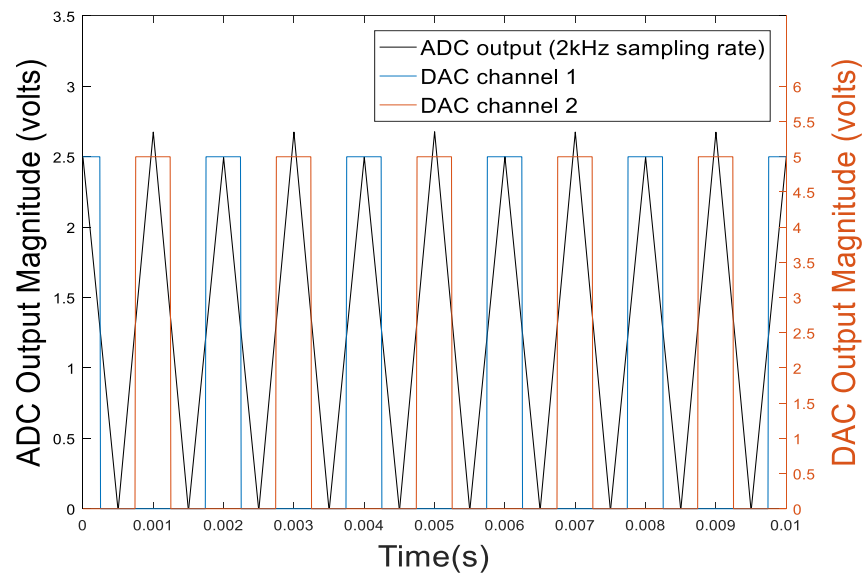


Figure 4.19. ADC output of two mixed PPG signals. Blue square wave is the output of DAC channel 1 which controls the switching-on/off of the red LED. Red square wave gives the output of the DAC channel 2 which controls the the switching-on/off of the infrared LED.

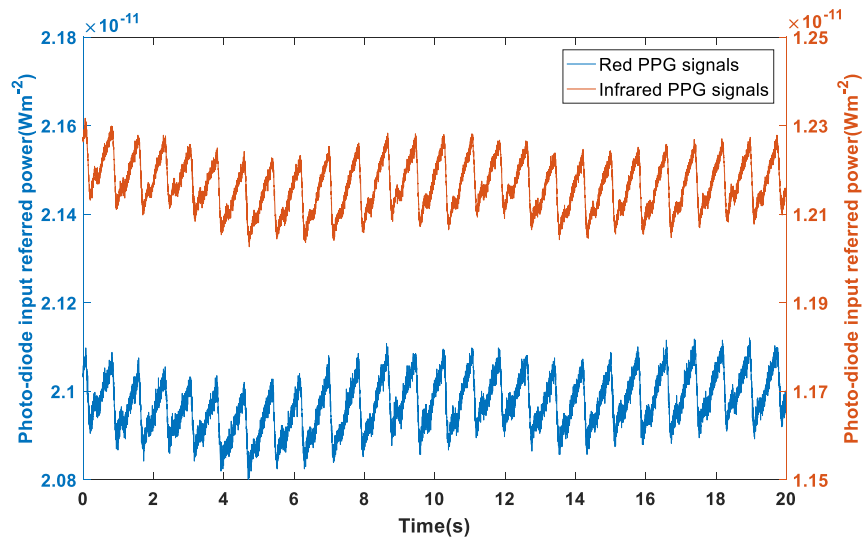


Figure 4.20. Photo-diode input referred PPG signals (raw data). In the diagram, the blue line is the photo-diode input referred red PPG signal without filtering whilst the red line is the photo-diode input referred infrared PPG signal.

4.3.2 PPG Signal Digital Filtering and Interpolation

Figure 4.21 presents the analysis of the 20 seconds long data as shown in figure 4.20. Figure 4.21a&b show the 20 seconds long raw PPG signals at the output of the ADC in time domain and frequency domain. The pulsatile PPG signal (AC component), breathing signal and dicrotic notch can be observed in figure 4.21a. In figure 4.21b, it can be observed that the frequency spectrum of PPG signals (extends as far as the 5th Harmonic), and the frequency spectrum of the breathing signal. By using these data, the heart rate and the breathing rate of subjects can be calculated.

According to the report published by Park et al. [133] in 2014, 0.05 to 10 Hz band-pass filter could separate the pulsatile AC component of PPG signals. Since the breathing rate for adult is normally ranged in 0.2-0.33Hz range [134], this study chosen 0.5 Hz to 10 Hz band-pass filter to extract AC components of PPG signals, and attenuate breathing waveforms. This study filtered raw PPG signals by using Matlab `fir1` – filter function.

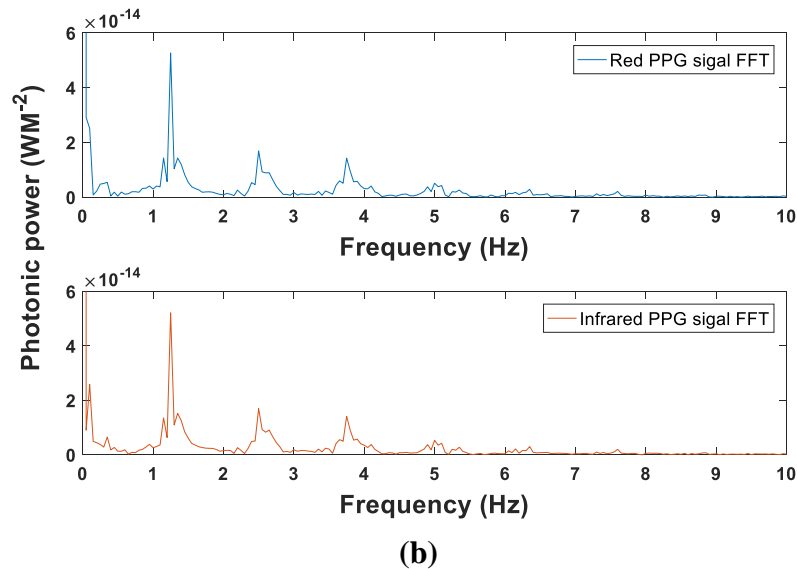
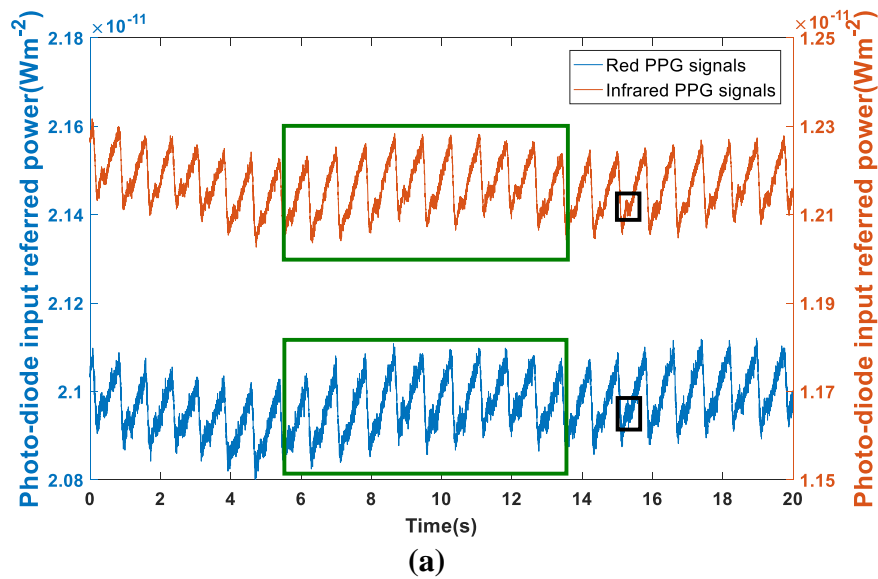


Figure 4.21. (a) Obtained PPG signal in time domain. Black frames squared the dicrotic notches in raw PPG data (both red and infrared) while green frames squared one breathing signal presented in both PPG signals. (b) Obtained PPG signal in frequency spectrum. Blue line shows the frequency spectrum of the red PPG whilst red line shows the frequency spectrum of infrared PPG.

In figure 4.22a, two curves in the diagram are DC components of PPG signals shown in figure 4.21a (blue curve for the red and red curve for the infrared signal) which gives the breathing rate of the subject. In figure 4.21d, two curves are the AC PPG signals extracted from figure 4.21a (blue curve for the red and red curve for the infrared signal) which were obviously clearer than signals shown in figure 4.21a. Based on figure 4.21 and 4.22, it can be seen that the infrared PPG signal had larger AC/DC ratio, which will be discussed later in section 4.3.3.1.

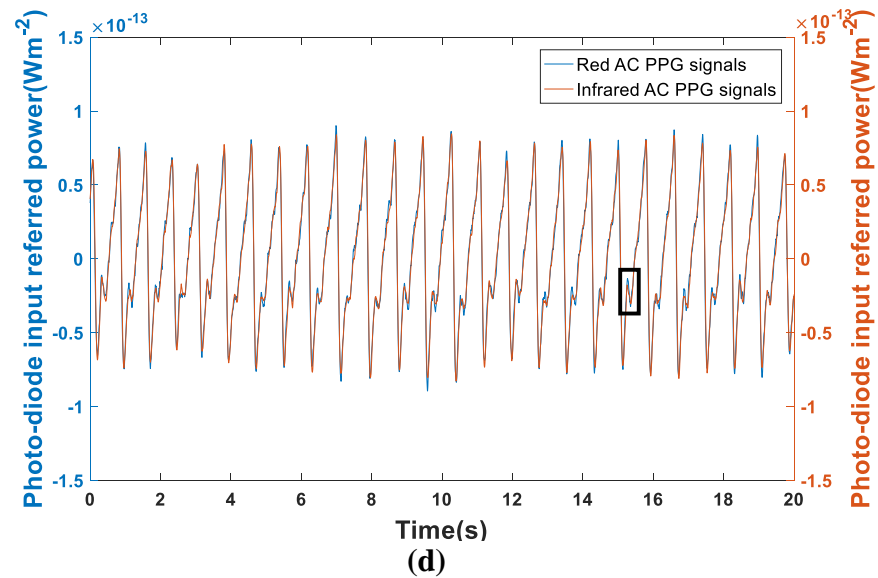
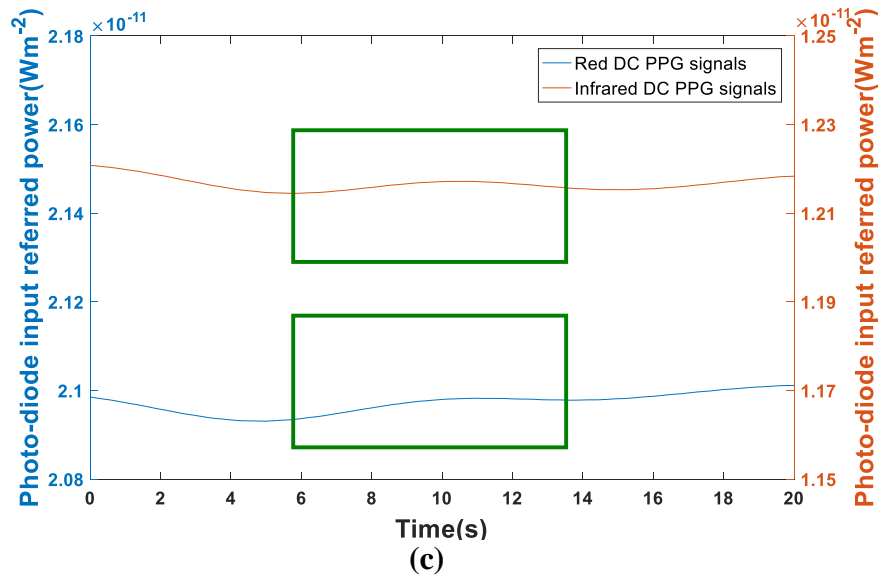
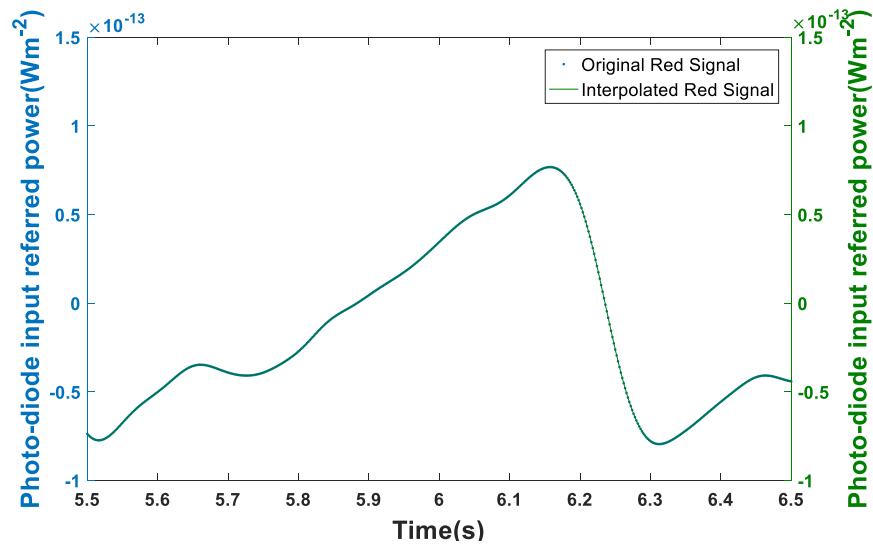


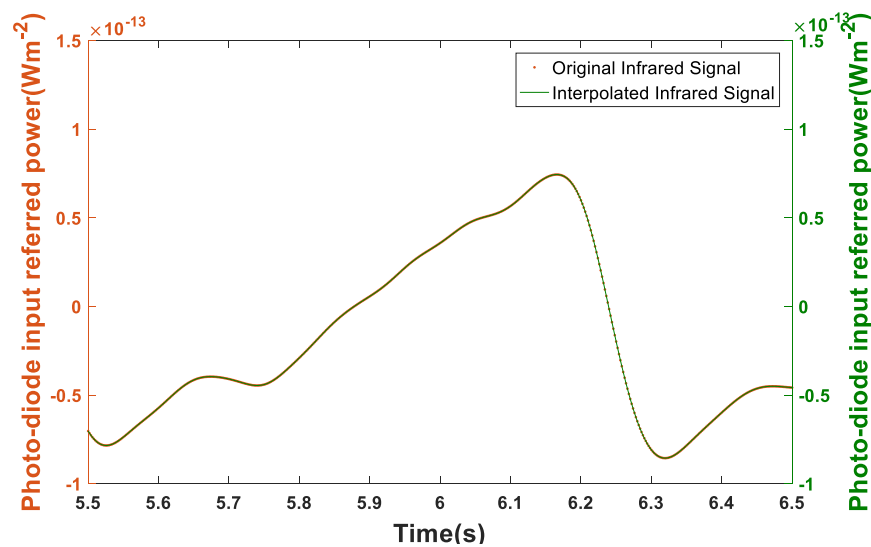
Figure 4.22 (a) DC component of both PPG signals. Blue bottom curve in the diagram is the DC component of the red PPG signal, and red top curve in the diagram is the DC component of the infrared PPG signal. The breathing signals in both PPG signals can be observed (covered in green frame). (b) AC component of PPG signals. The pulsatile components of two PPG signals (Blue bottom curve – Red AC PPG and red top curve – Infrared AC PPG) are matched with each other. Dicrotic notches are obvious in the diagram (the black frame shows an example).

As mentioned in section 4.3.1, the frequency of the demodulated PPG was 500 Hz. According to equation 4.12, the decrease in the sampling rate frequency from 2 kHz to 500 Hz will increase the system's quantisation noise. In order to avoid the increase in the quantisation noise, an interpolation process was applied to increase the sampling rate of the demodulated PPG signal to 2000 Hz. The signal interpolation process was fulfilled via Matlab interpolation function. Figure 4.23a and b present original and resampled pulsatile signals of two light wavelength PPG signals. Green curves in both

diagrams of figure 4.23 present the resampled PPG signals (2 kHz sampling rate) which are matched with the original signals. Thus, it proved that the oversampling method avoided increasing the quantisation noise without deteriorating signals.



(a)



(b)

Figure 4.23. Resampled PPG signals with 2 kHz sampling rate. (a) Resampled red AC PPG. The blue dotted line gives the filtered PPG signals (500 Hz sampling rate). The green curves presents the resampled PPG signal. (b) Resampled infrared AC PPG. The red dotted line gives the filtered PPG signals (500 Hz sampling rate). The green curves presents the resampled PPG signal.

Before proceeding to calculate S_pO_2 values, it is necessary to examine the quality of processed signals. The quality indices chosen for estimating PPG signals in this study were signal-to-noise ratio (SNR), perfusion index (PI) and skewness index (SKI). The

following section describes the detailed information of signal quality estimation processing.

4.3.3 Signal Quality Index of PPG Signals

There are a number of indices applied to judge the quality of signals. Elgendi [135] tested and evaluated eight signal quality indices for assessing PPG signals quality, and recommended the skewness index (SKI) as the best one [135]. Therefore, in this study, expect of the commonly quoted measure (SNR) and the gold standard PPG signal quality index (PI), skewness index (SKI) was also applied to assess the quality of obtained PPG signals SNR, PI and SKI. This section describes of using three different signal quality indices to assess obtained PPG signals.

The obtained PPG signals can be classified into three groups (i.e. “excellent signals”, “acceptable signals” and “unqualified signals”) depends on their qualities [135]. For “excellent signals”, PPG signals included in this group have clear and strong beats (pulsatile components) where the systolic and diastolic waves were salient as shown in figure 4.24a. Figure 4.24b gives the typical PPG signals existed in the “acceptable signals” group which consists of beats (pulsatile PPG signals) but without clear systolic and diastolic phases. In hence, it could not observe the dicrotic notches in figure 4.24b whilst clear notches could be easily found in figure 4.24a. Figure 4.24c presents the very noisy PPG signals annotated to the “unqualified signals” which were highly interference by noise. The annotation process of PPG signals is subjective, but later in this section, signal quality indices will be demonstrated.

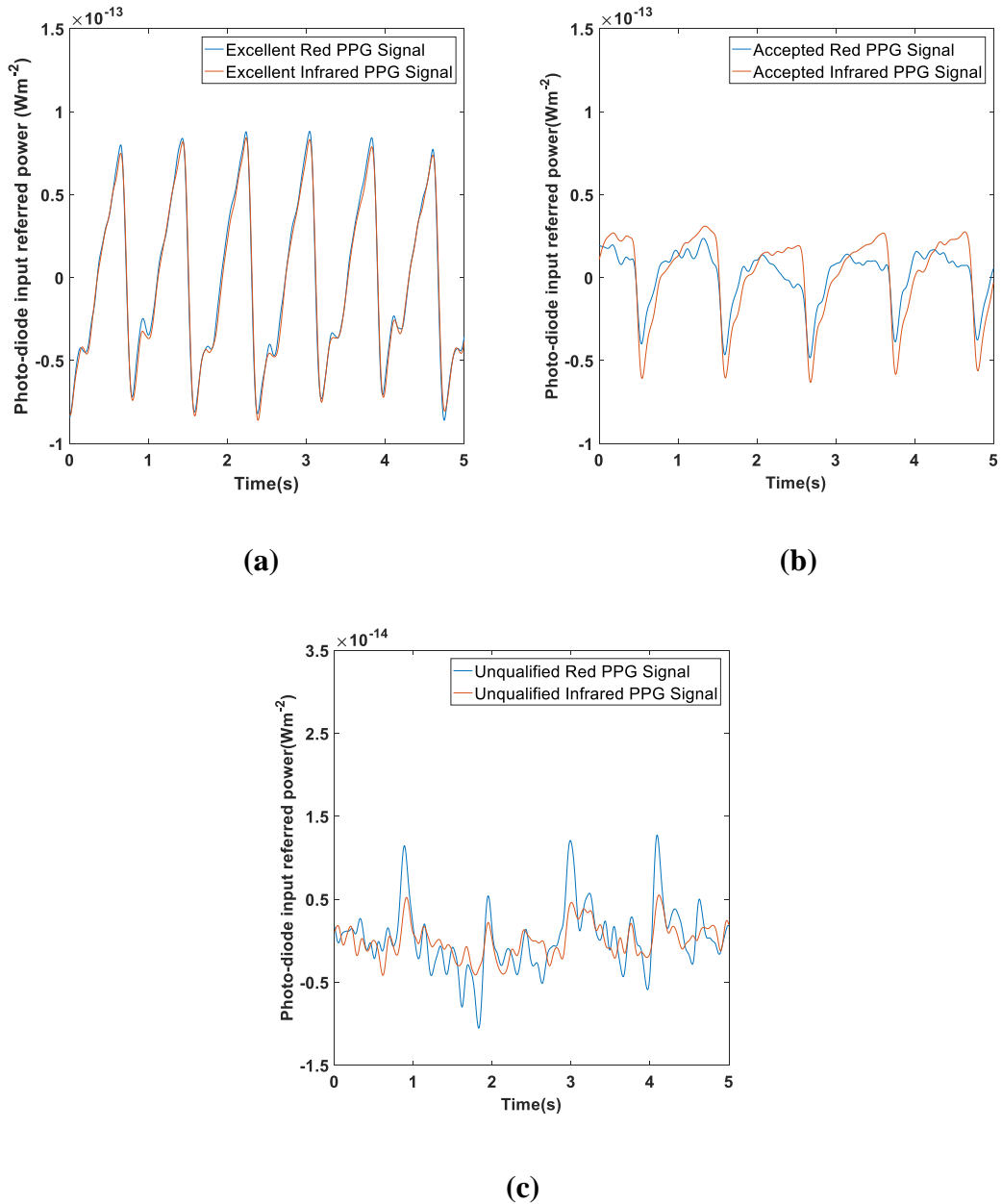


Figure 4.24. Subjective annotation of Photoplethysmogram (PPG). (a) High quality (“Excellent”) PPG signal. (b) Medium quality (“Accepted”) PPG signal. (c) Low quality (“Unqualified”) PPG signal.

4.3.3.1 Signal to Noise Ratio (SNR) Index

Signal-to-noise ratio is a measure widely used in science and engineering which compares the level of the signal to the level of the noise. There are many ways to define SNR, the most common is [136]:

$$\text{SNR} = 10 \times \log_{10} \left(\frac{P_{\text{signal}}}{P_{\text{noise}}} \right) \text{ dB} \quad (4.18)$$

Where P_{signal} is the power of signal, P_{noise} is the power of noise.

Table 4.3 summaries the signal-to-noise ratio of three PPG signals shown in figure 4.23.

Annotation of PPG signal	Raw PPG Red (dB)	Filtered PPG Red (dB)	Raw PPG Infrared (dB)	Filtered PPG Infrared (dB)
Excellent PPG Signal	11.0167	17.0241	13.3959	17.2620
Accepted PPG Signal	7.4030	12.0440	7.7903	15.7828
Unqualified PPG signal	-9.6748	6.6808	-11.8266	5.1818

Table 4.3 Signal-to-noise ratio of different quality PPG signals.

For PPG signals from group “excellent signal” and “acceptable signal”, their SNR were usually higher than 6 dB before filtering, and higher than 12 dB after band-pass filtering described in section 4.3.2. For the unqualified PPG signal, their SNR were close to 0 dB before filtering, and always lower than 10 dB after filtering. These unqualified PPG signals (noisy) were rejected in this research.

4.3.3.2 Perfusion Index (PI)

Perfusion index is a measure used to assess the pulsatile strength at a specific measuring location which is defined as the ratio of the pulsatile blood volume to non-pulsatile (static) blood in peripheral tissue. This allows the PI to provide a non-invasive indication of the peripheral perfusion [137]. This study chosen perfusion index as one of the signal quality indices in terms of two reasons as follows:

1. Perfusion index is the gold standard for assessing PPG signals quality [135], and is the most widely used [138].
2. Peripheral perfusion is easily disrupted by imposed pressure which influences the accuracy of the pulse oximeter [139].

As section 1.1 described, one aim of this research was finding the optimum contact pressure for S_pO_2 measurement. Therefore, PI is one of the most suitable measure for assessing quality of signals [135]:

$$PI = 100 \times \left(\frac{PPG_{max} - PPG_{min}}{|PPG_{raw}|} \right) \quad (4.19)$$

Where PI is the perfusion index, PPG is the filtered PPG signal and $\overline{PPG_{raw}}$ is the statistical mean of the raw PPG signal.

The perfusion indices of three signals (shown in figure 4.23) are shown in figure 4.25.

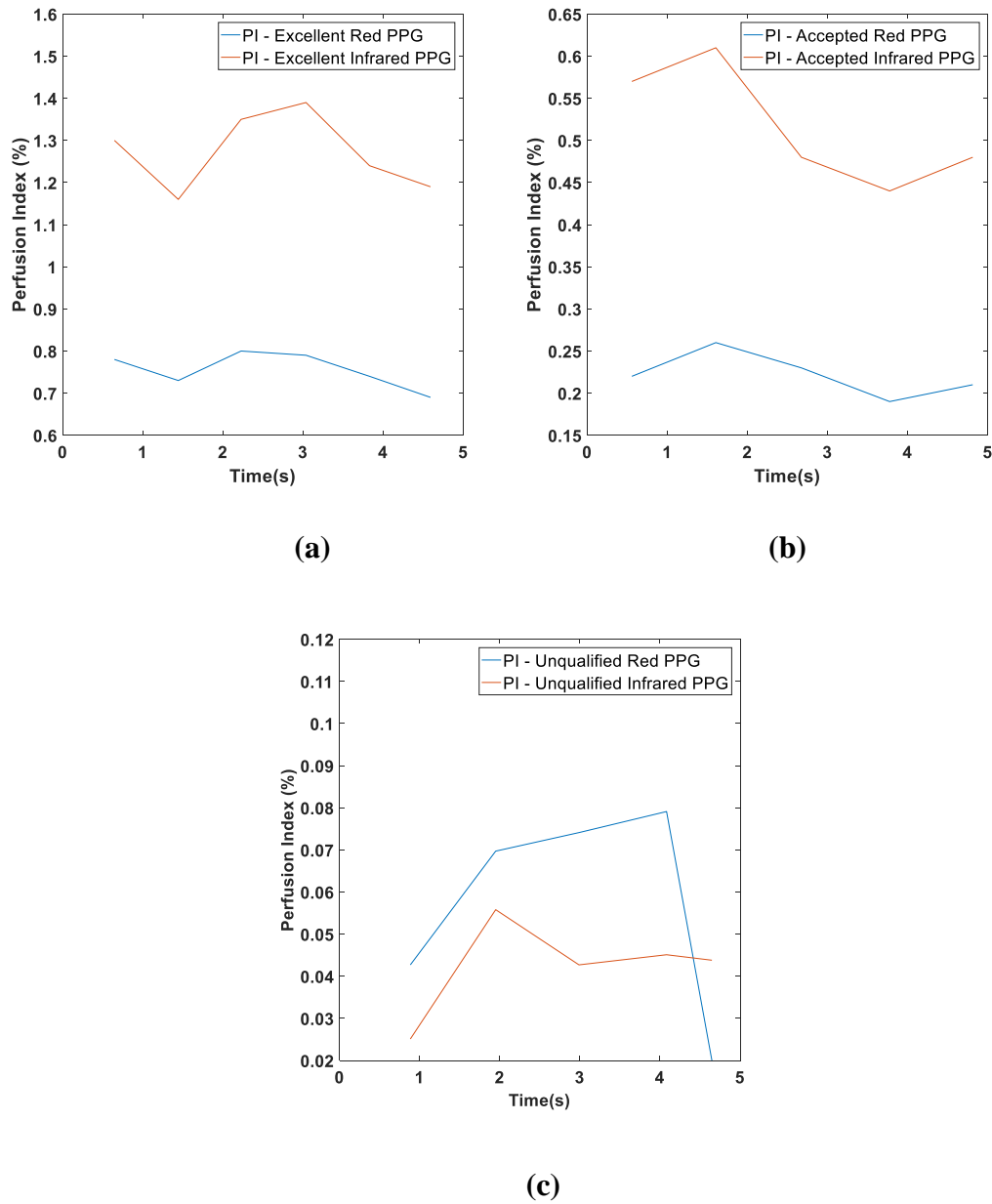


Figure 4.25. Perfusion indices of three PPG signals with different qualities. (a) PI of excellent PPG signals. (b) PI of acceptable PPG signals. (c) PI of unqualified PPG signals.

Figure 4.25a illustrates that the PI of excellent signals was higher than 0.6% for red PPG and 1% for infrared PPG. By analysing 30 figures for all PI experiment results (shown in Appendix C), it indicated that the perfusion index of infrared PPG signals was roughly two times larger than Red PPG signals. For acceptable PPG signals, figure 4.25b shows that the PI was higher than 0.45 for red and 0.55 for infrared. For unqualified PPG signals, the PI was lower than 0.1 for both red and infrared PPG signals. This indicates that the good quality PPG signals have a larger PI value. Based on empirical experience, the PI value of good quality infrared PPG signals is usually larger than 0.4%. Thus, the threshold of PI (infrared) was set at 0.4% for this study. 30 figures for all PI experiment results are shown in Appendix C.

Although PI is the gold standard for assessing PPG signals quality, it cannot identify noise sometimes. Figure 4.26a is a pure random noisy waveform (without PPG signal), and figure 4.26b is the PI of this noisy waveform. It can be found that PI of the noisy waveform (figure 4.26a) was still larger than 0.04% (figure 4.26b). Therefore, another signal quality index is required to confirm whether the processed signal is a PPG or not. In this study, skewness was selected which will be presented in the next section.

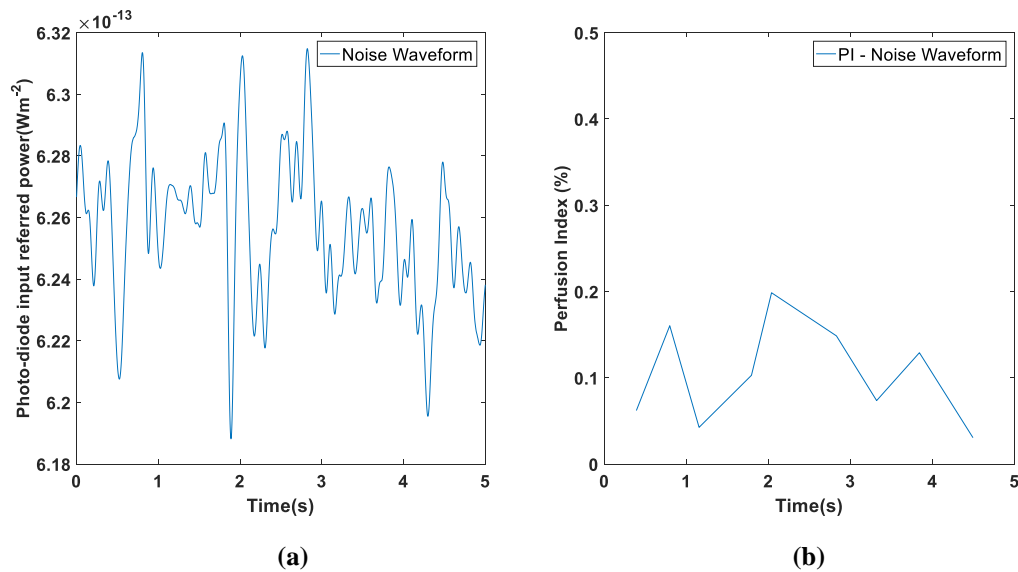


Figure 4.26. Pure Noise waveform. (a) AC pulsatile PPG signal of a 5 seconds long Noise waveform. (b) PI of the pure noise signal.

4.3.3.3 Skewness Index (SKI)

Skewness (SKI) is a measure of the symmetry of a distribution of data in statistics which can be defined as equation 4.20 [140]. If the distribution has a right tail, the skewness is positive, and vice versa. Figure 4.27 gives sketches of left skewed,

symmetric and right skewed distributions [141]. In section 1.2.1.2, it shown that the shape of PPG waveforms was very similar to the right skewed distribution. Therefore, skewness can be used to detect the corrupted PPG signals or noise [142].

$$SKI = \frac{3 \times (\text{mean} - \text{median})}{\text{standard deviation}} \quad (4.20)$$

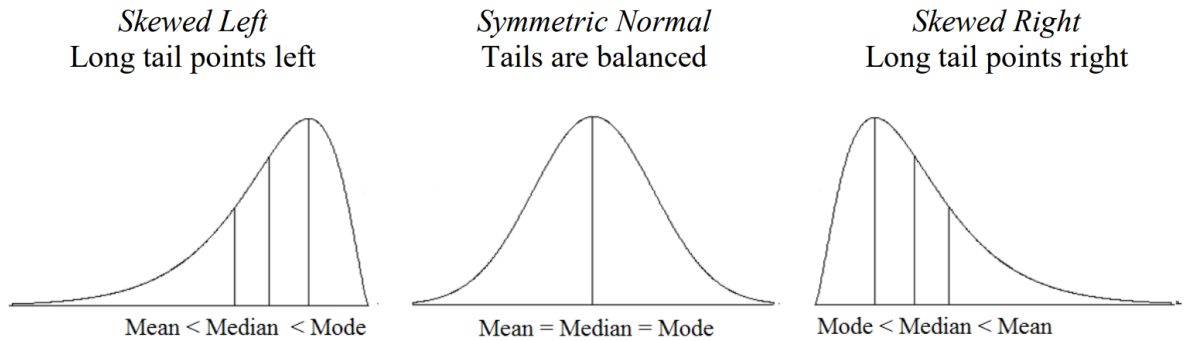
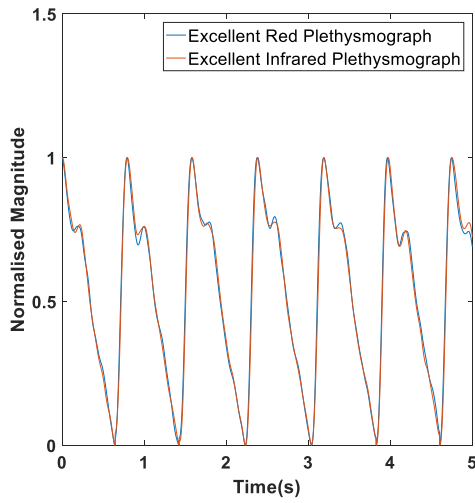
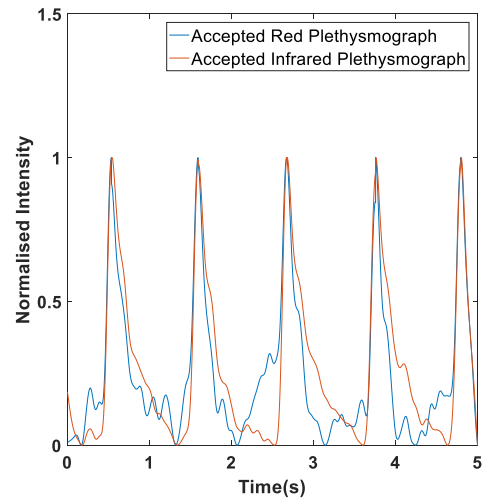


Figure 4.27. Sketches of left skewed, symmetric and right skewed distributions. When the distribution has a left tail (the left diagram), the skewness is negative. When the distribution has a right tail as shown in the right distribution, the skewness is positive. For the symmetric distribution, the skewness is equal to zero.

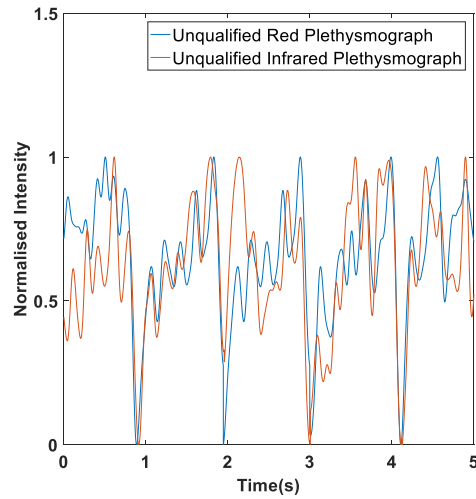
As mentioned in the beginning of section 4.3.3, Elgendi [135] has applied skewness index (SKI) to assess the quality of PPG signals, and recommended SKI as the best quality index. However, compared to the shape of PPG pulses assessed in Elgendi's research, the waveform of obtained reflected light intensity in this research was inverted. In section 1.2.1.2, it has introduced that the reflected light intensity was decreasing during the systolic period, which resulted in the shape of reflected light intensity change was opposite to the waveform of the PPG signal. Figure 4.28 shows the inverted and normalised pulse plethysmograph of the excellent, acceptable and unqualified PPG signals.



(a)



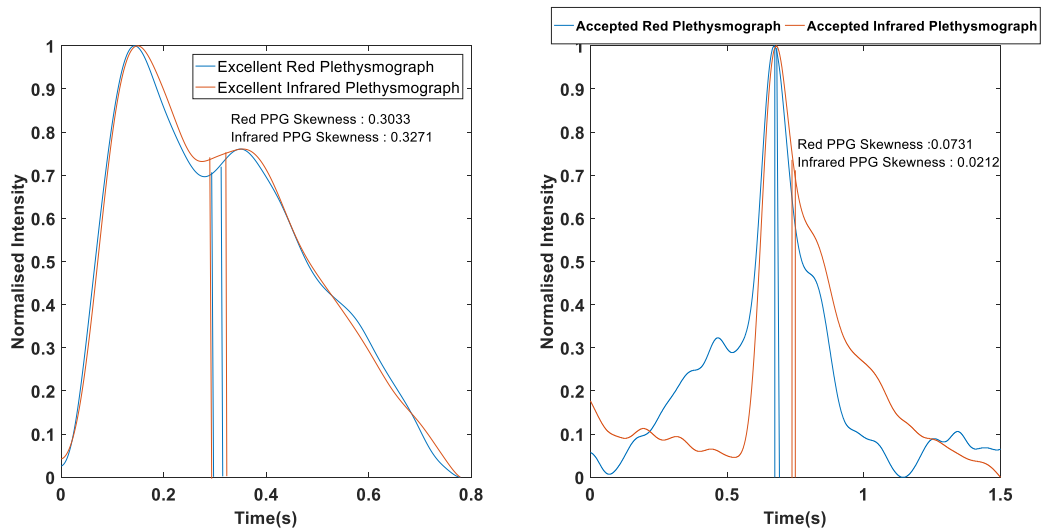
(b)



(c)

Figure 4.28. Inverted and normalised pulse plethysmograph. (a) Excellent signal (b) Acceptable signal (c) Unqualified signal

The next step is to detect the skewness of different quality PPG signals as figure 4.29 shown based on equation 4.20.

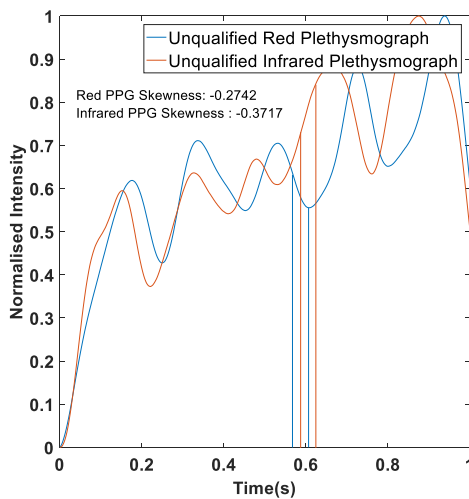


Median < Mean

Median < Mean

(a)

(b)



Mean < Median

(c)

Figure 4.29. Original PPG signals and simulated distribution. (a) Excellent PPG signals. The skewness of two PPG signals was higher than 0.3. (b) Acceptable PPG signals. The skewness was very close to zero. (c) Unqualified PPG signals. The skewness was negative and lower than -0.2.

Figure 4.30 shown that the degradation in the quality of PPG signals decreased its SKI. Figure 4.30 gives the skewness of the PPG signals shown in figure 4.28. The threshold of SKI (infrared) for this paper is zero.

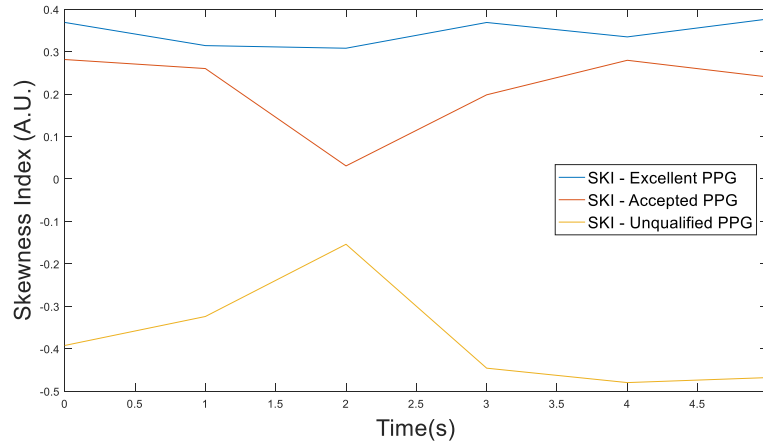


Figure 4.30. Skewness index of different quality PPG signals. Blue curve is the SKI of the excellent PPG which is always positive. Red curve is the SKI of the acceptable PPG which is always positive but lower than the SKI of the excellent PPG. Yellow curve is the SKI of the unqualified PPG which is always negative.

This research has examined the obtained PPG data of 10 volunteers using SNR, PI and SKI. The test results indicated that the signal quality indices chosen matched the subjective classification mentioned at the beginning of this section, which is shown as 30 figures in Appendix C.

4.4 SpO₂ Measurement Results

This section presents the SpO₂ results detected by the pulse oximetry sensing patch. Section 2.1 has illustrated that SpO₂ could be obtained from the R ratio which was defined in equation 2.12. In order to determine the empirical constants (K1 and K2) in equation 2.12, this research compared the POF sensing patch with a commercial pulse oximeter (Masimo Radical-7) which is shown in section 4.4.1. As the contact (skin) force and body temperature are two factors which would affect the SpO₂ measurement [76, 143], section 4.4.2 discussed the skin temperature effects on the SpO₂ measurement using the designed POF patch whilst section 4.4.3 compared the SpO₂ error between the designed sensor and the commercial pulse oximetry system in order to find out the impact of the pressure on SpO₂ measurement.

4.4.1 Preliminary SpO₂ Measurements

This research has tested the index finger SpO₂ of fourteen volunteers using the POF sensing patch with the commercial pulse oximeter recording SpO₂ on the middle finger simultaneously. The protocol of the experiment is described as follows:

1. 14 Volunteers' Demographic information:
 - a. 10 male participants and 4 female participants (only 10 groups of data is applied for deoxygenation calibration)
 - b. Age (mean \pm standard deviation): 31.0 \pm 3.3 years
 - c. Inclusion and exclusion criteria:

Inclusion	Exclusion
<ul style="list-style-type: none"> • Age over 18 • Have health circulatory and respiratory systems 	<ul style="list-style-type: none"> • Have any cardiovascular disease • Have any respiratory system diseases • Have any circulatory system diseases • Have any lung disease • Have any medicines or drugs related to respiratory conditions.

2. Each participant was required to clean their hands using a non-alcoholic antibacterial gel before putting the index finger on the designed POF sensor.
3. Each participant was then asked to sit quietly for 15 minutes to acclimatise before testing
4. Each participant was asked to breathe normally for 5 minutes in order to record SpO₂ values of subjects under normal situation.
5. Next, each participant was instructed to breathe out for 10 seconds, and then stop breathing for 20s to 30s. This process is to generate deoxygenation event. All participants were informed to stop holding breath if they felt uncomfortable.

All 14 volunteers are primarily recruited from the Optics and Photonics group including researchers/PhD students. Human volunteer studies were approved by the

Faculty of Engineering Ethics Committee at the University of Nottingham. This section shows S_pO_2 test results on one volunteer's index finger with a commercial pulse oximeter (Masimo Radical-7) recording the S_pO_2 value of the middle finger simultaneously. However, there were 4 volunteers who could not hold breath long enough to decrease their S_pO_2 values during the experiments. In this case, only 10 groups of data with deoxygenation events were applied for analysis. The rest experiment results are shown in Appendix C.

Figure 4.31a is PPG signals obtained from one volunteer for a period of 500 seconds. During the whole test, the volunteer stood still and breathed normally. Figures 4.33b and c demonstrates that the quality of PPG signals were good enough for S_pO_2 measurement. Figure 4.31d gives the R ratio calculated using equation 2.7.

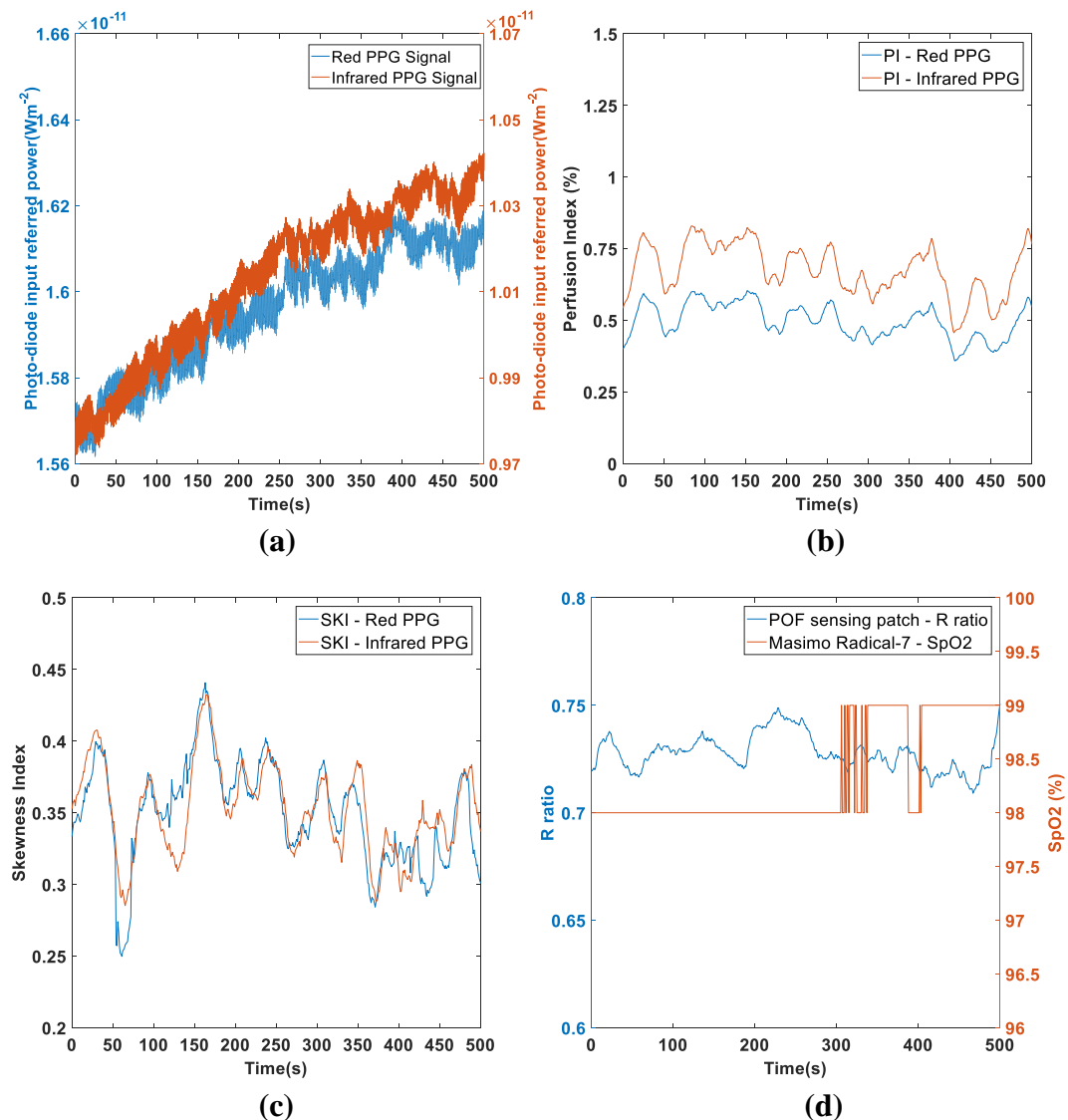


Figure 4.31. Test results of the subject for 500s long. (a) Both wavelength PPG signals. DC levels of two PPG signals increased following the same trace. (b) The perfusion index of test results. (c) The skewness index of test results. (d) Comparison of R ratio and the S_pO_2 .

As equation 2.12 shows, S_{pO_2} has a linear relationship with R ratio. By doing the linear fit, equation 4.21 is deduced. Figure 4.32 gives the comparison between the S_{pO_2} measured by the POF sensing patch and the commercial pulse oximeter (Masimo Radical-7) of which the resolution was 1% which can be seen as jumps in the S_{pO_2} value in fig. 4.31d. The test result of the POF sensing patch is very close to the commercial device (absolute error 0.443%). The information for more test results is shown in Appendix C.

$$S_{pO_2} = 112 + 25 \times R \quad (4.21)$$

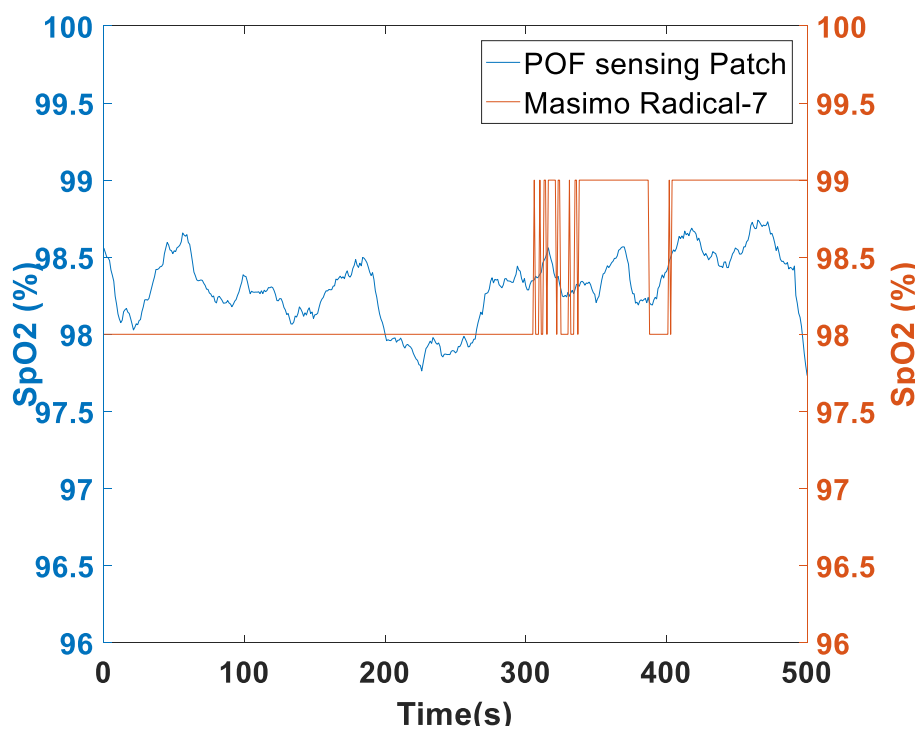


Figure 4.32 Comparison of POF sensing patch with commercial pulse oximeter. Normal breathing both devices record stable values with the absolute error 0.443 ± 0.466 %.

Figure 4.33 is the Bland-Altman plot [144](i.e. difference between two devices' S_{pO_2} vs. mean of two devices S_{pO_2}) which shows the comparison between the designed pulse oximetry system and the commercial pulse oximeter (Masimo Radical-7). In the figure 4.33, it shows that the bias (i.e. the mean difference between S_{pO_2} values detected by two pulse oximeters) is -0.25% and the limit of agreement (LOA) value (i.e. 1.96 times the standard deviation of difference between S_{pO_2} values detected by two oximeters) is 2.2%.

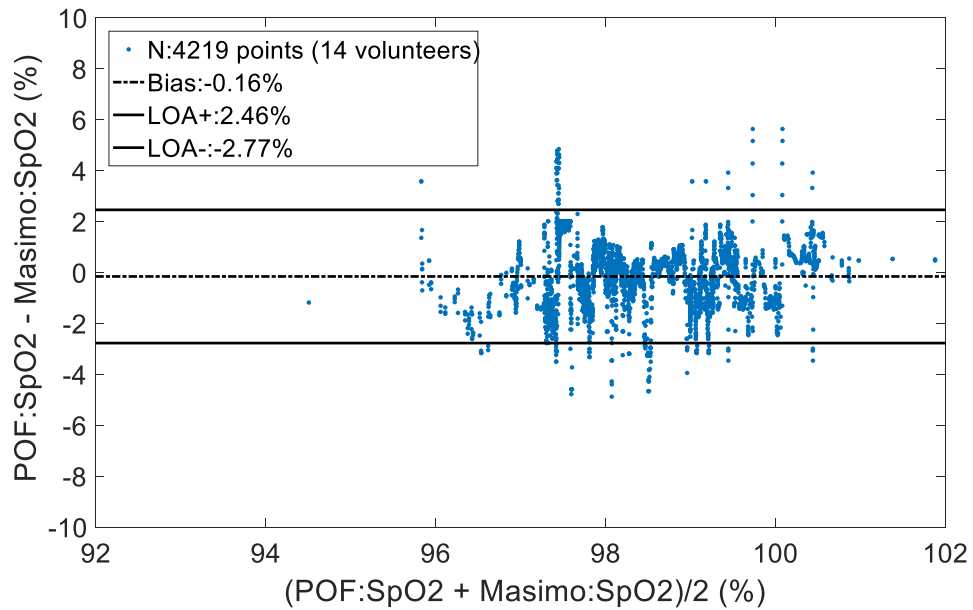


Figure 4.33 Bland-Altman plot of 14 volunteers' SpO₂ without deoxygenated activities. In the figure, there are 3200 sample points. The x-axis is the mean of SpO₂ values between the POF sensing patch and the Masimo Radical-7. The y-axis is the difference of SpO₂ values between the POF sensing patch and the Masimo Radical-7. Bias is the mean of the difference between two pulse oximeters' SpO₂ difference, whilst LOA is 1.96 times the standard deviation of SpO₂ difference values.

As mentioned in the protocol of the experiment, deoxygenation events were induced to estimate the accuracy of the POF sensing patch, under ethical approval by the Faculty of Engineering Ethics Committee at the University of Nottingham. Figure 4.34 shows the comparison between the POF sensing patch with the commercial pulse oximeter. The volunteer was required to breathe out for 14s after 80s long normally breathing, and then stop breathing for 19s before breathing normally again. In figure 4.34, both devices identify the deoxygenation event induced (absolute error 1.16 %). The information for more test results is shown in Appendix C. Figure 4.35 is the Bland-Altman plot which shows the comparison between the POF sensing patch and the commercial pulse oximeter with deoxygenation events. The bias of the Bland-Altman plot in figure 4.35 is -1.06%, and the LOA value is 1.96%.

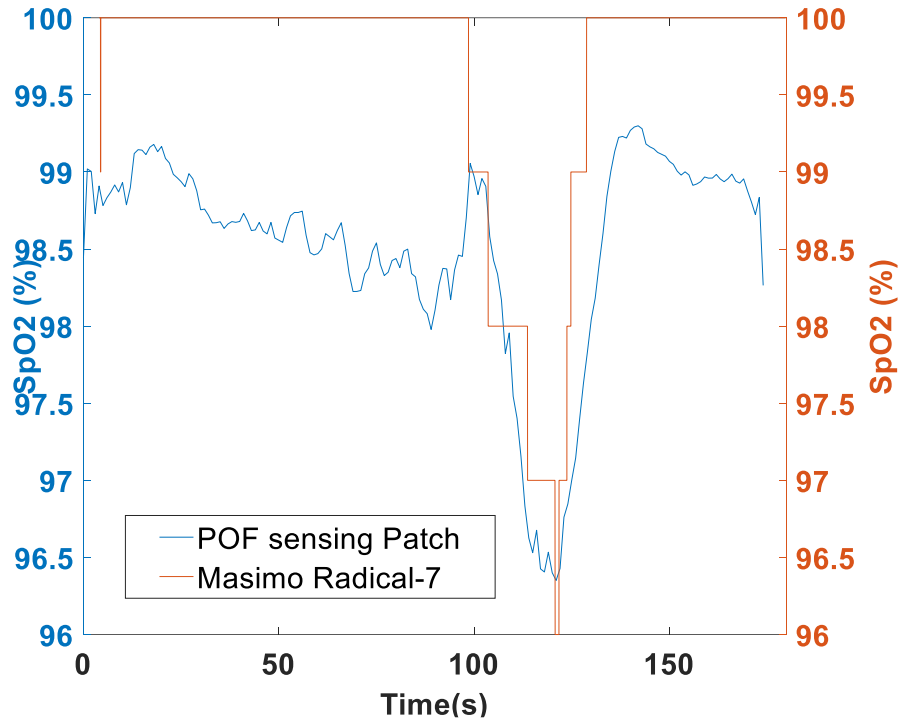


Figure 4.34 Comparison of POF sensing patch with commercial pulse oximeter for the induced deoxygenation event. S_{pO_2} test result with a deoxygenation event. Phase 1: Breathe normally (80s). Phase 2: Breathe out (14s). Phase 3: Hold breath (19s). Phase 4: Breathe Normally (66s). Both devices identify the desaturation event with the absolute error $1.16 \pm 0.423\%$

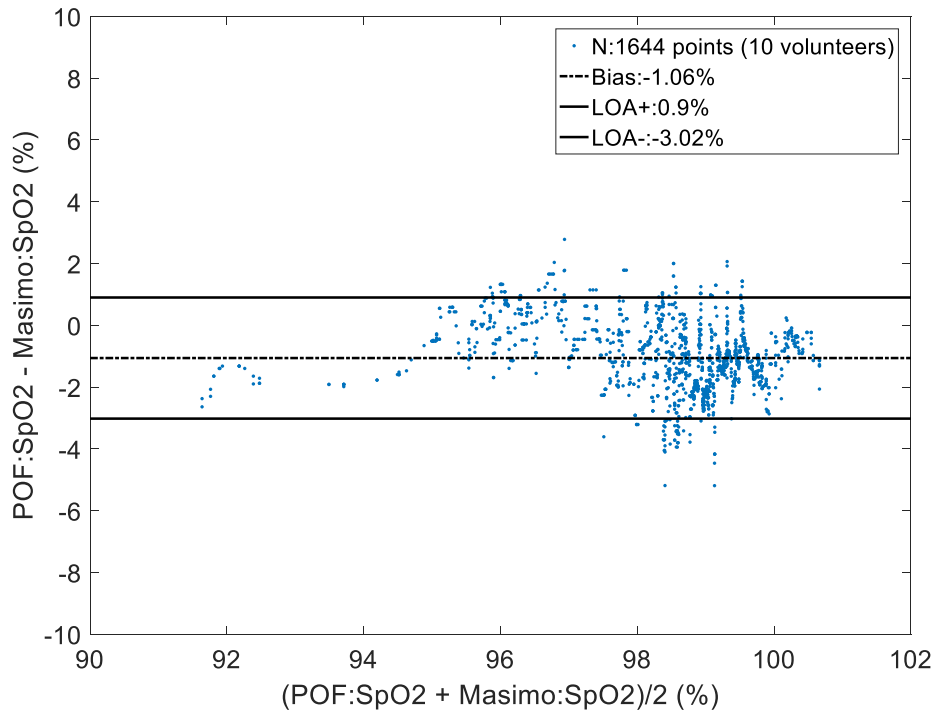


Figure 4.35 Bland-Altman plot of 10 volunteers' S_{pO_2} with deoxygenated activities. In the figure, there are 1644 sample points. The x-axis is the mean of S_{pO_2} values between the POF sensing patch and the Masimo Radical-7. The y-axis is the difference of S_{pO_2} values between the POF sensing patch and the Masimo Radical-7. Bias is the mean of the difference between two pulse oximeters' S_{pO_2} difference, whilst LOA is 1.96 times the standard deviation of S_{pO_2} difference values.

4.4.2 The Impact of Skin Temperature on SpO₂ Measurements

Section 4.4.1 has indicated that the POF sensing patch has the potential to provide reliable and accurate SpO₂ measurement with no external pressure on the tested finger. However, low skin temperature could degrade the performance of the sensing patch as previous research has demonstrated that this would lower the peripheral perfusion index [145, 146]. As the poor peripheral perfusion of the subject can result in inaccurate SpO₂ readings from the pulse oximeter (both transmission and reflectance modes) or even false alarms [147-150], this research has measured 12 volunteers' finger SpO₂ values with different skin temperature in order to find out how the skin temperature affects the designed sensor performance. Human volunteer studies were approved by the Faculty of Engineering Ethics Committee at the University of Nottingham.

In order to change the body temperature, the method applied in this research is cooling the testing fingers using a therapy disc (3D hot&cold therapy disc, Neo G, Harrogate, UK) as shown in figure 4.36. It is required to put the therapy disc into the freezer for approximately 90 minutes before use. In this case, the temperature of the therapy disc can be maintained at about 14 °C for 20 minutes after removing from the freezer. The experiment protocol designed for assessing the temperature effect on SpO₂ and CRT measurement is described as follows:

1. 12 Volunteers' Demographic information:
 - a. 8 male volunteers and 4 female volunteers
 - b. Age (mean \pm standard deviation): 29.7 \pm 3.0 years)
 - c. Inclusion and exclusion criteria for SpO₂ measurement

Inclusion	Exclusion
<ul style="list-style-type: none">• Age over 18• Have healthy circulatory and respiratory systems	<ul style="list-style-type: none">• Have any cardiovascular disease• Have any respiratory system diseases• Have any circulatory system diseases

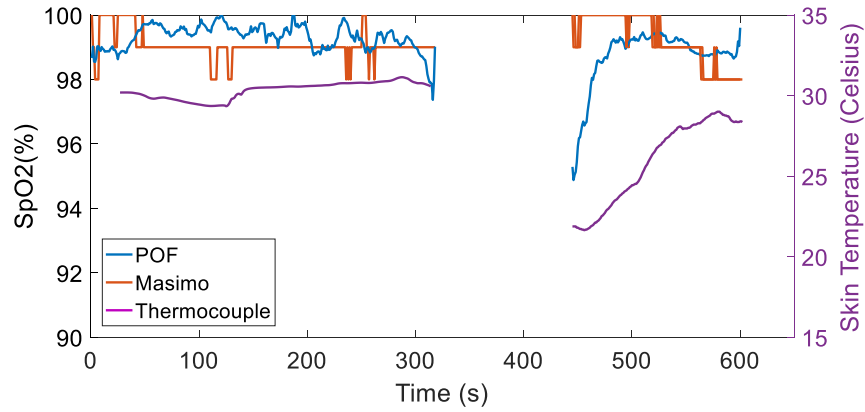
	<ul style="list-style-type: none"> • Have Raynaud’s syndrome • Have a history of cold injuries • Taking any pharmaceuticals which affect breathing. • Have suffered from poor perfusion, dehydration or septic shock.
--	---

2. Each Participant is required to clean the tested hand using a non-alcoholic antibacterial gel before putting the index finger on the designed POF sensor.
3. The participant then sits quietly for 15 minutes to acclimatise before testing.
4. Then, the participant will be required to normally breathe for about 5 minutes. The subject’s SpO₂ value will be recorded by both the designed pulse oximeter and the gold standard oximeter.
5. Next step, participant will be asked to put the tested finger (index finger) and the reference finger (middle finger) on a CE approved therapy disc (maintained at a temperature of 14°C) as shown in figure 4.36 for approximately 3 minutes. The therapy disc will have been previously placed into a freezer for 90 minutes beforehand.
6. When the volunteer’s finger temperature (measured by a thermocouple) drops within the range from 18 to 24 °C, the volunteer will be asked to lift the fingers away from the therapy disc. Then the volunteer will be asked to put the tested finger on the top of the POF sensor, and sit still until the temperature of the volunteer’s index finger return to the value before the cooling process.

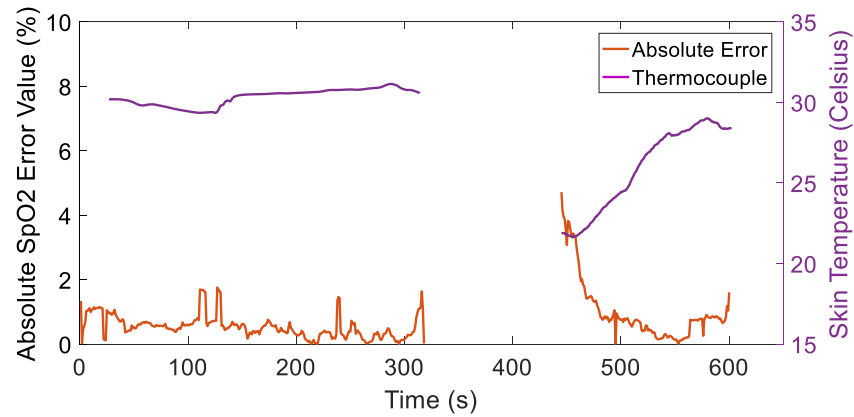


Figure 4.36. Neo G 3D hot&cold therapy disc. The tested finger (index finger) and the reference finger (middle finger) are located on the therapy disc during the cooling process.

By comparing the S_{pO_2} outputs obtained from the designed pulse oximetry sensor and the commercial pulse oximeter (Masimo Radical 7), it could assess the reliability and accuracy of the designed pulse oximeter. Figure 4.37a shows the S_{pO_2} test result of one volunteer during the skin temperature recording. The blue trace in the figure represents the S_{pO_2} values obtained from the designed sensor whilst the red trace represents S_{pO_2} values obtained by the commercial pulse oximeter. The purple trace is the skin temperature measured by the thermocouple. According to this plot, it shows that the performance of the designed sensor is degraded for the low skin temperature subject. The first part of the dataset ($t = 0$ to 300s) corresponds to breathing normally (point (4) above). After cooling ($t = 300$ s to 450s) the PPG is recorded again at a lower skin temperature. The Masimo device is always measured on a warm finger so the S_{pO_2} value remains high. On the cool finger, the S_{pO_2} sensor records a lower value before returning to a higher value as the skin temperature increases. In figure 4.37b, two curves present the absolute S_{pO_2} errors (red trace) between the designed sensor and the reference device and the skin temperature recording (purple). It is clearly shown that the error with the POF sensing patch is $< 2\%$ when the skin temperature is higher than 23 degrees Celsius. The test results of all 12 volunteers are shown in Appendix C.2.



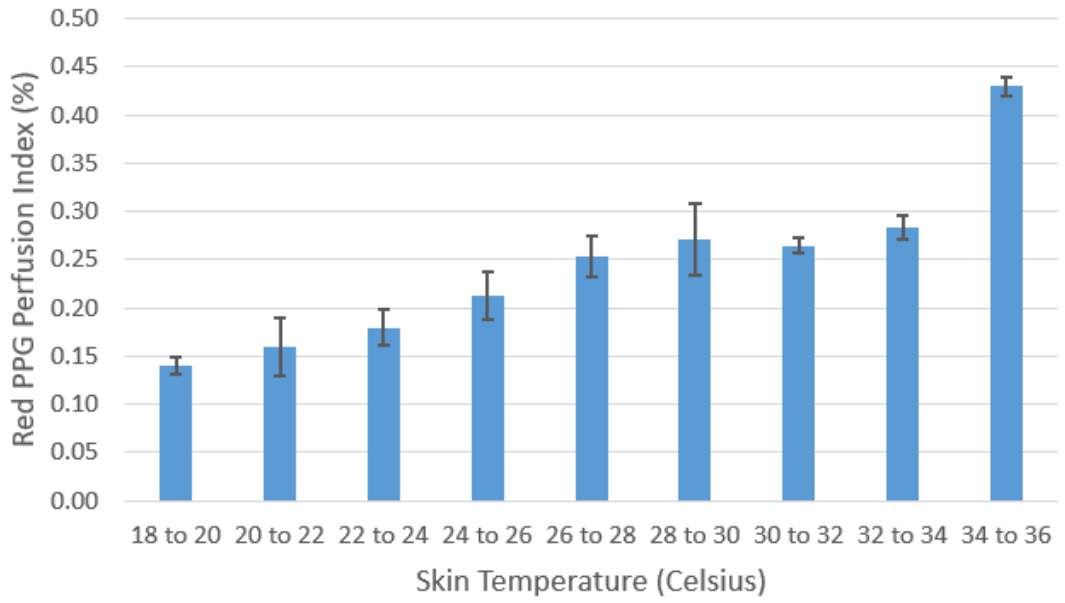
(a)



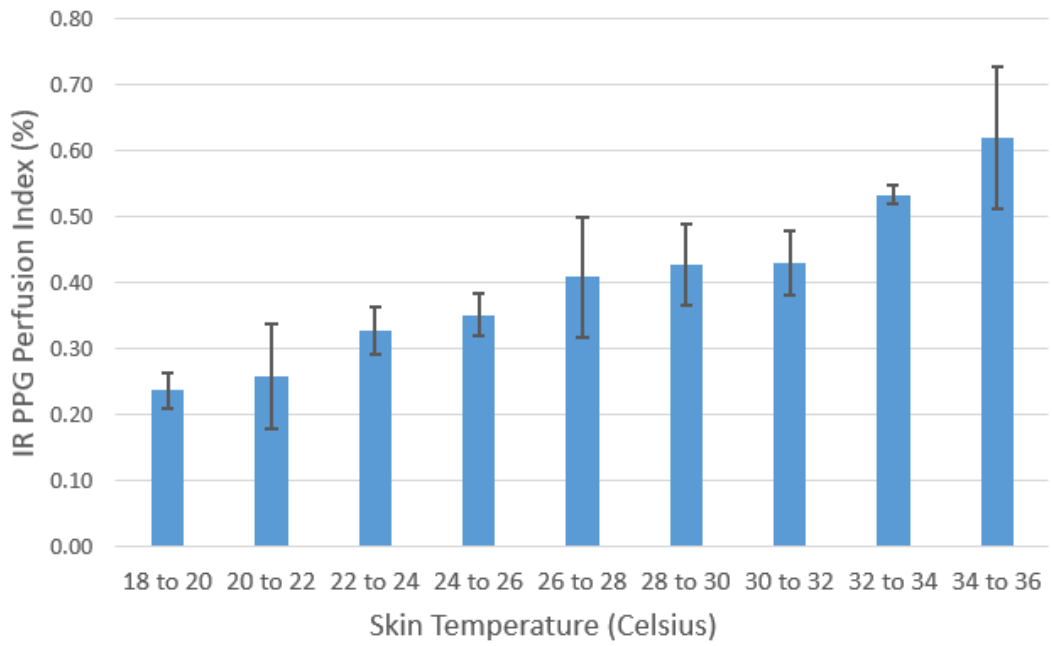
(b)

Figure 4.37 (a) . S_{pO_2} values of one volunteer obtained from the designed POF sensor (blue) and the Masimo Radical-7 pulse oximeter (red) under different skin temperature (purple). (b) absolute S_{pO_2} error (red) compared to an commercial temperature sensor.

Figure 4.38a and 4.38b are bar charts of the average perfusion index values of PPG signals (red and infrared) of 12 volunteers at different skin temperatures. As anticipated the perfusion index increases with increasing temperature. Figure 4.39 is the bar chart of the average S_{pO_2} errors at different skin temperatures. According to figure 4.38 and 4.39, the low skin temperature ($< 22^{\circ}C$) will result in low peripheral perfusion, and deteriorate the performance of the designed pulse oximetry system.



(a)



(b)

Figure 4.38. Effect of skin temperature on perfusion indices of PPG signals. The perfusion index value increases with increasing skin temperature. (a) For Red PPG signals, the perfusion index value is very small ($<0.15\%$) (b) For IR PPG signals, the perfusion index value is very small ($<0.25\%$).

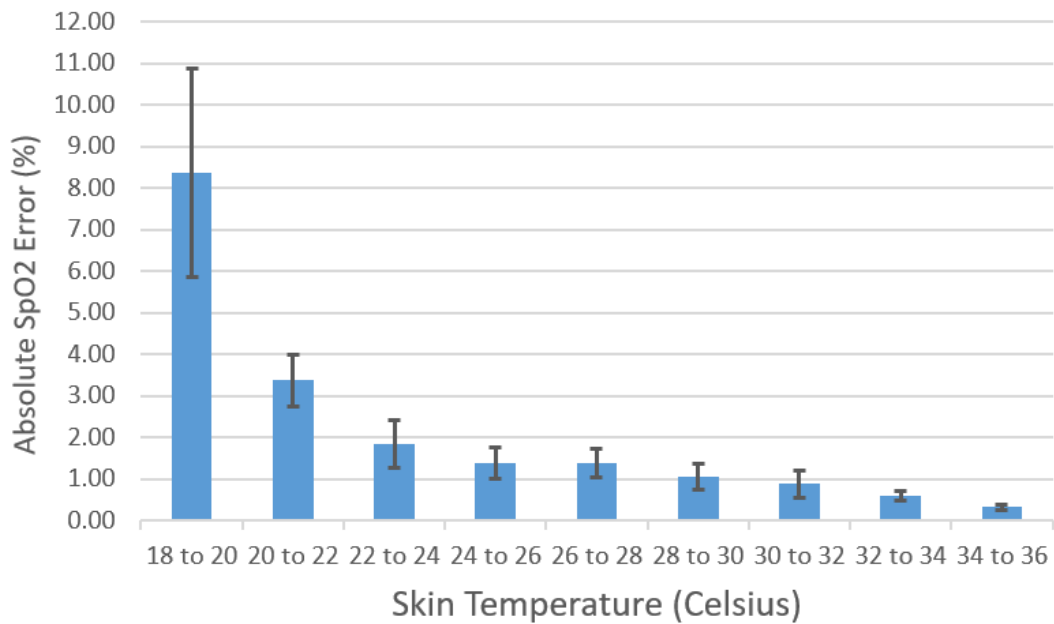


Figure 4.39. Effect of skin temperature on S_{pO_2} error between the optical fibre sensor and a Masimo commercial pulse oximeter for all volunteers. When the skin temperature is lower than $22^{\circ}C$, the S_{pO_2} error is larger than 3%. When the skin temperature of the subject is larger than $22^{\circ}C$, the S_{pO_2} error is lower than 2%. The S_{pO_2} error decreases with increasing skin temperature.

In the main study, the aim is to analyse the performance of the designed sensor under different contact pressure levels. In order to eliminate low skin temperature effects, all experiments were carried out in a laboratory environment with an electrical heating radiator which maintained the room temperature higher than $24^{\circ}C$. In this case, the skin temperature of all volunteers' tested fingers was kept high enough ($> 28^{\circ}C$) to provide high peripheral perfusion. Table 4.4 lists the tested finger skin temperature measured by the thermocouple for all 10 volunteers during the experiments of S_{pO_2} measurement under different contact pressure levels (Section 4.4.3) and CRT measurement (Section 5.2.1).

Volunteer (No.)	Temperature Mean (°C)± SD SpO ₂ measurement	Temperature Mean (°C) ± SD CRT measurement
No.1	33.15±0.48	32.45±0.54
No.2	34.81±0.18	29.34±0.99
No.3	32.87±0.17	32.91±0.17
No.4	33.81±0.46	32.05±0.98
No.5	34.74±0.37	34.35±0.46
No.6	31.98±0.85	28.08±0.30
No.7	29.15±0.29	28.66±0.48
No.8	32.66±0.63	33.56±0.85
No.9	34.63±0.21	34.83±0.18
No.10	34.04±0.47	34.38±0.13

Table 4.4 Perfusion index and skewness index of infrared PPG signals with different skin temperature.

As Table 4.4 shows, the tested finger skin temperatures of 10 volunteers in SpO₂ and CRT measurements were in the range from 28 to 35°C, which improved the quality of the SpO₂ and CRT estimation [151, 152]. The statistical test (paired student T test) was applied to test the difference between the volunteer's skin temperature values recorded in SpO₂ and CRT measurements. According to the statistical test results (p value = 0.116), there is no significant difference between 10 volunteers' skin temperature values recorded during SpO₂ and CRT measurements respectively. Since the skin temperature will affect the performance of the designed pulse oximetry system, the future design of this system is recommended to add a temperature sensor for measuring the subject's skin temperature.

4.4.3 The Impact of Contact Pressure on SpO₂ Measurements

Not only temperature affects the SpO₂ measurement, the contact pressure between the sensor and the skin also disturbs the SpO₂ measurement. Insufficient contact pressure can cause a weak PPG signal whilst too high pressure will block the blood circulation and attenuate the pulsatile PPG component. A range of contact force exists to generate optimal PPG signals with salient pulsatile components [2, 76, 153]. This research has measured 10 volunteers' finger SpO₂ values under different contact pressures in order to find the optimum contact pressure for pulse oximetry.

Human volunteer studies were approved by the Faculty of Engineering Ethics Committee at the University of Nottingham. Figure 4.40a shows the setup for the experiment. The POF sensing patch and the commercial pulse oximeter (Masimo Radical-7 Transmission probe) recorded the SpO₂ value of ten volunteers' index fingers and middle fingers respectively. The FBG patch recorded the contact pressure simultaneously. Pressure was increased in steps (approximately 7 kPa) to the index finger using the aluminium pole shown in figure 4.40b. As described in section 4.1.1, the designed probe (shown in figure 4.40b) combined measurement of SpO₂ with contact pressure. The calibration of the POF sensing patch was shown in section 4.3, and the calibration of the FBG sensing patch in Chapter 3. The manual screw plate noted as 'pressure control system' in figure 4.40a was also used for characterising the FBG patch pressure response described in sections 3.3 and 3.4. The protocol of the experiment is shown as follows:

1. 10 Volunteers' Demographic information:
 - a. 8 male participants and 2 female participants
 - b. Age (mean ± standard deviation): 28.9±4.3 years
 - c. Inclusion and exclusion criteria:

Inclusion	Exclusion
<ul style="list-style-type: none"> • Age over 18 • Have healthy circulatory and respiratory systems 	<ul style="list-style-type: none"> • Have any cardiovascular disease • Have any respiratory system diseases • Have any circulatory system diseases

	<ul style="list-style-type: none"> • Have any lung disease • Have any medicines or drugs which affect breathing.
--	--

- d. Participant was required to clean their hands using a non-alcoholic antibacterial gel before putting the index finger on the designed POF sensor.
- e. Participant was then asked to sit quietly for 15 minutes to acclimatise before testing
- f. The iron pole was set just contact the index finger nail of participant.
- g. After every 30s, the manual platform lowers the iron pole to increase the contact force by 0.5N each time until the PI is too low to observe any pulsatile PPG component on the screen. The pressure increasing process should be stopped if the contact force is increased to 4N.
- h. Then, the manual platform lifts the iron pole to decrease the contact force by 0.5N step by step until the iron pole does not contact the nail.
- i. For each participant, it was required to repeat the process from 4 to 6 three times in total.

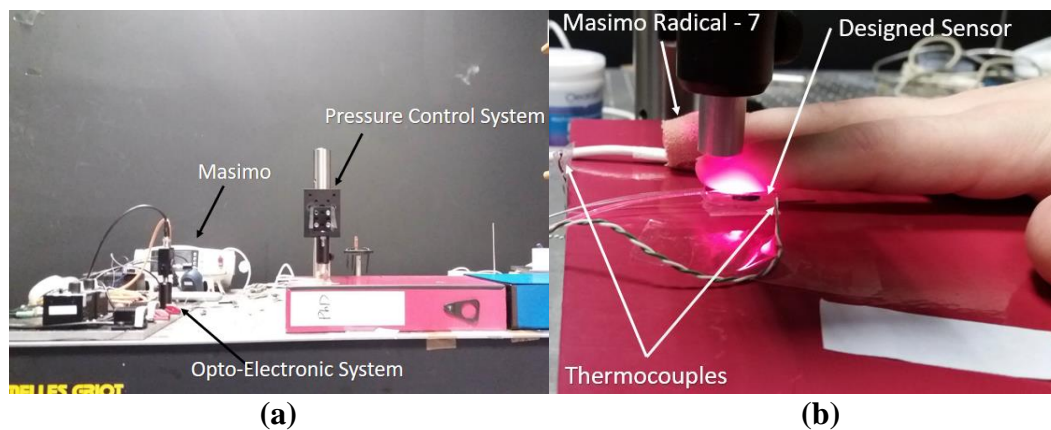


Figure 4.40. Experiment set up. (a) Photo of the overall experiment set up. (b) The patch beneath the index finger is the designed epoxy patch. The middle finger is covered by the transmission mode tapping sensor (Masimo Radical-7). There are two thermocouple sensors (wires with mixed green and white colour) measuring the environment and the index finger temperature.

As section 4.4.2 mentioned, the skin temperature also affected the measurement. In this study, the temperature of the volunteers' index fingers was maintained higher than 30 °C (measured by PICO Technology SE0000 thermocouple) using an electrical

heater to maintain the room temperature higher than 26 °C during the whole experiment.

Figure 4.41 illustrates the test result of one volunteer. The rest of the test results are shown in Appendix C. Figure 4.41a shows the infrared PPG signal (red line) and the contact force (blue line). When the contact pressure increased, the pulsatile PPG component (AC PPG) decreased and the DC light level increased. This is to be expected as the blood flow is occluded and the tissue blanches. In figure 4.41b, two curves presents the absolute S_{pO_2} error (red curve) between the POF sensing patch and the commercial device, and the contact pressure (blue curve). As the pressure is lower than 15 kPa, the POF sensing patch is reliable and accurate. When the pressure is higher than 15 kPa, the performance of the POF sensing patch is degraded. Figure 4.41c and d give the PI and SKI of the infrared PPG signals under different contact pressures. Both PI and SKI of the infrared PPG signals decreased when the contact pressure increased over 15 kPa. When the pressure returned below 15 kPa, the PI and SKI recovered.

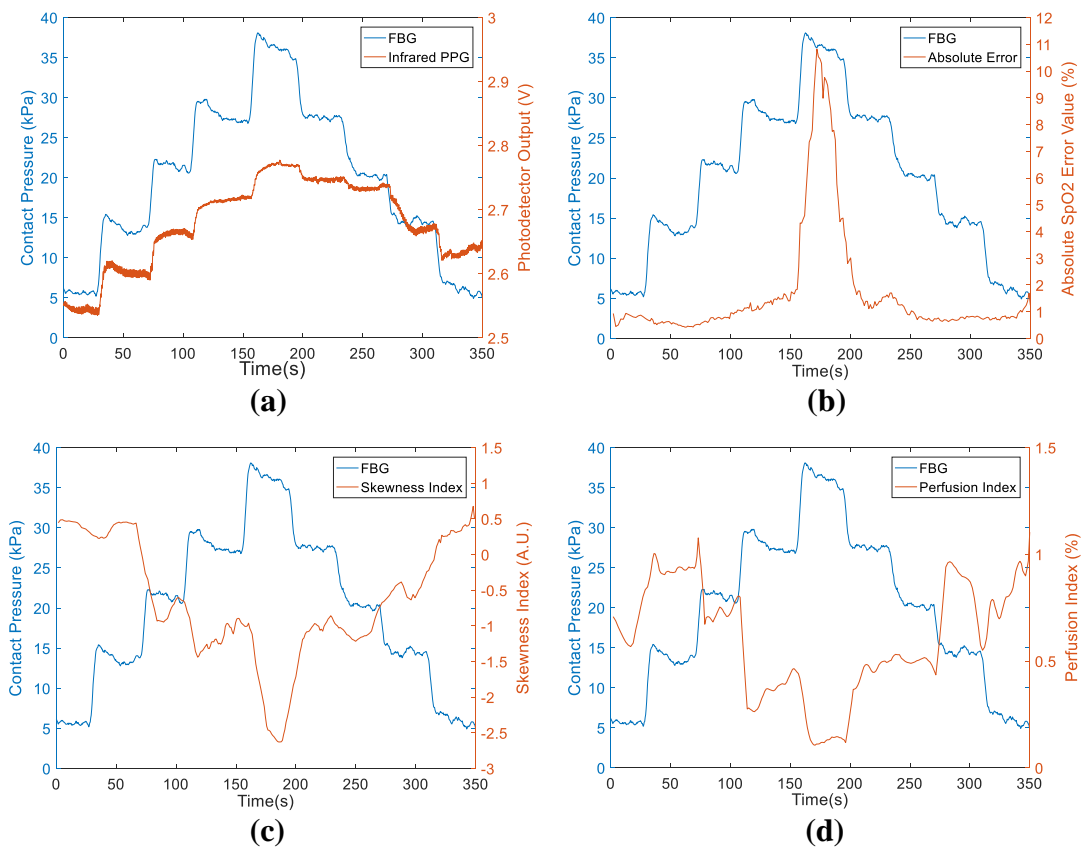
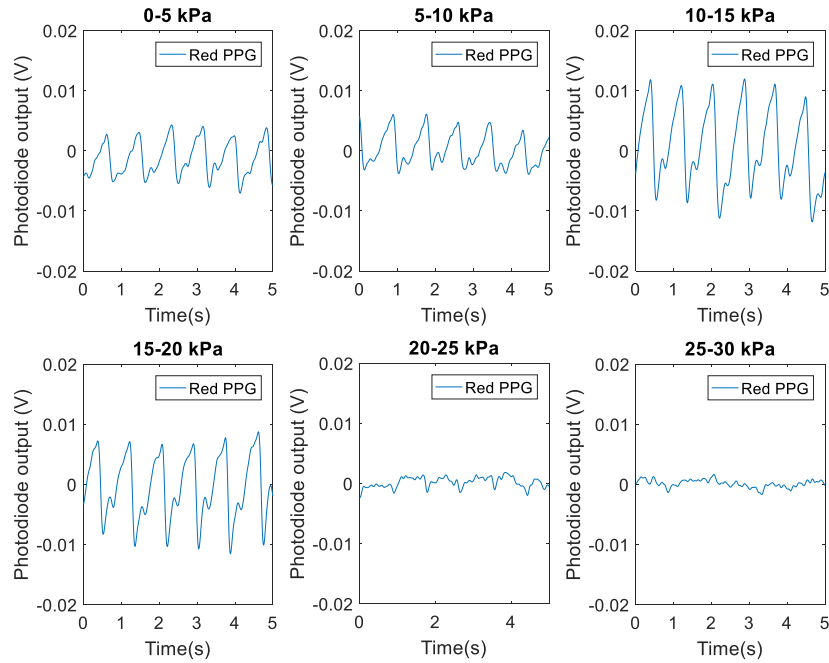
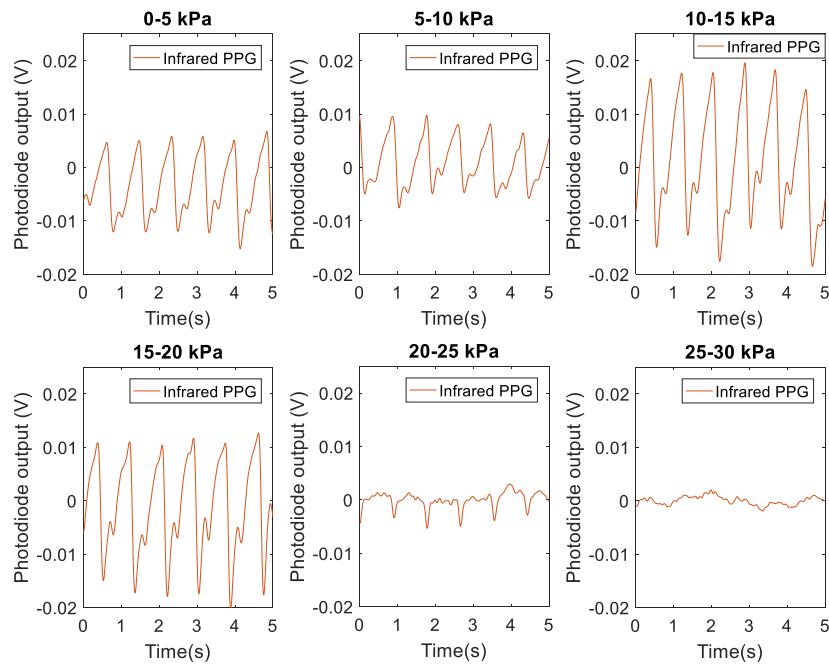


Figure 4.41 (a) . Infrared PPG signals (red) under different contact pressures (blue). (b) absolute S_{pO_2} error (red) compared to an unloaded commercial device (c) skewness index of infrared PPG (red) (d) Perfusion index of infrared PPG (red).

From figure 4.41a, it illustrates that AC component of PPG signals will be affected by the contact pressure. Figure 4.42a and 4.42b below clearly show the effect of contact pressure on AC PPG signals (red and infrared) from a typical volunteer.



(a)



(b)

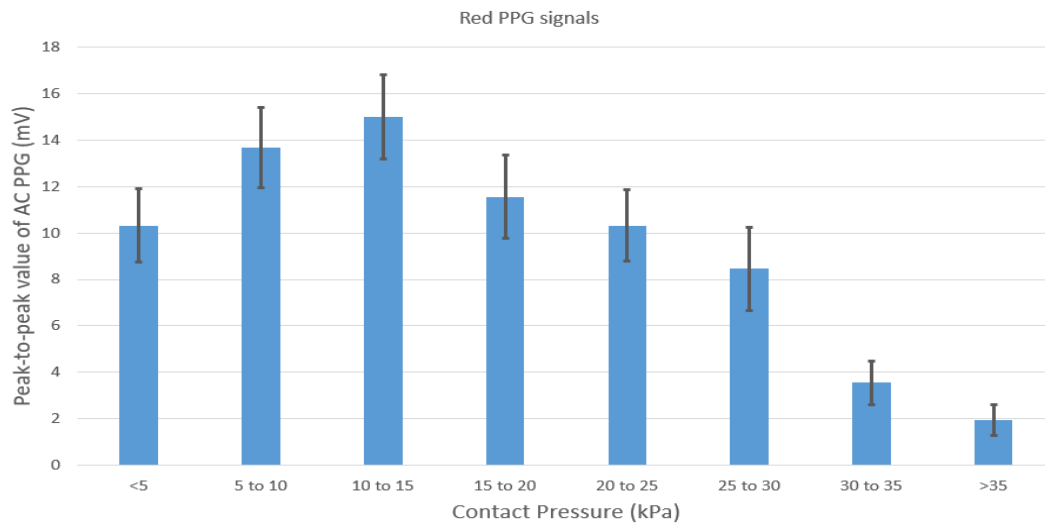
Figure 4.42 AC PPG signals at different contact pressure levels. (a) Red AC PPG signals under different contact pressures. (b) IR AC PPG signals under different contact pressures. From figure a and b, it can be seen that AC PPG signals are larger when the contact pressure is in a certain range of pressure.

As the contact pressure affected the amplitude of AC PPG signals, the S_{pO_2} measurement using the POF sensor will be affected by the contact pressure as figure 4.42b shown. Table 4.5 below lists the average amplitudes of AC PPG signals, average peripheral perfusion values and the average S_{pO_2} error at different contact pressure levels of ten volunteers. According to the statistical test (pair T test) results ($p = 0.001$), there is a statistical significant difference between the peripheral perfusion index of two wavelength PPG signals at different contact pressure levels. The further study is recommended to research the performance of different wavelength PPG signals at different contact pressure levels.

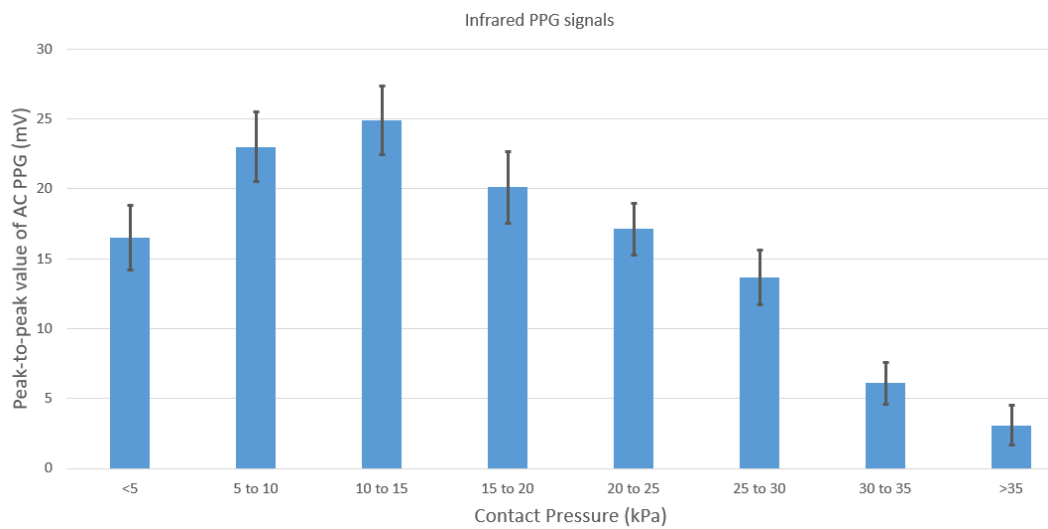
Contact pressure (kPa)	IR PPG signal peak-to-peak value (mV) \pm SD	Average IR PPG perfusion index (%)	Red PPG signal peak-to-peak value (mV) \pm SD	Average Red PPG perfusion index (%)	SpO2 error (%) \pm SD
0-5 kPa	16.52 \pm 4.65	0.74	10.32 \pm 3.13	0.39	2.12 \pm 1.82
5-10 kPa	23.01 \pm 4.94	0.83	13.68 \pm 3.47	0.44	1.29 \pm 1.00
10-15 kPa	24.90 \pm 4.96	0.79	15.00 \pm 3.61	0.39	1.59 \pm 1.71
15-20 kPa	20.11 \pm 5.16	0.63	11.56 \pm 3.58	0.31	2.09 \pm 2.35
20-25 kPa	17.12 \pm 3.72	0.44	10.32 \pm 3.07	0.23	3.24 \pm 3.12
25-30 kPa	13.68 \pm 3.92	0.37	8.46 \pm 3.56	0.15	5.35 \pm 6.18
30-35 kPa	6.10 \pm 2.96	0.19	3.55 \pm 1.89	0.10	5.94 \pm 6.35
> 35 kPa	3.10 \pm 2.90	0.15	1.95 \pm 1.30	0.08	10.24 \pm 7.41

Table 4.5 AC PPG signal and S_{pO_2} errors at different contact pressure levels.

Figure 4.43a and 4.43b are bar charts of the average peak-to-peak value of AC PPG signals (red and infrared) of 30 datasets (10 for each volunteer) at different contact pressure levels whilst figure 4.44 is the bar chart of the average S_{pO_2} errors at different contact pressure levels. According to two bar charts, it has shown that the best pressure range for S_{pO_2} measurement is from 5 to 15 kPa.



(a)



(b)

Figure 4.43. Effect of contact pressure on peak-to-peak values of AC PPG signal. (a) For Red PPG signals, the peak-to-peak value of the AC PPG signal is very small (lower than 5 mV) when the contact pressure is higher than 30 kPa. When the contact pressure is in the range from 10 to 15 kPa, the AC signal peak-to-peak value reaches the maximum value (15 mV). (b) For IR PPG signals, the peak-to-peak value of AC PPG signal is very small (lower than 10 mV) when the contact pressure is higher than 30 kPa. When the contact pressure is in the range from 10 to 15 kPa, the AC signal peak-to-peak value reaches the maximum value (24.9 mV).

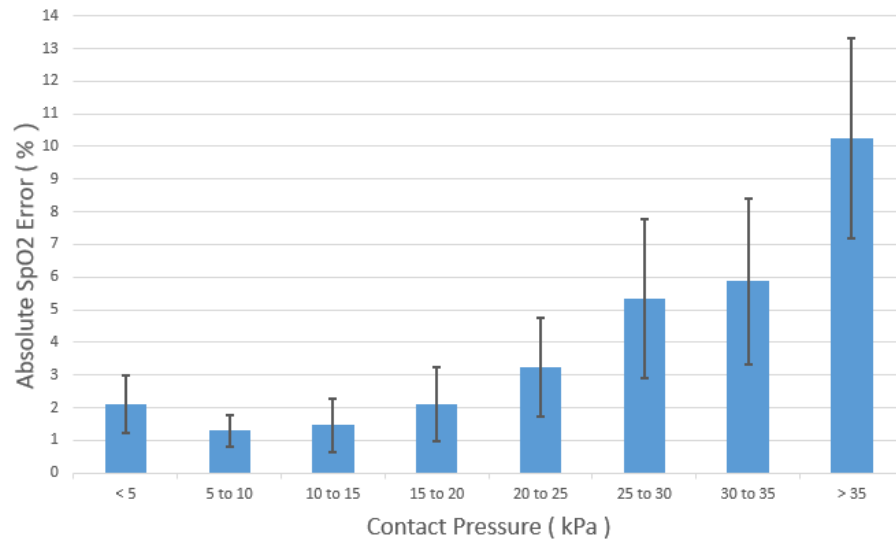


Figure 4.44. Effect of contact pressure on S_{pO_2} error between optical fibre sensor and Masimo commercial pulse oximeter. When the contact pressure is higher than 25 kPa, the S_{pO_2} error is very high. When the contact pressure is lower than 15 kPa, the S_{pO_2} error is lower than 2%. The S_{pO_2} error reached the lowest value while the contact pressure is in the range from 5 to 15 kPa.

4.5 Discussion and Conclusion

Section 4.1.1 has described the design and the performance of the sensing patch for S_{pO_2} measurement. The sensor probe consists of two parts which are POF sensing patch and FBG sensing patch. Both patches are $20 \times 10 \times 2$ mm which makes the integration process easier. The substances of the two patches are two different epoxy resins (NOA 65 and Vitralit 1655). The study chosen the Vitralit 1655 epoxy which was bio compatible to make the POF sensing patch. The detailed information of the FBG patch has been discussed in Chapter 4. For the POF patch, it integrated three 500 μ m diameter POFs with 45° cleaved ends into the epoxy resin substance to transfer light from/to the opto-electrical unit which was introduced in section 4.2. As three POFs were housed in the epoxy substance, the POF patch design reduced the motion artefact in the PPG caused by the displacement between the sensor and the skin. The configuration of integrating both patches makes the designed sensor available to measure the reflectance PPG and the contract pressure simultaneously.

Section 4.1.2 and section 4.1.3 have described the design of the opto-electronic unit of the system, and analysed the gain and noise of the analogue front-end of the opto-electrical unit of the designed pulse oximetry system. This unit consisted of light source (two LEDs), photo-detector (Si photo-diode with trans-impedance amplifier)

and the data acquisition system (ADC and DACs). The gain of the front-end before the ADC is $1.2788 \times 10^{11} \text{VW}^{-1} \text{m}^{-2}$ at 660 and $2.0096 \times 10^{11} \text{VW}^{-1} \text{m}^{-2}$ at 850nm. Under this gain situation, signals recorded performed well which can be observed in test results (Appendix C). The theoretical quantisation noise was $7.67 \times 10^{-18} \text{Wm}^{-2} \text{Hz}^{-0.5}$ for red and $4.90 \times 10^{-18} \text{Wm}^{-2} \text{Hz}^{-0.5}$ for infrared. The measured floor noise (discussed in section 4.2.3) was $9.29 \times 10^{-17} \text{Wm}^{-2} \text{Hz}^{-0.5}$ at 660 nm and $6.972 \times 10^{-18} \text{Wm}^{-2} \text{Hz}^{-0.5}$ at 850 nm which was little higher than the theoretical noise. This was probably caused by the voltage noise of the ADC reference.

For the ADC, its input impedance ($>10 \text{G}\Omega \parallel 100 \text{pF}$) was much higher than the output impedance of the transimpedance (50Ω) which was the front circuit of the ADC. For this study, this would not cause any problem since the signals were not processed in high frequency range. However, in the further study, the lock-in technique might be involved which requires a relatively high frequency modulating carrier [154] which would significantly reduce the effect of flicker noise. In high frequency applications, it is required to minimise the signal reflection which gives rise to the ringing of the circuit [155]. In this case, matching the load to the source impedance could minimise the signal reflection from the load and increase the bandwidth of the system [156]. What's more, according to Frenzel [157], the maximum power to the load is achieved by matching load and source impedance of which the efficiency is 50% [157]. Therefore, to match the load impedance with series resistor (50Ω) optimise the power transferred to the load as well.

In this study, the ADC and the photodetector were not powered by the same power supplies, the negative side of the analogue signal was connected to the ground of the NI myDAQ to share the same ground reference. The output impedance (50Ω) of the photodetector gives the rise to the slightly imbalance in the differential signal path. As the ADC had a high impedance, this slightly imbalance would not cause any problem in this study. However, for the further study, the input impedance of the ADC might be reduced to match the output impedance of the photo-detector. In this case, two connections shown in figure 4.45a & b are recommended to partially/fully balance the signal path in the future design. The input signal of the DAQ system will then be transferred to the ADC (ADS8319, Texas Instruments) through the buffer amplifier (OPA 1642, Texas Instruments).

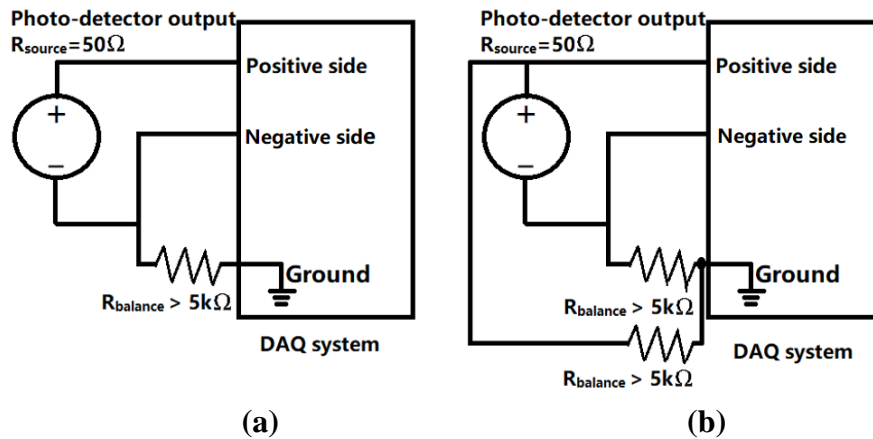


Figure 4.45 (a) Partially balanced differential connection. This connection adds a resistor which is larger than 100 times of the source impedance between the negative line and the ground. In this case, the resistor puts signal path almost in balance and does not load down the source. (b) Fully balanced differential connection. Both positive and negative analogue input lines are connected to the ground through the resistor which is larger than 100 times of the source impedance. The disadvantage of this connection is loading down the source.

4.3 has discussed the demodulation of PPG signals based on TDMA technique. Demodulated signals were filtered through a band-pass filter (0.5Hz to 10Hz) for pulsatile PPG components extraction. Compared the SNR of the raw signals and the filtered signals, it demonstrated that the band-pass filter largely reduced the noise. After obtaining filtered signals, an interpolation process was carried out to prevent the increase in quantisation noise. For estimating the quality of filtered and oversampled signals, three signal quality indices were introduced which were signal-to-noise ratio, perfusion index and skewness index. 30 datasets shown in Appendix C have improved that the combination of three signals quality indices was capable of assessing the quality of obtained PPG signals.

Section 4.4 provided S_{pO_2} results of 10 volunteers detected by the POF sensing patch. The commercial pulse oximeter (Masimo Radical-7) was chosen as the gold standard for validating the designed sensor. By analysing the test results, it was found that the S_{pO_2} calculated from poor quality PPG signals, which assessed by three signal quality indices, was less reliable. In this case, three signals indices were capable of assessing the performance of the designed pulse oximetry sensor. By comparing the 42 datasets presented in Appendix C, the POF sensing patch was demonstrated as a reliable and accurate pulse oximeter when the skin temperature (over 22°C) and pressure (5 kPa to 15 kPa) were in the suitable range. Chapter 5 will continue use this sensor to measure the capillary refill time of subjects.

Chapter 5 Capillary Refill Time Measurement

Chapters 3 and 4 described the design and performance of the integrated sensing patch (FBG patch and POF patch) for measuring reflected light intensity and contact pressure. This chapter describes the development of this non-invasive sensing patch to measure the capillary refill time (CRT) of a subject. According to section 1.2.3, CRT was defined as the time taken for a distal capillary bed to recover its colour after blanching via externally applied pressure. Currently, the most common method of measuring CRT is through manual assessment, i.e. a clinician looks at the tissue and counts the time taken for the skin tone to regain the colour to an external capillary bed after manually applying sufficient pressure to blanch the tissue [32]. In this research the detected reflected light from the skin is used to measure the colour change while simultaneously recording the contact pressure. The key parameters (reflected light and contact pressure) were obtained using the designed sensing patch.

This chapter also describe how to process the intensity and pressure data recorded by the designed sensor for measuring the capillary refill time (CRT) (i.e. refilling signal extraction, normalisation, two-parts fitting process and thresholds calculation). Following this the finger CRT test results of 10 volunteers using the designed pulse oximetry sensor will be presented and discussed.

5.1 Capillary Refilling Signal Processing

Considerable research is presented in the literature for recording the time taken, using a stopwatch, for the skin to regain its colour after blanching [99, 101, 102]. However, the stopwatch applied to time the CRT was manually controlled which degraded the accuracy and reliability of CRT measurement. In this chapter the processing of the recording data to obtain the CRT was via the Matlab software in order to avoid human errors caused by manual operation.

5.1.1 Refilling Signal Extraction

As described in section 2.4, when the blood is pushed out from the distal capillary bed due to the blanching pressure, the colour of the pressed skin becomes pale. According to the Beer-Lambert law, the intensity of light (at 660nm or 850nm) reflected from the

skin will increase as the skin colour fades. When the skin regains its normal colour, the intensity of the reflected light is reduced to a baseline. As the POF patch (top layer of the designed sensor) is capable of detecting the reflected light intensity changes (at 660nm and 850nm), the designed patch is available to measure the skin colour changes arising from the blanching pressure. With the FBG patch (bottom layer of the designed sensor) recording contact pressure, figure 5.1 presents the reflected light intensity changes for the blood pushing out and refilling back with the recorded pressure. In figure 5.1, the pulsatile signal disappears when the blanching pressure was high enough (> 30 kPa) to evacuate the capillary blood. In this case, the blanching pressure changes in the high pressure range (> 30 kPa) will not significantly affect the reflected light intensity. This is the reason that there is only a small light level decrease caused by a large pressure decrease in the period from 15 to 18 seconds. Therefore, in finger CRT measuring experiments (described in section 5.2), the presence of a pulsatile component of PPG signal shown on the screen was used for guiding pressure adjustment.

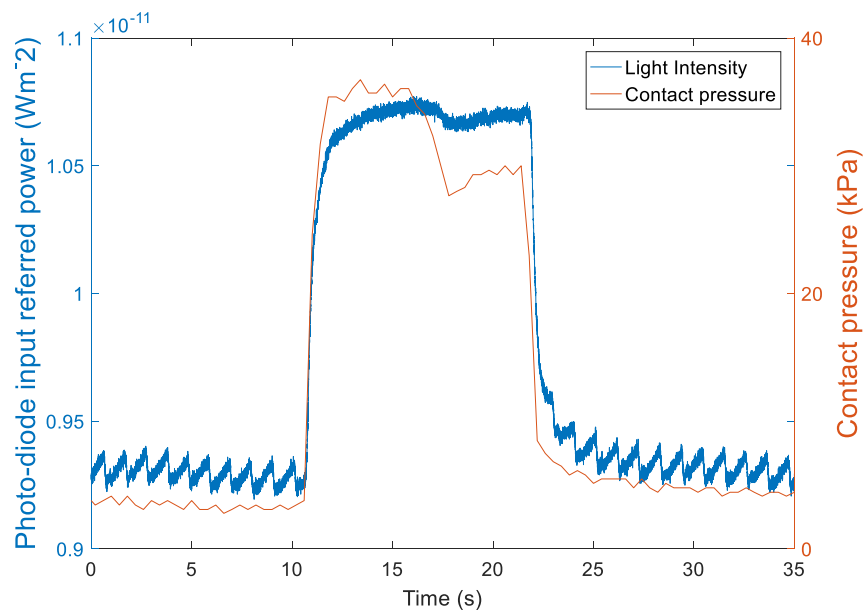


Figure 5.1 Reflected light intensity changes with contact pressure recording. The blue curve presents the reflected light intensity and the red curve presents the contact pressure measured by the FBG sensor. The changes in the reflected light intensity follow the contact pressure changes that arise from the blanching pressure. Note the disappearance of the PPG when full pressure is applied.

In figure 5.1, the intensity data reflected the blood volume under normal, blanching and refilling situations. However, as described in section 2.4, only the time taken for blood refilling was required for CRT measurement. Therefore, the contact pressure

data was applied in this research to isolate each refill interval as the ten seconds following each point where the contact pressure continually decreased by 10 kPa having previously risen above 15 kPa and remained above for at least 5 seconds. Based on this selection, the refilling curve presented in figure 5.1 could be extracted and is presented in figure 5.2.

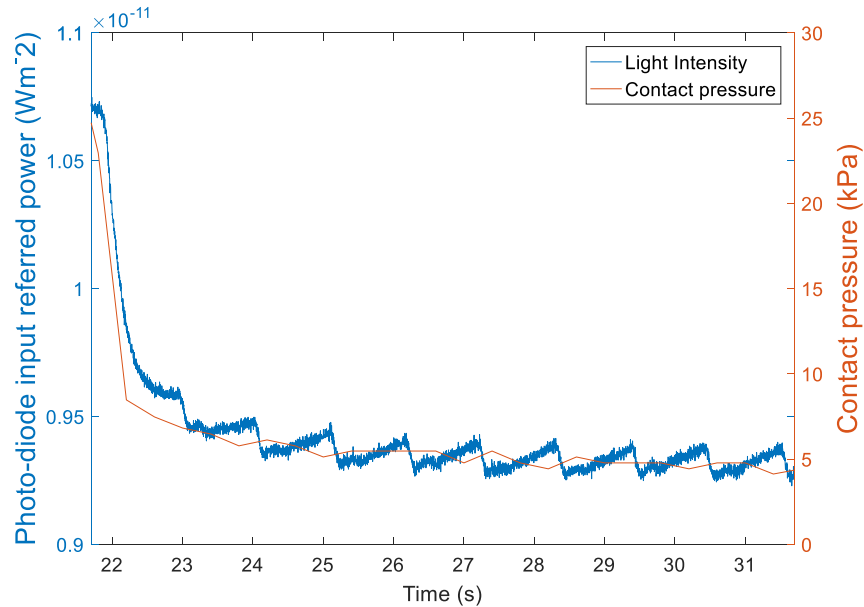


Figure 5.2 Extracted Refilling curve. The blue curve shows blood refilling, and the red curve is the pressure recorded by the FBG sensor simultaneously.

However, the refilling curve shown in figure 5.2 was not suitable for CRT measurement due to two problems. The first is the varying intensity baseline of each refill curve caused by ambient light changes, motion artefacts and physiological changes (skin temperature and post occlusion reactive hyperaemia). In this case, this study normalised each refill curve which will be discussed in section 5.1.2. The second problem is that the impact of motion artefacts deformed the refill curves of each volunteer. To reduce the impact of volunteers' motion upon the CRT metric, a fitting process is applied, which is discussed in section 5.1.3. After obtaining the processed signals, the CRT is estimated via three different methods which will be discussed in section 5.1.4.

5.1.2 Refilling Signal Normalisation

In most cases, the baseline of the intensity data during experiments was stable as figure 5.1 has shown. However, on occasions the motion artefact, ambient light changes and

physiological changes will affect this baseline. In this case, normalisation of the extracted refilling curve aims to eliminate the impact of value changes in the baseline. In section 2.1, equation 2.6 presented how to normalise the optical signal from the pulse oximeter. As this research monitored CRT of subjects using the designed pulse oximetry sensing patch, equation 5.1 can be deduced from equation 2.6 which gives the normalisation of refilling signals. Based on equation 5.1, the refilling signal shown in figure 5.2 can be normalised as presented in figure 5.3 presented.

$$I_{RN} = \frac{I - I_{Rmin}}{I_{Rmax} - I_{Rmin}} \quad (5.1)$$

Where I_{RN} is the light intensity of the normalised refilling signal, I is the light intensity of original refilling signal, I_{Rmax} is the high peak of the refill and I_{Rmin} is the low peak of the refill.

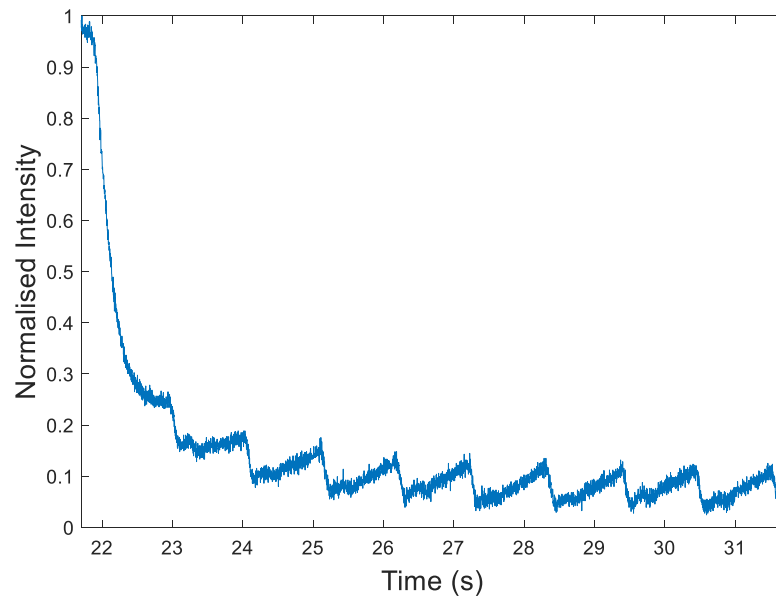


Figure 5.3 Normalised refilling signal. In the diagram, y-scale is the normalised amplitude of the refilling signal which aims to eliminate the impact of value changes in the baseline.

5.1.3 Refilling Signal Fitting Process

As shown in figure 5.3, the deformations that exist on refill curves, generated by motion artefacts, ambient light and physiological changes, can affect the accuracy and reliability of CRT measurement. One method to reduce the impact of motion artefacts for a given volunteer is to curve fit through the data [32]. This fitting process separated the refilling signal into two parts which were the blood refilling part and the baseline

part [32]. As described in section 5.1, when the blood was refilling back to the capillary bed, the reflected light intensity obtained by the sensor would decline significantly at first, and then slowly decreases to the baseline. The decreasing changes in the intensity during the blood refilling could be fitted exponentially [158]. For the baseline part, a simple straight line fit was made to this region of intensity data since the baseline was less fluctuating. Equation 5.2 is the function of the two part fitting of the refilling signal.

$$I_{FN} = e^{a \times x} + B_0 \quad (5.2)$$

Where I_{FN} is the fitted normalised intensity data, a is the exponential order and B_0 is the baseline of the intensity data.

Figure 5.4 gives the fitting curve of the normalised refill intensity (shown in figure 5.3). Figure 5.4 shown the original normalised refilling signal (blue curve) with the two part fitting (exponential fitting and straight line fitting) curve (green curve). Both curves were matched with each other whilst the two part fitting curve (green one) ignored the glitches and pulsatile signals.

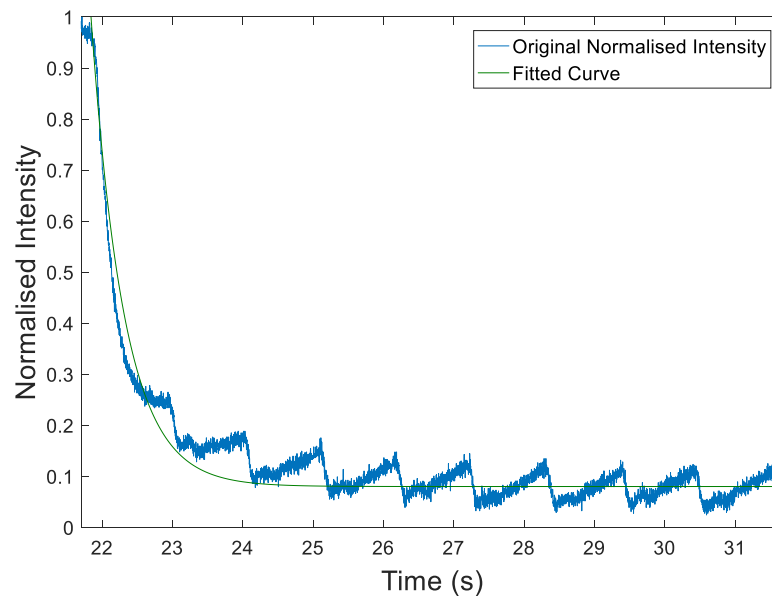


Figure 5.4 Normalised refilling signal with the two part fitting curve. The blue curve represents the original signal which consists of a pulsatile PPG signals and noise. The green curve is the two part fitting curve.

Before proceeding to measure the CRT, the research assessed the fitting curves, and then rejected unqualified refills based on three thresholds as follows:

1. Refill had an excessive root mean squared fit error (RMSE). Excessive RMSE (> 0.1) demonstrated that the shape of the refilling signal was not

matched with the exponential fitting curve. Under this circumstance, it was required to re-check the signal processing work of this refill.

2. Refill had a positive gradient for the blood refilling part. During the period of the blood refilling, the light intensity of reflected light should be continuously dropping. The gradient of the intensity data was thus negative.
3. Refill had an absolute excessive gradient (> 0.5) for the baseline part. For the normal situation, the baseline of intensity data was almost constant. Therefore, an excessive gradient reflected the deformation existed in the baseline region.

5.1.4 Capillary Refill Time Estimation

One of the most common and simplest CRT measurement method is to count the time for the blanching skin to regain the red colour [159]. This method calculated the CRT by using a stopwatch to time the skin return to normal colour. However, the manual operation required in this method will likely lead to an unreliable result. In this research, the CRT was deduced from the intensity data of refilling signals via the use of Matlab software.

The method (threshold method) calculated refilling times for the accepted refills was called the threshold method. This method started recording CRT when the intensity first fell below the maximum threshold, and stopped recording CRT at which the intensity fell below the minimum threshold. For some research, the maximum threshold was chosen as the peak of the refilling signals, and the minimum was chosen as the baseline approximation [104, 158, 160]. According to experiments results, maximum threshold was set at 0.9 for normalised refilling signals whilst minimum threshold was set at 0.1 in this research. In future study, it is required to investigate most suitable threshold values for CRT measurement. In figure 5.5, two black lines parallel to the x-axis were thresholds applied for CRT measurement.

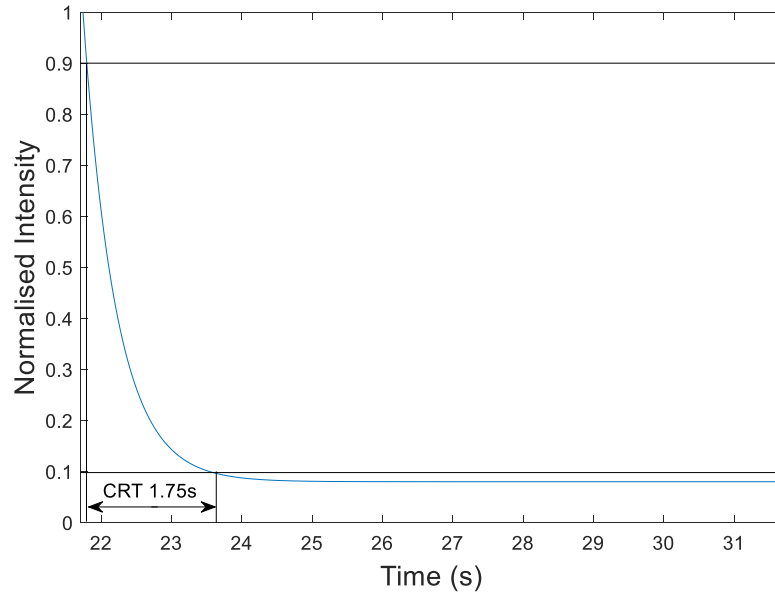
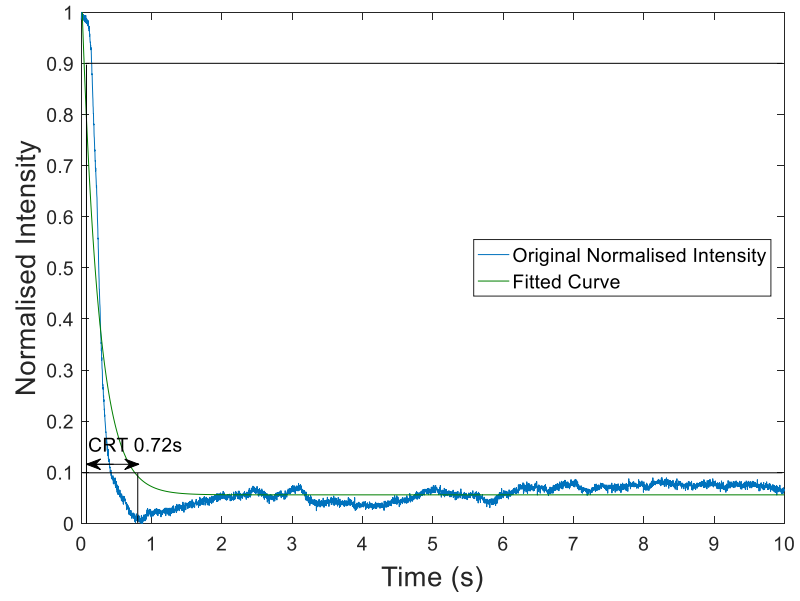
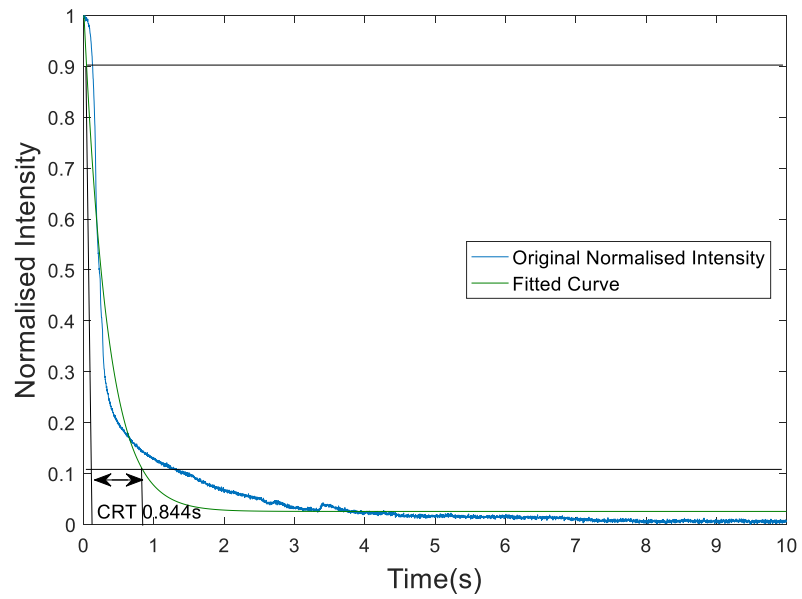


Figure 5.5 CRT measurement using maximum/minimum thresholds. The two black lines indicate maximum and minimum thresholds. The time taken for refilling signal to fall from 0.9 to 0.1 is defined as CRT which was 1.75 seconds.

However, in some cases, the fit does not work well for some refilling signals which have relatively rapid or slow fall in light intensity as shown in figure 5.6. For refills with sharper fall, CRT counted using the threshold method was longer than the actual CRT (shown in figure 5.6a) since the fitted curve had a slower fall compared to the original signal. For refills with slower fall, CRT calculated was smaller than the actual CRT (shown in figure 5.6b) since the fitted curve had a shaper fall compared to the original signal. Therefore, in future studies, it would be required to improve the fitting function (equation 5.2), which gives the highly matched fitted curves for all refilling signals. The blue curves in figure 5.6 are the original normalised refilling signals whilst the green curves are fitting curves. Table 5.1 summaries the CRT estimation and fitting curve exponential orders.



(a)



(b)

Figure 5.6 (a) Refilling signal with sharper fall. Exponential order of the fitting curve is -4.12 . (b) Refilling signal with slower fall. Exponential order of the fitting curve is -2.97 .

Refilling signals	CRT estimation (s)	Exponential orders of fitting curves	RMSE
Sharper refilling	0.72	-4.12	0.04475
Slower refilling	0.844	-2.97	0.03498

Table 5.1 Summary of CRT measurements, exponential orders and RMSE.

5.2 Finger Capillary Refill Time Measurement Using the Sensing Patch

Section 5.1 discussed the signal processing of refilling data to obtain the CRT of subjects. This section describes deployment of the designed sensing patch to record key parameters (reflected light intensity and contact pressure) and processing the obtained data as described in section 5.1 to calculate CRT.

5.2.1 Finger CRT Measurement Setup

The experimental setup for CRT measurement was similar to the S_{pO_2} test setup which was shown in figure 4.40. The sensing patch was located beneath the index finger to measure the light reflected from the skin, and pressure between the tested index finger and the patch. The lab temperature was kept at 26°C for all CRT experiments.

There were 10 volunteers recruited in this study for tests. Human volunteer studies were approved by the Faculty of Engineering Ethics Committee at the University of Nottingham. The protocol of the experiment is described as follows:

1. 10 Volunteers' Demographic information:
 - a. 8 male participants and 2 female participants
 - b. Age (mean \pm standard deviation): 28.9 \pm 4.3 years
 - c. Inclusion and exclusion criteria:

Inclusion	Exclusion
<ul style="list-style-type: none"> • Age over 18 • Have healthy circulatory systems 	<ul style="list-style-type: none"> • Have any cardiovascular disease • Have any circulatory system diseases

	<ul style="list-style-type: none">• Have suffered from poor perfusion, dehydration or septic shock.
--	---

2. Each participant was required to clean their hands using a non-alcoholic antibacterial gel before putting the index finger on the designed POF sensor.
3. Each participant was then asked to sit quietly for 15 minutes to acclimatise before testing
4. Each participant was asked to press the index finger on the fixed sensing patch, and keep pressing the patch until the pulsatile PPG signals disappeared from the screen. All participants should stop pressing if they felt uncomfortable.
5. Each participant was requested to maintain the pressure for 10 seconds, and then released the pressure for 10 seconds to finish the blood blanching and return process.
6. For each participant, the blanching and return process (4 and 5) was repeated 10 times.

Figure 5.7 presents the typical light intensity and contact pressure during 10 blood blanching and return processes from one volunteer. The information of all 10 volunteer test results are provided in Appendix C.

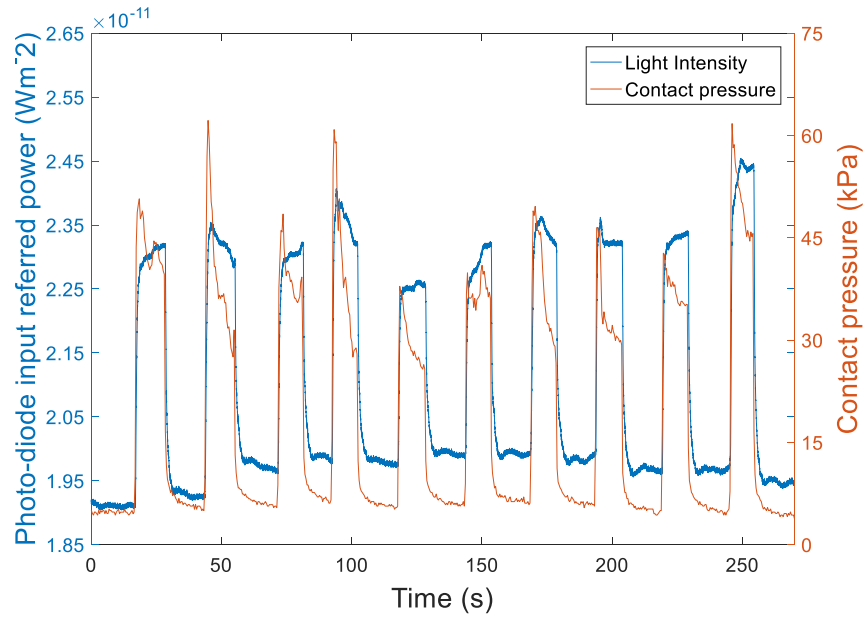


Figure 5.7 Light intensity and pressure record for one volunteer. During the whole experiment, the external pressure is applied to blanch the skin 10 times. The blue line gives the intensity of the reflected light, and red line gives the pressure recorded by the FBG patch.

5.2.2 Finger CRT Measurement Results

According to section 5.1, 10 refilling signals existed in figure 5.7 could be extracted, normalised and fitting using the two part fitting process. From figure 5.8, it shown that all refilling signals obtained by the sensing patch were high qualified, which had small RMSEs, negative gradients for the refilling part and low gradient for the baseline region. Based on the CRT estimation described in section 5.1.4, table 5.2 summaries the estimated CRT, fitting curve exponential orders and RMSEs of volunteer one.

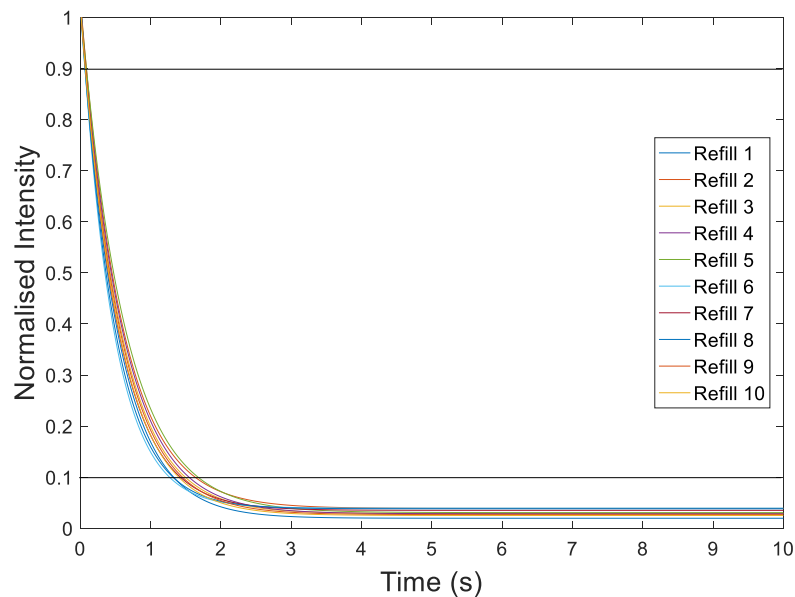


Figure 5.8 10 Fitting curves of volunteer one. All ten fitted refilling signals are matched with each other.

No. of refills	Estimated CRT (s)	Exponential order	RMSE
1	1.534	-1.701	0.0305
2	1.91	-1.399	0.0360
3	1.87	-1.448	0.0253
4	1.81	-1.459	0.0264
5	1.92	-1.382	0.0294
6	1.49	-1.903	0.0338
7	1.77	-1.71	0.0325
8	1.39	-1.985	0.0342
9	1.55	-1.783	0.0258
10	1.42	-1.842	0.0198

Table 5.2 Summary of CRT measurements of volunteer one.

In table 5.2, the estimated CRT of volunteer one is approximately linearly related to the exponential orders of fitting curves. Figure 5.9 shows the dot plot of estimated

CRT versus fitting curves exponential orders (blue dots), and the red line was the fitting line of the dot plot.

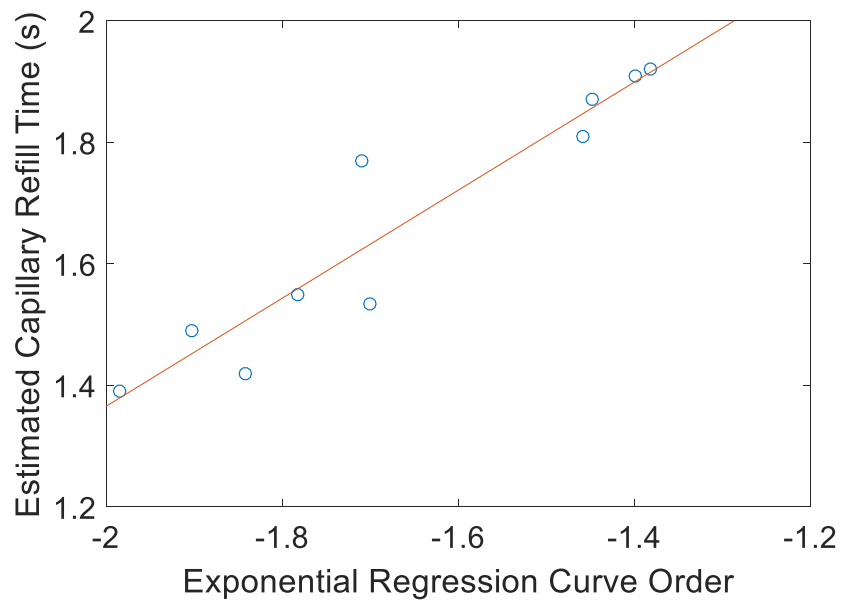


Figure 5.9 Estimation CRT versus exponential order of fitting curves for volunteer one.

Table 5.3 summaries the average estimated CRT, exponential orders and RMSE of all 10 volunteers. After assessing the quality of 100 refilling signals of 10 volunteers, 10 refilling signals were rejected (90 % qualified) according to three thresholds described in section 5.1.3. Figure 5.10 plots the diagram of estimated CRTs versus exponential orders of accepted refilling signals of 10 volunteers, and improved the exponential-like relationship between the CRT estimation time and the exponential order of fitting curve. This exponential-like relationship gives the potential of using an exponential order to calculate CRT directly, which has been recommended for investigation in future work.

No. of volunteers	Average Estimated CRT (s)	Average Exponential order	Average RMSE
1	1.234	-2.4937	0.0267
2	1.89	-1.6637	0.0294
3	1.7958	-1.6825	0.0477
4	0.711	-4.1297	0.0455
5	1.992	-1.3303	0.0389
6	1.6664	-1.6612	0.0293
7	1.2604	-2.0918	0.0664
8	1.1958	-2.0389	0.0603
9	0.8514	-2.7334	0.0356
10	1.1598	-2.3963	0.0777

Table 5.3 Summary of average estimated CRT, exponential orders and RMSEs of all 10 volunteers.

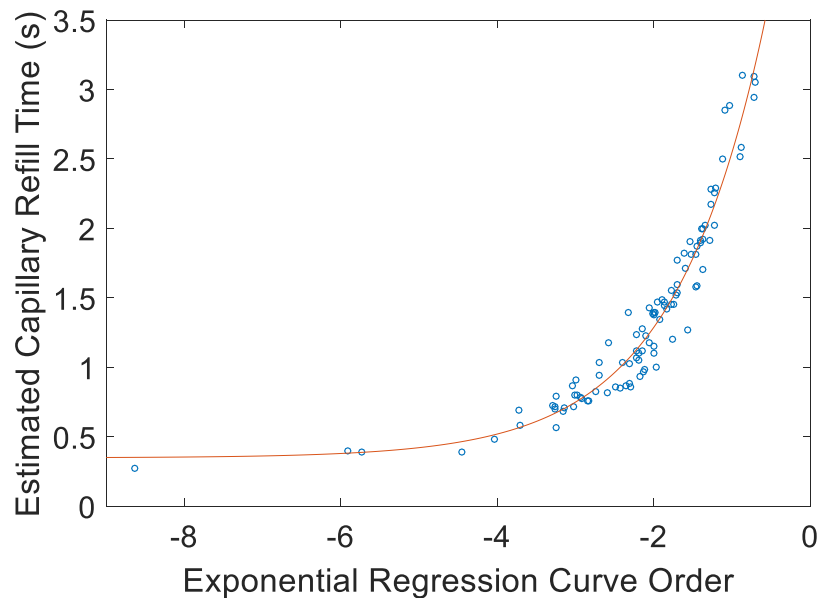


Figure 5.10 Estimated CRT versus exponential order of fitting curves for all 10 volunteers. The blue dot plot (consisting of 90 dots) displays the estimation CRT versus exponential orders of fitting curves. The red line shows the exponential-like relationship between the calculated CRT and the exponential orders.

5.3 Discussion and Conclusion

This chapter has presented the obtained reflected light intensity and contact pressure data for CRT calculation. As defined in section 5.1, the light intensity changes reflected the skin colour changes which was caused by the volume of blood in the capillaries. Since the evacuation and refilling of blood were controlled by the blanching pressure in CRT experiments, pressure could be used as an index to extract refilling signals. In consequence, the study normalised the obtained extracted refilling signals in order to reduce the impact of the change in baseline. A two part fitting process (exponential fitting and straight line fitting) was then used to reduce the impact of motion artefacts and other noise present in the refilling signals, and unqualified fitting curves would be rejected based on the three thresholds. The method of calculating CRT was called the “threshold” method. Two thresholds (maximum and minimum) approximately extracted the decreasing part in the refilling signal, and obtained the time (CRT) of light intensity dropping from the maximum threshold to minimum threshold. The exponential order of fitting curves was chosen as the index to declare the fitting curves’ downward trends. By comparing the estimated CRT and the exponential orders, an exponential-like relationship was found between them. Further research is required to improve the fitting function to present a more accurate fitted curve.

There was one sensor application introduced in this chapter namely the sensing patch. The sensing patch measured the reflected light intensity using the top layer (the POF patch), and monitored the pressure data using the bottom layer (the FBG patch).

Chapter 6 Summary and Further Work

6.1 Discussion

In healthcare applications, measurement of the photoplethysmogram (PPG) is very popular and widely applied. Photoplethysmography can be applied to medical diagnosis (e.g. hypoxaemia, vascular and heart diseases) and to measure a patient's physiological parameters (blood oxygen saturation (S_{pO_2}) and heart rate). In terms of maintaining a healthy lifestyle, PPG can be utilised in detecting the deoxygenation caused by sleep-apnoea and measuring a subject's physiological parameters during exercising. For reliable detection of PPG signals, the contact force between the skin and the sensor plays an important role since both insufficient and too high pressure will distort the PPG signal. Previous research has demonstrated that there is an optimum range of contact pressures for obtaining accurate PPG signals [22, 76, 161]. In this research, a novel optical fibre based pulse oximeter probe was developed that combines measurement of heart rate (HR), blood oxygen saturation and capillary refill time (CRT) whilst measuring the applied contact pressure.

The need for PPG measurement is already recognised and Chapter 1 gave the background knowledge of the sensor designed for PPG, S_{pO_2} and CRT measurement of the subject. Chapter 1 firstly introduced the oxygen transportation in human body, and then briefly presented the working principle of two different types of PPG sensors (transmission/reflectance). As described in Chapter 1, the reflectance PPG sensor mode is more flexible and convenient. Thus the design of sensor was based on the reflectance mode.

The deduction of calculating S_{pO_2} using two different wavelength PPG signals was discussed in detail in Chapter 2. Since there exists large differences of the extinction coefficient between oxy-haemoglobin and deoxy-haemoglobin in the red and the near infrared (NIR) regions, this research chose PPG signals at 660nm and 850nm for S_{pO_2} calculation. Chapter 2 also provided a review of studies of reflectance mode pulse oximeter design. Much research on pulse oximeter design has been conducted in the fields of telemedicine, smart textiles and wearable computing. In particular in wearable technology the optical fibre was popular for pulse oximetry design. This study used plastic optical fibres (POF), which was cheap and easily manufactured, to deliver and

collect light for pulse oximetry. Additionally, in Chapter 2, a review of papers of fibre Bragg grating (FBG) pressure sensing revealed that it was required to increase the pressure sensitivity of FBG sensor for contact pressure sensing, and to reduce the temperature crosstalk on the FBG sensor. Chapter 3 reported the configuration of the designed FBG which was a dual FBG configuration. In this case, an additional reference FBG was fabricated adjacent to the pressure sensing FBG to compensate temperature crosstalk.

The design of using FBG sensors and systems for measuring the contact pressure between the skin and sensor remains challenging. In addition to the temperature crosstalk that occurs on the FBG sensor, the low sensitivity of FBG sensors that needs to be addressed for contact pressure measurement. Chapter 3 reported the FBG sensor designed for recording the contact pressure during experiments. The designed FBG sensor was housed in a low Young's modulus epoxy patch, which transduced transverse loading into an axial strain in the FBG. With the epoxy housing, the pressure sensitivity of the FBG pressure sensor was significantly increased. Chapter 3 also indicated the temperature and pressure responses of the designed FBG sensor. Test results show that using a combination of pressure measuring FBG with a reference FBG, reliable results are possible with low hysteresis which are relatively immune to the effects of temperature.

Chapter 4 presented the design of POF sensor for pulse oximetry and the combination of the POF sensor with the FBG sensor. Three 45° end cleaved POF which were used to deliver and collect light for pulse oximetry were housed into a biocompatible epoxy patch, which serves the purpose of reducing relative movements between three POFs. However, this patch cannot reduce the relative movement between the fibre and tested body area. Motion artefacts therefore will affect the reflected PPG signals detected by the designed sensor. As the frequency of the motion artefacts signal and the PPG signal are in the same range, it is difficult to separate two signals in the frequency domain. In order to improve the designed pulse oximetry system, the future work of removing motion artefacts is recommended. The designed POF patch was then attached to the FBG patch in order to combine the pulse oximeter and contact pressure sensor. Chapter 4 also discussed the noise in the analogue front-end of the electronic system. The reflectance PPG signals obtained by the designed probe were assessed through three signal quality indices (i.e. signal-to-noise ratio (SNR), perfusion index (PI) and

skewness index (SKI)). For poor quality PPG signals, it usually has a low SNR (approximately $< 7\text{dB}$), a relatively low PI ($< 0.4\%$) and a negative SKI for the pulsatile PPG component. Using simple peak detection or FFT technique, it can calculate the heart rate (HR) of subjects from good quality PPG signals. Comparing results of index finger reflectance S_{pO_2} tests with a commercial pulse oximeter, the test results of the designed sensor was close to the commercial device ($\sim 1\%$) both the situation of normal breathing and existing deoxygenation events under warm environmental temperature. In this research, the environmental temperature was set higher than 24°C which resulted in ten volunteers' index finger skin temperature higher than 28°C degree. However, as the low body temperature will reduce the accuracy of the pulse oximetry, it is suggested to calibrate the performance of the designed POF pulse oximeter in the future.

The combined sensor was used to measure the S_{pO_2} of 10 volunteers under different contact pressures with PI and SKI indices applied to assess the PPG quality. The results revealed that the contact force ranging from 5 kPa to 15 kPa provides errors $< 2\%$. This result show the potential of this combined sensor to improve the reliability of reflectance oximeters. Especially in wearable technology, the probe should find use in optimising the fitting of garments incorporating this technology. As too tightly fitting garments worn are not comfortable, the designed probe could be beneficial for providing the optimum pressure without being too tight. For loosely fitting garments, the probe could be used measurement S_{pO_2} value of the subject when the appropriate pressure is applied.

Furthermore, Chapter 1 also illustrated that the reflectance pulse oximeter with pressure sensor was capable of measuring the capillary refill time (CRT). As CRT is the time taken for the skin to regain the colour after blanching caused by an external loaded pressure, the reflectance pulse oximeter can detect the colour changes via analysing the intensity of light reflected from the skin. The designed sensor in this research was used to record key parameters (reflected light intensity and contact pressure) of subjects during CRT measurements.

Chapter 5 described the performance of the designed sensor for CRT measurement. The POF sensor monitored the skin colour changes caused by blanching via detecting the intensity of light reflected from the skin whilst the FBG sensor recorded the

external pressure applied simultaneously. Based on pressure recording data, refills could be extracted and normalised from the obtained intensity data. After extracting and normalising refilling signals, two part fitting (exponential fitting and straight line fitting) was applied to reduce the impact of motion artefacts upon the refill time metric. Poor quality refills were rejected if they had an excessive root mean square fit error (RMSE), a positive gradient for the exponential fitting (refilling) region or an excessive gradient for the straight line fitting (baseline) region. Finally, refill time were calculated for accepted refilling signals using two-threshold method, which measures the time from the 90% to 10% of the maximum value of the fitted refill curves. As fitted curves were not highly matched with refilling signals which had too rapid/slow falls, it was required to improve the fitting function in future work. Compared to the data of 10 volunteers' CRT with orders of exponential fitting curves, an exponential-like relationship was obtained between them. This relationship has shown the potential of using orders of exponential fitting curves to calculate CRT of subjects. In this research, the background temperature was maintained higher than 24°C by using a heating radiator. In this case, the body temperature of all 10 volunteers were maintained at a high level. However, subjects' body temperature will affect their capillary refilling time. In this research, it only focused on the performance of the sensor sited on the high temperature skin (28 to 34°C). Therefore, the further research work is suggested on calibrating the CRT sensor performance when subjects' skin temperatures are low.

Past research in this area has focused mainly on using dozens of POFs to fulfil the pulse oximetry measurement, for example, stitched dozens of POF in a certain embroidery pattern or bent stitched POF in a certain degree to illuminate light [57, 74]. In this research, the end of the POF applied for delivering/collecting light was 45° cleaved. In this case, the light coupling efficiency of each POF significantly increased so that only three POFs were capable of coupling light for pulse oximetry. What's more, the sensor embedded POF in the epoxy patch fixed the position of each POF to reduce relative movement between the light sources and photo-detector. The integrated sensor also incorporated a dual FBG with epoxy housing which was available to measure the contact pressure at same time. Three signal quality indices applied for assessing PPG signal, and the fitting process of refilling signals enhance the reliability of the designed sensor.

6.2 Conclusion

This research has built an optical fibre based system which can detect the reflectance PPG signals and contact pressure levels simultaneously. According to the S_{pO_2} and CRT test results of using the designed optical fibre based system, it can find that the simultaneous pressure and PPG detections improve the performance of PPG systems for S_{pO_2} and CRT measurements.

In order to simultaneously measure the contact pressure and PPG signals, the designed sensor integrated the POF based PPG system with the FBG pressure sensor. The transversely loading calibration result shows that the FBG pressure sensor was competent for the sensor contact pressure measurement due to its high sensitivity (2.01 kPa/pm) within the pressure range from 0 to 45 kPa. However, the designed FBG pressure sensor is very vulnerable to the strain interference. Although the thermal extension caused strain interference was compensated by the additional pressure immune FBG sensor, the strain caused by axial force was still remained and deteriorated the pressure sensing results. Therefore, the future study is recommended to eliminate the axial force caused strain interference on the FBG sensor. This research has applied the designed optical fibre sensor to analyse the performance of the PPG system under different contact pressure circumstances. According to the S_{pO_2} test results, the error between the designed sensor and the gold standard pulse oximeter was less than 2% when the contact pressure was in the range from 5 to 15 kPa. If the contact pressure was too low (<5 kPa) or too high (>15 kPa), the S_{pO_2} error would be increased even larger than 10%. In terms of the peripheral perfusion, the perfusion indices of IR and red PPG signals were firstly increased with loading the contact pressure until 10 kPa, and then decreased as the contact pressure increasing. Take the S_{pO_2} error and perfusion index into consideration, the designed optical fibre sensor performs the best when the contact pressure is in the range from 5 to 15 kPa.

Although the optical fibre sensor was successfully designed for measuring the contact pressure and PPG signals simultaneously, it has two big limitations. The one limitation is that the sensor performs really poor when the subject has a low peripheral perfusion state. As discussed above in Chapter 4, both the skin temperature and contact pressure will affect the subject's perfusion. Using the pressure recording data during the measurement, it could detect and remove the high contact pressure caused low

perfusion signals. However, the sensor cannot detect the low perfusion signals arisen from the low skin temperature. The further design of the sensor is thus recommended to add the skin temperature sensor to eliminate the low perfusion signals. The other limitation is that the designed sensor is very vulnerable to the motion artefacts. However, the sensor has the capability to indicate when the device is in contact with the skin as the contact pressure increases. Therefore, the null contact pressure can be used to recognise when artefacts might be present. The future study is recommended to use the pressure sensor to detect the motion artefacts.

This research has also used the designed sensor to measure the CRT of the subjects. As the contact pressure records reflects the blanching pressure changes, the calculation of CRT can be more accurate by using the contact pressure records to isolate the refilling period. This research also used an exponential module to simulate the refilling signals, which makes the CRT calculation more accurate and simple.

6.3 Future Work

As described in the above, this research has some limitations required further works. Therefore, the further research is recommended in the following areas:

1) Axial Loading Strain Interference Compensation.

At present, the system does not compensate for axial strain. An additional reference FBG could be used to compensate for this effect.

2) Temperature Caused Low Perfusion Signals Detection

Currently, the system cannot detect the low body temperature caused low peripheral perfusion signal. An additional temperature sensing FBG could be used to measure the skin temperature which indicates the low peripheral perfusion caused by the low body temperature.

3) Estimation of Breathing Rate Using Reflectance PPG Signals

As the breathing rate can be observed as a low frequency periodic variation in the baseline drift of PPG signals, it is recommended to use obtained PPG signals to measure the breathing rate of subjects in future work.

4) Motion Artefact Detection

As the designed sensor has a direct way of measuring the displacement between the sensor and the skin, an experiment could be designed to validate the capability of the designed sensor for measuring the motion artefacts.

5) Plethysmography Using an FBG Pressure Sensor

Since the blood volume changes in arteries and veins could be detected via the contact pressure changes, it could use the designed FBG pressure sensor to count HR of subjects in future work.

6) *Lock-in Detection with Quadrature Demodulation*

This research did not consider flicker noise. A lock-in amplifier could be applied to detect target signals in the presence of flicker noise.

7) *CRT Simulation System*

As the predominant method of measuring CRT is highly observer dependent, it is difficult to validate the CRT device such as the designed system in this research project. In this case, a flexible CRT simulation system is recommended to be designed in order to prove the accuracy and reproducibility of the CRT sensor

8) *Photonic Sensing Sock*

At present, the CRT sensor is only compatible for finger CRT measurements and requires the subject to load and release the external pressure to complete the blanching process. As the blanching pressure can be naturally generated during the walking process, the POF based PPG sensor could be combined with a pressure sensing sock to measure the CRT from the sole of the foot in future study.

Further details can be found in Appendix D.

References

- [1] S. E. Brill and J. A. Wedzicha, "Oxygen therapy in acute exacerbations of chronic obstructive pulmonary disease," *International journal of chronic obstructive pulmonary disease*, vol. 9, p. 1241, 2014.
- [2] X. Teng and Y.-T. Zhang, "The effect of contacting force on photoplethysmographic signals," *Physiological measurement*, vol. 25, no. 5, p. 1323, 2004.
- [3] A. Nobuyuki, N. Yasuhiro, T. Taiki, Y. Miyae, M. Kiyoko, and H. Terumasa, "Trial of measurement of sleep apnea syndrome with sound monitoring and SpO₂ at home," in *e-Health Networking, Applications and Services, 2009. Healthcom 2009. 11th International Conference on*, 2009, pp. 66-69: IEEE.
- [4] J. K. Takayesu and A. W. Lozner, "Pediatrics, dehydration," *Pediatrics*, vol. 8, p. 18, 1910.
- [5] B. I. Levy *et al.*, "Impaired tissue perfusion: a pathology common to hypertension, obesity, and diabetes mellitus," *Circulation*, vol. 118, no. 9, pp. 968-976, 2008.
- [6] F. Carpi and D. De Rossi, "Electroactive polymer-based devices for e-textiles in biomedicine," *IEEE transactions on Information Technology in biomedicine*, vol. 9, no. 3, pp. 295-318, 2005.
- [7] J. Coosemans, B. Hermans, and R. Puers, "Integrating wireless ECG monitoring in textiles," *Sensors and Actuators A: Physical*, vol. 130, pp. 48-53, 2006.
- [8] P. A. Kyriacou, "Pulse oximetry in the oesophagus," *Physiological measurement*, vol. 27, no. 1, p. R1, 2005.
- [9] P. A. Kyriacou, "Direct pulse oximetry within the esophagus, on the surface of abdominal viscera, and on free flaps," *Anesthesia & Analgesia*, vol. 117, no. 4, pp. 824-833, 2013.
- [10] J. M. May, J. P. Phillips, T. Fitchat, S. Ramaswamy, S. Snidvongs, and P. A. Kyriacou, "A Novel Photoplethysmography Sensor for Vital Signs Monitoring from the Human Trachea," *Biosensors*, vol. 9, no. 4, p. 119, 2019.
- [11] Q. Zhang, G. Andersson, L.-G. Lindberg, and J. Styf, "Muscle blood flow in response to concentric muscular activity vs. passive venous compression," *Acta Physiologica Scandinavica*, vol. 180, no. 1, pp. 57-62, 2004.
- [12] S. McMaster, B. Hayes-Gill, S. Morgan, and S. Korposh, "Combined textile pressure and optic sensor," ed: Google Patents, 2019.
- [13] M. Rothmaier, B. Selm, S. Spichtig, D. Haensse, and M. Wolf, "Photonic textiles for pulse oximetry," *Optics express*, vol. 16, no. 17, pp. 12973-12986, 2008.
- [14] P. Polygerinos, T. Schaeffter, L. Seneviratne, and K. Althoefer, "A fibre-optic catheter-tip force sensor with MRI compatibility: A feasibility study," in *2009 Annual International Conference of the IEEE Engineering in Medicine and Biology Society*, 2009, pp. 1501-1054: IEEE.

- [15] J. Brunelle and N. Chandel, "Oxygen deprivation induced cell death: an update," *Apoptosis*, vol. 7, no. 6, pp. 475-482, 2002.
- [16] A. Sandoel and M. O. Hengartner, "Apoptotic cell death under hypoxia," *Physiology*, vol. 29, no. 3, pp. 168-176, 2014.
- [17] (2019). *Cerebral Hypoxia Information Page*. Available: <https://www.ninds.nih.gov/Disorders/All-Disorders/Cerebral-Hypoxia-Information-Page>
- [18] H. S. Cabin and S. Henry, "The heart and circulation," *Yale University School of Medicine heart book*. New York: Hearst Books, p. 5, 1992.
- [19] (2016). *The Circulatory System In Animals Physical Education Essay*. Available: <https://www.ukessays.com/essays/physical-education/the-circulatory-system-in-animals-physical-education-essay.php>
- [20] F. B. Jensen, A. Fago, and R. E. Weber, "Hemoglobin structure and function," *Fish physiology*, vol. 17, pp. 1-40, 1998.
- [21] J. G. Webster, *Design of pulse oximeters*. CRC Press, 1997.
- [22] T. Tamura, Y. Maeda, M. Sekine, and M. Yoshida, "Wearable photoplethysmographic sensors—past and present," *Electronics*, vol. 3, no. 2, pp. 282-302, 2014.
- [23] J. Allen, "Photoplethysmography and its application in clinical physiological measurement," *Physiological measurement*, vol. 28, no. 3, p. R1, 2007.
- [24] J. Crowe, M. Grubb, B. Hayes-Gill, and N. Miles, "Photoplethysmography," ed: Google Patents, 2014.
- [25] Y. Maeda, M. Sekine, and T. Tamura, "The advantages of wearable green reflected photoplethysmography," *Journal of medical systems*, vol. 35, no. 5, pp. 829-834, 2011.
- [26] J. De Kock, L. Tarassenko, C. Glynn, and A. Hill, "Reflectance pulse oximetry measurements from the retinal fundus," *IEEE Transactions on biomedical engineering*, vol. 40, no. 8, pp. 817-823, 1993.
- [27] R. Graaff, "Tissue optics applied to reflectance pulse oximetry," *Groningen, Stichting C. Regenboog*, 1993.
- [28] S. Bagha and L. Shaw, "A real time analysis of PPG signal for measurement of SpO₂ and pulse rate," *International journal of computer applications*, vol. 36, no. 11, pp. 45-50, 2011.
- [29] D. King, R. Morton, and C. Bevan, "How to use capillary refill time," *Archives of Disease in Childhood-Education and Practice*, pp. edpract-2013-305198, 2013.
- [30] D. L. Schriger, Baraff, L., , "Schriger D L, Baraff L. Defining normal capillary refill: variation with age, sex, and temperature," *Annals of emergency medicine*, vol. 17, no. 9, pp. 932-935, 1988.
- [31] M. H. Gorelick, K. N. Shaw, and M. D. Baker, "Effect of ambient temperature on capillary refill in healthy children," *Pediatrics*, vol. 92, no. 5, pp. 699-702, 1993.

- [32] L. Blaxter, Morris, David E, Crowe, John A, C. Henry, S. Hill, D. Sharkey, H. Vyas, and B. R. Hayes-Gill, "An automated quasi-continuous capillary refill timing device," *Physiological measurement*, vol. 37, no. 1, p. 83, 2015.
- [33] Y. Pole, "Evolution of the pulse oximeter," in *International Congress Series*, 2002, vol. 1242, pp. 137-144: Elsevier.
- [34] W. Headquarters, "Global Pulse Oximetry Project."
- [35] J. W. Salyer, "Neonatal and pediatric pulse oximetry," *Respiratory care*, vol. 48, no. 4, pp. 386-398, 2003.
- [36] D. H. Rushton and J. H. Barth, "What is the evidence for gender differences in ferritin and haemoglobin?," *Critical reviews in oncology/hematology*, vol. 73, no. 1, pp. 1-9, 2010.
- [37] J. W. Severinghaus and P. B. Astrup, "History of blood gas analysis. VI. Oximetry," *Journal of clinical monitoring*, vol. 2, no. 4, pp. 270-288, 1986.
- [38] E. D. Chan, M. M. Chan, and M. M. Chan, "Pulse oximetry: understanding its basic principles facilitates appreciation of its limitations," *Respiratory medicine*, vol. 107, no. 6, pp. 789-799, 2013.
- [39] T. Guo, Z. Cao, Z. Zhang, D. Li, and M. Yu, "Reflective oxygen saturation monitoring at hypothenar and its validation by human hypoxia experiment," *Biomedical engineering online*, vol. 14, no. 1, p. 76, 2015.
- [40] E. D. Burman, J. Keegan, and P. J. Kilner, "Pulmonary artery diameters, cross sectional areas and area changes measured by cine cardiovascular magnetic resonance in healthy volunteers," *Journal of Cardiovascular Magnetic Resonance*, vol. 18, no. 1, p. 12, 2016.
- [41] J. De Kock and L. Tarassenko, "Pulse oximetry: Theoretical and experimental models," *Medical and Biological Engineering and Computing*, vol. 31, no. 3, pp. 291-300, 1993.
- [42] S. Chatterjee, J. Phillips, and P. Kyriacou, "Investigating optical path in reflectance pulse oximetry using a multilayer Monte Carlo model," in *European Conference on Biomedical Optics*, 2017, p. 1041106: Optical Society of America.
- [43] N. Stubán and N. Masatsugu, "Non-invasive calibration method for pulse oximeters," *Periodica Polytechnica Electrical Engineering*, vol. 52, no. 1-2, pp. 91-94, 2008.
- [44] M. Nitzan, A. Romem, and R. Koppel, "Pulse oximetry: fundamentals and technology update," *Medical Devices (Auckland, NZ)*, vol. 7, p. 231, 2014.
- [45] S. Fouzas, K. N. Priftis, and M. B. Anthracopoulos, "Pulse oximetry in pediatric practice," *Pediatrics*, vol. 128, no. 4, pp. 740-752, 2011.
- [46] S. J. Barker, J. Curry, D. Redford, and S. Morgan, "Measurement of Carboxyhemoglobin and Methemoglobin by Pulse Oximetry A Human Volunteer Study," *Anesthesiology: The Journal of the American Society of Anesthesiologists*, vol. 105, no. 5, pp. 892-897, 2006.
- [47] J. W. McLean, D. R. Crawford, and C. L. Hindman, "Limits of small angle scattering theory," *Applied optics*, vol. 26, no. 11, pp. 2053-2054, 1987.

- [48] J. C. Hebden *et al.*, "Simultaneous reconstruction of absorption and scattering images by multichannel measurement of purely temporal data," *Optics letters*, vol. 24, no. 8, pp. 534-536, 1999.
- [49] I. M. Stockford, S. P. Morgan, P. Chang, and J. G. Walker, "Analysis of the spatial distribution of polarized light backscattered from layered scattering media," *Journal of Biomedical Optics*, vol. 7, no. 3, pp. 313-320, 2002.
- [50] D. A. Paulus and M. C. Monroe, "Cool fingers and pulse oximetry," *Anesthesiology: The Journal of the American Society of Anesthesiologists*, vol. 71, no. 1, pp. 168-168, 1989.
- [51] F. G. Mihm and B. D. Halperin, "Noninvasive detection of profound arterial desaturations using a pulse oximetry device," *Anesthesiology: The Journal of the American Society of Anesthesiologists*, vol. 62, no. 1, pp. 85-87, 1985.
- [52] C. M. Alexander, L. E. Teller, and J. B. Gross, "Principles of pulse oximetry: theoretical and practical considerations," *Anesthesia & Analgesia*, vol. 68, no. 3, pp. 368-376, 1989.
- [53] E. Calzia, Z. Iványi, and P. Radermacher, "Determinants of blood flow and organ perfusion," in *Functional hemodynamic monitoring*: Springer, 2005, pp. 19-32.
- [54] (2007). *Assessing the Accuracy of Pulse Oximetry in True Clinical Settings*. Available: http://www.masimo.it/siteassets/uk/documents/pdf/clinical-evidence/whitepapers/lab4709a_whitepapers_pulse_oximetry_accuracy.pdf
- [55] M. Rothmaier, M. P. Luong, and F. Clemens, "Textile pressure sensor made of flexible plastic optical fibers," *Sensors*, vol. 8, no. 7, pp. 4318-4329, 2008.
- [56] B. Selm, E. A. Gürel, M. Rothmaier, R. M. Rossi, and L. J. Scherer, "Polymeric optical fiber fabrics for illumination and sensorial applications in textiles," *Journal of intelligent material systems and structures*, vol. 21, no. 11, pp. 1061-1071, 2010.
- [57] B. M. Quandt *et al.*, "Body-monitoring with photonic textiles: a reflective heartbeat sensor based on polymer optical fibres," *Journal of The Royal Society Interface*, vol. 14, no. 128, p. 20170060, 2017.
- [58] S. Rommel, L. C. P. Cavalcante, J. V. Olmos, I. T. Monroy, and A. K. Mishra, "Requirements for bend insensitive fiber in millimeter-wave fronthaul systems," in *2015 International Topical Meeting on Microwave Photonics (MWP)*, 2015, pp. 1-4: IEEE.
- [59] B. M. Quandt, "Optical Fibre Textiles in Non-Invasive Medical Applications," ETH Zurich, 2016.
- [60] A. A. Boechat, D. Su, D. R. Hall, and J. D. Jones, "Bend loss in large core multimode optical fiber beam delivery systems," *Applied optics*, vol. 30, no. 3, pp. 321-327, 1991.
- [61] J. Phillips, R. Langford, P. Kyriacou, and D. Jones, "Preliminary evaluation of a new fibre-optic cerebral oximetry system," *Physiological measurement*, vol. 29, no. 12, p. 1383, 2008.

- [62] M. Hickey, N. Samuels, N. Randive, R. Langford, and P. A. Kyriacou, "A new fibre optic pulse oximeter probe for monitoring splanchnic organ arterial blood oxygen saturation," *Computer methods and programs in biomedicine*, vol. 108, no. 3, pp. 883-888, 2012.
- [63] J. P. Phillips, R. M. Langford, S. H. Chang, K. Maney, P. A. Kyriacou, and D. P. Jones, "Evaluation of a fiber-optic esophageal pulse oximeter," in *2009 Annual International Conference of the IEEE Engineering in Medicine and Biology Society*, 2009, pp. 1509-1512: IEEE.
- [64] K. Hung, C. Lee, W. Chan, S.-O. Choy, and P. Kwok, "Development of novel wearable sensors for mobile health," in *Proceedings of 2012 IEEE-EMBS International Conference on Biomedical and Health Informatics*, 2012, pp. 745-747: IEEE.
- [65] S. Morgan *et al.*, "Optical fiber sensors for monitoring in critical care," in *2019 41st Annual International Conference of the IEEE Engineering in Medicine and Biology Society (EMBC)*, 2019, pp. 1139-1143: IEEE.
- [66] C. Liu, R. Correia, H. Ballaji, S. Korposh, B. Hayes-Gill, and S. Morgan, "Optical Fibre-Based Pulse Oximetry Sensor with Contact Force Detection," *Sensors*, vol. 18, no. 11, p. 3632, 2018.
- [67] C. Brochier and A. Lysenko, "Optical fiber fabrics," *Fibre chemistry*, vol. 40, no. 4, pp. 303-307, 2008.
- [68] B. Derick and J. Synder, "Luminous Textile Products," 1967.
- [69] V. Koncar, "Optical fiber fabric displays," *Optics and photonics news*, vol. 16, no. 4, pp. 40-44, 2005.
- [70] A. Boczkowska and M. Leonowicz, "Intelligent materials for intelligent textiles," *Fibres & Textiles in Eastern Europe*, vol. 59, pp. 13-17, 2006.
- [71] J. P. Phillips, P. A. Kyriacou, K. J. George, J. V. Priestley, and R. M. Langford, "An optical fiber photoplethysmographic system for central nervous system tissue," in *Engineering in Medicine and Biology Society, 2006. EMBS'06. 28th Annual International Conference of the IEEE*, 2006, pp. 803-806: IEEE.
- [72] J. J. Davenport, M. Hickey, J. P. Phillips, and P. Kyriacou, "Method for producing angled optical fiber tips in the laboratory," *Optical Engineering*, vol. 55, no. 2, p. 026120, 2016.
- [73] O. Ziemann, J. Krauser, P. E. Zamzow, and W. Daum, "POF handbook," *Springer*, 2008.
- [74] M. Krehel, M. Wolf, L. F. Boesel, R. M. Rossi, G.-L. Bona, and L. J. Scherer, "Development of a luminous textile for reflective pulse oximetry measurements," *Biomedical optics express*, vol. 5, no. 8, pp. 2537-2547, 2014.
- [75] F. A. Reifler, R. Hufenus, M. Krehel, E. Zraggen, R. M. Rossi, and L. J. Scherer, "Polymer optical fibers for textile applications—bicomponent melt spinning from cyclic olefin polymer and structural characteristics revealed by wide angle X-ray diffraction," *Polymer*, vol. 55, no. 22, pp. 5695-5707, 2014.
- [76] R. P. Drescher and Y. Mendelson, "Reflectance forehead pulse oximetry: Effects of contact pressure during walking," in *Engineering in Medicine and*

Biology Society, 2006. EMBS'06. 28th Annual International Conference of the IEEE, 2006, pp. 3529-3532: IEEE.

- [77] R. P. Drescher, "Wearable forehead pulse oximetry: Minimization of motion and pressure artifacts," Citeseer, 2006.
- [78] P. Santos, V. Almeida, J. Cardoso, and C. Correia, "Photoplethysmographic logger with contact force and hydrostatic pressure monitoring," in *Bioengineering (ENBENG), 2013 IEEE 3rd Portuguese Meeting in*, 2013, pp. 1-6: IEEE.
- [79] F. Xu *et al.*, "Recent developments for flexible pressure sensors: A review," *Micromachines*, vol. 9, no. 11, p. 580, 2018.
- [80] A. Razak, A. Hadi, A. Zayegh, R. K. Begg, and Y. Wahab, "Foot plantar pressure measurement system: A review," *Sensors*, vol. 12, no. 7, pp. 9884-9912, 2012.
- [81] W. F. A. Besling, M. Goossens, J. T. M. Van Beek, P. G. Steeneken, and O. Wunnicke, "MEMS capacitive pressure sensor," ed: Google Patents, 2017.
- [82] K.-H. Kim, S. K. Hong, N.-S. Jang, S.-H. Ha, H. W. Lee, and J.-M. Kim, "Wearable resistive pressure sensor based on highly flexible carbon composite conductors with irregular surface morphology," *ACS applied materials & interfaces*, vol. 9, no. 20, pp. 17499-17507, 2017.
- [83] F. Juelich and J. Roths, "OP2-Determination of the Effective Refractive Index of Various Single Mode Fibres for Fibre Bragg Grating Sensor Applications," *Proceedings OPTO 2009 & IRS² 2009*, pp. 119-124, 2009.
- [84] S. Li, X. Liu, Y. Li, S. Yang, and C. Liu, "FBG sensing temperature characteristic and application in oil/gas down-hole measurement," *Frontiers of Optoelectronics in China*, vol. 2, no. 2, pp. 233-238, 2009.
- [85] X. Pan *et al.*, "Enhanced FBG Temperature Sensitivity in PbS-Doped Silica Optical Fiber," *Journal of Lightwave Technology*, vol. 37, no. 18, pp. 4902-4907, 2019.
- [86] R. Li, Y. Chen, Y. Tan, Z. Zhou, T. Li, and J. Mao, "Sensitivity enhancement of FBG-based strain sensor," *Sensors*, vol. 18, no. 5, p. 1607, 2018.
- [87] V. R. Pachava, S. Kamineni, S. S. Madhuvarasu, K. Putha, and V. R. Mamidi, "FBG based high sensitive pressure sensor and its low-cost interrogation system with enhanced resolution," *Photonic Sensors*, vol. 5, no. 4, pp. 321-329, 2015.
- [88] M. Xu, H. Geiger, and J. Dakin, "Fibre grating pressure sensor with enhanced sensitivity using a glass-bubble housing," *Electronics Letters*, vol. 32, no. 2, pp. 128-129, 1996.
- [89] X. Weng, J. Chen, and J. Wang, "Fiber Bragg grating-based performance monitoring of piles fiber in a geotechnical centrifugal model test," *Advances in Materials Science and Engineering*, vol. 2014, 2014.
- [90] R. Correia *et al.*, "Fibre Bragg grating based effective soil pressure sensor for geotechnical applications," in *20th International Conference on Optical Fibre*

Sensors, 2009, vol. 7503, p. 75030F: International Society for Optics and Photonics.

- [91] R. Correia, E. Chehura, J. Li, S. W. James, and R. P. Tatam, "Enhanced sensitivity fibre Bragg grating (FBG) load sensor," *Measurement Science and Technology*, vol. 21, no. 9, p. 094006, 2010.
- [92] M. Xu, J. Archambault, L. Reekie, and J. Dakin, "Thermally-compensated bending gauge using surface-mounted fibre gratings," *International Journal of Optoelectronics*, vol. 9, no. 3, pp. 281-283, 1994.
- [93] W. Morey, "Evaluation of a fiber Bragg grating hydrostatic pressure sensor," *Proc. OFS8, Monterey, USA, Post-Deadline Session*, 1982.
- [94] M. Xu, J.-L. Archambault, L. Reekie, and J. Dakin, "Discrimination between strain and temperature effects using dual-wavelength fibre grating sensors," *Electronics letters*, vol. 30, no. 13, pp. 1085-1087, 1994.
- [95] M. Xu, L. Dong, L. Reekie, J. Tucknott, and J. Cruz, "Temperature-independent strain sensor using a chirped Bragg grating in a tapered optical fibre," *Electronics Letters*, vol. 31, no. 10, pp. 823-825, 1995.
- [96] D. L. Romanyk, H. Yu, M. Grotski, S. Seo, O. Addison, and C. R. Dennison, "In situ measurement of dental resin-based composite volumetric shrinkage and temperature effects using in-fibre bragg grating methods," *Journal of the mechanical behavior of biomedical materials*, vol. 95, pp. 89-95, 2019.
- [97] W. Yuan, A. Stefani, and O. Bang, "Tunable polymer fiber Bragg grating (FBG) inscription: fabrication of dual-FBG temperature compensated polymer optical fiber strain sensors," *IEEE Photonics Technology Letters*, vol. 24, no. 5, pp. 401-403, 2011.
- [98] A. Ariander, "The effect of pressure on capillary refill time: A clinical study on healthy volunteers," ed, 2015.
- [99] S. M. Tibby, M. Hatherill, and I. A. Murdoch, "Capillary refill and core-peripheral temperature gap as indicators of haemodynamic status in paediatric intensive care patients," *Archives of disease in childhood*, vol. 80, no. 2, pp. 163-166, 1999.
- [100] M. K. Aasuri, N. Venkata, P. Preetam, and N. T. Rao, "Management of pediatric aphakia with silsoft contact lenses," *The CLAO journal: official publication of the Contact Lens Association of Ophthalmologists, Inc*, vol. 25, no. 4, pp. 209-212, 1999.
- [101] D. Osborn, N. Evans, and M. Kluckow, "Clinical detection of low upper body blood flow in very premature infants using blood pressure, capillary refill time, and central-peripheral temperature difference," *Archives of Disease in Childhood-Fetal and Neonatal Edition*, vol. 89, no. 2, pp. F168-F173, 2004.
- [102] B. Anderson, A.-M. Kelly, D. Kerr, M. Clooney, and D. Jolley, "Impact of patient and environmental factors on capillary refill time in adults," *The American journal of emergency medicine*, vol. 26, no. 1, pp. 62-65, 2008.
- [103] E. Kviesis-Kipge, E. Curkste, J. Spigulis, and D. Gardovska, "Optical studies of the capillary refill kinetics in fingertips," in *World Congress on Medical*

Physics and Biomedical Engineering, September 7-12, 2009, Munich, Germany, 2009, pp. 377-379: Springer.

- [104] V. Bezzerides and M. I. Neuman, "Capillary refill time diagnostic apparatus and methods," ed: Google Patents, 2017.
- [105] W. Cui, L. E. Ostrander, and B. Y. Lee, "In vivo reflectance of blood and tissue as a function of light wavelength," *IEEE transactions on biomedical engineering*, vol. 37, no. 6, pp. 632-639, 1990.
- [106] H. Ugnell and P. Öberg, "The time-variable photoplethysmographic signal; dependence of the heart synchronous signal on wavelength and sample volume," *Medical engineering & physics*, vol. 17, no. 8, pp. 571-578, 1995.
- [107] S. Chino, H. Ishizawa, S. Hosoya, S. Koyama, K. Fujimoto, and T. Kawamura, "Research for wearable multiple vital sign sensor using fiber Bragg Grating—Verification of several pulsate points in human body surface," in *2017 IEEE International Instrumentation and Measurement Technology Conference (I2MTC)*, 2017, pp. 1-6: IEEE.
- [108] Z. Chen *et al.*, "Monitoring respiration and cardiac activity during sleep using microbend fiber sensor: A clinical study and new algorithm," in *2014 36th annual international conference of the IEEE engineering in medicine and biology society*, 2014, pp. 5377-5380: IEEE.
- [109] J. P. Phillips, P. A. Kyriacou, D. P. Jones, R. M. Langford, and S. H. Chang, "Photoplethysmographic measurements from the esophagus using a new fiber-optic reflectance sensor," *Journal of biomedical optics*, vol. 16, no. 7, p. 077005, 2011.
- [110] R. Correia *et al.*, "Highly sensitive contact pressure measurements using FBG patch in endotracheal tube cuff," presented at the Sixth European Workshop on Optical Fibre Sensors, 2016.
- [111] A. D. Kersey *et al.*, "Fiber grating sensors," *Journal of lightwave technology*, vol. 15, no. 8, pp. 1442-1463, 1997.
- [112] S. J. Mihailov, "Fiber Bragg grating sensors for harsh environments," *Sensors*, vol. 12, no. 2, pp. 1898-1918, 2012.
- [113] M.-f. Liang, X.-q. Fang, G. Wu, G.-z. Xue, and H.-w. Li, "A fiber Bragg grating pressure sensor with temperature compensation based on diaphragm-cantilever structure," *Optik-International Journal for Light and Electron Optics*, vol. 145, pp. 503-512, 2017.
- [114] Z. Ahmed, J. Filla, W. Guthrie, and J. Quintavalle, "Fiber Bragg Grating Based Thermometry," *Ncsli Measure*, vol. 10, no. 4, pp. 28-31, 2015.
- [115] R. M. Peters, E. Hackeman, and D. Goldreich, "Diminutive digits discern delicate details: fingertip size and the sex difference in tactile spatial acuity," *Journal of Neuroscience*, vol. 29, no. 50, pp. 15756-15761, 2009.
- [116] M. Voracek, J. Pietschnig, and M. Oeckher, "Finger, sex, and side differences in fingertip size and lack of association with image-based digit ratio (2D: 4D) measurements," *Perceptual and motor skills*, vol. 107, no. 2, pp. 507-512, 2008.

- [117] G. Meltz, W. W. Morey, and J. R. Dunphy, "Fiber Bragg grating chemical sensor," in *Chemical, Biochemical, and Environmental Fiber Sensors III*, 1992, vol. 1587, pp. 350-362: International Society for Optics and Photonics.
- [118] S. W. James, R. P. Tatam, A. Twin, M. Morgan, and P. Noonan, "Strain response of fibre Bragg grating sensors at cryogenic temperatures," *Measurement Science and Technology*, vol. 13, no. 10, p. 1535, 2002.
- [119] (2018). *Fiber-Coupled LED M660F1* Available: <https://www.thorlabs.com/drawings/cf13e571545bd3a2-D26F60C3-954D-23AF-BF0F708385532899/M660F1-SpecSheet.pdf>
- [120] (2018). *Fiber-Coupled LED M850F2* Available: <https://www.thorlabs.com/drawings/cf13e571545bd3a2-D26F60C3-954D-23AF-BF0F708385532899/M850F2-SpecSheet.pdf>
- [121] (2018). *Thorlabs T-Cube LED Driver Operation Manual*. Available: <https://www.thorlabs.com/drawings/cf13e571545bd3a2-D26F60C3-954D-23AF-BF0F708385532899/LEDD1B-Manual.pdf>
- [122] (2017). *PDA36A(-EC) Si Switchable Gain Detector User Guide*. Available: <https://www.thorlabs.com/drawings/cf13e571545bd3a2-D26F60C3-954D-23AF-BF0F708385532899/PDA36A-EC-Manual.pdf>
- [123] (2016). *User Guide NI myDAQ*. Available: <http://www.ni.com/pdf/manuals/373060g.pdf>
- [124] S. Engelberg and Y. Bendelac, "Measurement of physical constants using noise," *IEEE instrumentation & measurement magazine*, vol. 6, no. 4, pp. 49-52, 2003.
- [125] W. Shockley and J. Pierce, "A theory of noise for electron multipliers," *Proceedings of the Institute of Radio Engineers*, vol. 26, no. 3, pp. 321-332, 1938.
- [126] M. Grubb, "intelligent clothing for monitoring occupational health and safety," University of Nottingham, 2009.
- [127] H. Nyquist, "Thermal agitation of electric charge in conductors," *Physical review*, vol. 32, no. 1, p. 110, 1928.
- [128] R. F. Voss, "1/f (flicker) noise: A brief review," in *33rd Annual Symposium on Frequency Control. 1979*, 1979, pp. 40-46: IEEE.
- [129] (2011). *Analog Devices AD829 Data Sheet*. Available: <http://www.analog.com/media/en/technical-documentation/data-sheets/AD829.pdf>
- [130] D. D. Falconer, F. Adachi, and B. Gudmundson, "Time division multiple access methods for wireless personal communications," *IEEE Communications Magazine*, vol. 33, no. 1, pp. 50-57, 1995.
- [131] H. H. Asada, P. Shaltis, A. Reisner, S. Rhee, and R. C. Hutchinson, "Mobile monitoring with wearable photoplethysmographic biosensors," *IEEE engineering in medicine and biology magazine*, vol. 22, no. 3, pp. 28-40, 2003.
- [132] M. J. Hayes and P. R. Smith, "Artifact reduction in photoplethysmography," *Applied Optics*, vol. 37, no. 31, pp. 7437-7446, 1998.

- [133] S. Y. Park, H. J. Baek, K. S. Park, and Y. C. Kim, "Photoplethysmographic signals to predict the success of lumbar sympathetic blockade for lower extremity pain," *Journal of International Medical Research*, vol. 42, no. 4, pp. 938-948, 2014.
- [134] G. Yuan, N. A. Drost, and R. A. McIvor, "Respiratory rate and breathing pattern," *McMaster University Medical Journal*, vol. 10, no. 1, pp. 23-25, 2013.
- [135] M. Elgendi, "Optimal Signal Quality Index for Photoplethysmogram Signals," *Bioengineering*, vol. 3, no. 4, p. 21, 2016.
- [136] S. V. Vaseghi, *Advanced digital signal processing and noise reduction*. John Wiley & Sons, 2008.
- [137] H.-w. He, D.-w. Liu, Y. Long, and X.-t. Wang, "The peripheral perfusion index and transcutaneous oxygen challenge test are predictive of mortality in septic patients after resuscitation," *Critical Care*, vol. 17, no. 3, p. R116, 2013.
- [138] D. A. Colquhoun, K. T. Forkin, M. E. Durieux, and R. H. Thiele, "Ability of the Masimo pulse CO-Oximeter to detect changes in hemoglobin," *Journal of clinical monitoring and computing*, vol. 26, no. 2, pp. 69-73, 2012.
- [139] S. H.-L. Chang, "Clinical evaluation of a new optical fibre method of measuring oxygen saturation using photoplethysmograph signals reflected from internal tissues," Queen Mary University of London, 2013.
- [140] M. G. Kendall, *Advanced Theory Of Statistics Vol-I*. Charles Griffin: London, 1943.
- [141] D. P. Doane and L. E. Seward, "Measuring skewness: a forgotten statistic?," *Journal of Statistics Education*, vol. 19, no. 2, 2011.
- [142] R. Krishnan, B. Natarajan, and S. Warren, "Two-stage approach for detection and reduction of motion artifacts in photoplethysmographic data," *IEEE transactions on biomedical engineering*, vol. 57, no. 8, pp. 1867-1876, 2010.
- [143] Y. Mendelson and B. D. Ochs, "Noninvasive pulse oximetry utilizing skin reflectance photoplethysmography," *IEEE Transactions on Biomedical Engineering*, vol. 35, no. 10, pp. 798-805, 1988.
- [144] D. Giavarina, "Understanding bland altman analysis," *Biochemia medica: Biochemia medica*, vol. 25, no. 2, pp. 141-151, 2015.
- [145] A. Hasanin, A. Mukhtar, and H. Nassar, "Perfusion indices revisited," *Journal of intensive care*, vol. 5, no. 1, p. 24, 2017.
- [146] A. Lima and J. Bakker, "Noninvasive monitoring of peripheral perfusion," in *Applied Physiology in Intensive Care Medicine*: Springer, 2006, pp. 131-141.
- [147] V. König, R. Huch, and A. Huch, "Reflectance pulse oximetry—principles and obstetric application in the Zurich system," *Journal of Clinical Monitoring and Computing*, vol. 14, no. 6, pp. 403-412, 1998.
- [148] R. Webb, A. Ralston, and W. Runciman, "Potential errors in pulse oximetry," *Anaesthesia*, vol. 46, no. 3, pp. 207-212, 1991.
- [149] L. Wiklund, B. Hök, K. Ståhl, and A. Jordeby-Jönsson, "Postanesthesia monitoring revisited: frequency of true and false alarms from different

- monitoring devices," *Journal of clinical anesthesia*, vol. 6, no. 3, pp. 182-188, 1994.
- [150] A. Jubran, "Pulse oximetry," *Intensive care medicine*, vol. 30, no. 11, pp. 2017-2020, 2004.
- [151] M. Khan, C. G. Pretty, A. C. Amies, R. Elliott, G. M. Shaw, and J. G. Chase, "Investigating the effects of temperature on photoplethysmography," *IFAC-PapersOnLine*, vol. 48, no. 20, pp. 360-365, 2015.
- [152] K. Shinozaki, Capilupi, M. J., Saeki, K., Hirahara, H., Horie, K., Kobayashi, N., Weisner, S., Kim, J., Lampe, J.W., Becker, L. B, "Low temperature increases capillary blood refill time following mechanical fingertip compression of healthy volunteers: prospective cohort study," *Journal of clinical monitoring and computing*, vol. 33, no. 2, pp. 259-267, 2019.
- [153] R. Drescher and Y. Mendelson, "Attachment of a wearable skin reflectance pulse oximeter," in *Proceedings of the 2005 BMES Annual Fall Meeting, Baltimore, MD, USA*, 2005, vol. 28.
- [154] D. He *et al.*, "A single-chip CMOS pulse oximeter with on-chip lock-in detection," *Sensors*, vol. 15, no. 7, pp. 17076-17088, 2015.
- [155] J. Han and C. Nguyen, "A new ultra-wideband, ultra-short monocycle pulse generator with reduced ringing," *IEEE Microwave and wireless components letters*, vol. 12, no. 6, pp. 206-208, 2002.
- [156] H. F. Pues and A. R. Van De Capelle, "An impedance-matching technique for increasing the bandwidth of microstrip antennas," *IEEE transactions on antennas and propagation*, vol. 37, no. 11, pp. 1345-1354, 1989.
- [157] L. Frenzel, "Back to basics: Impedance matching (part 1)," *Electronic Design*, vol. 24, 2011.
- [158] E. Kviesis-Kipge, E. Curkste, J. Spigulis, and L. Eihvalde, "Real-time analysis of skin capillary-refill processes using blue LED," in *Biophotonics: Photonic Solutions for Better Health Care II*, 2010, vol. 7715, p. 771523: International Society for Optics and Photonics.
- [159] J. A. Evans *et al.*, "Capillary refill time as an independent prognostic indicator in severe and complicated malaria," *The Journal of pediatrics*, vol. 149, no. 5, pp. 676-681, 2006.
- [160] U. Bal, "CAPILLARY REFILL TIME MEASUREMENT DEVICE," *Mugla Journal of Science and Technology*, vol. 4, no. 1, pp. 37-40.
- [161] T. Tamura and W. Chen, *Seamless Healthcare Monitoring: Advancements in Wearable, Attachable, and Invisible Devices*. Springer, 2017.
- [162] L. Nilsson, A. Johansson, and S. Kalman, "Respiratory variations in the reflection mode photoplethysmographic signal. Relationships to peripheral venous pressure," *Medical and Biological Engineering and Computing*, vol. 41, no. 3, pp. 249-254, 2003.
- [163] L. Nilsson, A. Johansson, and S. Kalman, "Macrocirculation is not the sole determinant of respiratory induced variations in the reflection mode

- photoplethysmographic signal," *Physiological measurement*, vol. 24, no. 4, p. 925, 2003.
- [164] M. Vegfors, H. Ugnell, B. Hok, P. Oberg, and C. Lennmarken, "Experimental evaluation of two new sensors for respiratory rate monitoring," *Physiological measurement*, vol. 14, no. 2, p. 171, 1993.
- [165] E. Grossman, A. Grossman, M. Schein, R. Zimlichman, and B. Gavish, "Breathing-control lowers blood pressure," *Journal of human hypertension*, vol. 15, no. 4, p. 263, 2001.
- [166] M. Cretikos *et al.*, "The objective medical emergency team activation criteria: a case-control study," *Resuscitation*, vol. 73, no. 1, pp. 62-72, 2007.
- [167] J. F. Fieselmann, M. S. Hendryx, C. M. Helms, and D. S. Wakefield, "Respiratory rate predicts cardiopulmonary arrest for internal medicine inpatients," *Journal of general internal medicine*, vol. 8, no. 7, pp. 354-360, 1993.
- [168] L. Norton, B. Squires, N. Craig, G. McLeay, P. McGrath, and K. Norton, "Accuracy of pulse oximetry during exercise stress testing," *International journal of sports medicine*, vol. 13, no. 07, pp. 523-527, 1992.
- [169] M. Hayes, P. Smith, D. Barnett, M. Morgan, S. Singh, and D. Vara, "Quantitative investigation of artefact in photoplethysmography and pulse oximetry for respiratory exercise testing," in *Proc. CNVD 97 Frontiers in Computer-Aided Visualization of Vascular Functions*, 1998, pp. 117-124.
- [170] N. Selvaraj and K. H. Chon, "Algorithms for Real-time Detection of Motion Artifacts and Accurate Estimation of Respiratory Rates using Pulse Oximeter," *no. Table*, vol. 1, p. 750, 2008.
- [171] M. R. Ram, K. V. Madhav, E. H. Krishna, N. R. Komalla, and K. A. Reddy, "A novel approach for motion artifact reduction in PPG signals based on AS-LMS adaptive filter," *IEEE Transactions on Instrumentation and Measurement*, vol. 61, no. 5, pp. 1445-1457, 2012.
- [172] S. Hanyu and C. Xiaohui, "Motion artifact detection and reduction in PPG signals based on statistics analysis," in *Control And Decision Conference (CCDC), 2017 29th Chinese*, 2017, pp. 3114-3119: IEEE.
- [173] H.-W. Lee, J.-W. Lee, W.-G. Jung, and G.-K. Lee, "The periodic moving average filter for removing motion artifacts from PPG signals," *International Journal of Control, Automation, and Systems*, vol. 5, no. 6, pp. 701-706, 2007.
- [174] P. Caravaggi, C. Giacomozzi, and A. Leardini, "Foot segments mobility and plantar pressure in the normal foot," in *Journal of foot and ankle research*, 2014, vol. 7, no. 1, p. A11: BioMed Central.
- [175] J. A. A. AL-Baghdadia, A. K. Chongb, and P. D. Milburnc, "FABRICATION AND TESTING OF A LOW-COST FOOT PRESSURE SENSING SYSTEM," 2015.
- [176] D. Grieve and T. Rashdi, "Pressures under normal feet in standing and walking as measured by foil pedobarography," *Annals of the rheumatic diseases*, vol. 43, no. 6, p. 816, 1984.

- [177] E. A. Mendoza, Y. Esterkin, C. Kempen, and S. Sun, "Monolithic integrated optic fiber Bragg grating sensor interrogator," in *Photonics in the Transportation Industry: Auto to Aerospace III*, 2010, vol. 7675, p. 76750S: International Society for Optics and Photonics.
- [178] E. A. Mendoza, Y. Esterkin, C. Kempen, and Z. Sun, "Multi-channel monolithic integrated optic fiber Bragg grating sensor interrogator," *Photonic sensors*, vol. 1, no. 3, pp. 281-288, 2011.
- [179] E. A. Mendoza, C. Kempen, and C. Lopatin, "Miniature fiber Bragg grating sensor interrogator (FBG-Transceiver) system," in *Sensors and Smart Structures Technologies for Civil, Mechanical, and Aerospace Systems 2007*, 2007, vol. 6529, p. 652921: International Society for Optics and Photonics.
- [180] S. A. McMaster, "Method for Optimizing Contact Resistance in Electrically Conductive Textiles," ed: Google Patents, 2015.
- [181] C. Isaia, D. S. McNally, S. A. McMaster, and D. T. Branson, "Effect of mechanical preconditioning on the electrical properties of knitted conductive textiles during cyclic loading," *Textile Research Journal*, p. 0040517517748496, 2018.

Appendix A

Fibre Bragg Grating (FBG) Sensor Calibration

A.1 Temperature Response of the FBG sensor

For the bare FBG sensor which consisted of two FBGs, the temperature calibration experiment was repeated 5 times in this study which are shown from A1 to A5. Blue trace in each figure represents Bragg wavelength shifts of FBG1 whilst black trace in each figure represents Bragg wavelength shifts of FBG2. The ambient temperature was measured by Pico TC-08 thermocouple which was shown as red line in each figure.

For the FBG sensor housed in the patch, the temperature calibration experiment was repeated 5 times in this study which are shown from A6 to A10. From A6 to A10, blue trace in each figure represents Bragg wavelength shifts of FBG1 whilst black trace in each figure represents Bragg wavelength shifts of FBG2. The ambient temperature was measured by Pico TC-08 thermocouple which was shown as red line in each figure from A6 to A10.

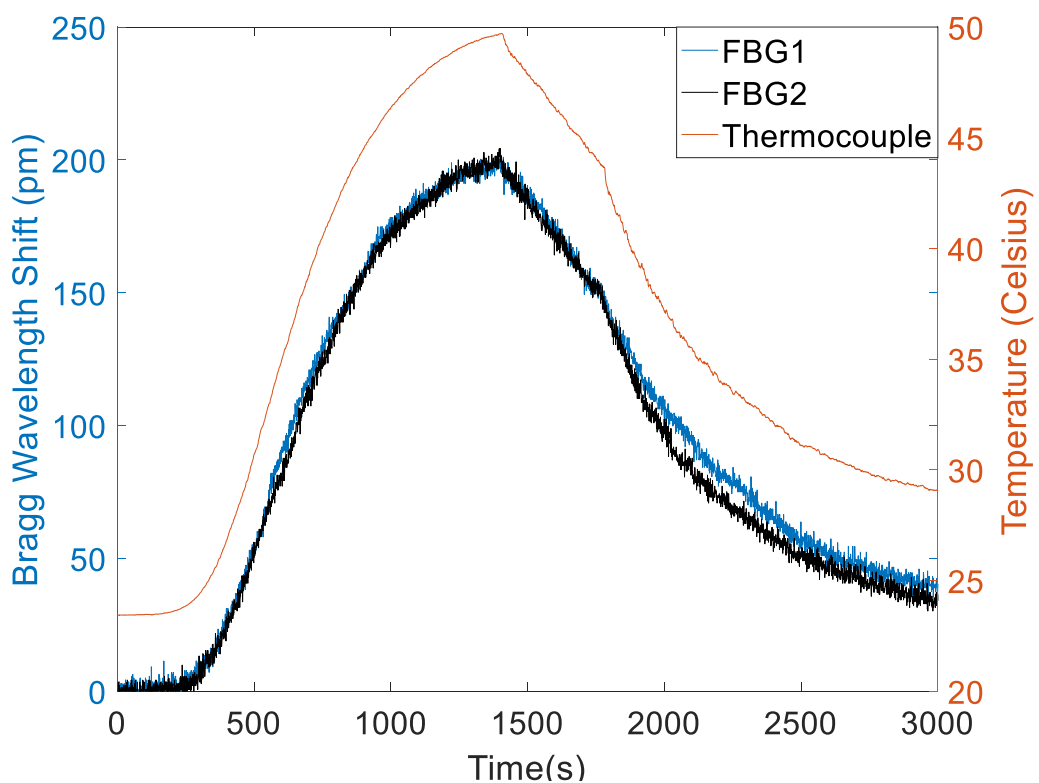


Figure A.1. Temperature response of two bare FBGs (First experiment).

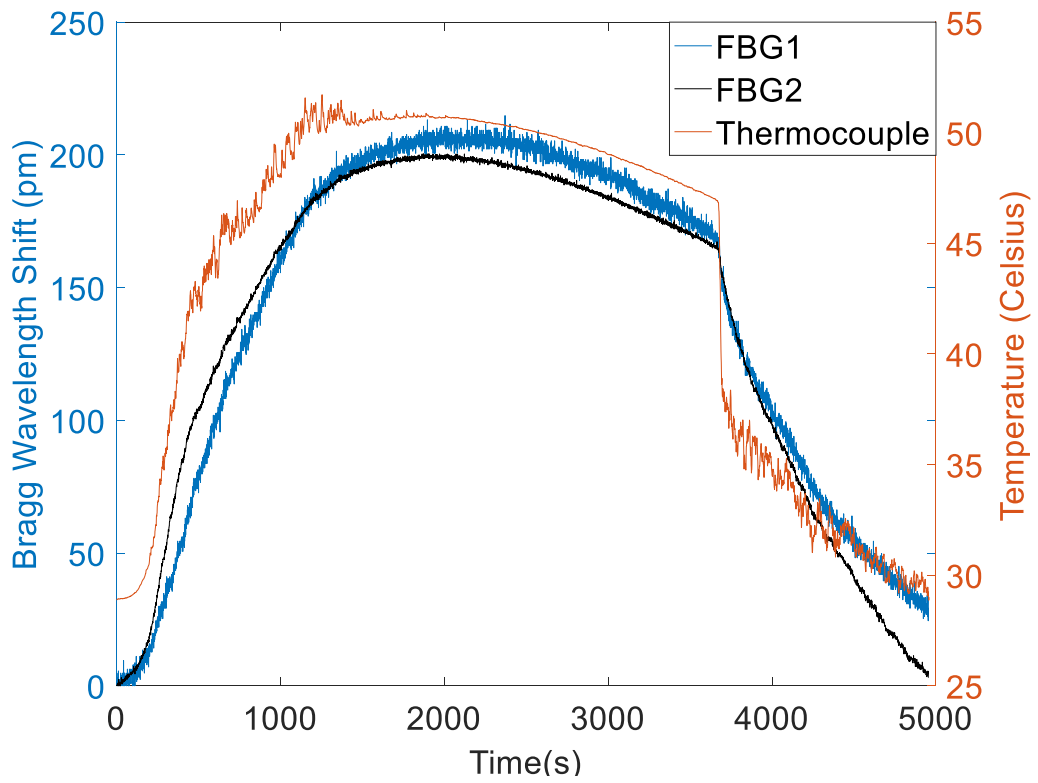


Figure A.2. Temperature response of two bare FBGs (Second experiment).

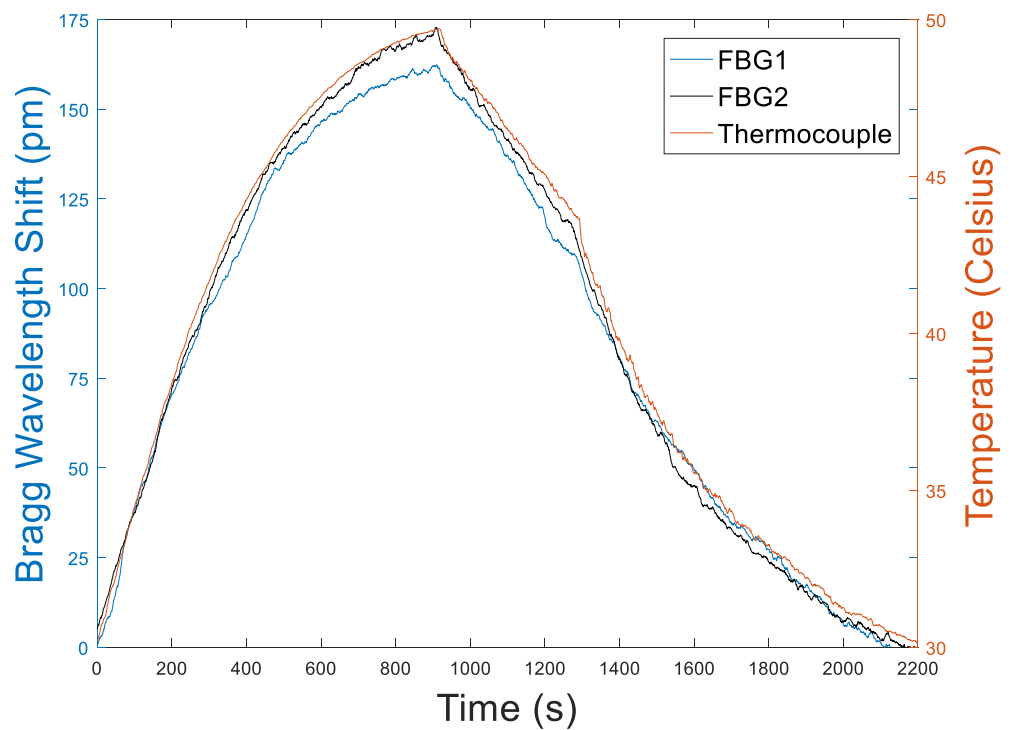


Figure A.3. Temperature response of two bare FBGs (Third experiment).

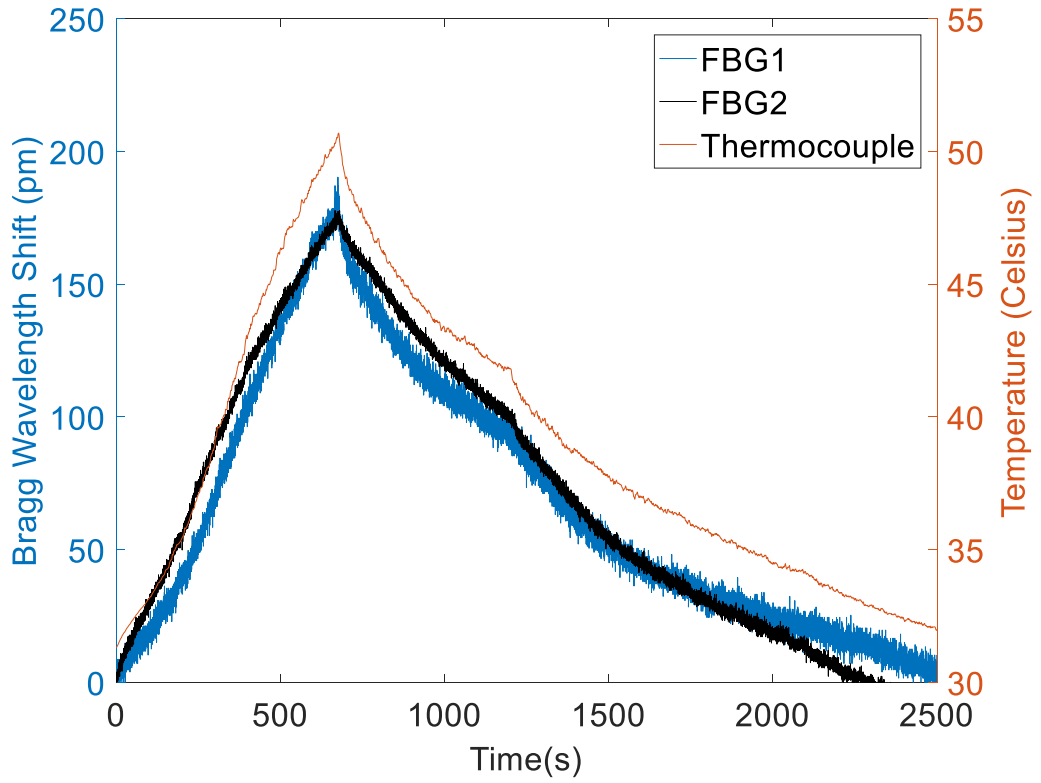


Figure A.4. Temperature response of two bare FBGs (Forth experiment).

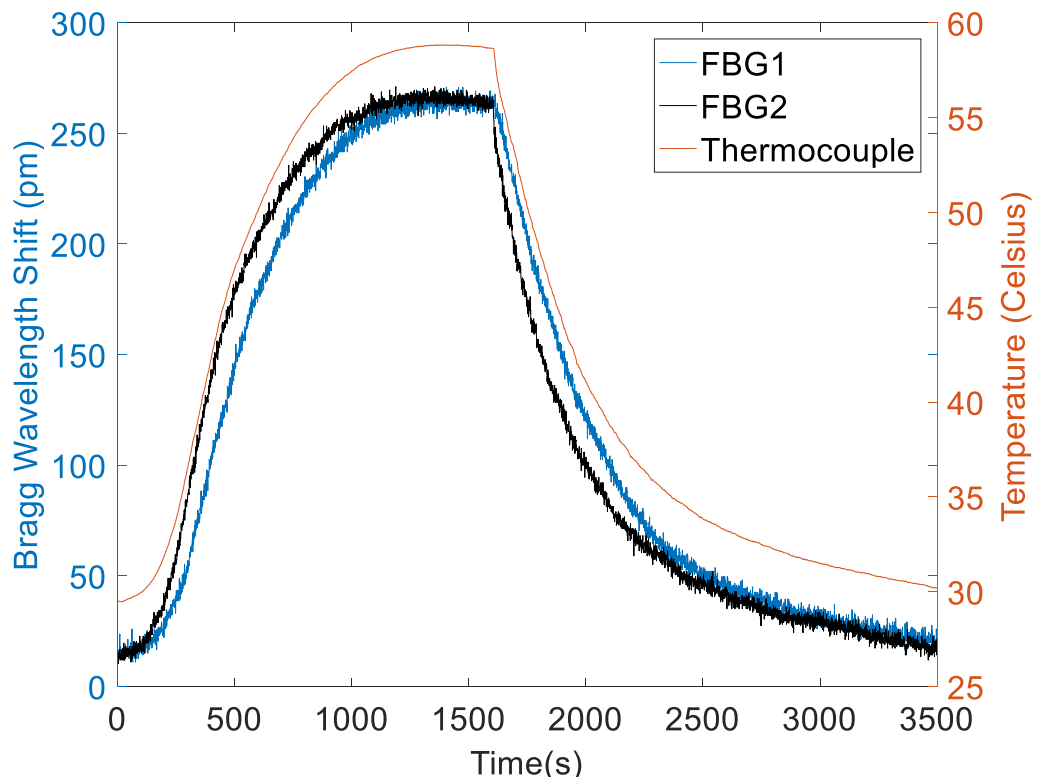


Figure A.5. Temperature response of two bare FBGs (Fifth experiment).

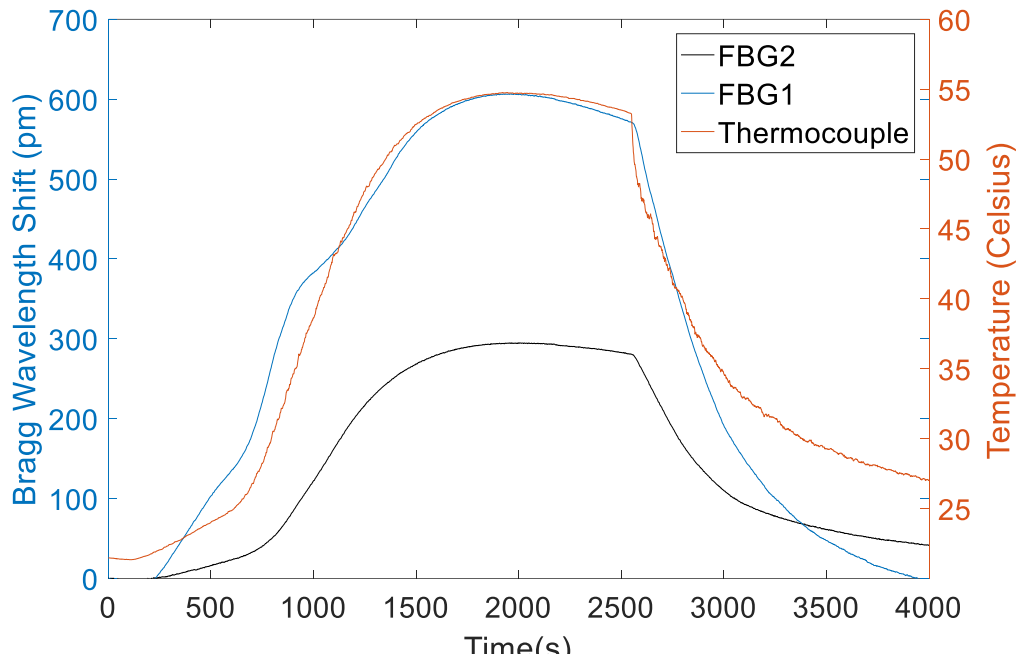


Figure A.6. Temperature response of two housed FBGs (First experiment).

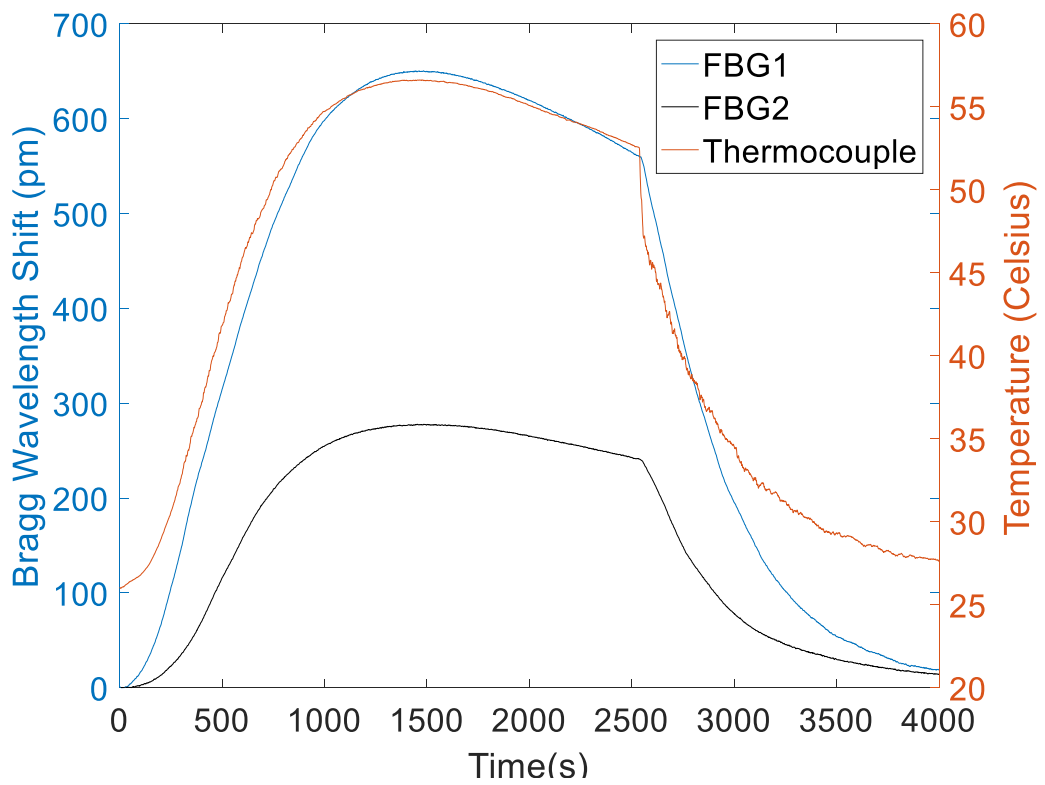


Figure A.7. Temperature response of two housed FBGs (Second experiment).

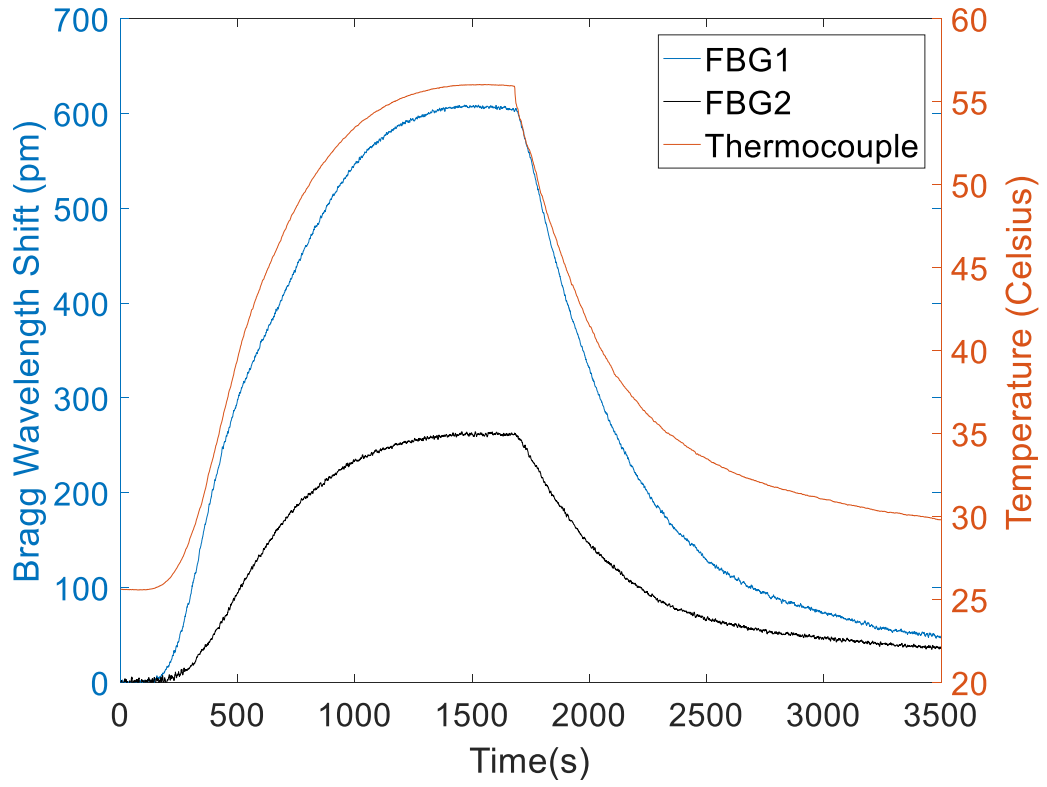


Figure A.8. Temperature response of two housed FBGs (Third experiment).

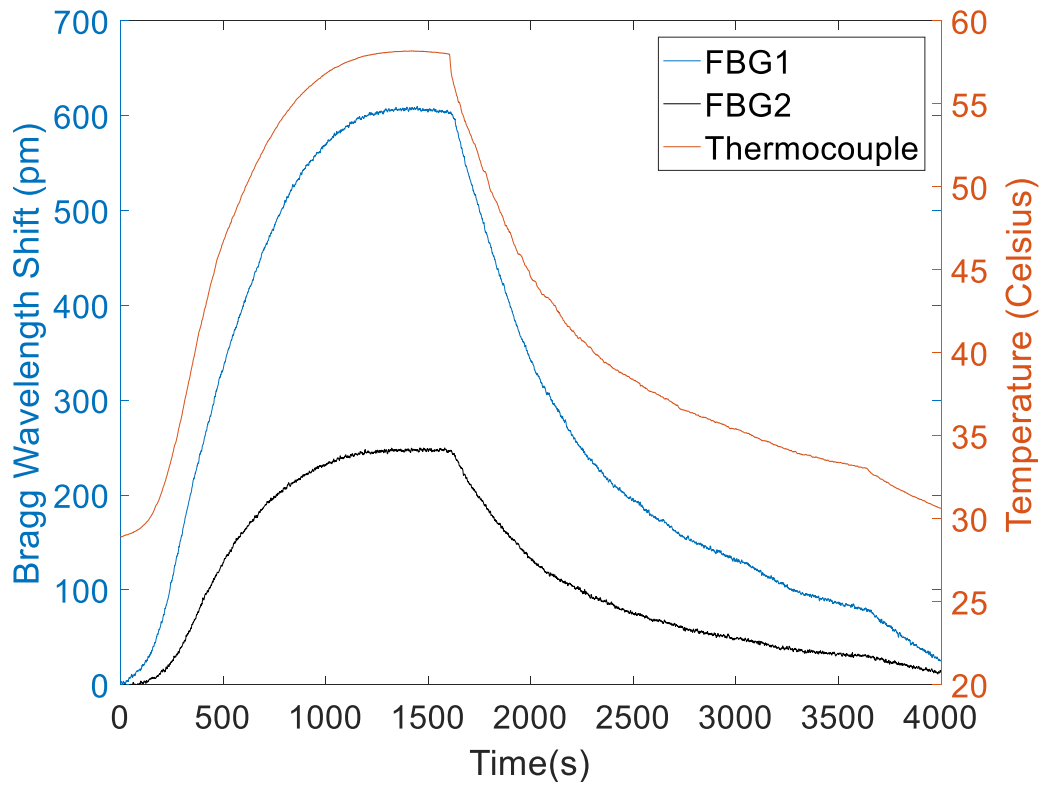


Figure A.9. Temperature response of two housed FBGs (Forth experiment).

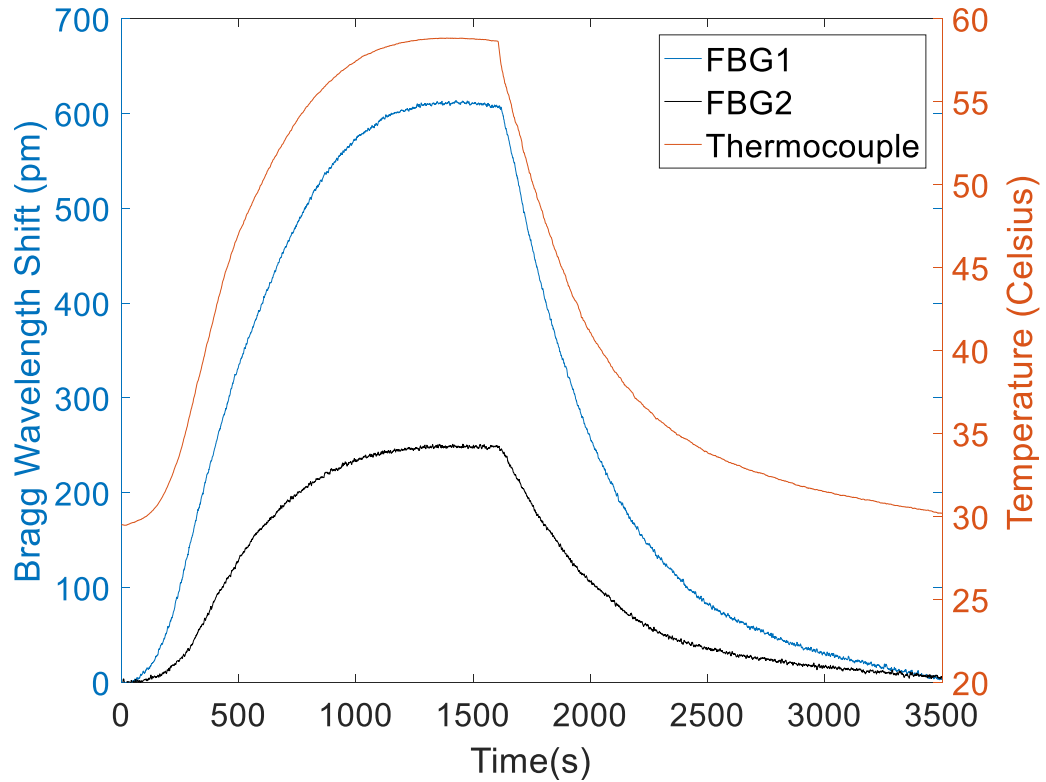


Figure A.10. Temperature response of two housed FBGs (Fifth experiment).

A.2 Pressure Response of the FBG Sensor

For the FBG sensor housed in the patch, the pressure calibration experiment was repeated 3 times in this study which are shown from A11 to A13. From A11 to A13, blue curves are the FBG1 (pressure sensor) output with temperature compensation. External applied contact pressures were measured by a KERN weighing scale which was shown as red line in each figure

For the integrated sensor which combined the FBG sensor and the POF sensor together, the pressure experiment was repeated 3 times in this study which are shown from A14 to A16. From A14 to A16, blue trace in each figure represents the FBG1 output with temperature compensation whilst red line in each figure represents the weighing scale output.

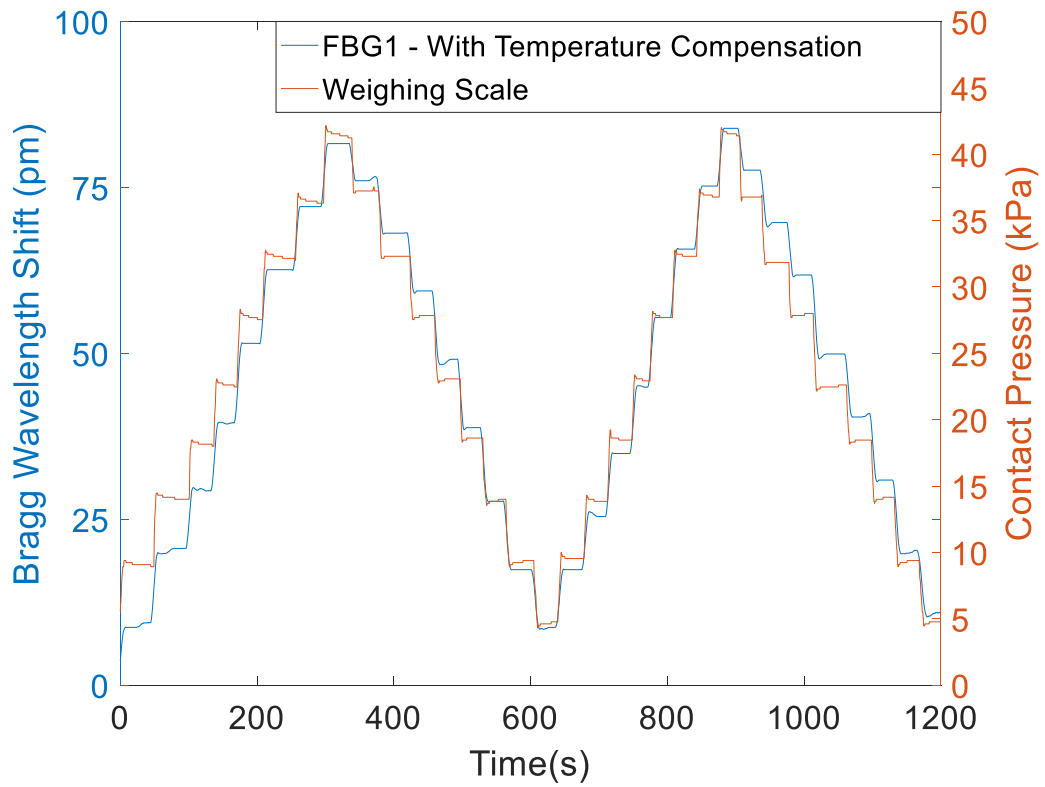


Figure A.11. Pressure response of the housed FBG patch (First experiment).

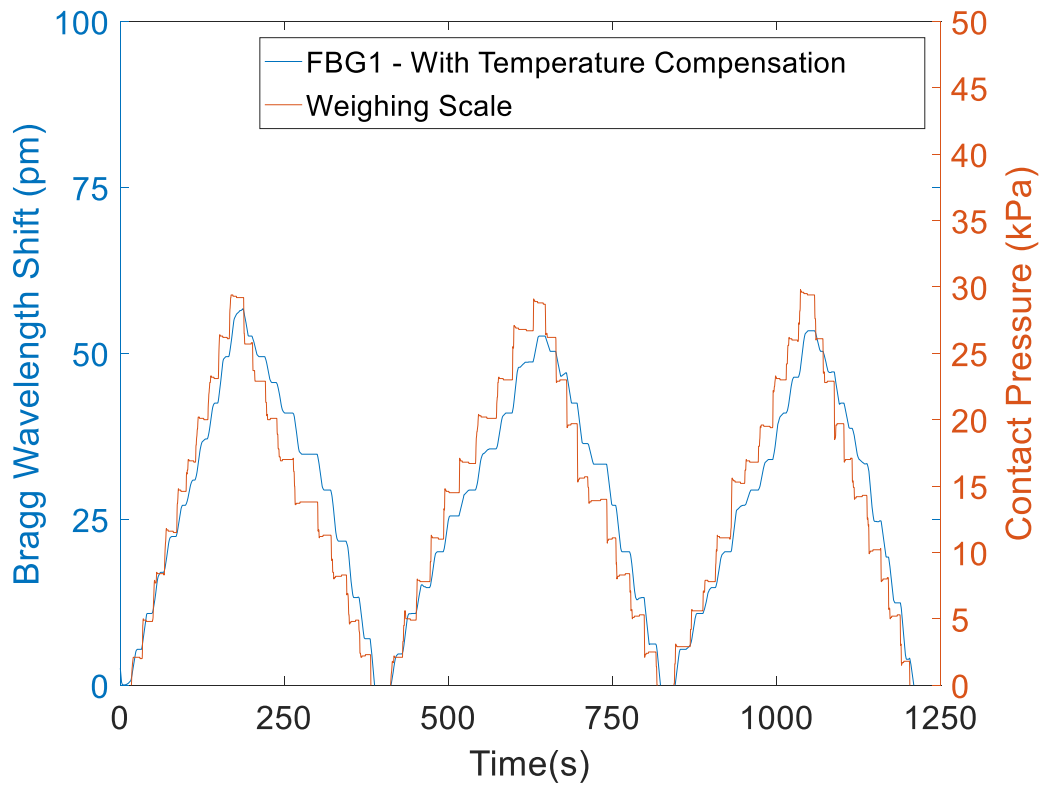


Figure A.12. Pressure response of the housed FBG patch (Second experiment).

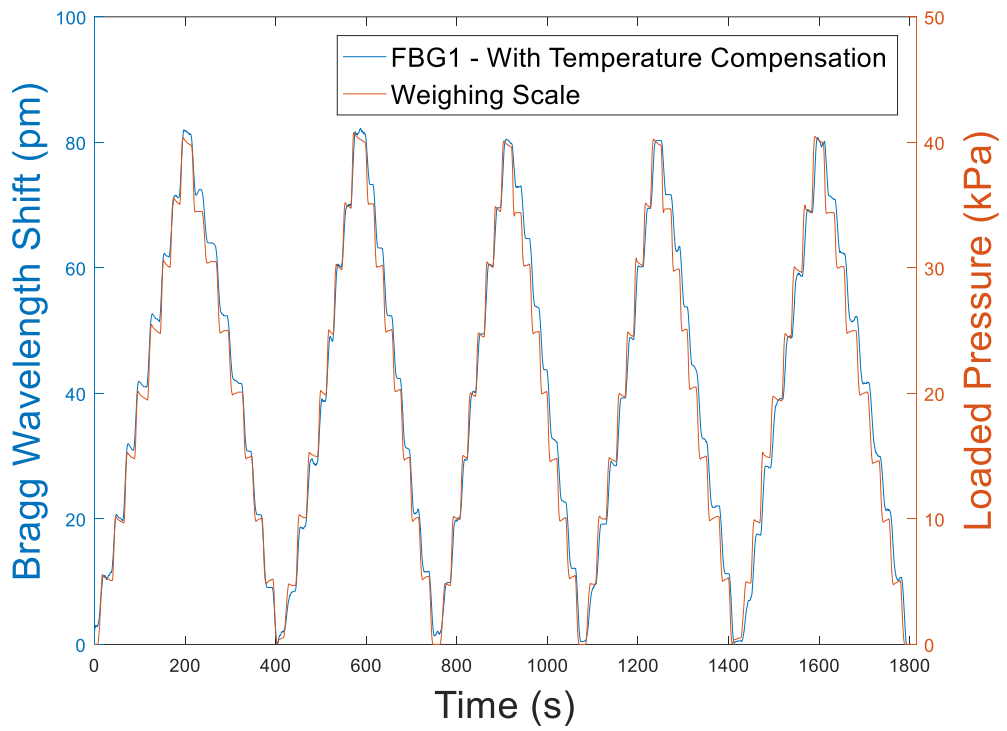


Figure A.13. Pressure response of the housed FBG patch (Third experiment).

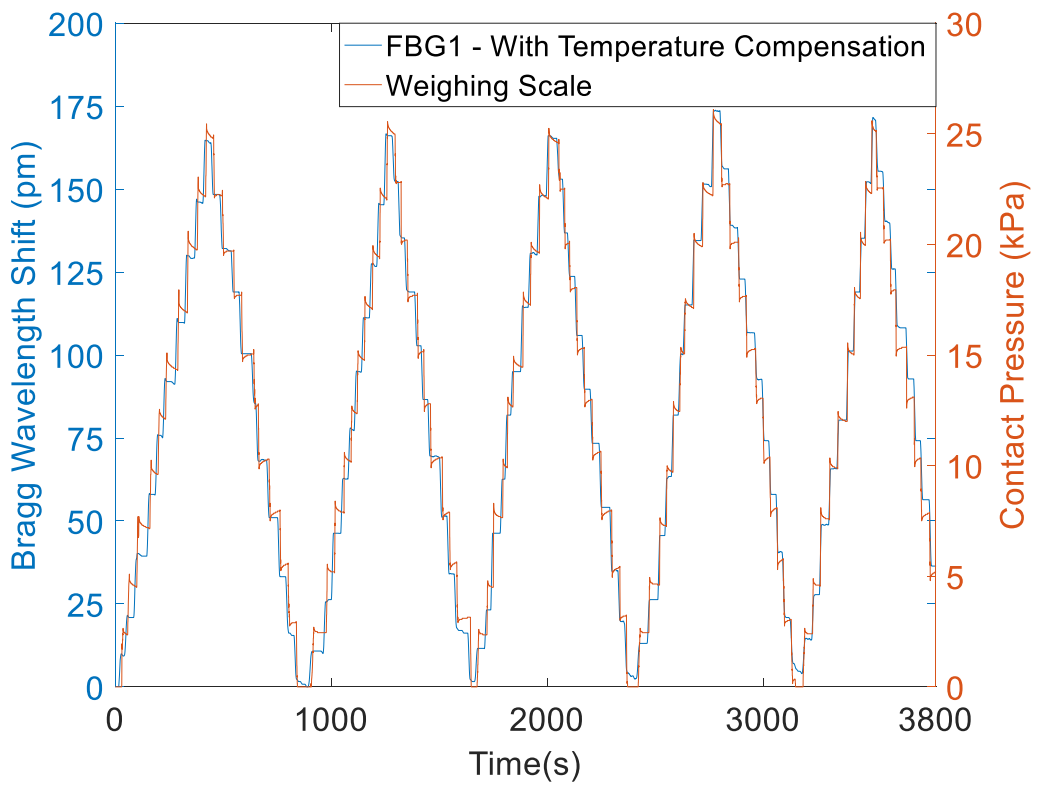


Figure A.14. Pressure response of the integrated sensor (First experiment).

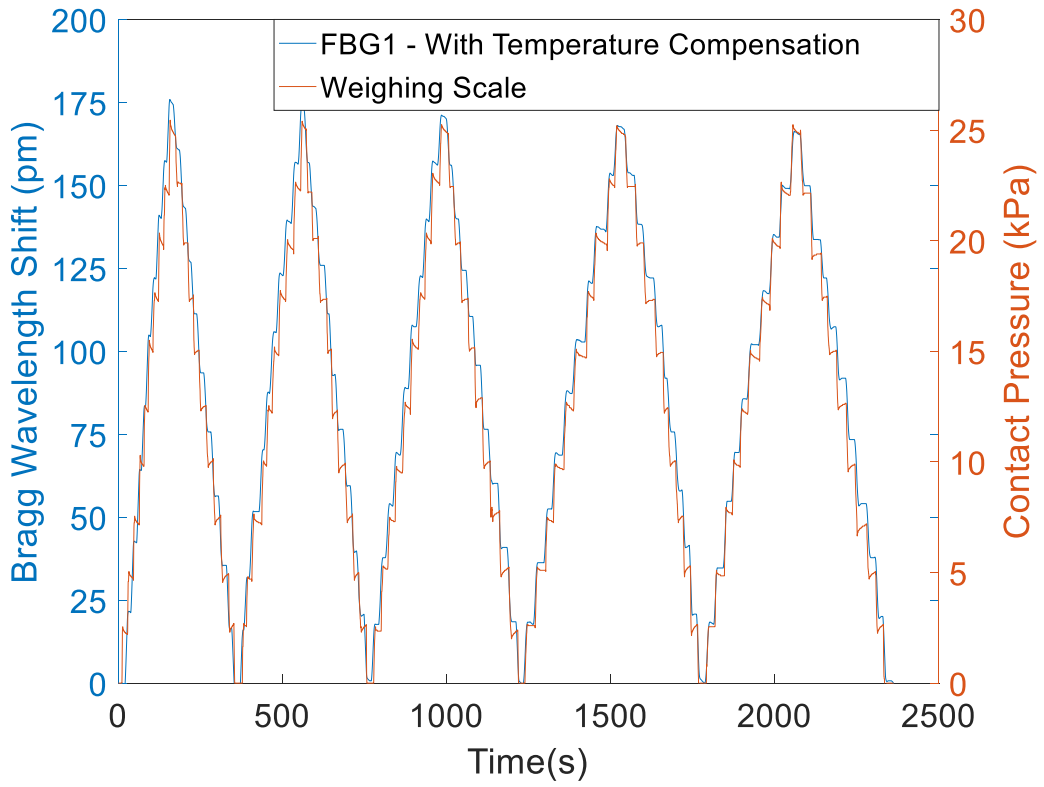


Figure A.15. Pressure response of the integrated sensor (Second experiment).

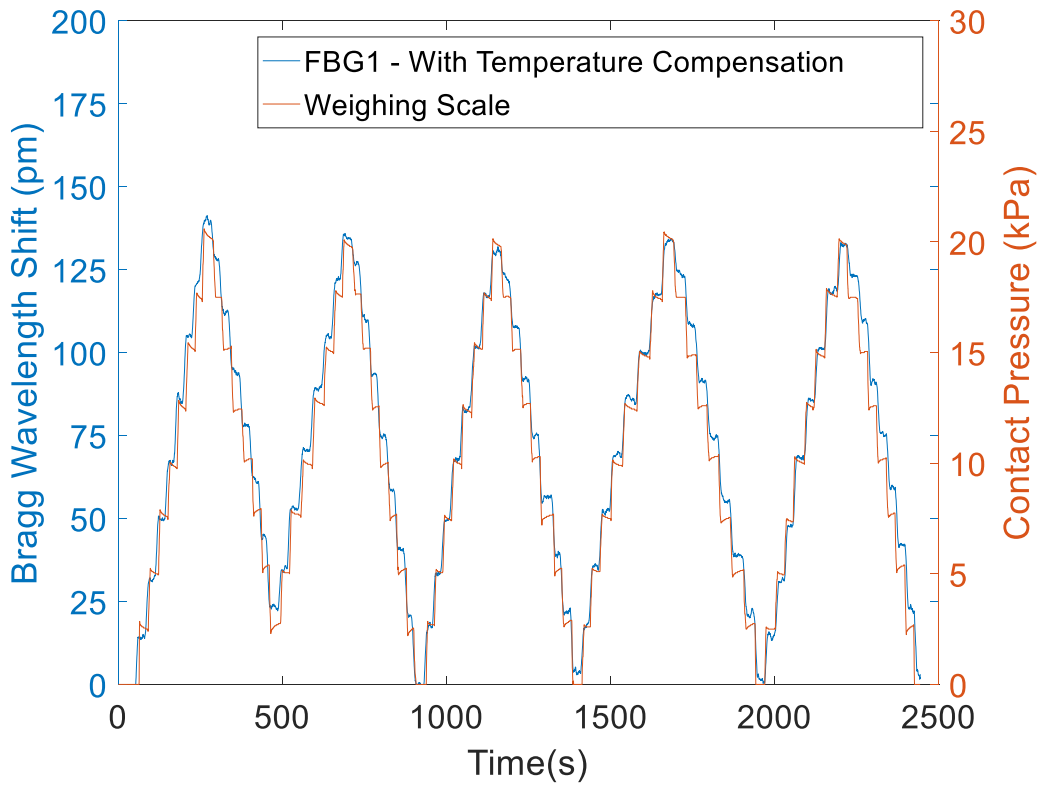


Figure A.16. Pressure response of the integrated sensor (Third experiment).

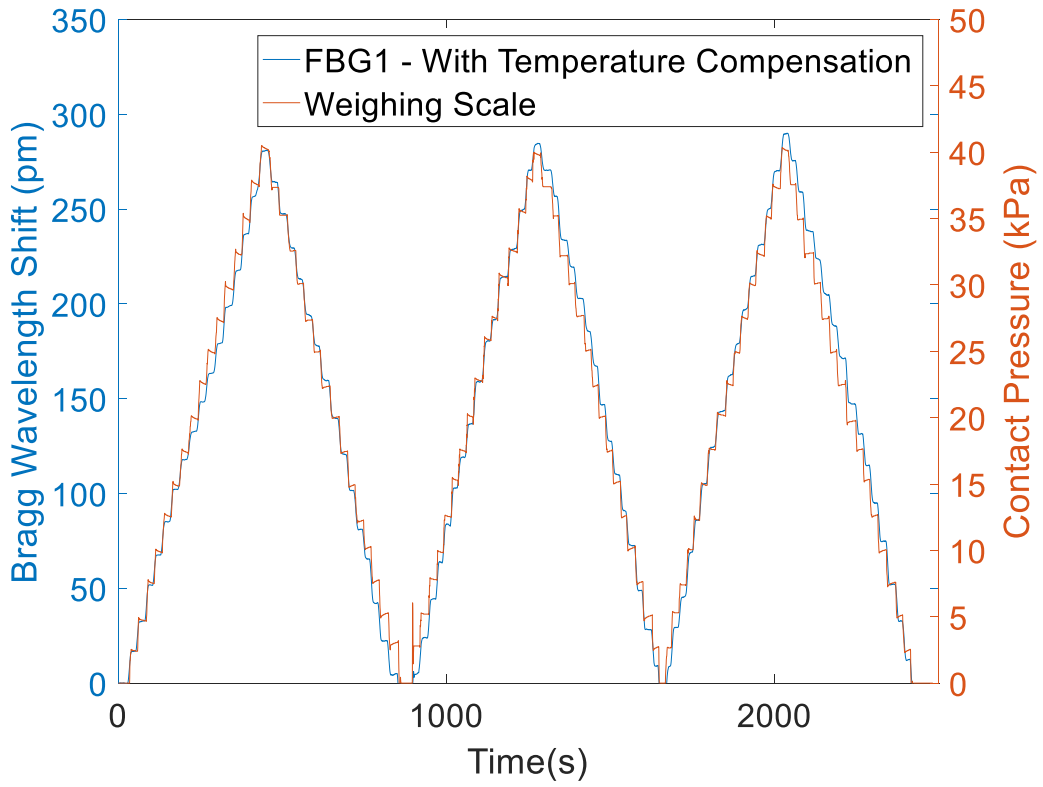


Figure A.17. Pressure response of the integrated sensor (Forth experiment).

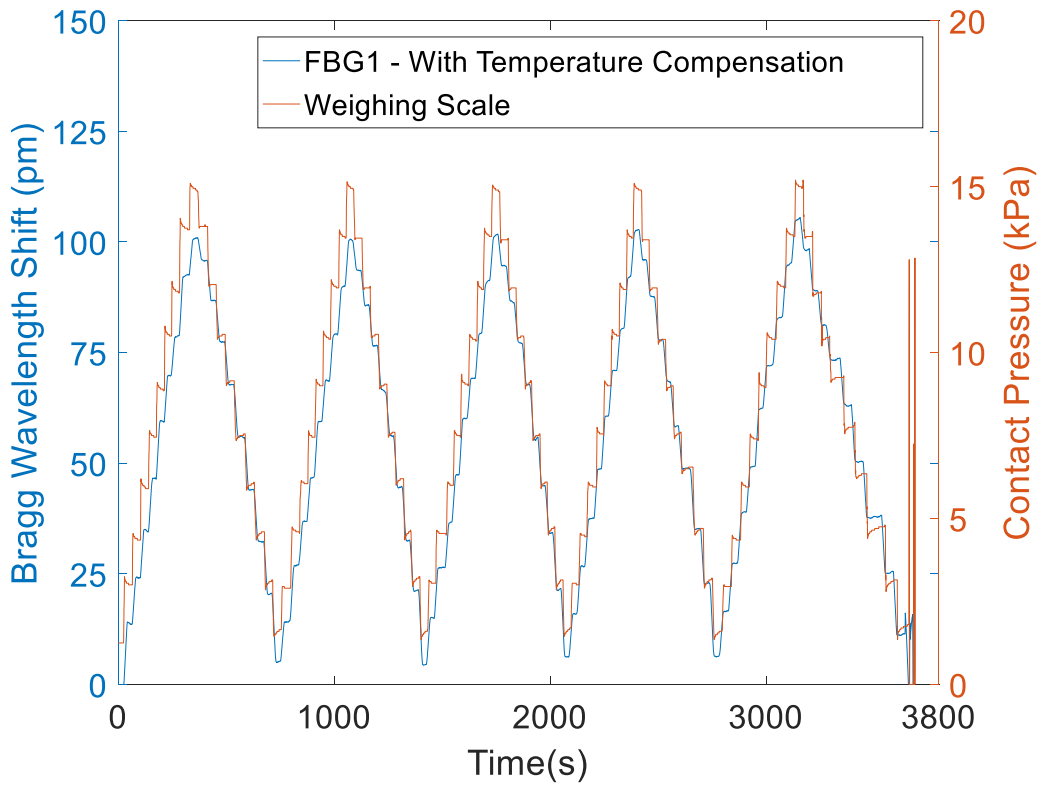


Figure A.18. Pressure response of the integrated sensor (Fifth experiment).

Appendix B

Performance of Electronic Components in the Analogue Front-End

M660F1 Spectrum

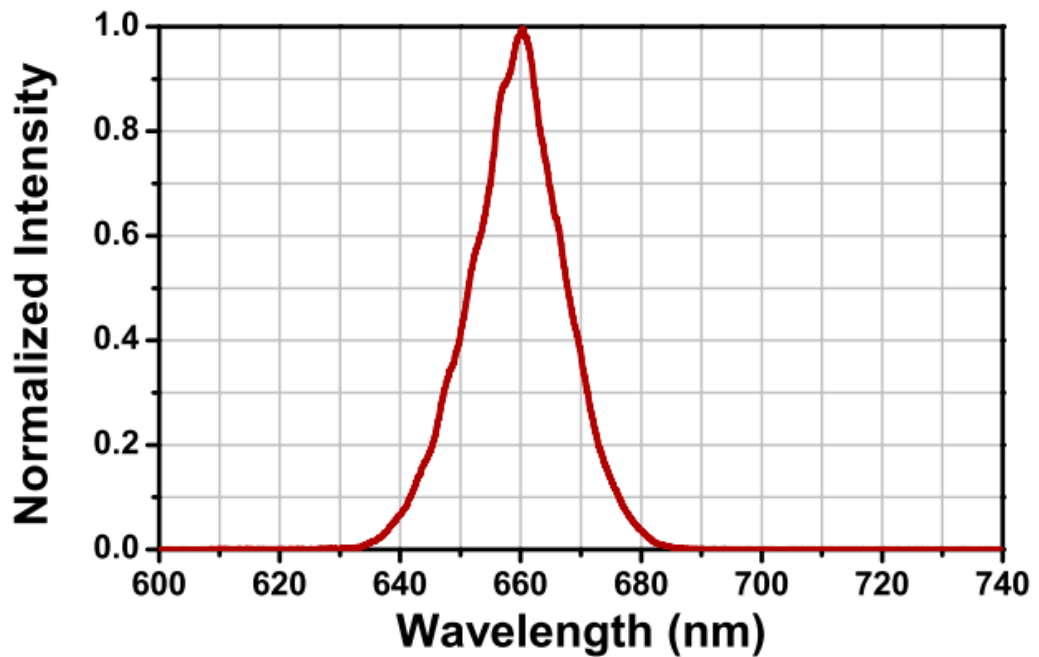


Figure B.1. Normalised intensity spectrum of Red LED (660 nm) [119].

M850F2 Spectrum

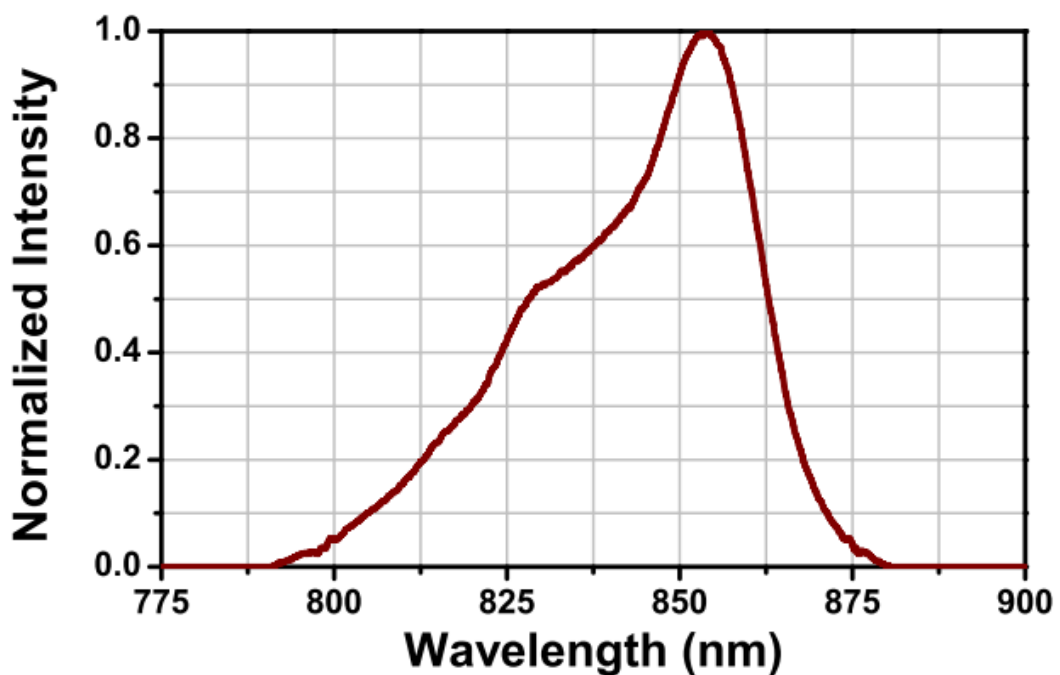


Figure B.2. Normalised intensity spectrum of Infrared LED (850 nm) [120].

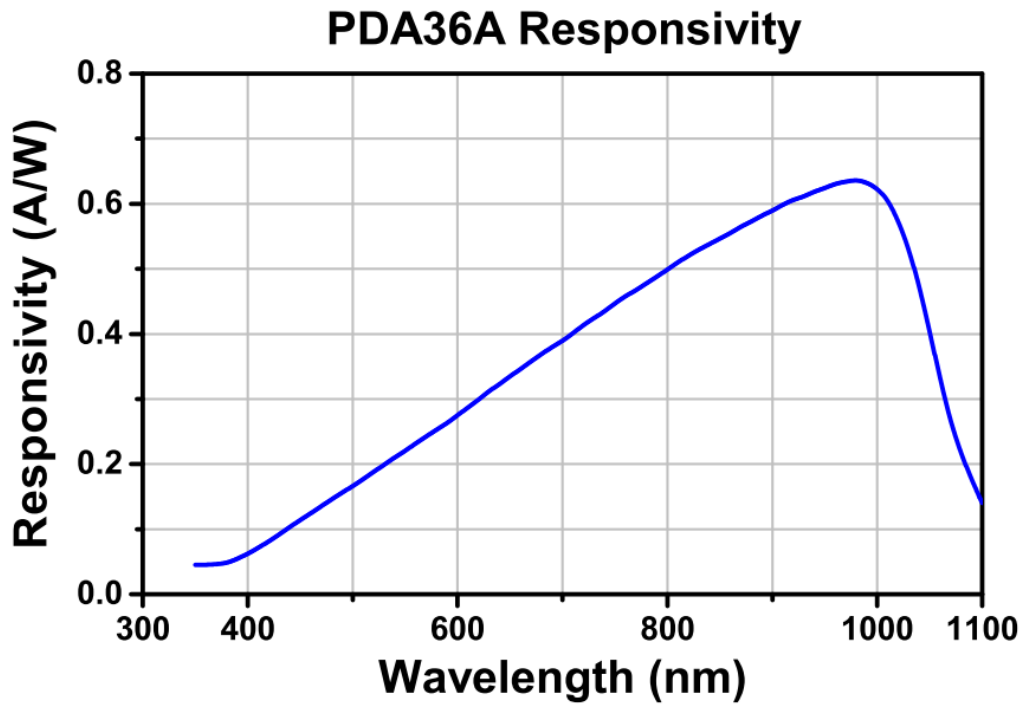


Figure B.3. Response curve of the PIN photo diode (PDA-36A) [122].

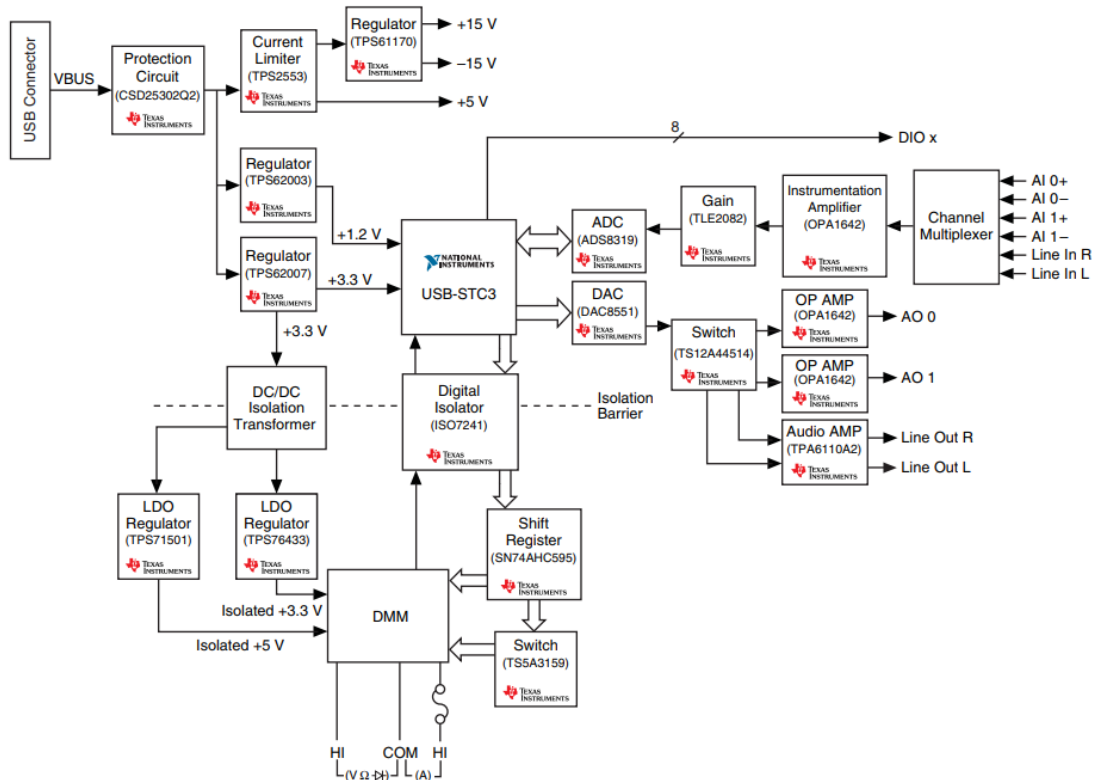


Figure B.4. Arrangement of NI myDAQ subsystem (components may be changed or substituted) [123].

Appendix C

In Vivo Experiments Results

C.1 Pulse Oximetry Sensor Calibration

The designed pulse oximetry sensor was used to measure subjects' S_{pO_2} value when they were stay still or holding breath. A commercial pulse oximeter (Masimo Radical-7) was applied to verify the reliability of the designed pulse oximetry sensor. C1 to C14 present the experiment results of measuring S_{pO_2} of 14 volunteers when they breathed normally and sat quietly. C11 to C20 are the test results of measuring S_{pO_2} of 14 volunteers with desaturation activities. Blue line in each figure is the output of the designed pulse oximetry sensor whilst red line in each figure represents the output of the Masimo device.

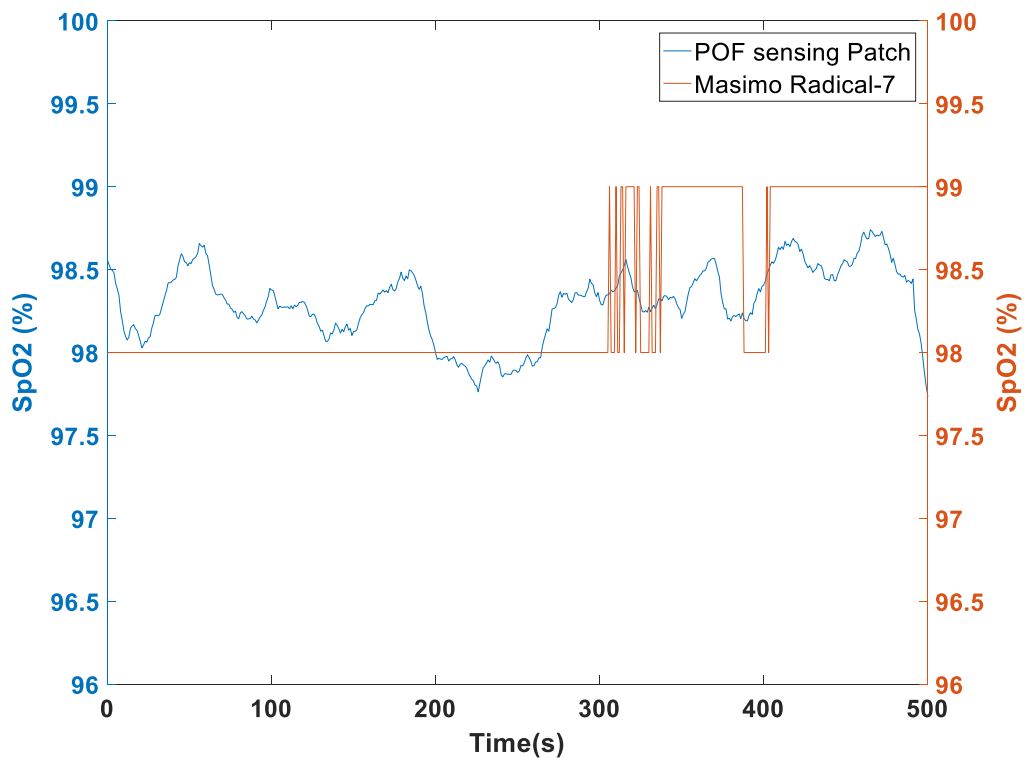


Figure C.1. Comparison of POF sensing patch with commercial pulse oximeter (First experiment).

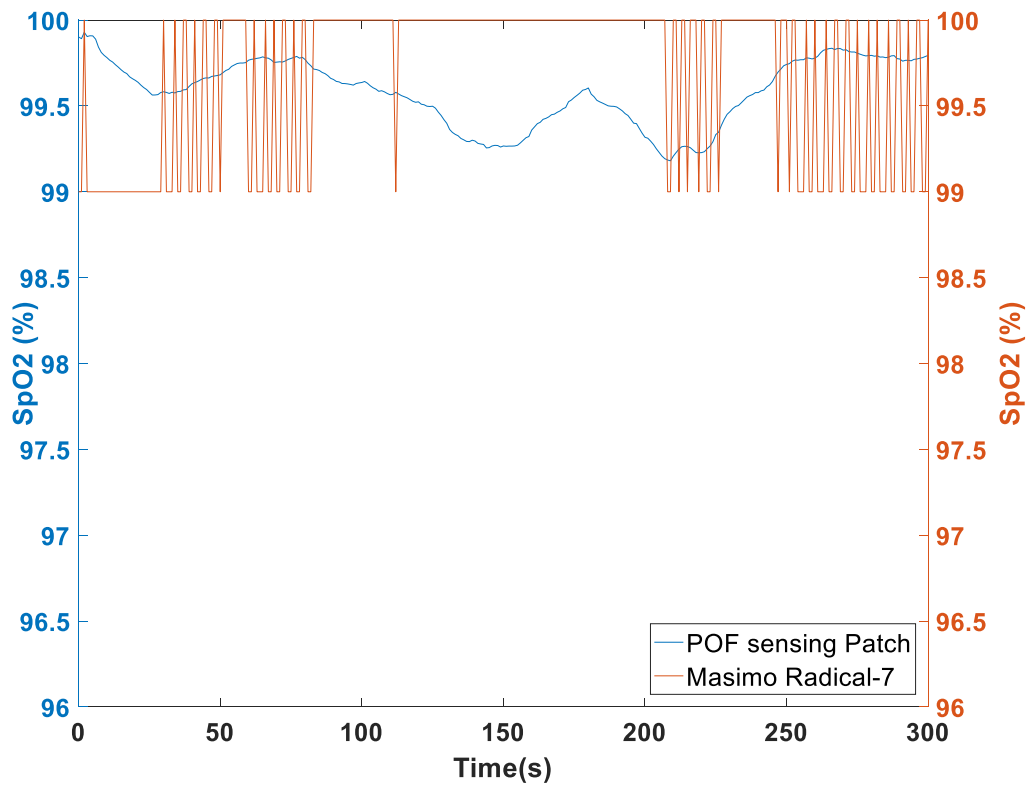


Figure C.2. Comparison of POF sensing patch with commercial pulse oximeter (Second experiment).

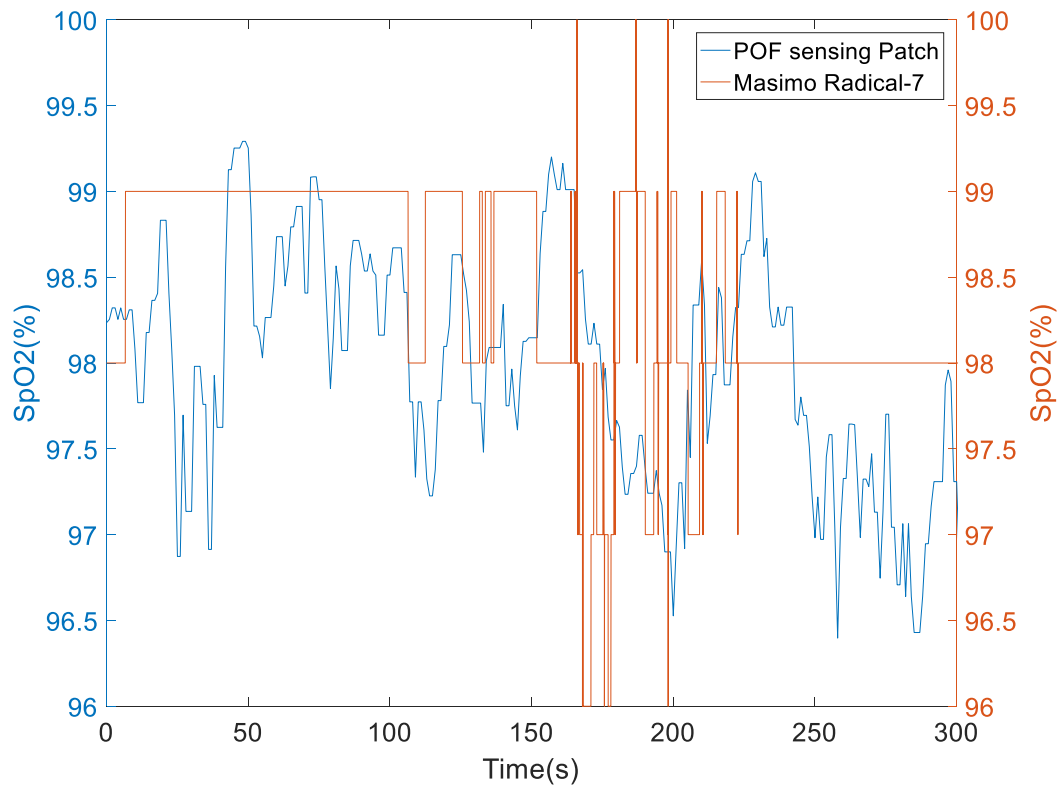


Figure C.3. Comparison of POF sensing patch with commercial pulse oximeter (Third experiment).

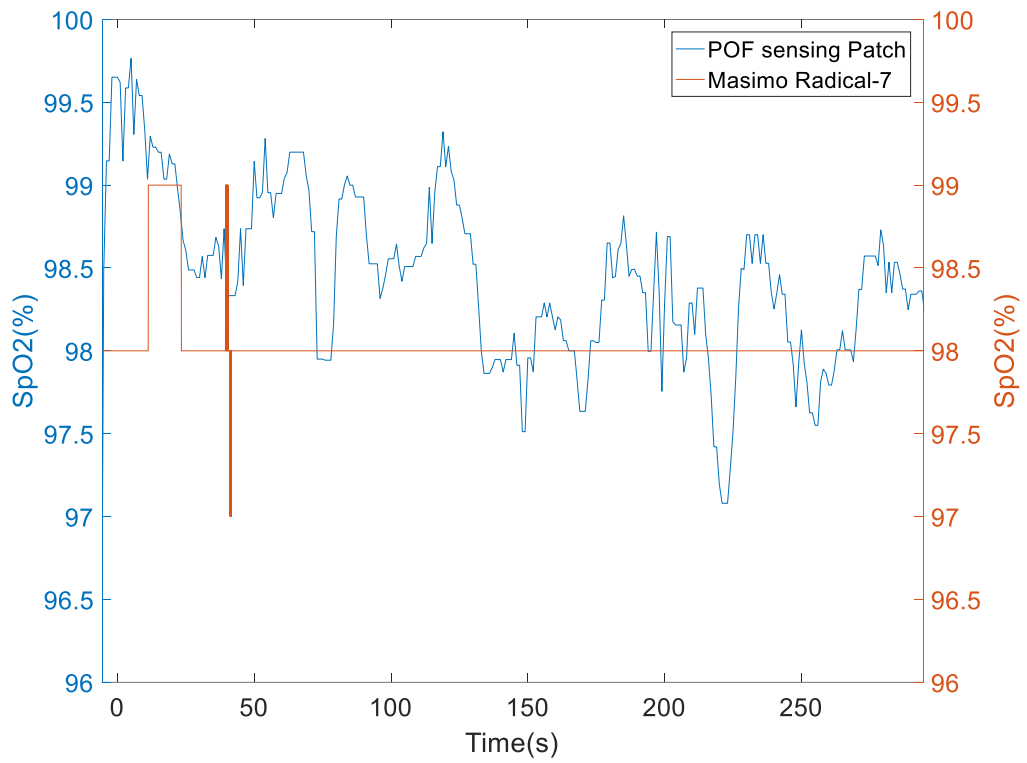


Figure C.4. Comparison of POF sensing patch with commercial pulse oximeter (Forth experiment).

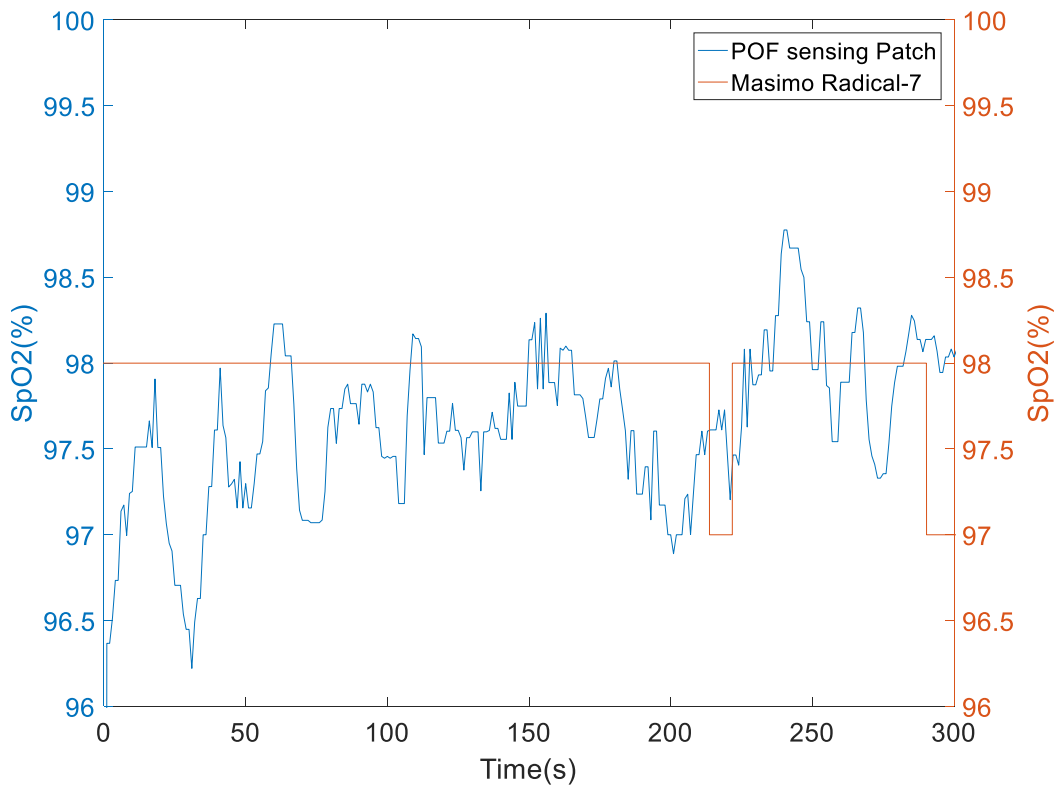


Figure C.5. Comparison of POF sensing patch with commercial pulse oximeter (Fifth experiment).

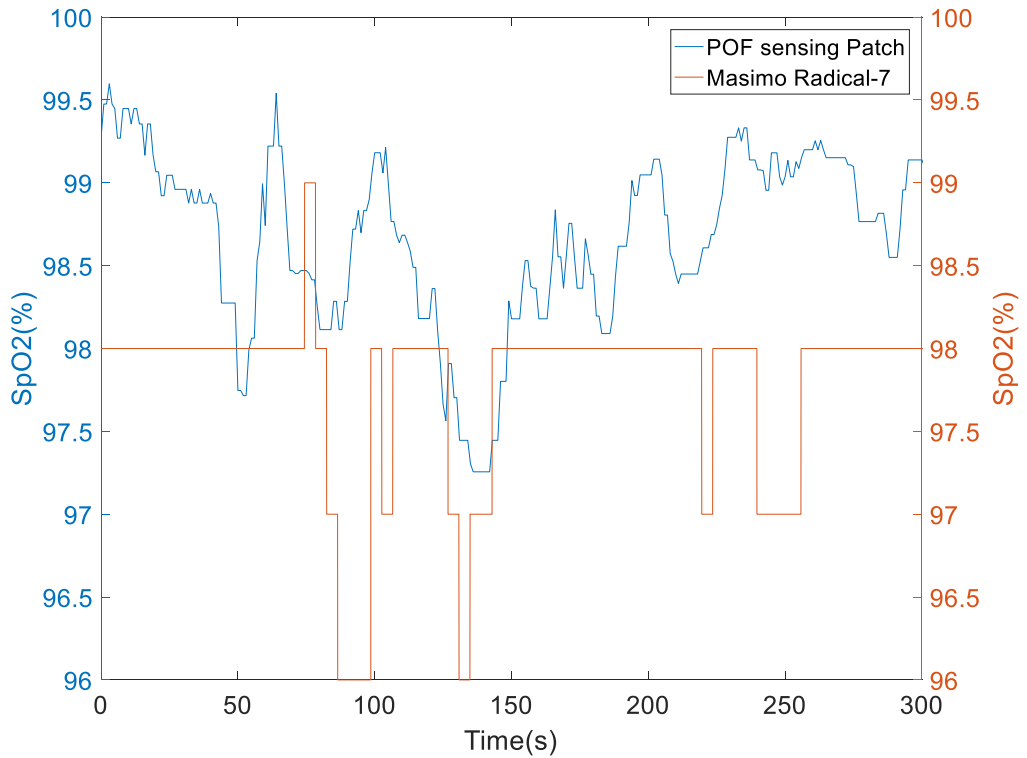


Figure C.6. Comparison of POF sensing patch with commercial pulse oximeter (Sixth experiment).

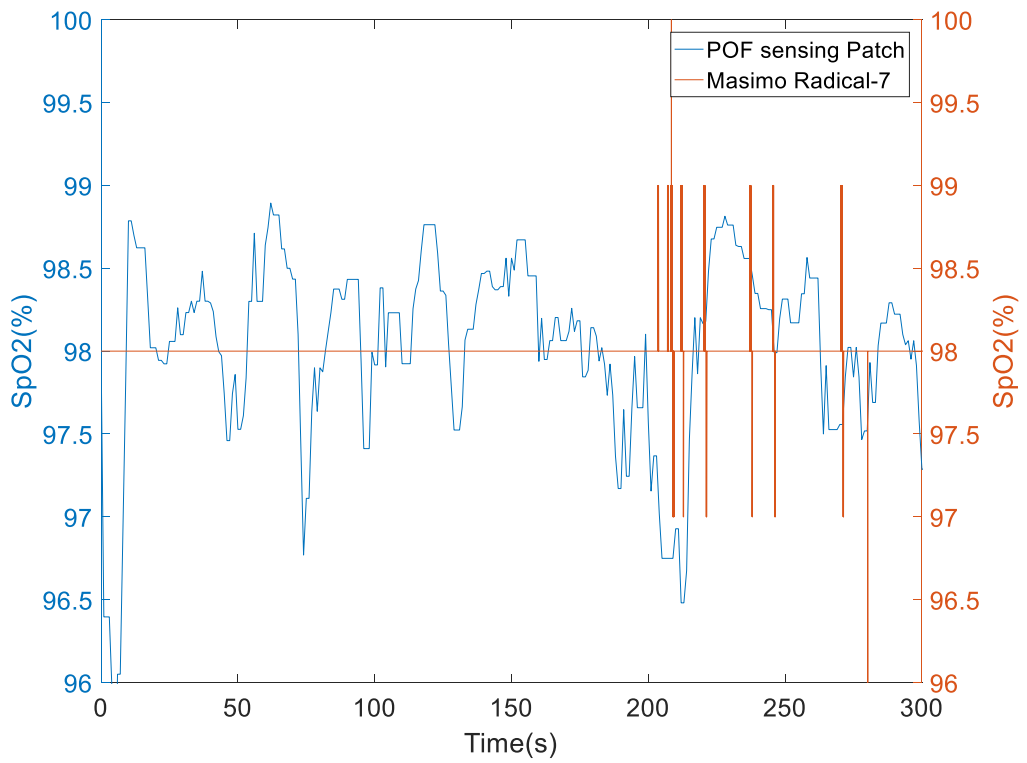


Figure C.7. Comparison of POF sensing patch with commercial pulse oximeter (Seventh experiment).

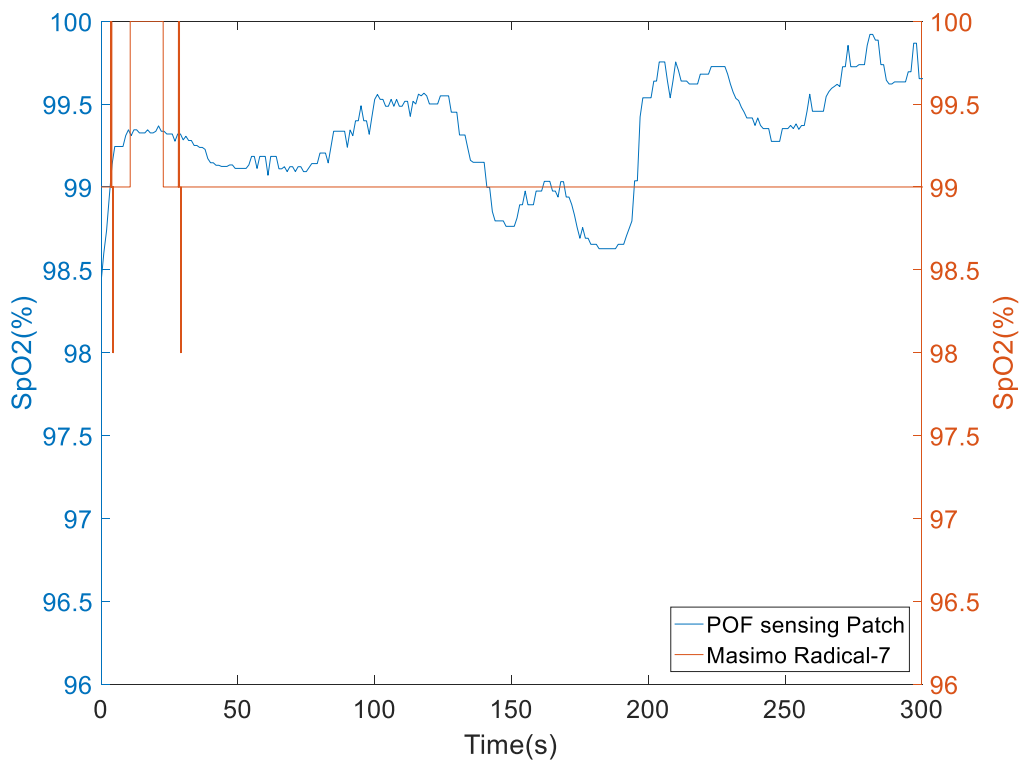


Figure C.8. Comparison of POF sensing patch with commercial pulse oximeter (Eighth experiment).

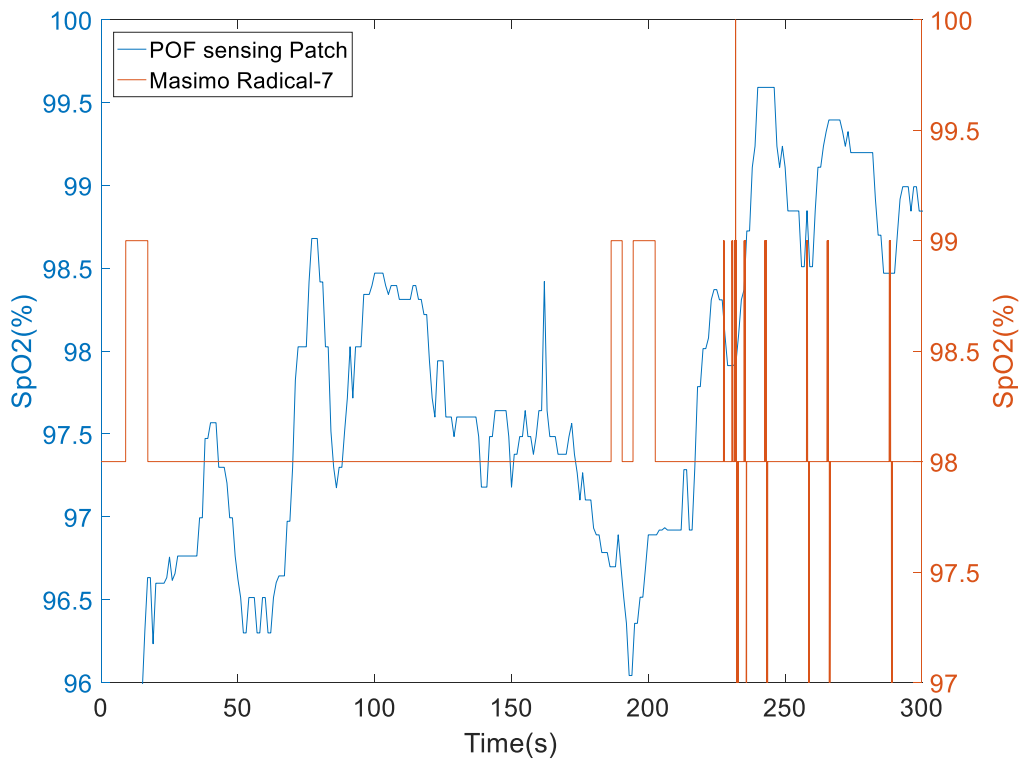


Figure C.9. Comparison of POF sensing patch with commercial pulse oximeter (Ninth experiment).

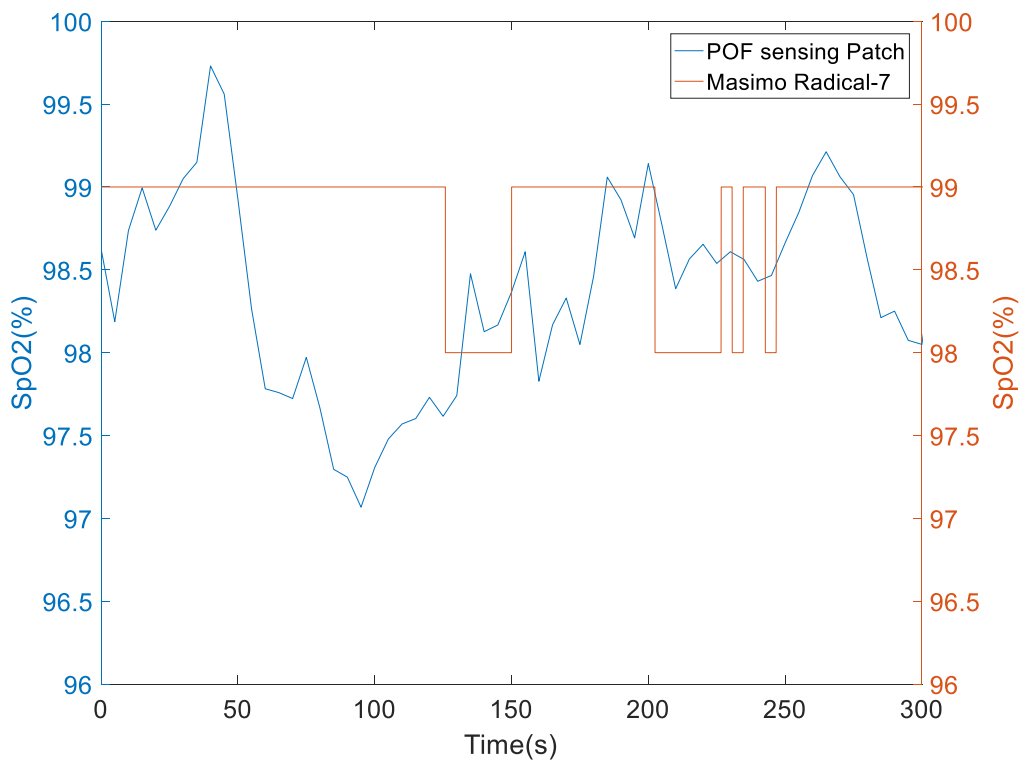


Figure C.10. Comparison of POF sensing patch with commercial pulse oximeter (Tenth experiment).

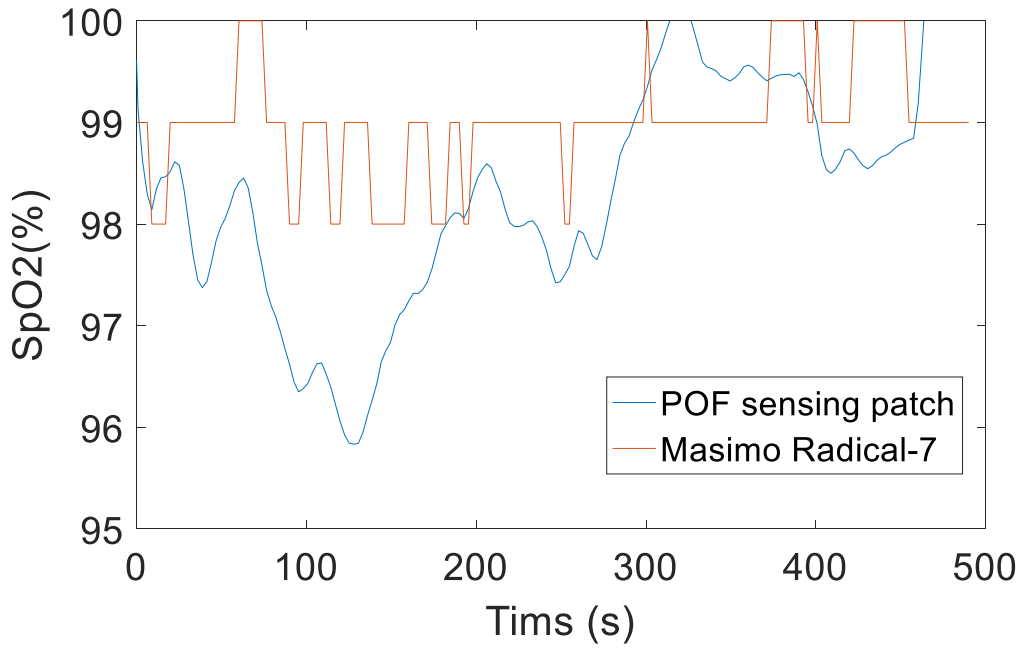


Figure C.11. Comparison of POF sensing patch with commercial pulse oximeter (Eleventh experiment).

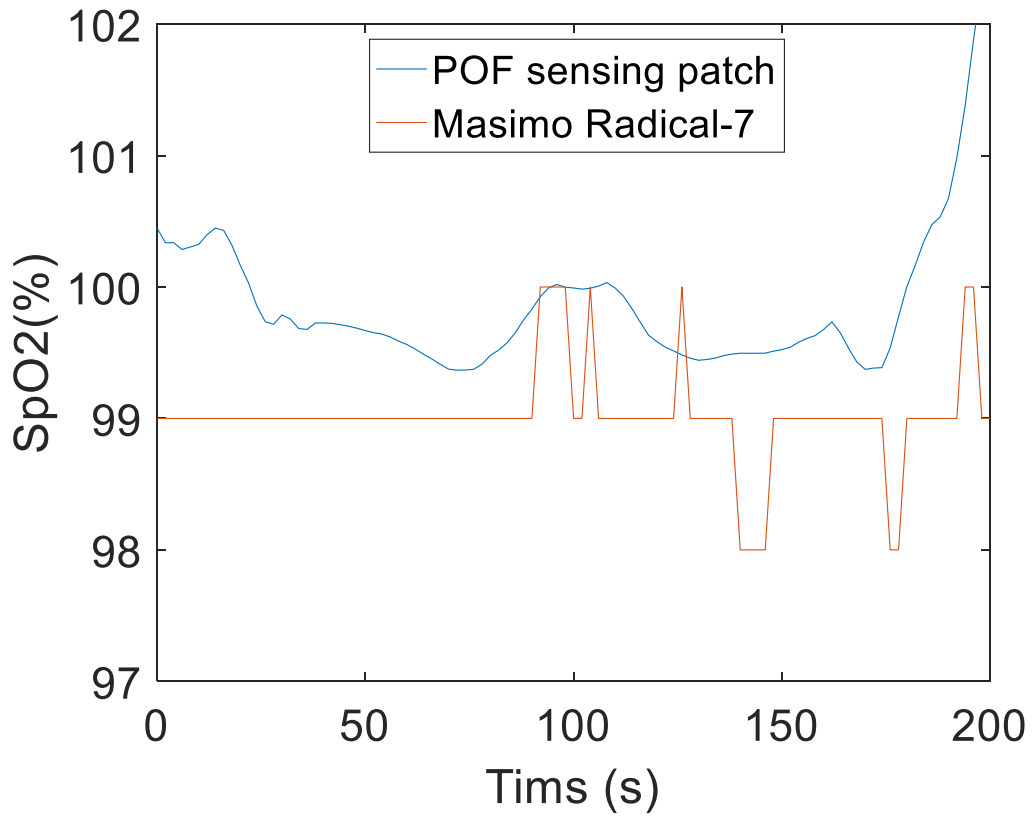


Figure C.12. Comparison of POF sensing patch with commercial pulse oximeter (Twelveth experiment).

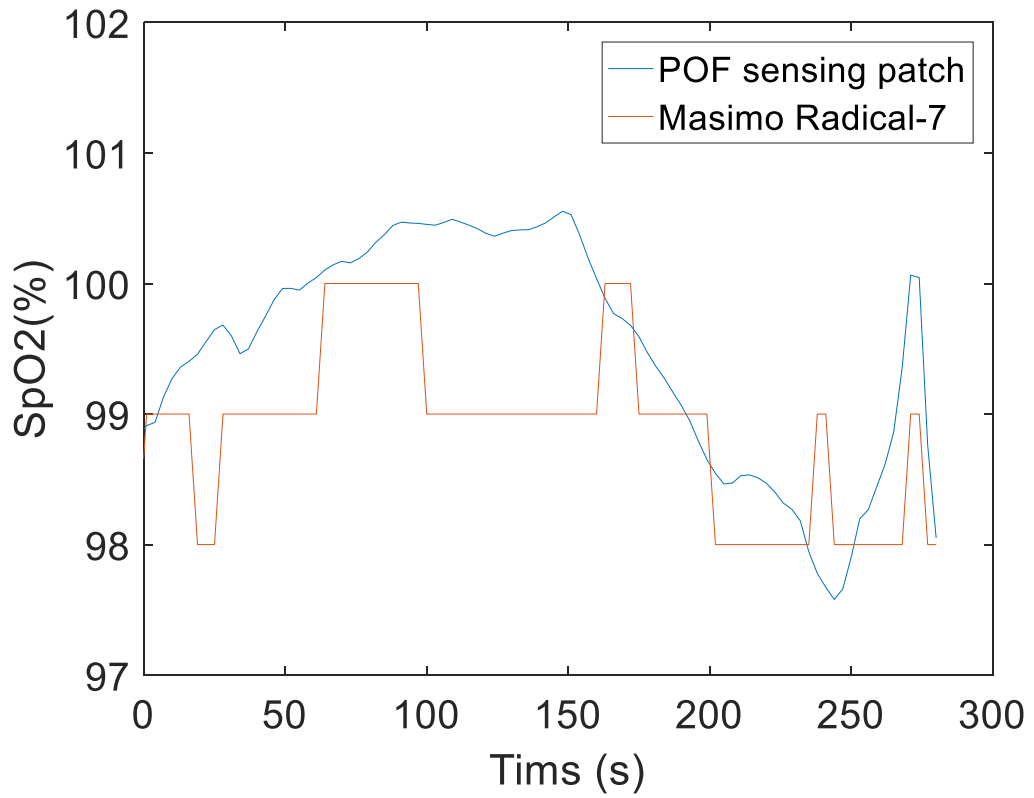


Figure C.13. Comparison of POF sensing patch with commercial pulse oximeter (Twelveth experiment).

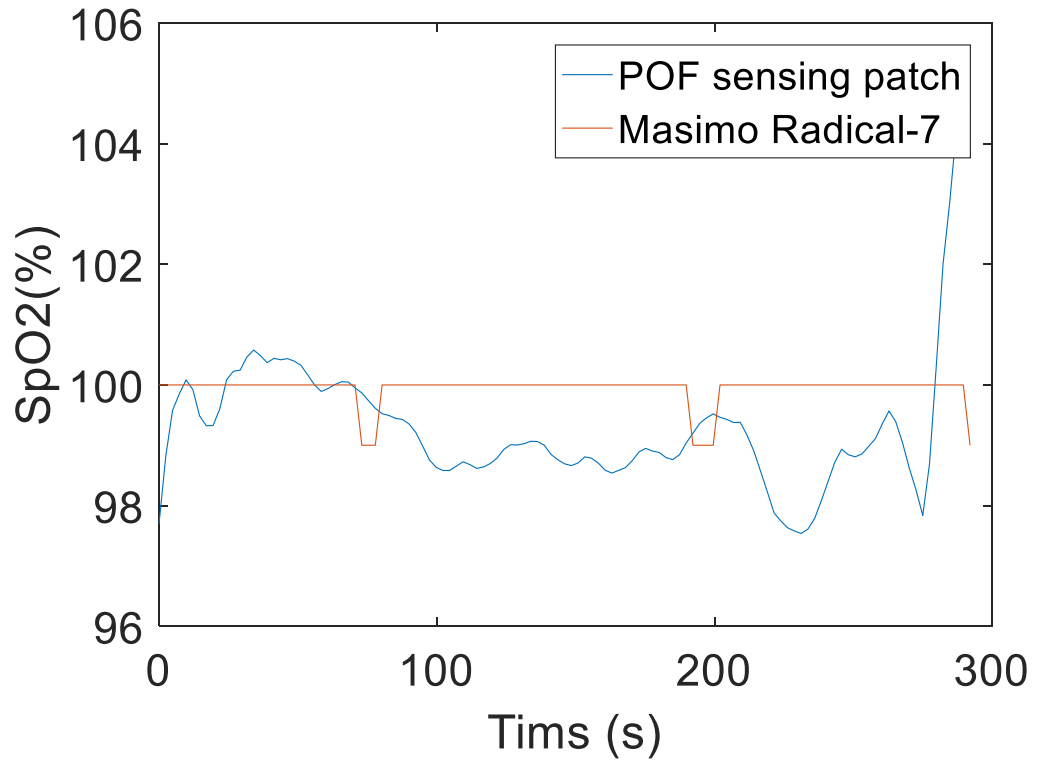


Figure C.14. Comparison of POF sensing patch with commercial pulse oximeter (Twelveth experiment).

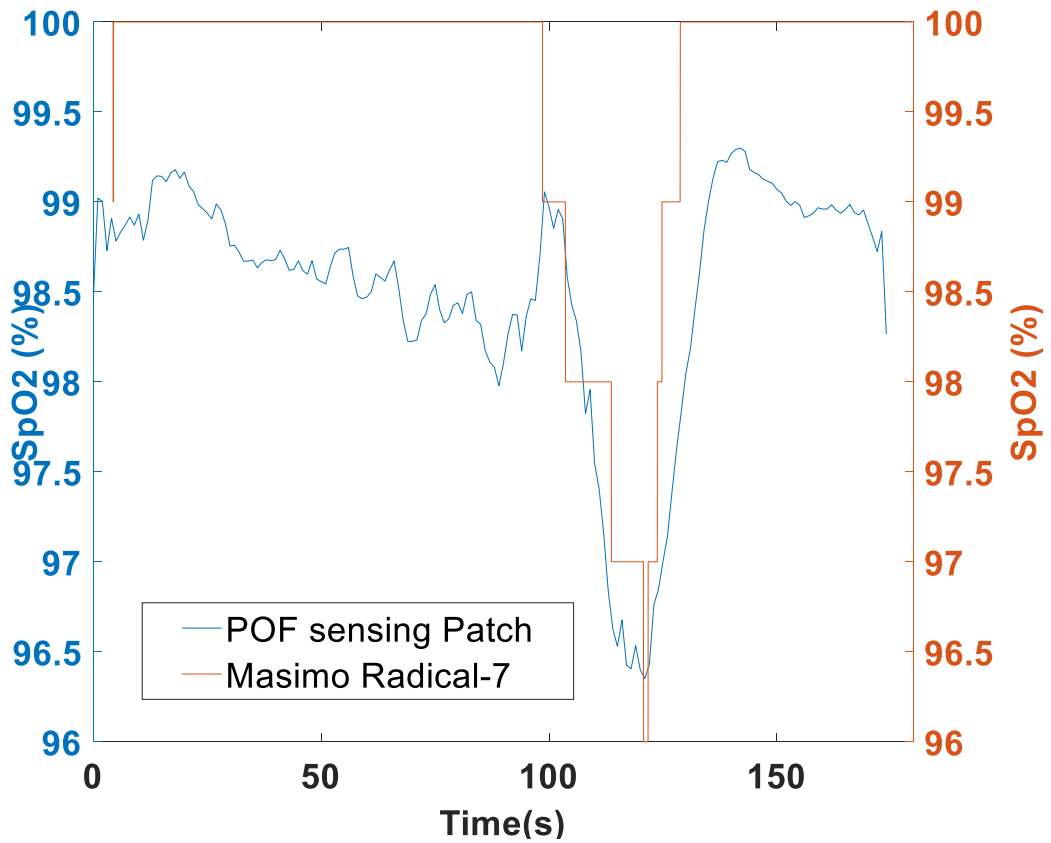


Figure C.15. Comparison of POF sensing patch with commercial pulse oximeter for induced deoxygenation event (First experiment).

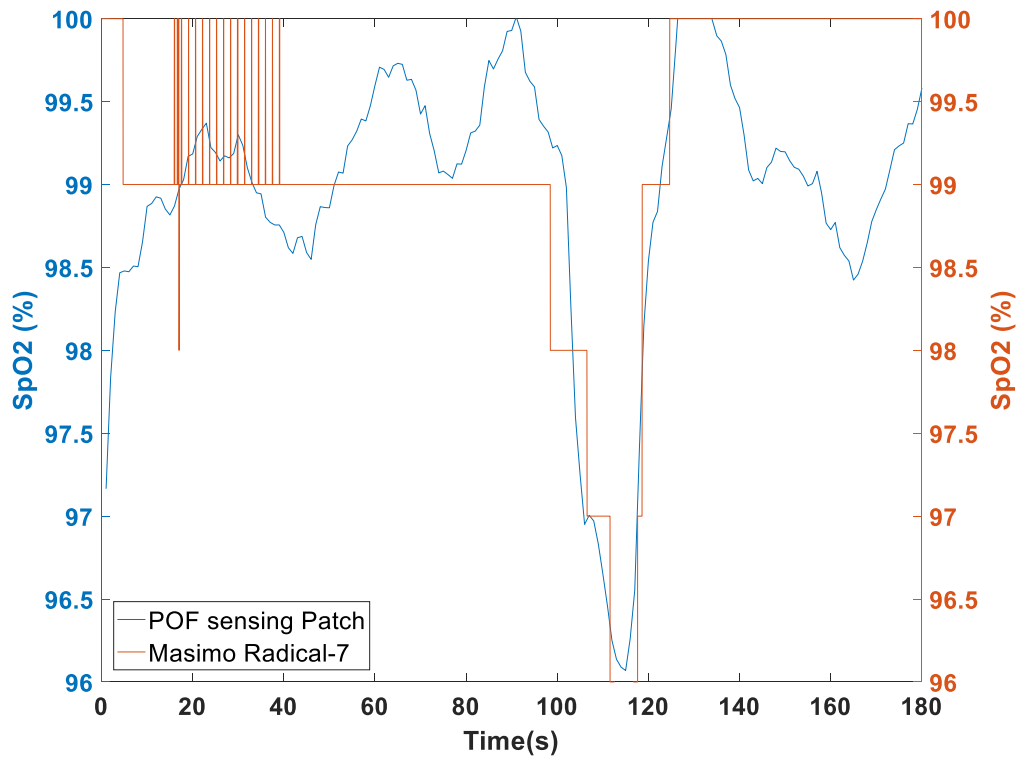


Figure C.16. Comparison of POF sensing patch with commercial pulse oximeter for induced deoxygenation event (Second experiment).

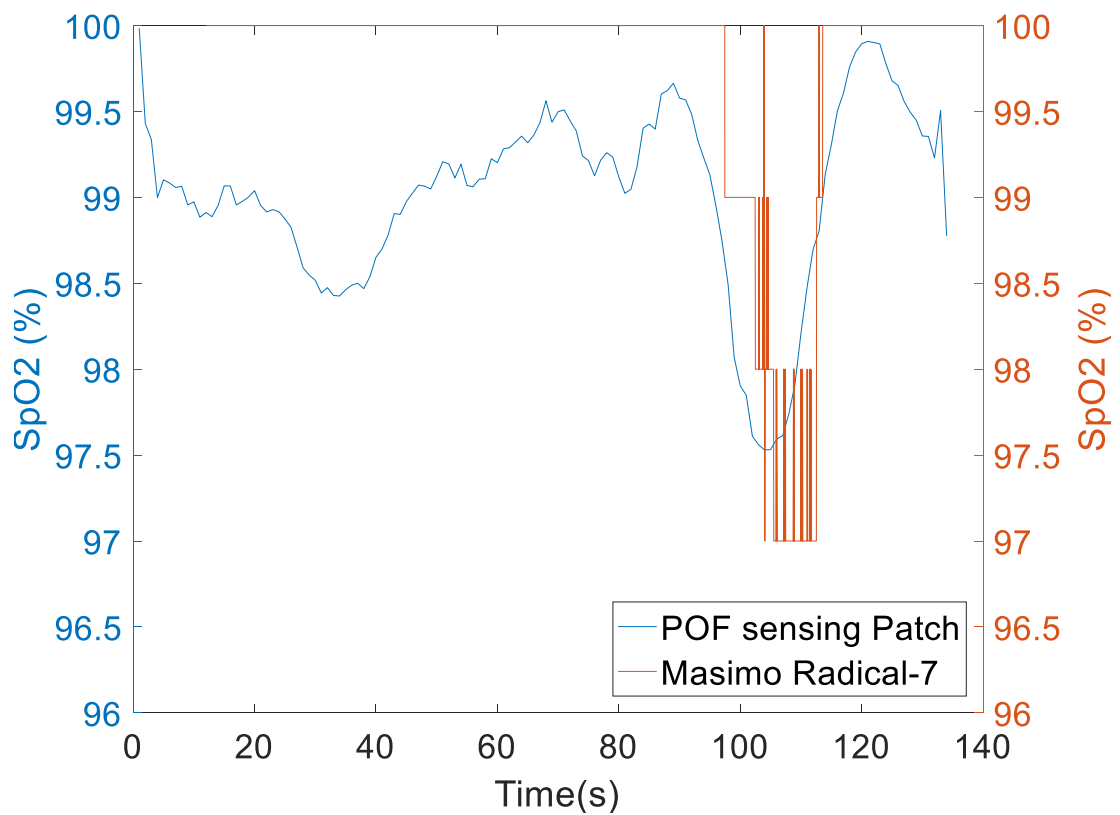


Figure C.17. Comparison of POF sensing patch with commercial pulse oximeter for induced deoxygenation event (Third experiment).

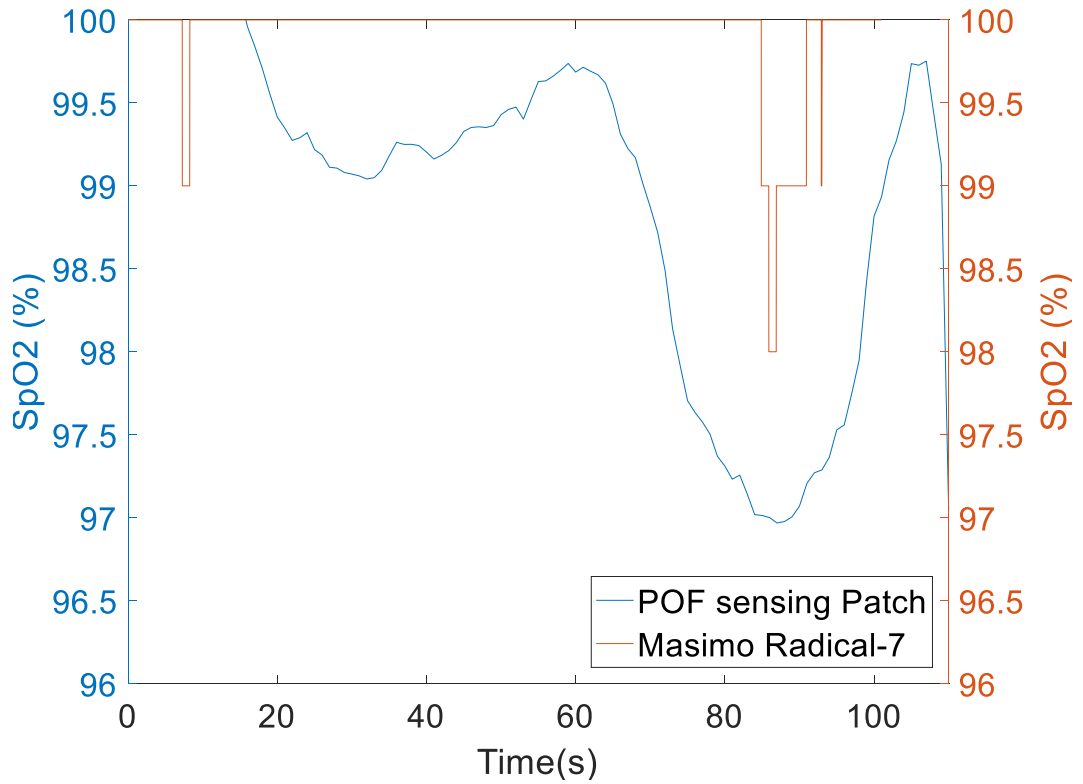


Figure C.18. Comparison of POF sensing patch with commercial pulse oximeter for induced deoxygenation event (Forth experiment).

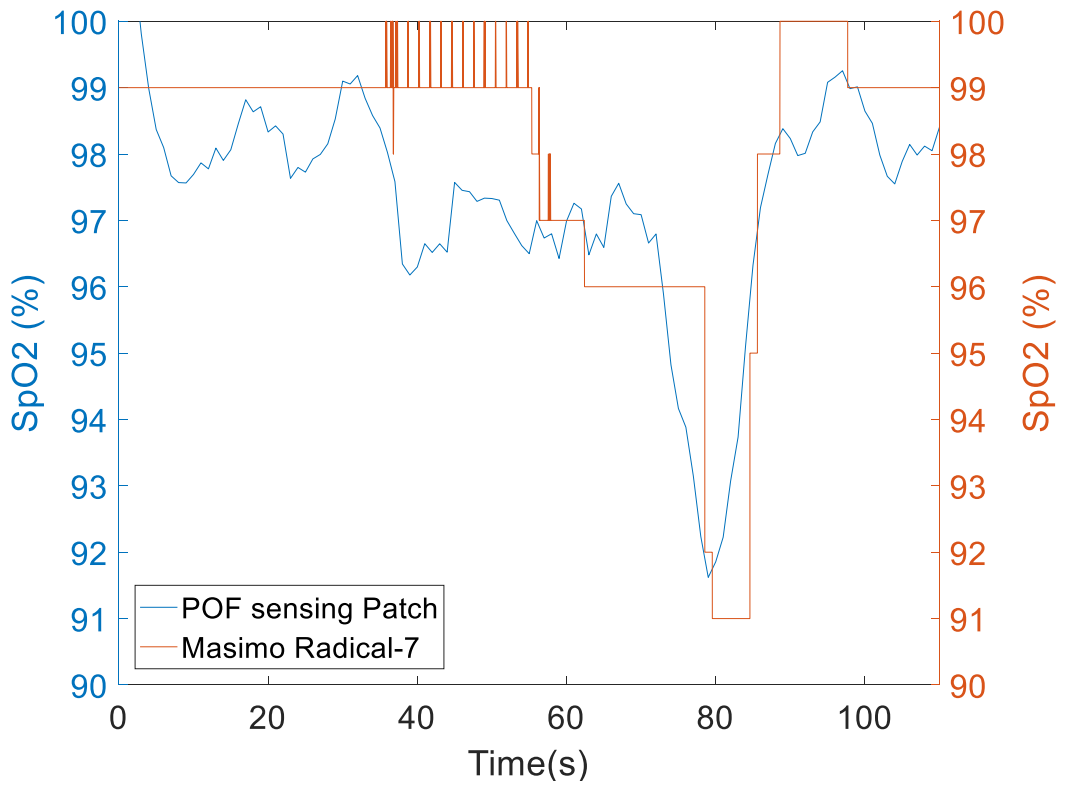


Figure C.19. Comparison of POF sensing patch with commercial pulse oximeter for induced deoxygenation event (Fifth experiment).

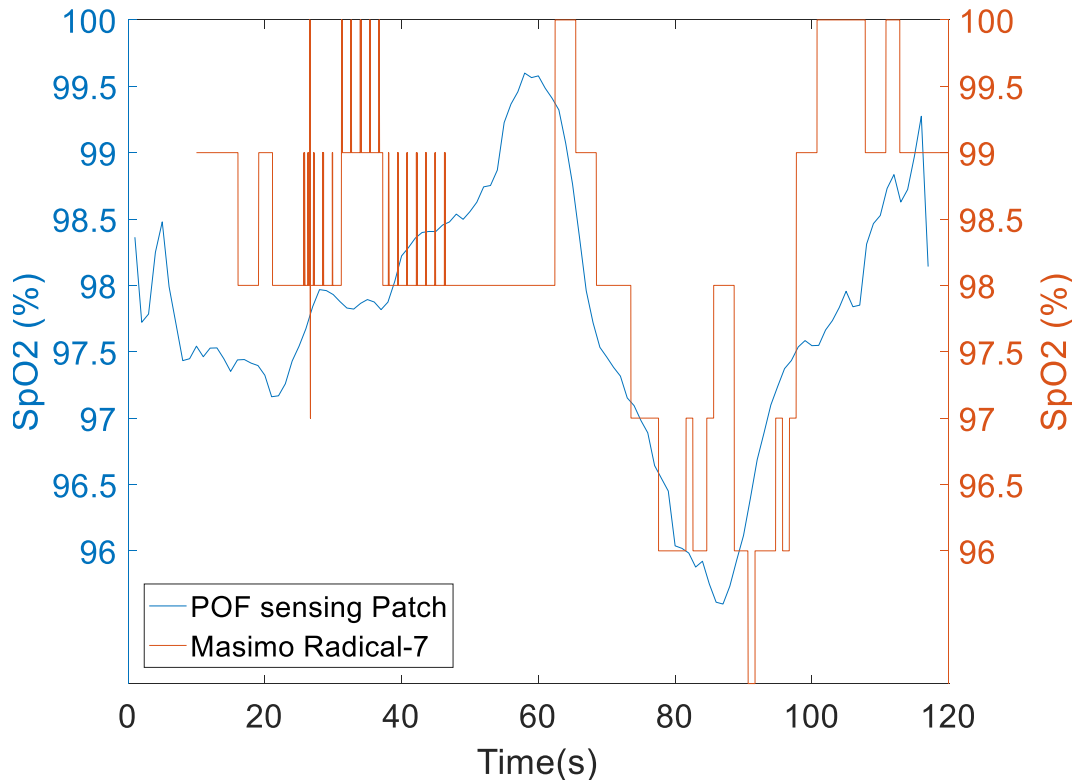


Figure C.20. Comparison of POF sensing patch with commercial pulse oximeter for induced deoxygenation event (Sixth experiment).

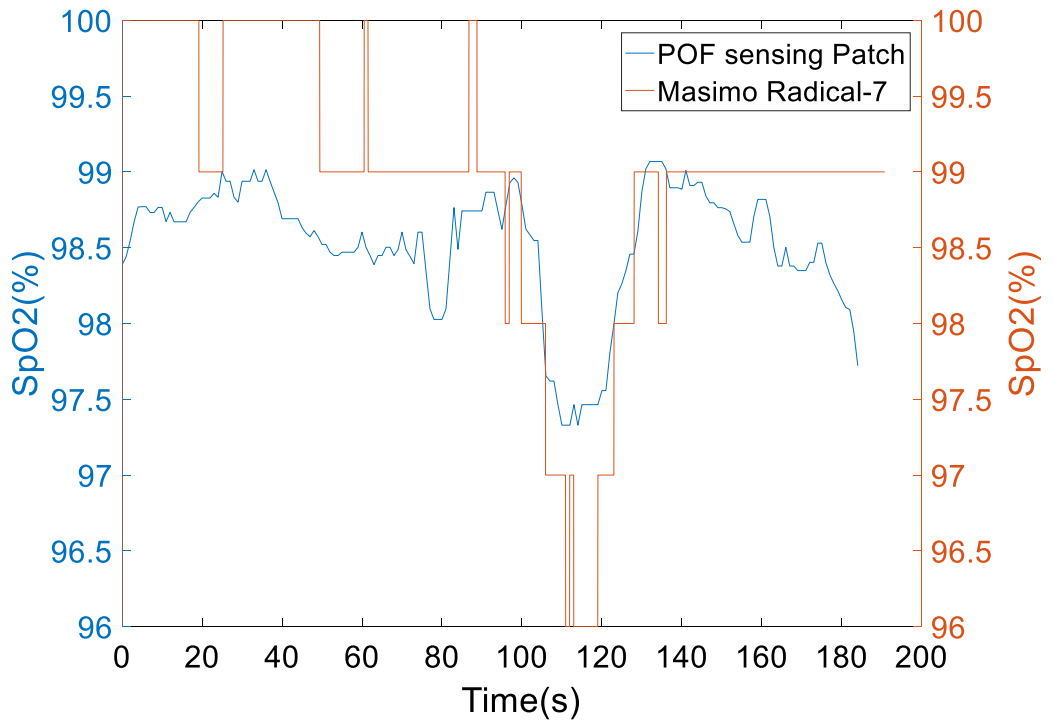


Figure C.21. Comparison of POF sensing patch with commercial pulse oximeter for induced deoxygenation event (Seventh experiment).

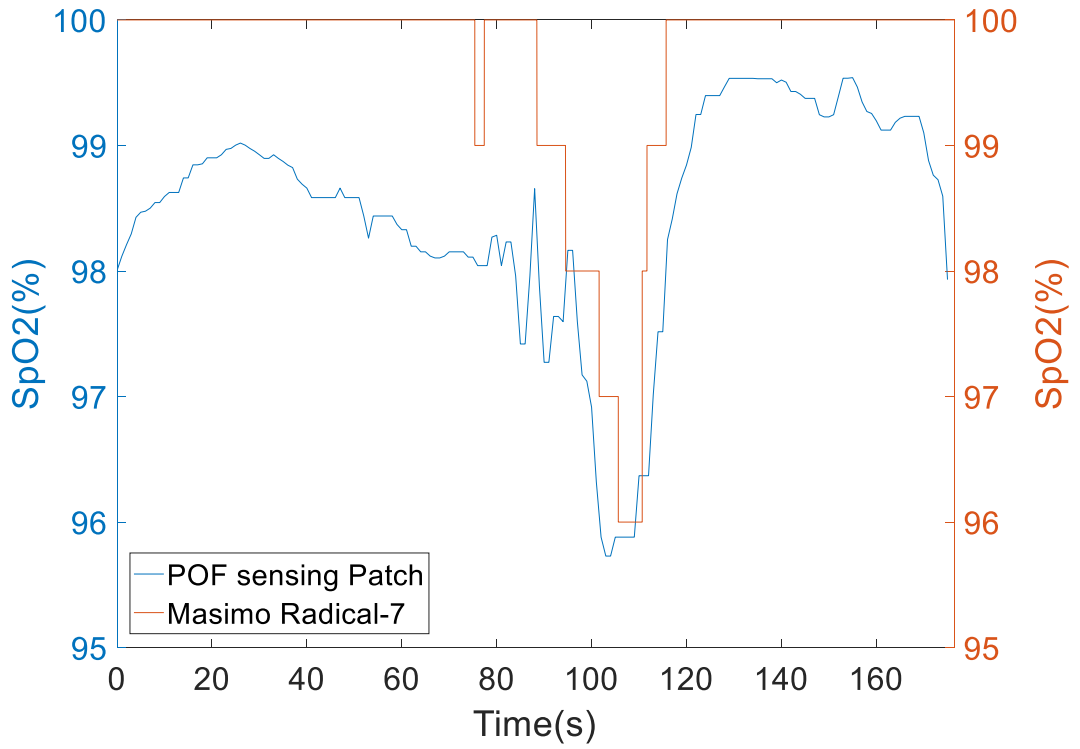


Figure C.22. Comparison of POF sensing patch with commercial pulse oximeter for induced deoxygenation event (Eighth experiment).

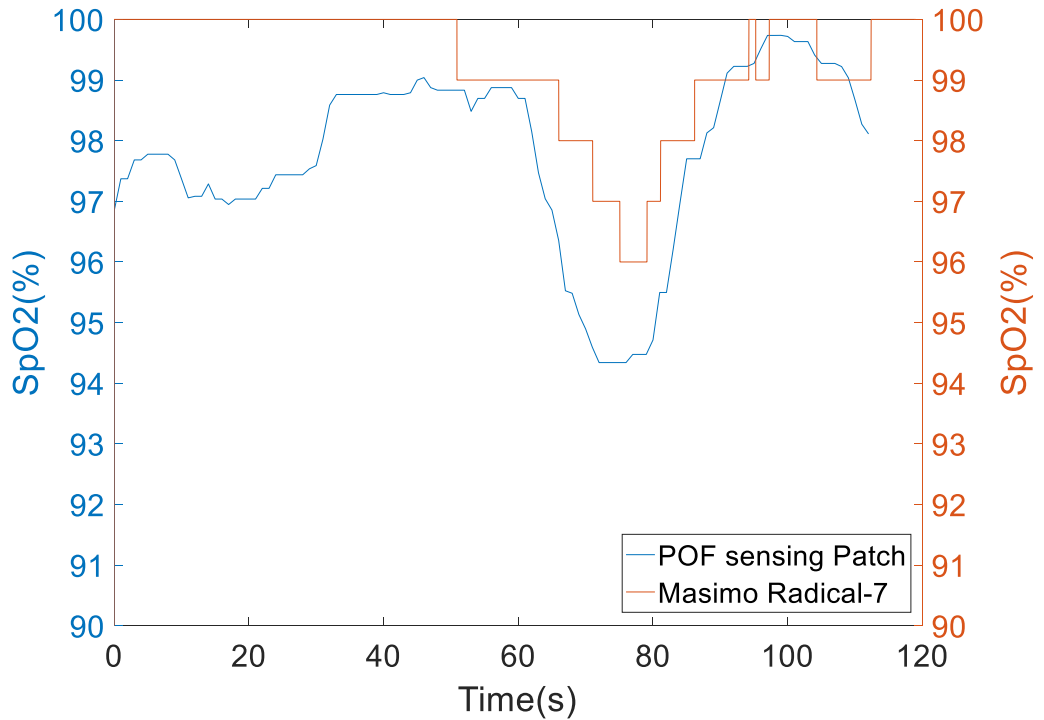


Figure C.23. Comparison of POF sensing patch with commercial pulse oximeter for induced deoxygenation event (Ninth experiment).

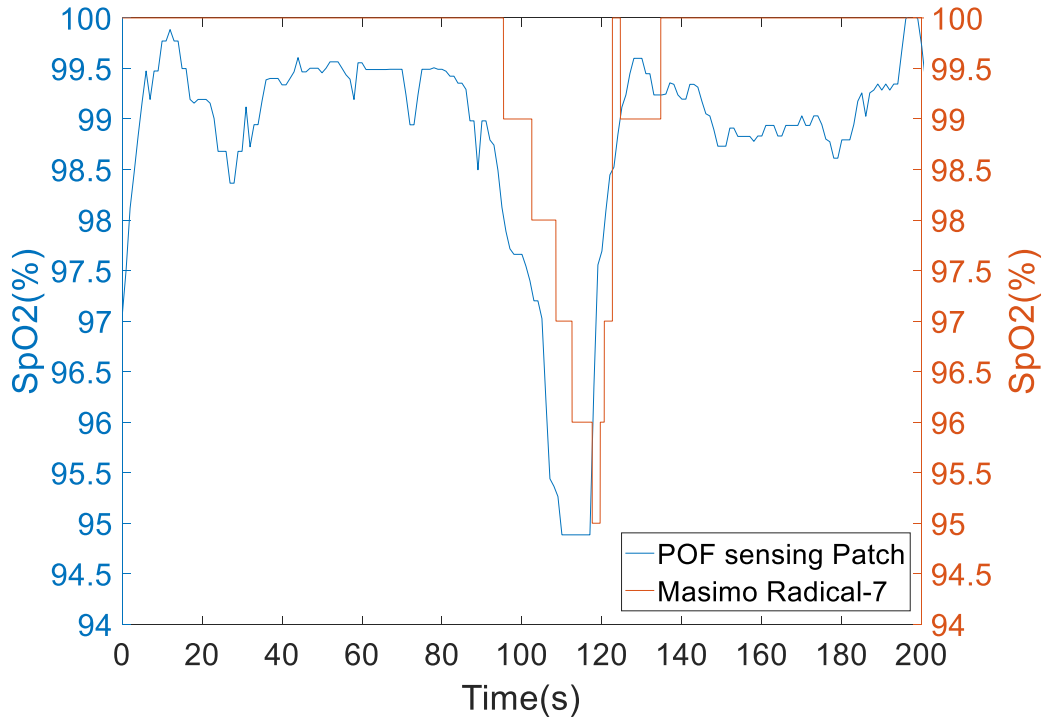
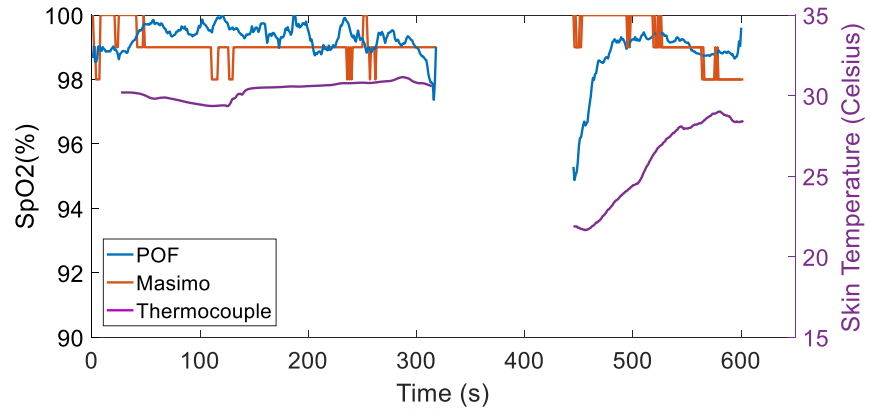


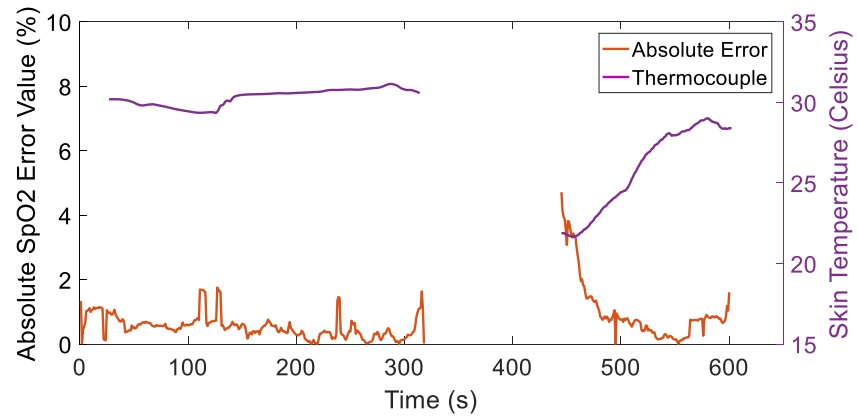
Figure C.24. Comparison of POF sensing patch with commercial pulse oximeter for induced deoxygenation event (Tenth experiment).

C.2 12 Experiment Results of S_{pO_2} Measurements under Different Skin Temperature Situations

In this study, the designed pulse oximetry sensor was applied to measure the S_{pO_2} value of 12 volunteers with different skin temperatures. There are 12 groups of data recorded in total which shown from Cxx to Cxx. Every figure contains 3 diagrams which show the subject's S_{pO_2} obtained from the designed POF sensor and the Masimo Radical-7 pulse oximeter (a), the absolute S_{pO_2} error (b) and the perfusion indices of the red and IR PPG signals (c).



(a)



(b)

Figure C.25. Volunteer 1. (a) SpO_2 values obtained from the designed sensor and the Masimo. (b) Thermocouple VS. Absolute SpO_2 error.

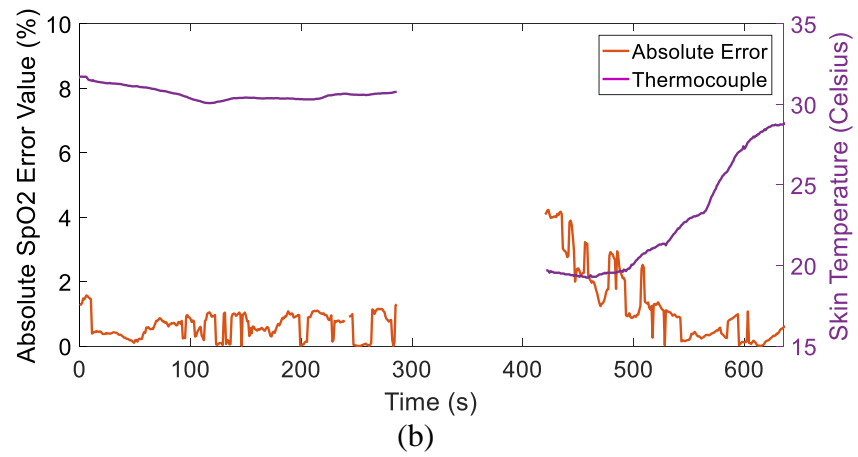
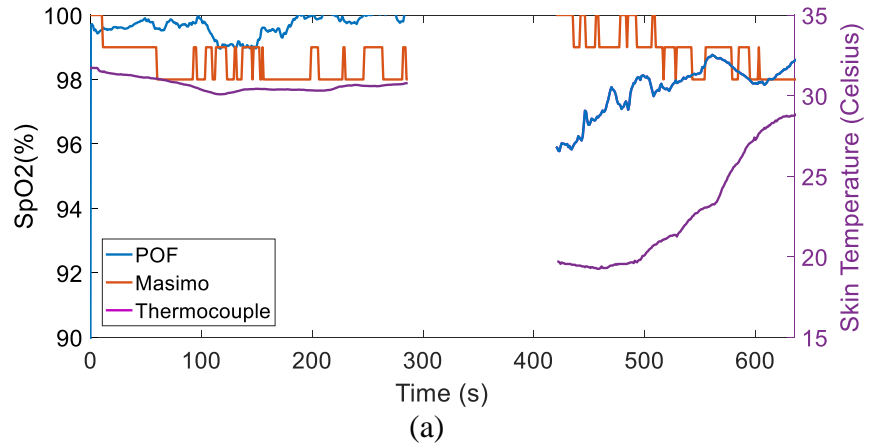
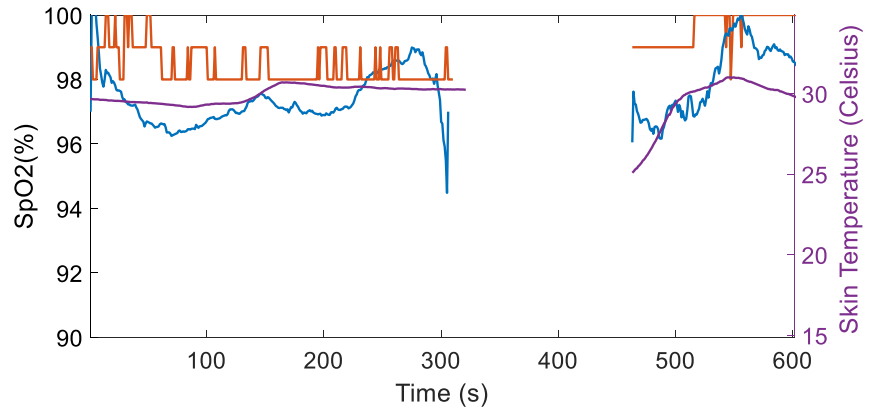
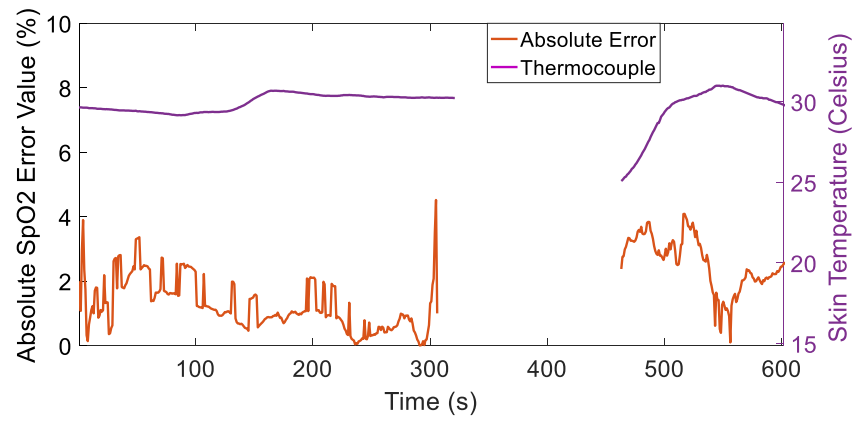


Figure C.26 Volunteer 2. (a) SpO_2 values obtained from the designed sensor and the Masimo. (b) Thermocouple VS. Absolute SpO_2 error.

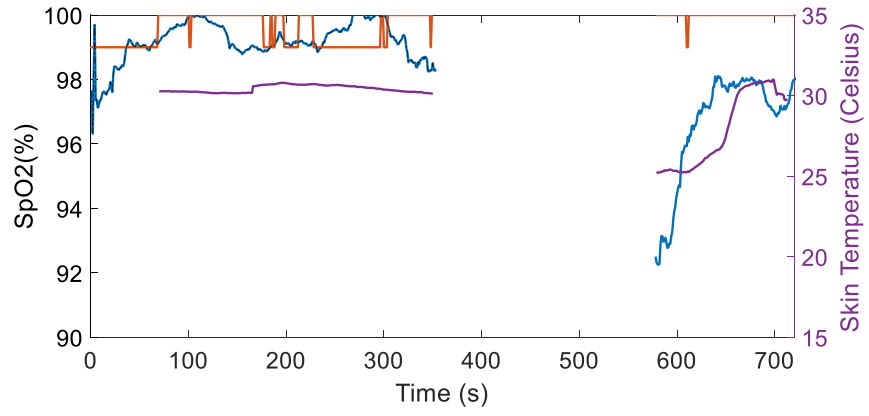


(a)

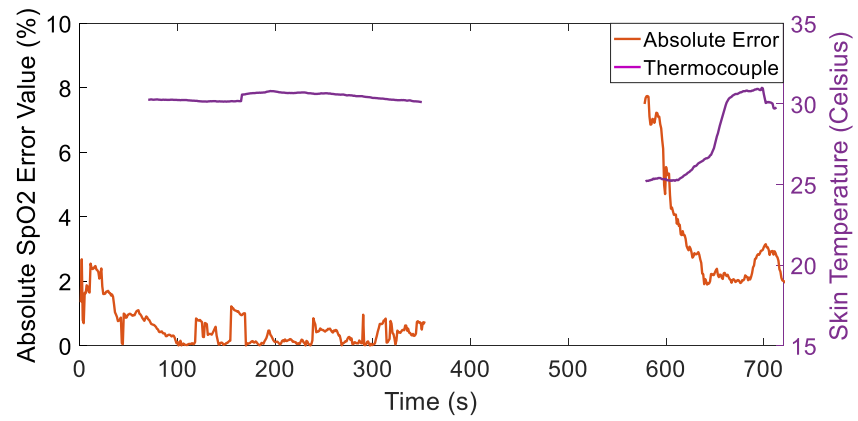


(b)

Figure C.27. Volunteer 3. (a) SpO₂ values obtained from the designed sensor and the Masimo. (b) Thermocouple VS. Absolute SpO₂ error.

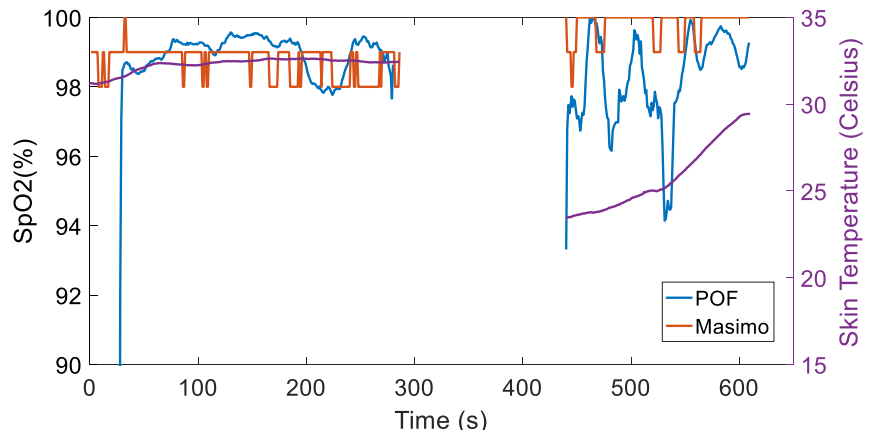


(a)

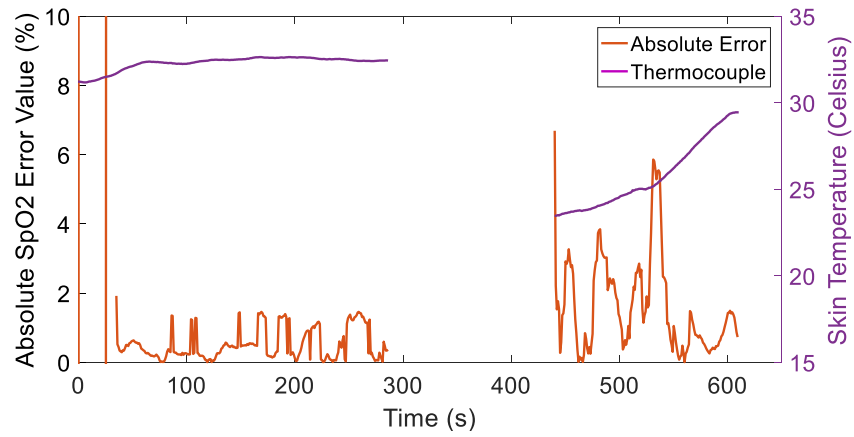


(b)

Figure C.28. Volunteer 4. (a) SpO₂ values obtained from the designed sensor and the Masimo. (b) Thermocouple VS. Absolute SpO₂ error.

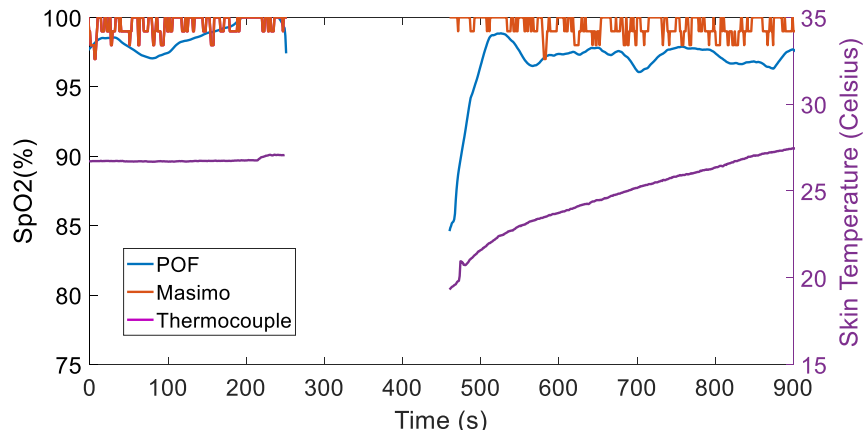


(a)

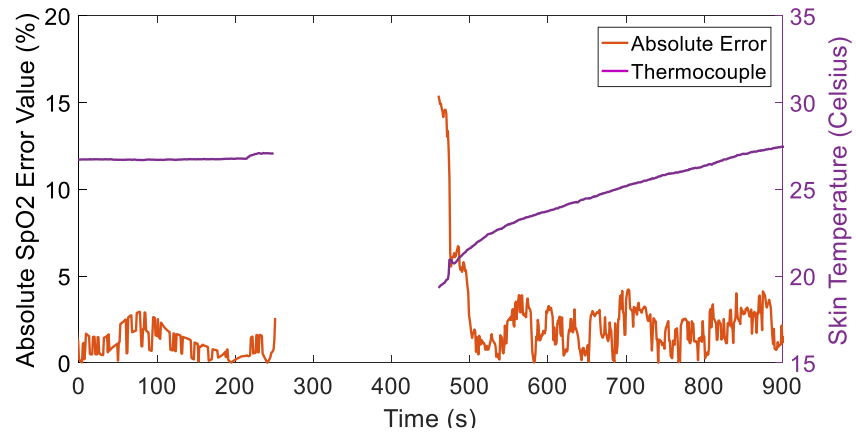


(b)

Figure C.29. Volunteer 5. (a) S_{pO_2} values obtained from the designed sensor and the Masimo. (b) Thermocouple VS. Absolute S_{pO_2} error.

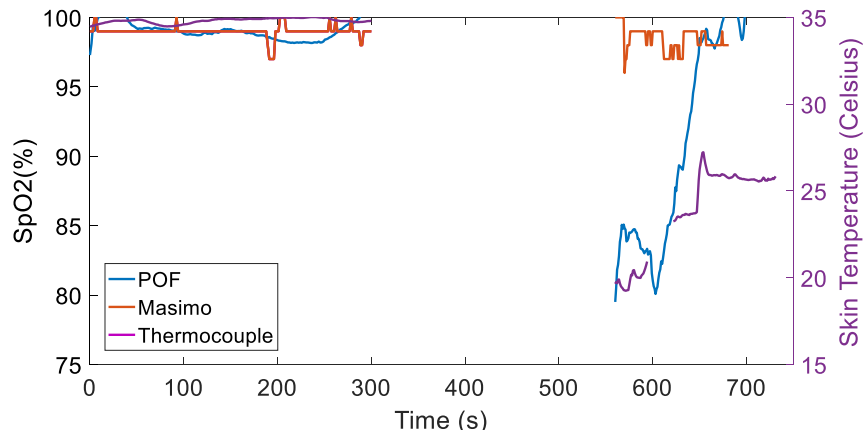


(a)

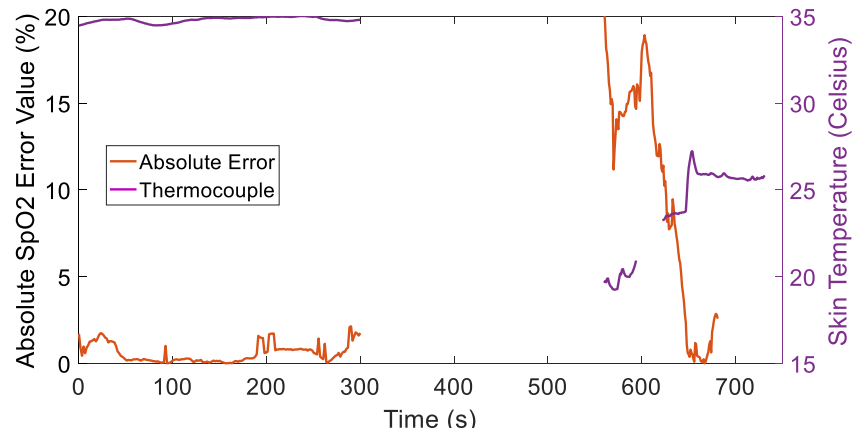


(b)

Figure C.30. Volunteer 6. (a) SpO₂ values obtained from the designed sensor and the Masimo. (b) Thermocouple VS. Absolute SpO₂ error.

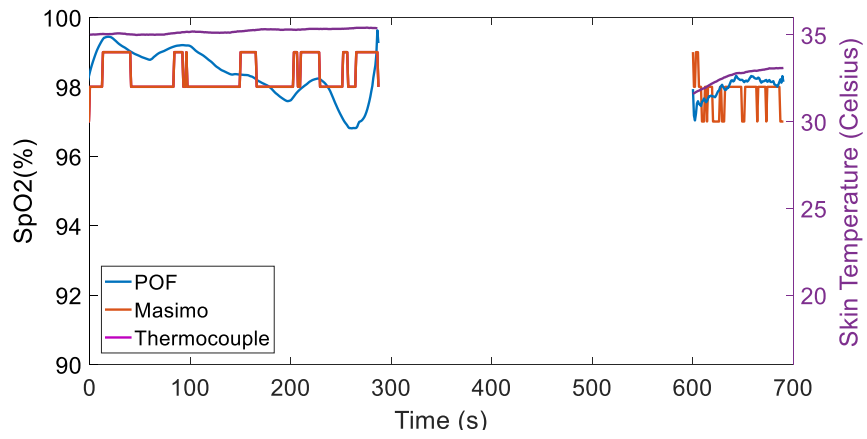


(a)

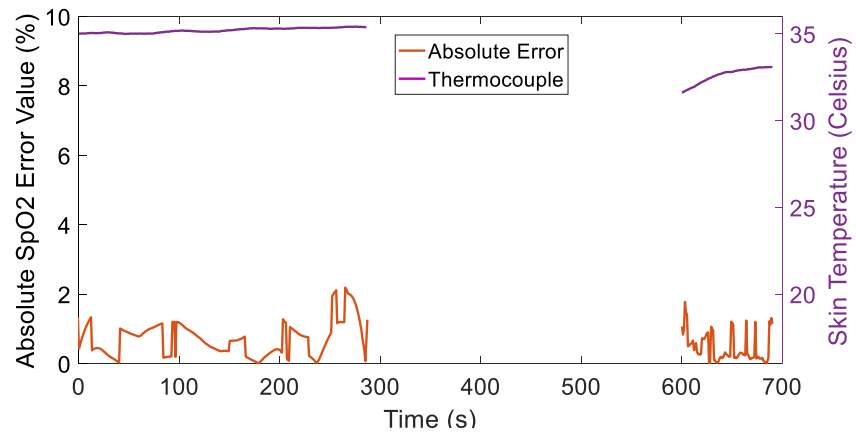


(b)

Figure C.31. Volunteer 7. (a) SpO₂ values obtained from the designed sensor and the Masimo. (b) Thermocouple VS. Absolute SpO₂ error.

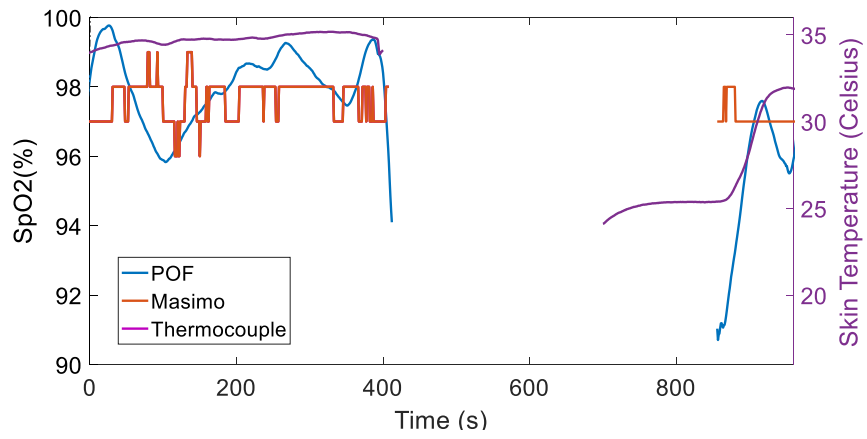


(a)

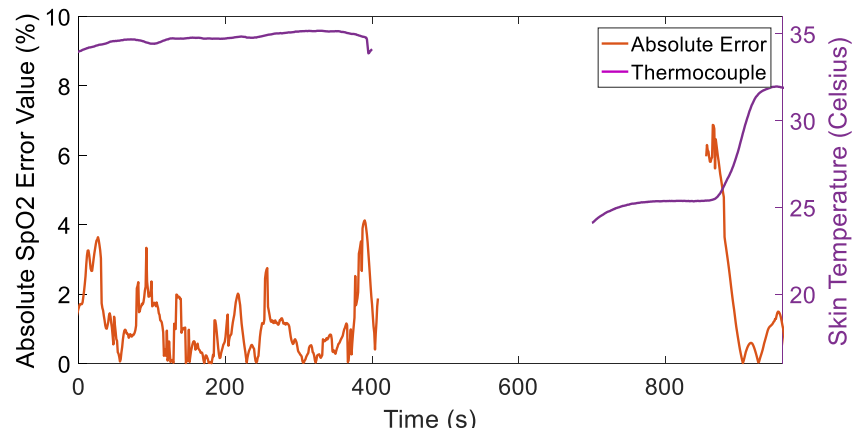


(b)

Figure C32 Volunteer 8. (a) S_{pO_2} values obtained from the designed sensor and the Masimo. (b) Thermocouple VS. Absolute S_{pO_2} error.

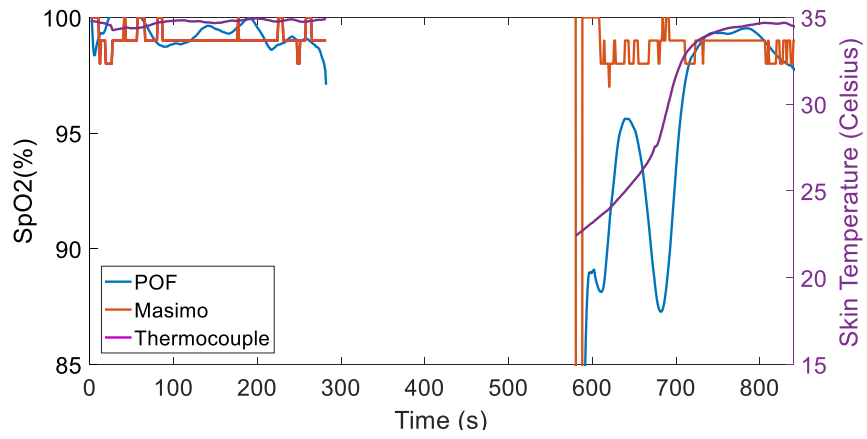


(a)

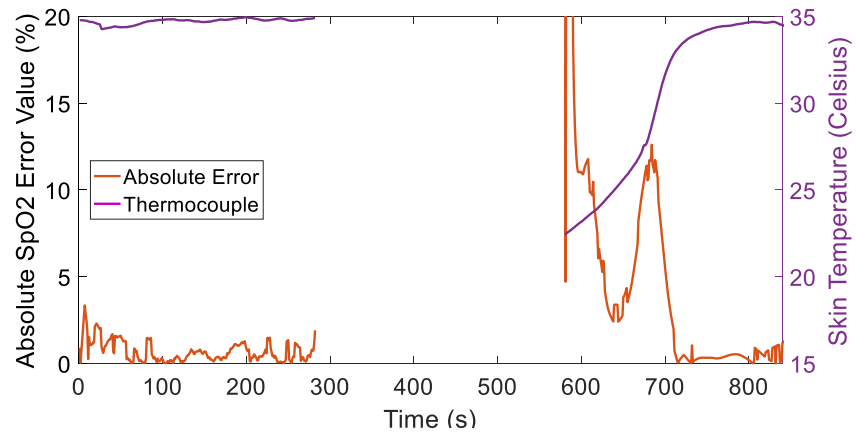


(b)

Figure C.33. Volunteer 9. (a) S_PO₂ values obtained from the designed sensor and the Masimo. (b) Thermocouple VS. Absolute S_PO₂ error.

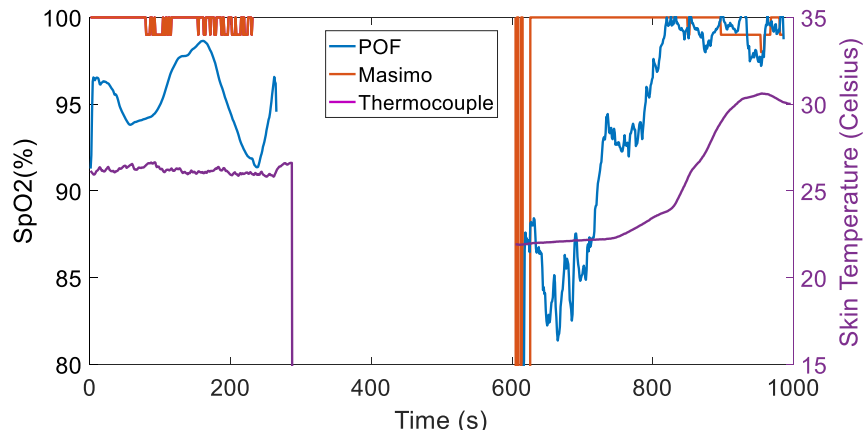


(a)

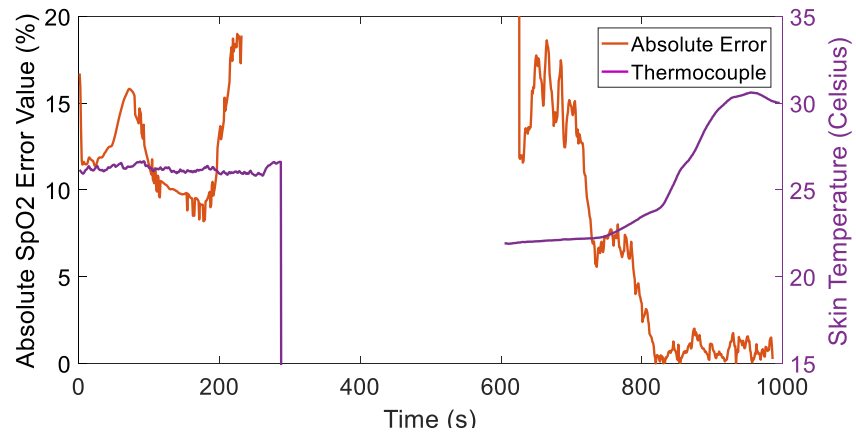


(b)

Figure C.34. Volunteer 10. (a) SpO_2 values obtained from the designed sensor and the Masimo. (b) Thermocouple VS. Absolute SpO_2 error.

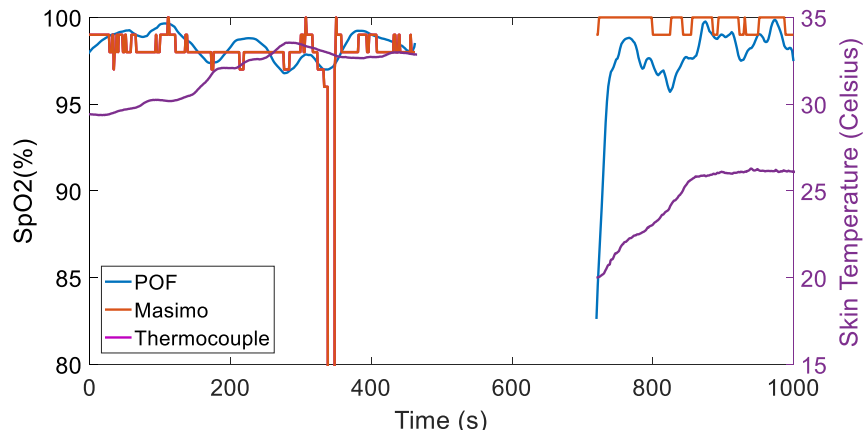


(a)

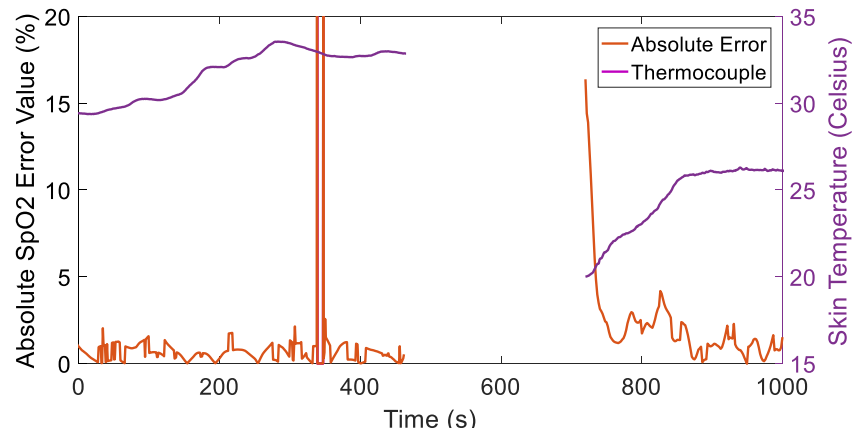


(b)

Figure C.35. Volunteer 11. (a) SpO₂ values obtained from the designed sensor and the Masimo. (b) Thermocouple VS. Absolute SpO₂ error.



(a)



(b)

Figure C.36. Volunteer 12. (a) SpO_2 values obtained from the designed sensor and the Masimo. (b) Thermocouple VS. Absolute SpO_2 error.

C.3 30 Experimental Results of SpO₂ Measurements under Different Contact Pressures

In this study, the designed pulse oximetry sensor was applied to measure the SpO₂ value of 10 volunteers under different contact pressure levels. For each volunteer, the experiment is required to repeat the whole pressure changing process for three times. Therefore, there are 30 groups of data recorded in total which are shown from C13 to C42. Every figure contains 4 diagrams which show the infrared PPG signal (a), the absolute SpO₂ error (b), the skewness index (c) and the perfusion index (d) under different pressure levels.

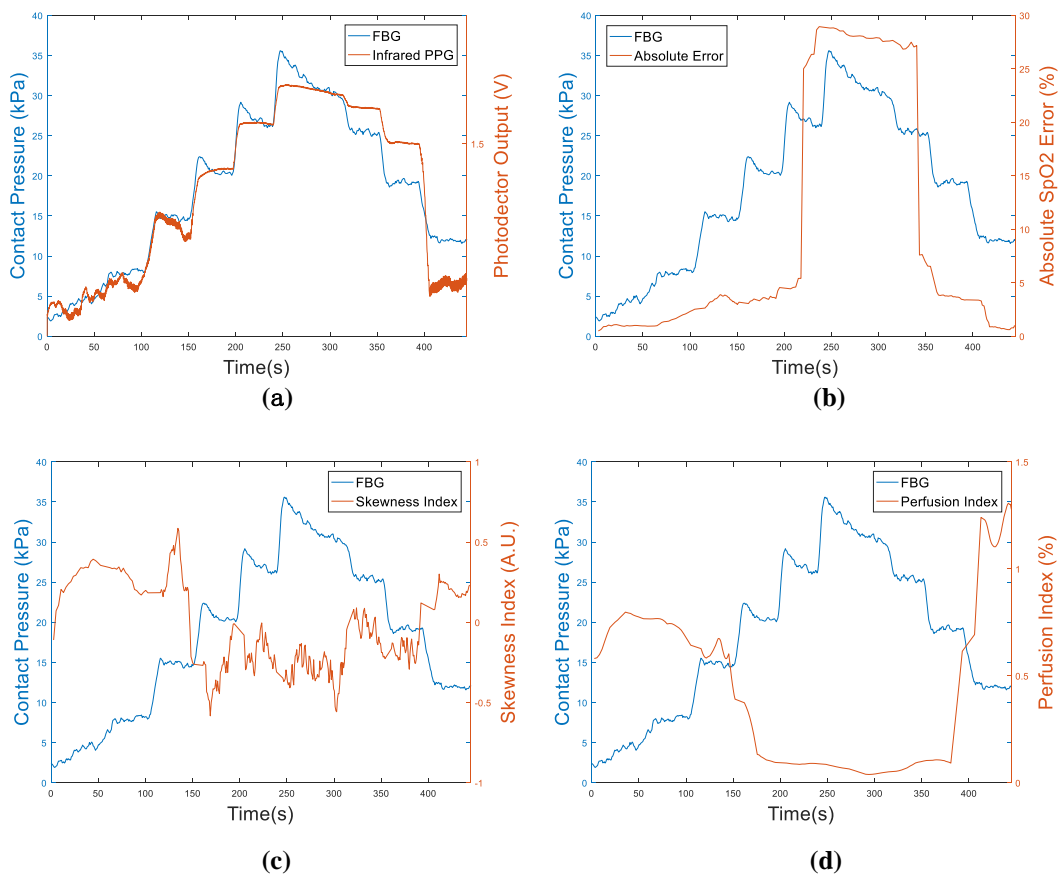
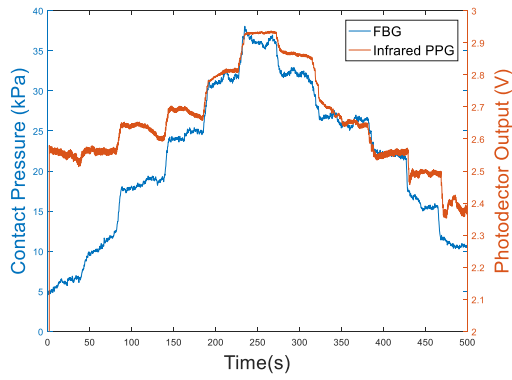
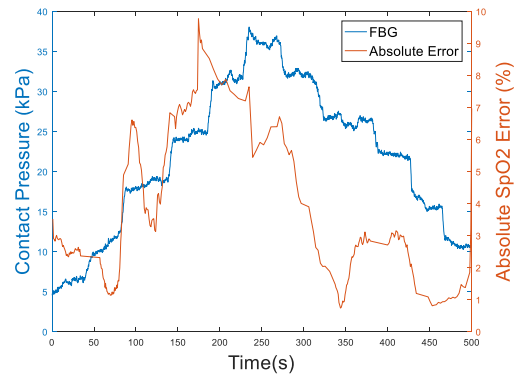


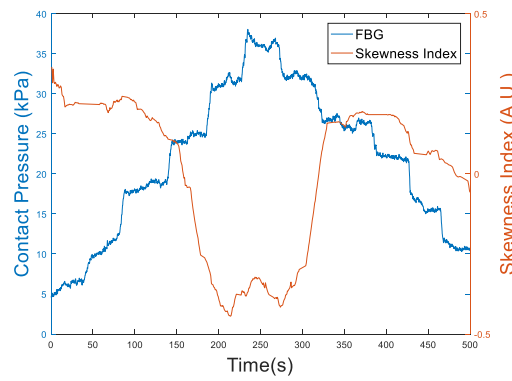
Figure C.37. Volunteer 1-1. (a) FBG VS. Infrared PPG signals. (b) FBG VS. Absolute SpO₂ error. (c) FBG VS. Skewness index. (d) FBG VS. Perfusion index.



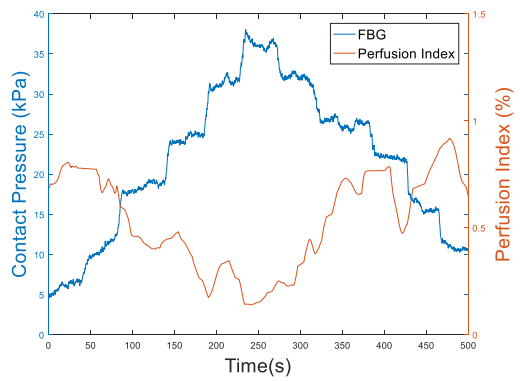
(a)



(b)

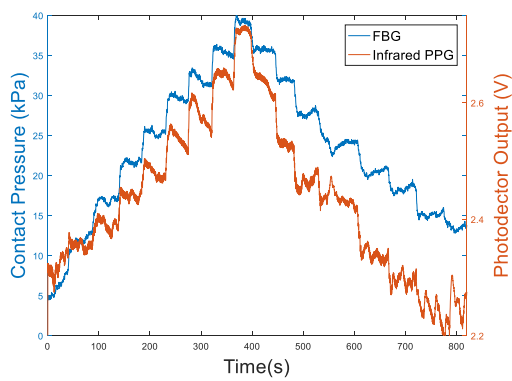


(c)

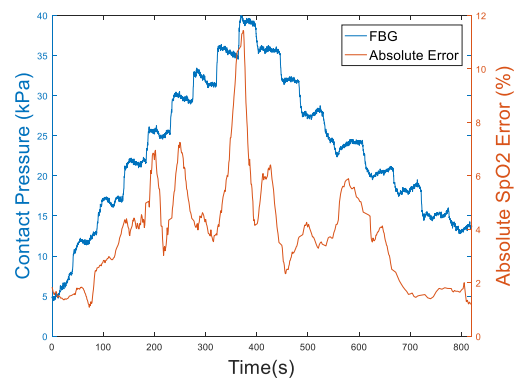


(d)

Figure C38. Volunteer 1-2. (a) FBG VS. Infrared PPG signals. (b) FBG VS. Absolute S_{pO_2} error. (c) FBG VS. Skewness index. (d) FBG VS. Perfusion index.



(a)



(b)

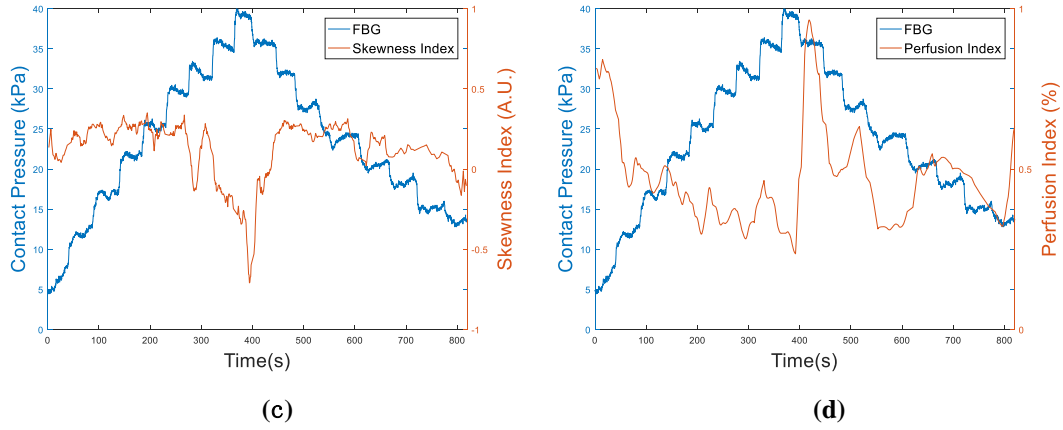


Figure C.39. Volunteer 1-3. (a) FBG VS. Infrared PPG signals. (b) FBG VS. Absolute S_{pO_2} error. (c) FBG VS. Skewness index. (d) FBG VS. Perfusion index.

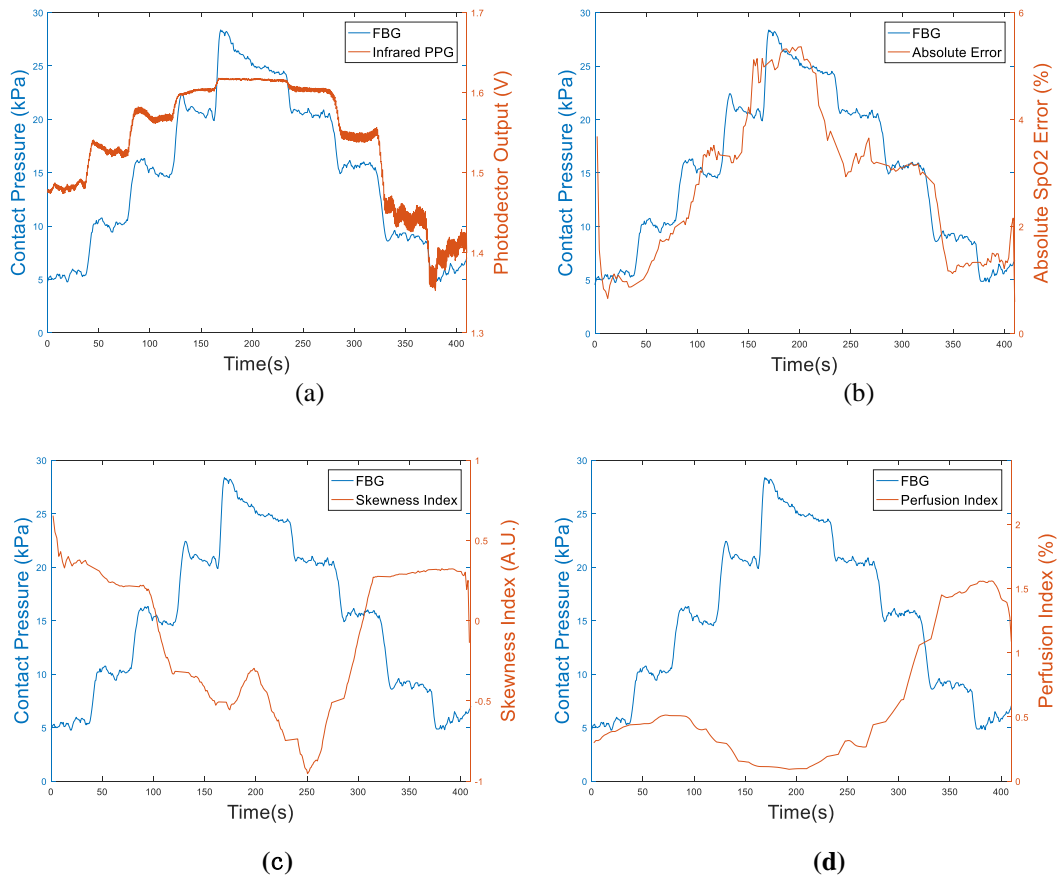
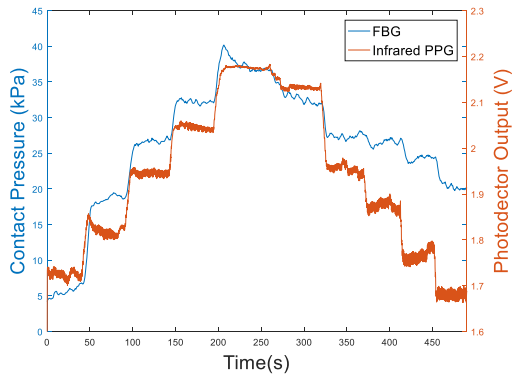
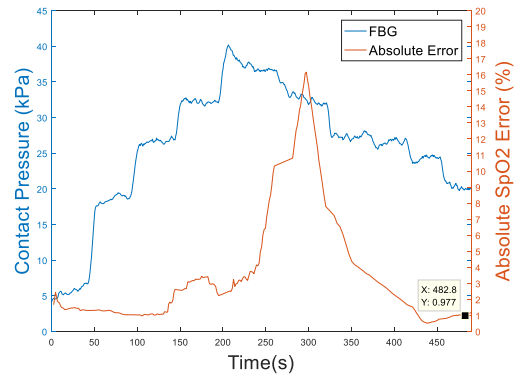


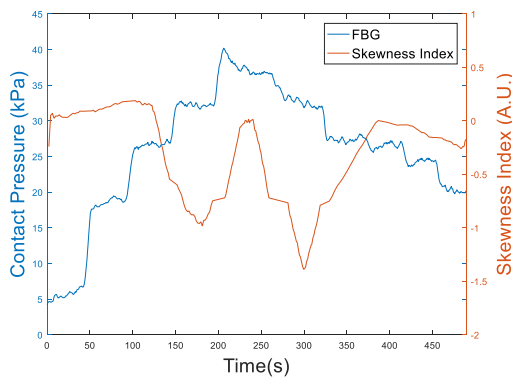
Figure C.40. Volunteer 2-1. (a) FBG VS. Infrared PPG signals. (b) FBG VS. Absolute S_{pO_2} error. (c) FBG VS. Skewness index. (d) FBG VS. Perfusion index.



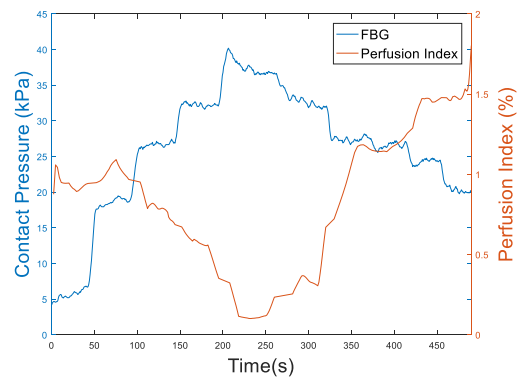
(a)



(b)

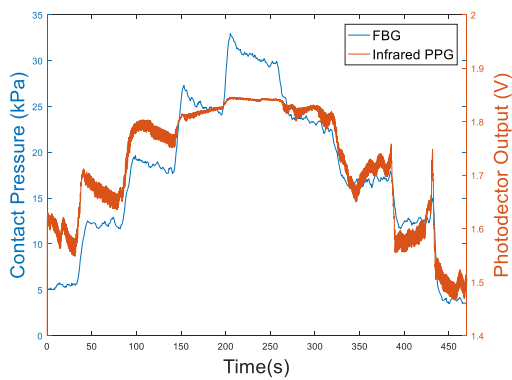


(c)

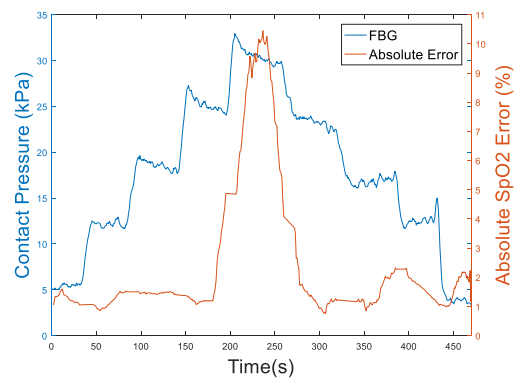


(d)

Figure C.41. Volunteer 2-2. (a) FBG VS. Infrared PPG signals. (b) FBG VS. Absolute S_{pO_2} error. (c) FBG VS. Skewness index. (d) FBG VS. Perfusion index.



(a)



(b)

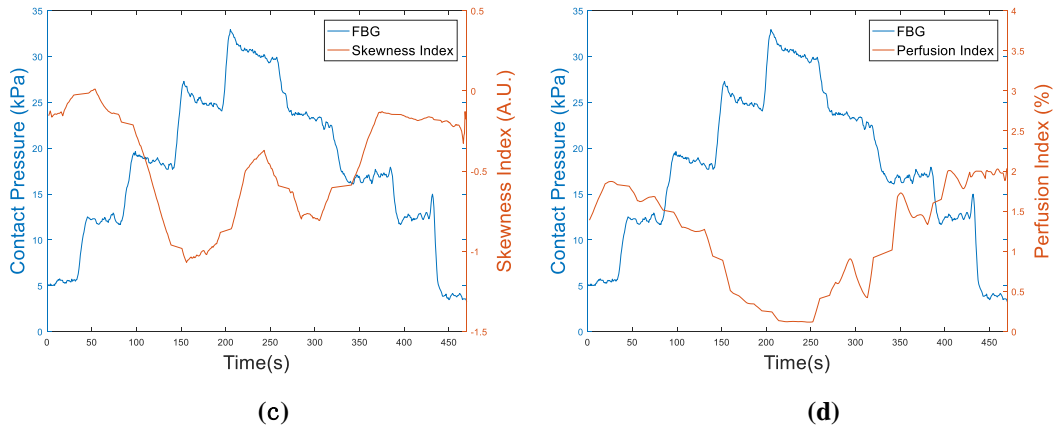


Figure C.42. Volunteer 2-3. (a) FBG VS. Infrared PPG signals. (b) FBG VS. Absolute S_{pO_2} error. (c) FBG VS. Skewness index. (d) FBG VS. Perfusion index.

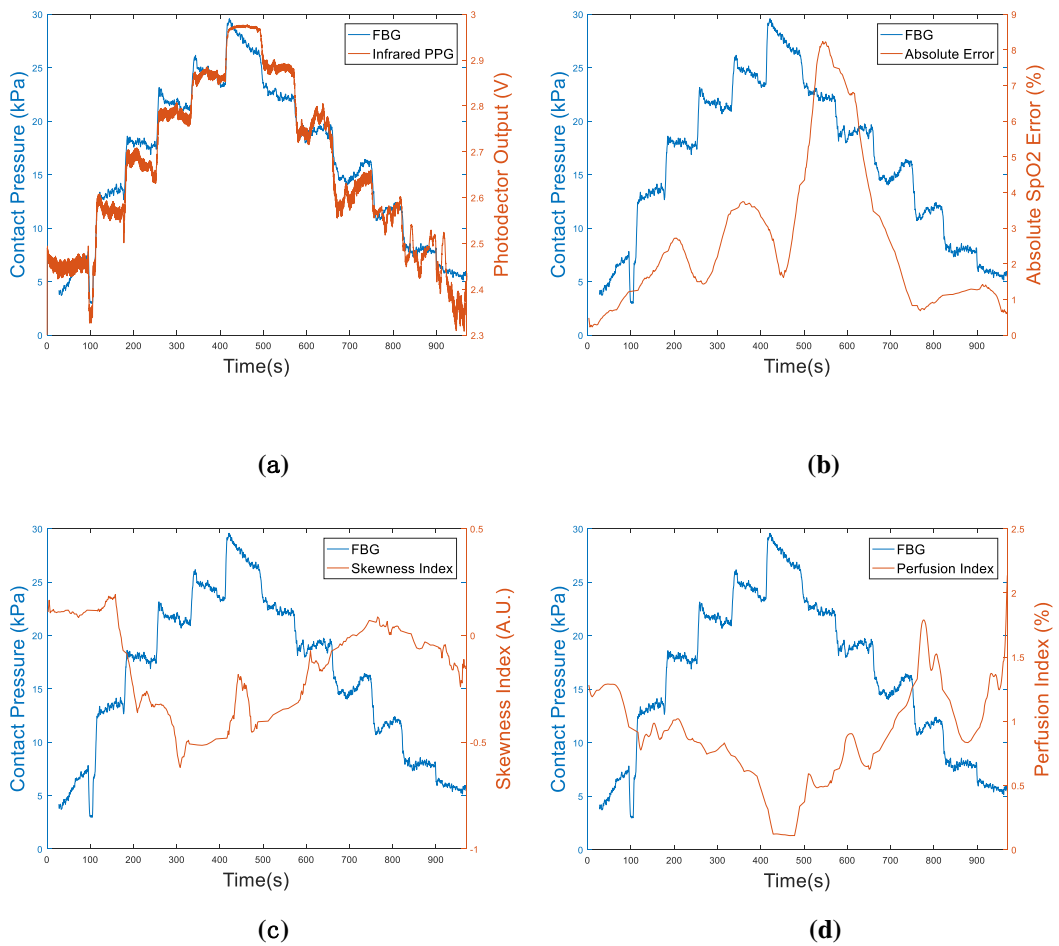
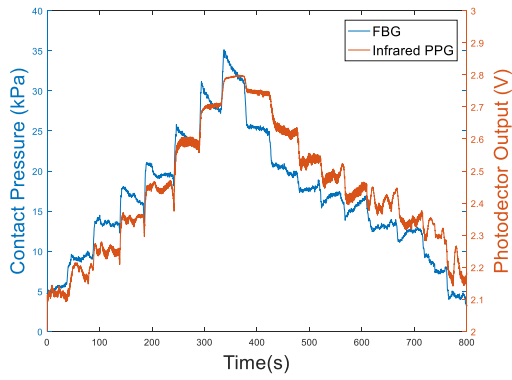
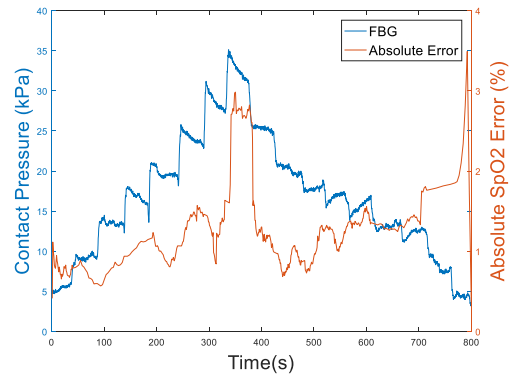


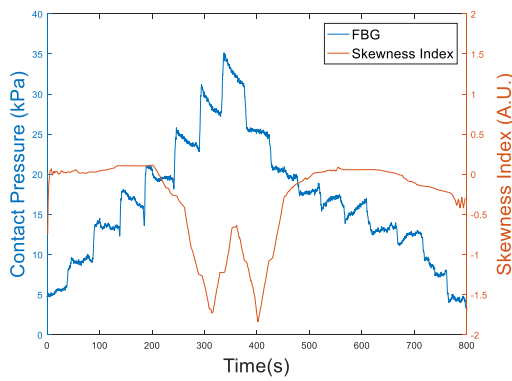
Figure C.43. Volunteer 3-1. (a) FBG VS. Infrared PPG signals. (b) FBG VS. Absolute S_{pO_2} error. (c) FBG VS. Skewness index. (d) FBG VS. Perfusion index.



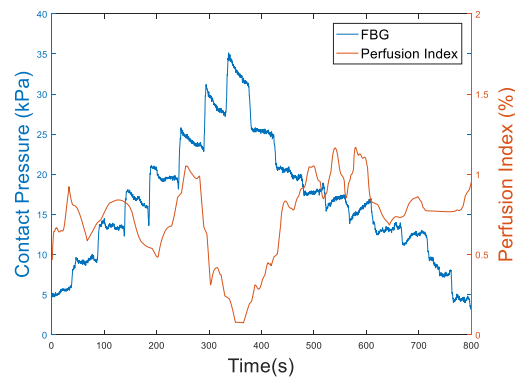
(a)



(b)

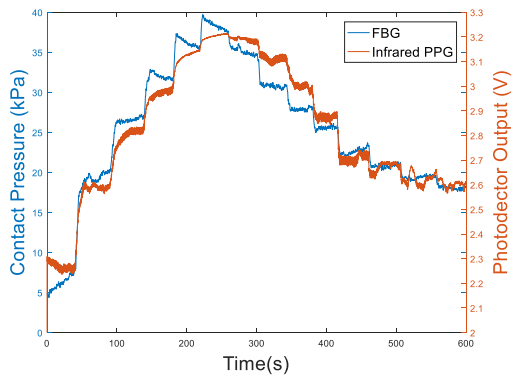


(c)

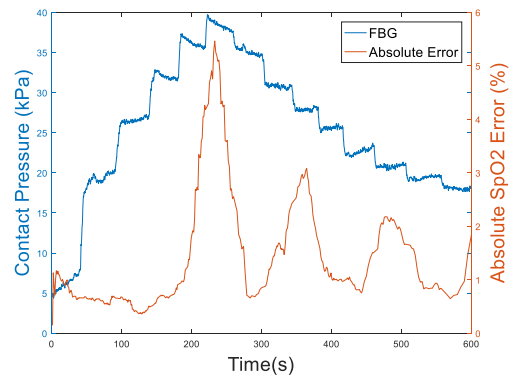


(d)

Figure C.44. Volunteer 3-2. (a) FBG VS. Infrared PPG signals. (b) FBG VS. Absolute SpO₂ error. (c) FBG VS. Skewness index. (d) FBG VS. Perfusion index.



(a)



(b)

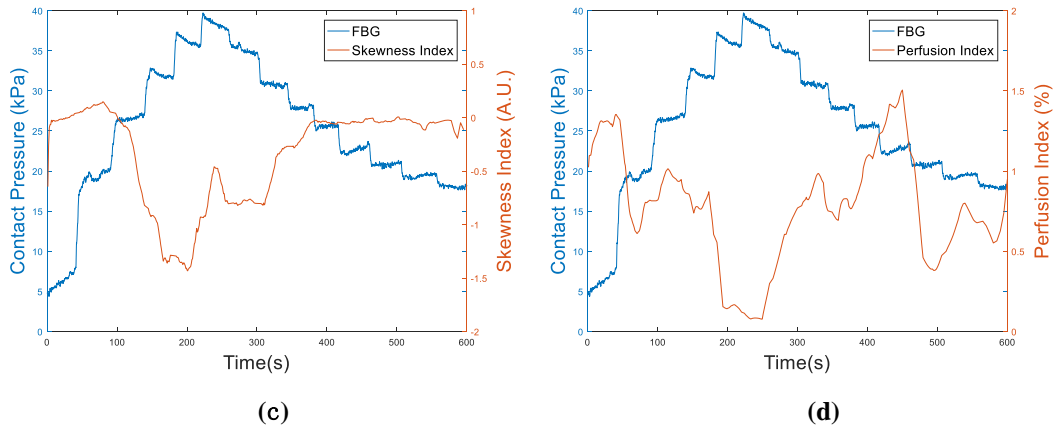


Figure C.45. Volunteer 3-3. (a) FBG VS. Infrared PPG signals. (b) FBG VS. Absolute S_{pO_2} error. (c) FBG VS. Skewness index. (d) FBG VS. Perfusion index.

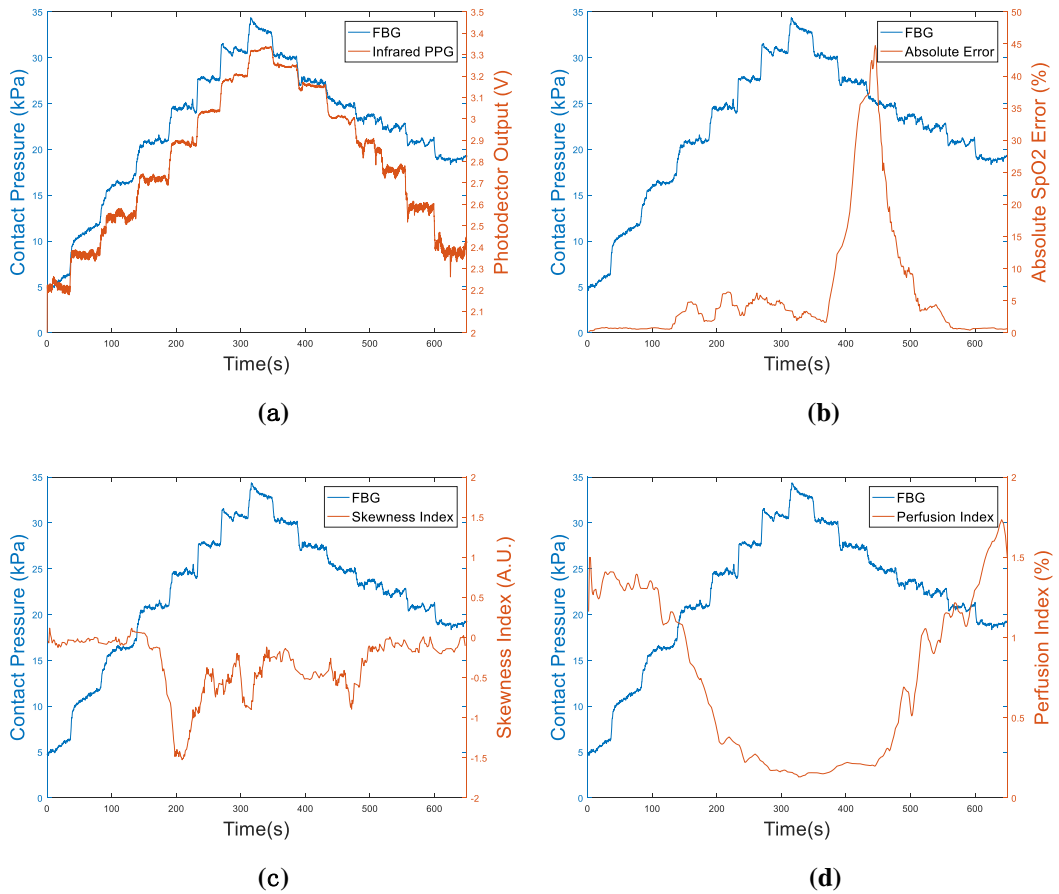
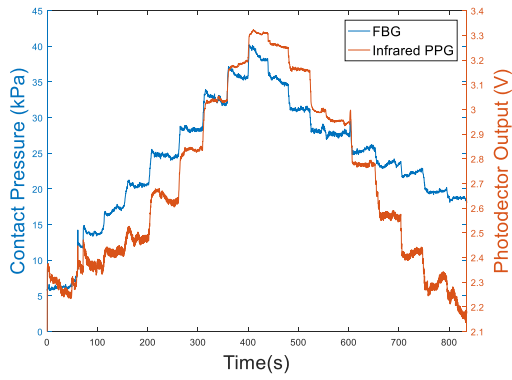
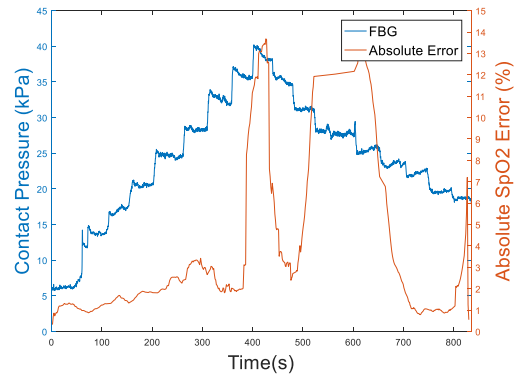


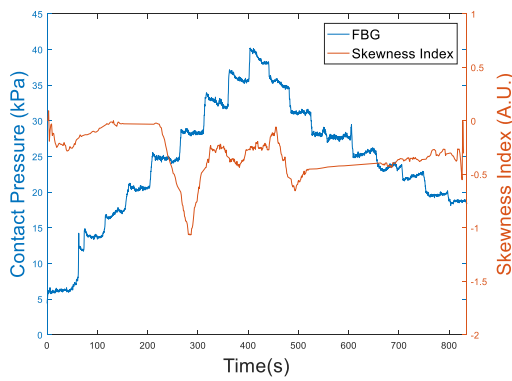
Figure C.46. Volunteer 4-1. (a) FBG VS. Infrared PPG signals. (b) FBG VS. Absolute S_{pO_2} error. (c) FBG VS. Skewness index. (d) FBG VS. Perfusion index.



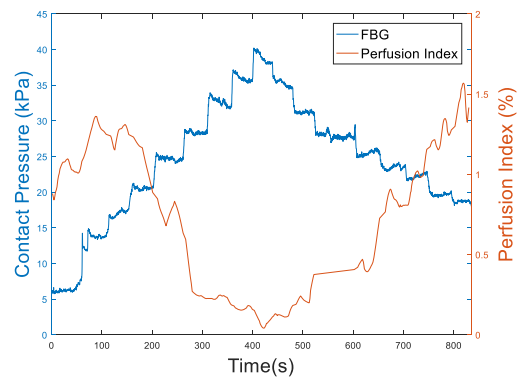
(a)



(b)

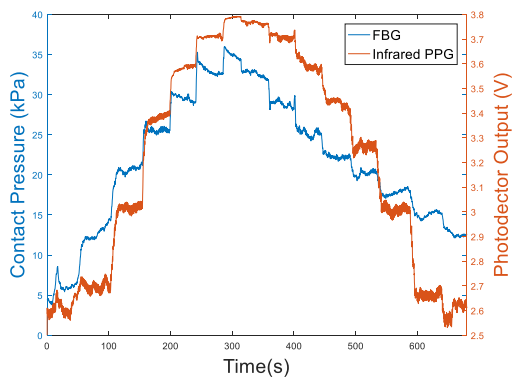


(c)

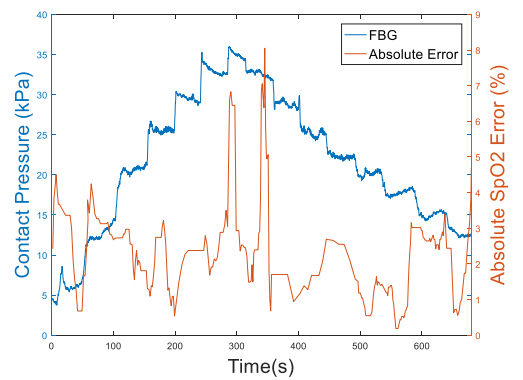


(d)

Figure C.47. Volunteer 4-2. (a) FBG VS. Infrared PPG signals. (b) FBG VS. Absolute S_{pO_2} error. (c) FBG VS. Skewness index. (d) FBG VS. Perfusion index.



(a)



(b)

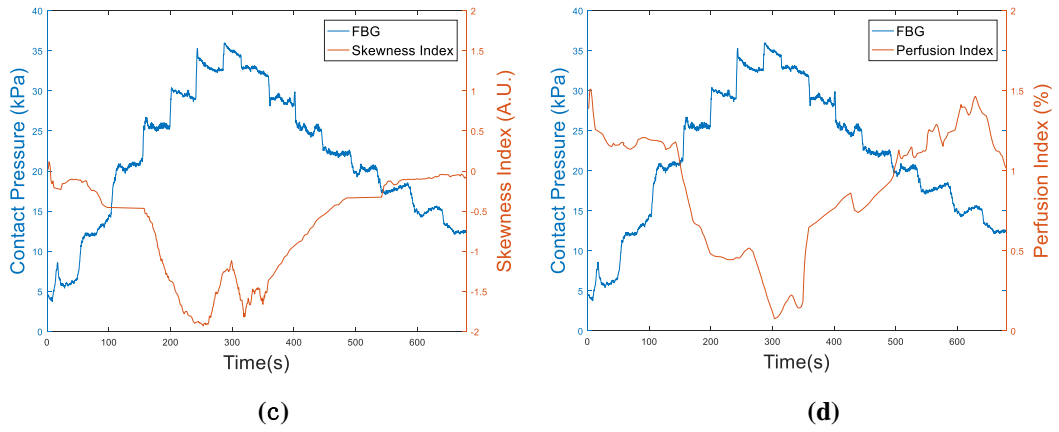


Figure C.48. Volunteer 4-3. (a) FBG VS. Infrared PPG signals. (b) FBG VS. Absolute S_{pO_2} error. (c) FBG VS. Skewness index. (d) FBG VS. Perfusion index.

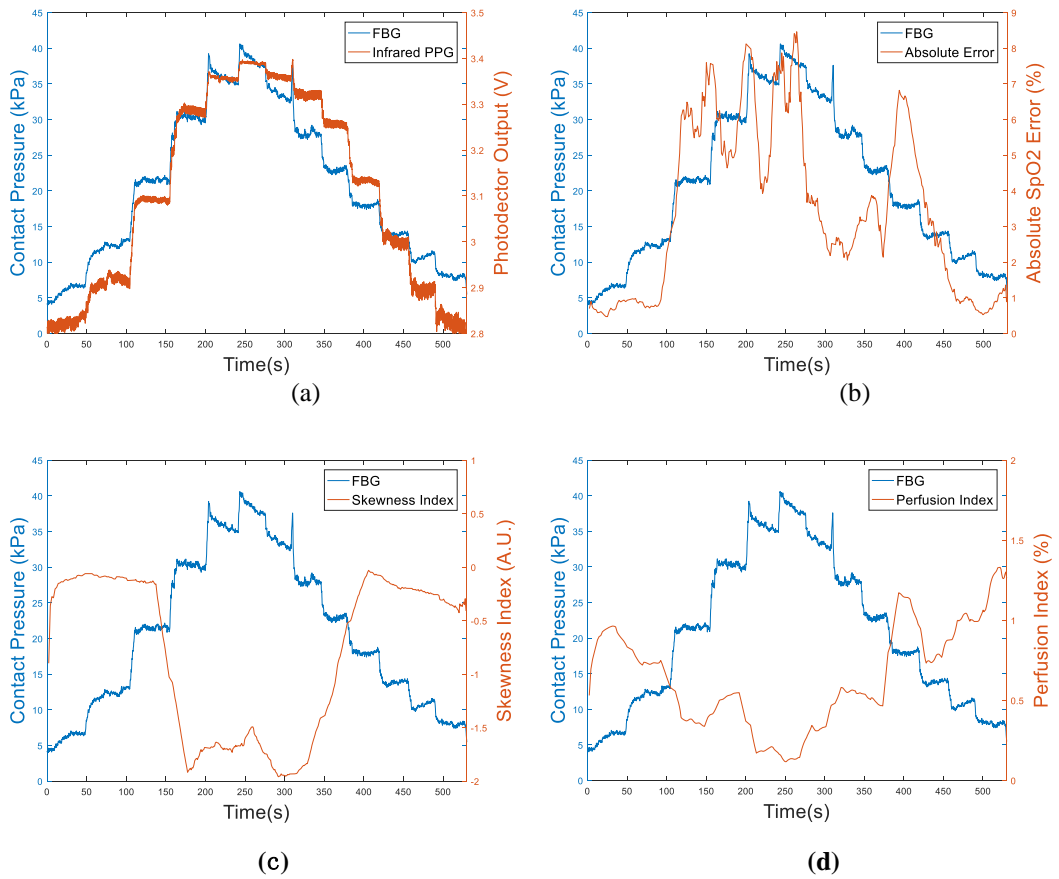
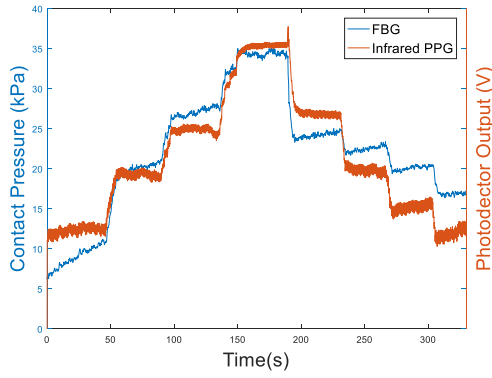
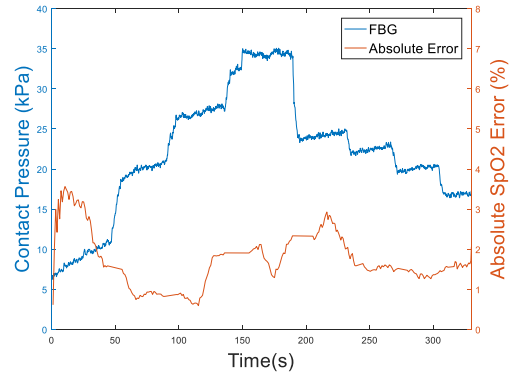


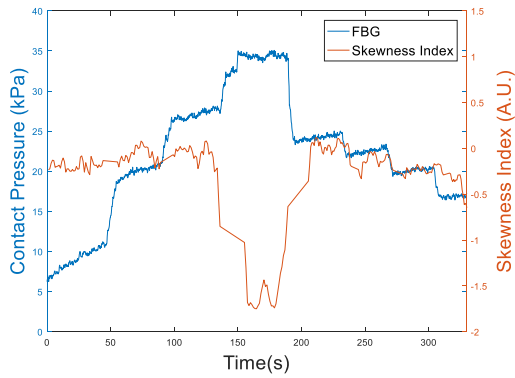
Figure C.49. Volunteer 5-1. (a) FBG VS. Infrared PPG signals. (b) FBG VS. Absolute S_{pO_2} error. (c) FBG VS. Skewness index. (d) FBG VS. Perfusion index.



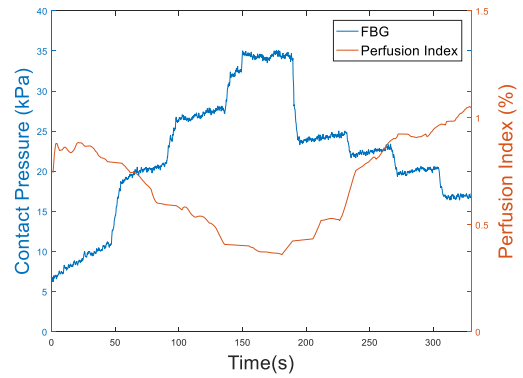
(a)



(b)

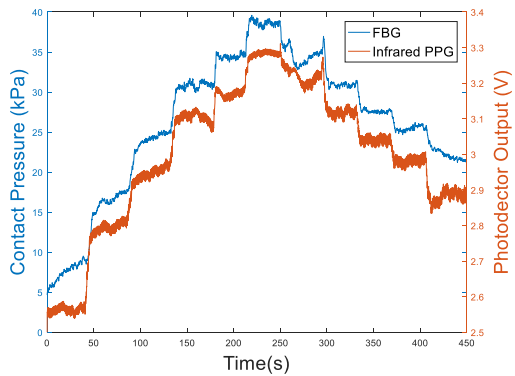


(c)

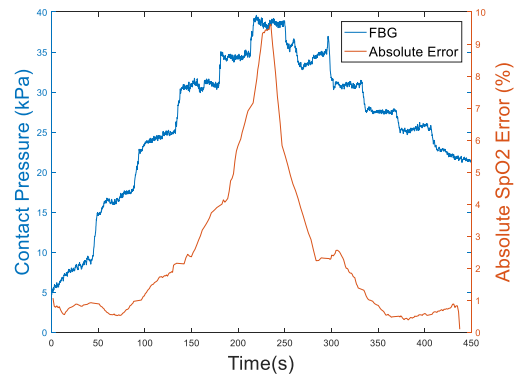


(d)

Figure C.50. Volunteer 5-2. The connection between the opto-electronic system and which generated the gap existed in the experiment results. (a) FBG VS. Infrared PPG signals. (b) FBG VS. Absolute SpO_2 error. (c) FBG VS. Skewness index. (d) FBG VS. Perfusion index.



(a)



(b)

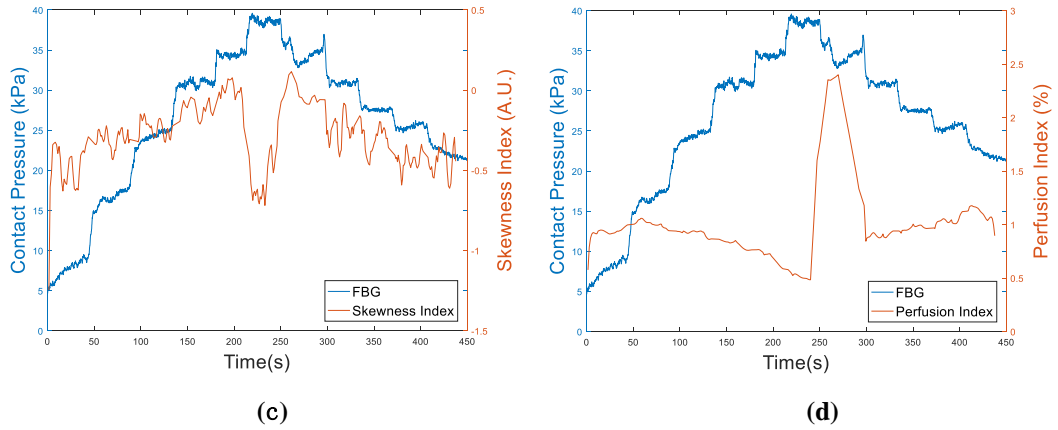


Figure C.51. Volunteer 5-3. (a) FBG VS. Infrared PPG signals. (b) FBG VS. Absolute S_{pO_2} error. (c) FBG VS. Skewness index. (d) FBG VS. Perfusion index.

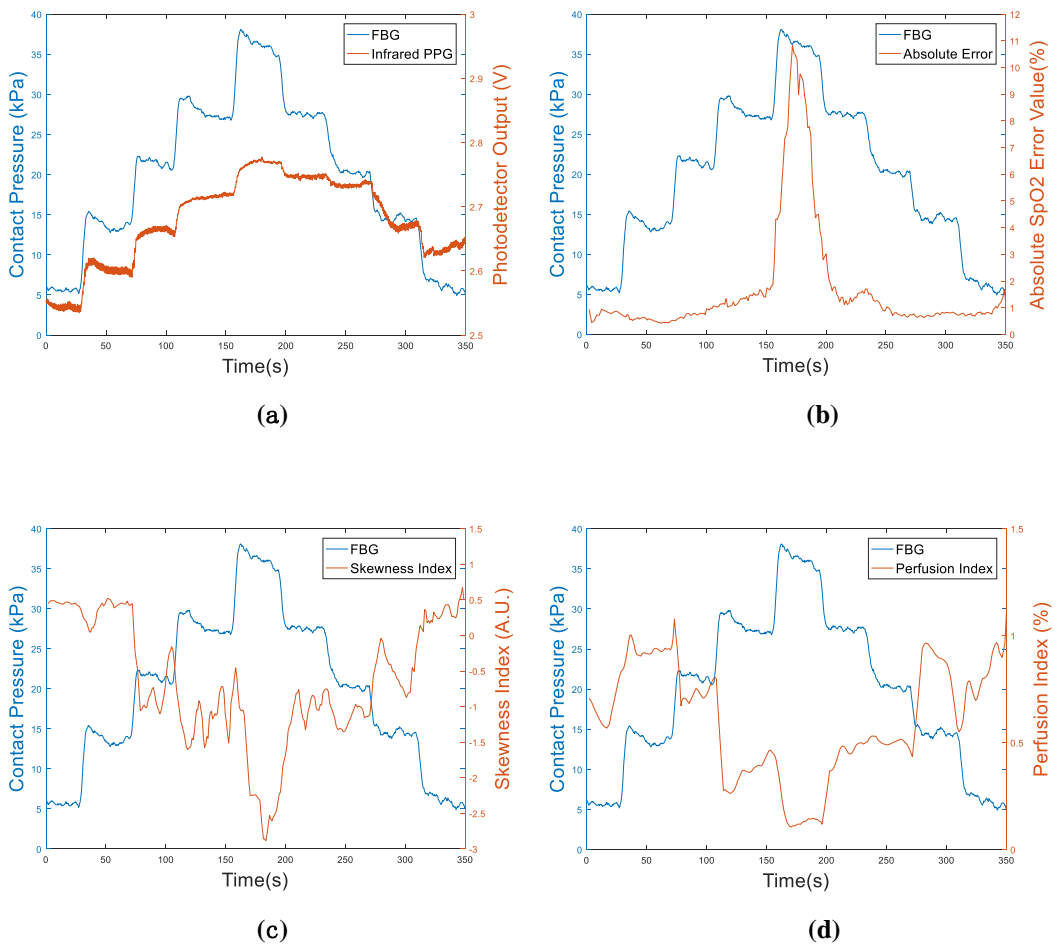
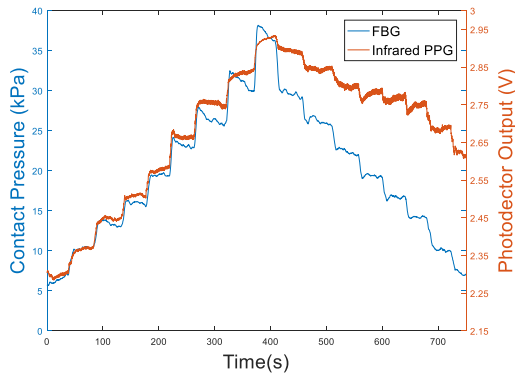
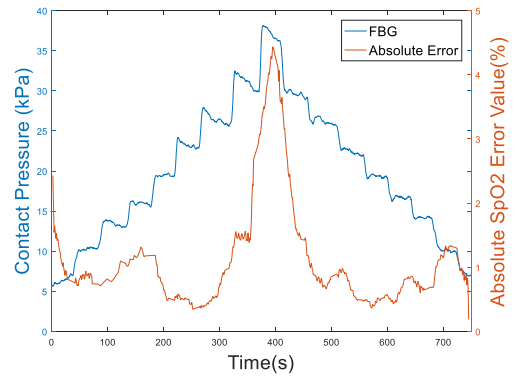


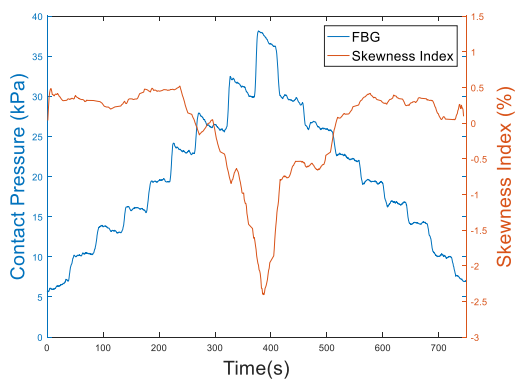
Figure C.52. Volunteer 6-1. (a) FBG VS. Infrared PPG signals. (b) FBG VS. Absolute S_{pO_2} error. (c) FBG VS. Skewness index. (d) FBG VS. Perfusion index.



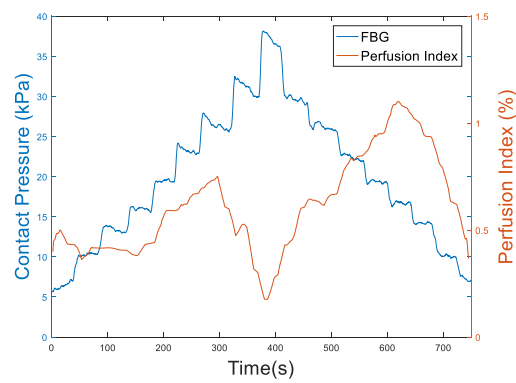
(a)



(b)

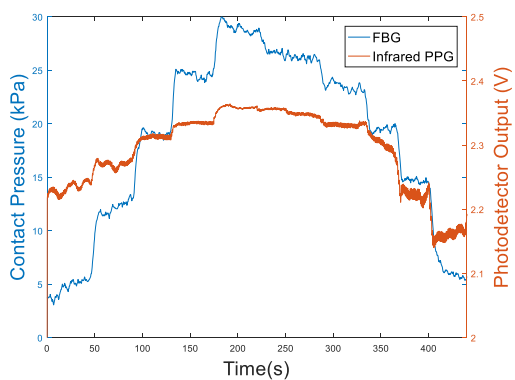


(c)

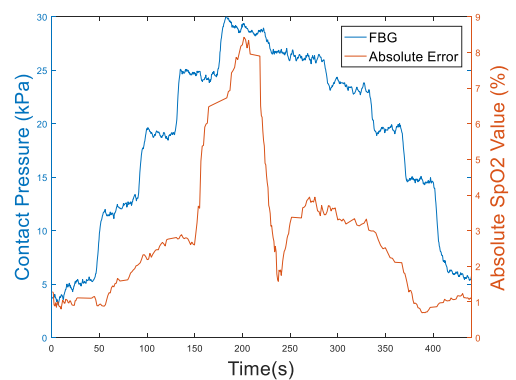


(d)

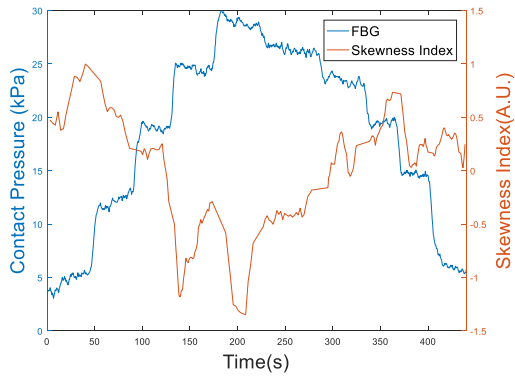
Figure C.53. Volunteer 6-2. (a) FBG VS. Infrared PPG signals. (b) FBG VS. Absolute SpO₂ error. (c) FBG VS. Skewness index. (d) FBG VS. Perfusion index.



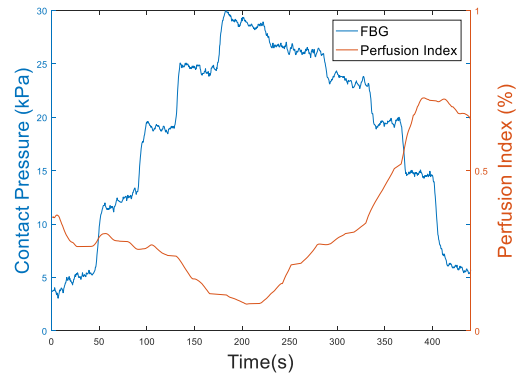
(a)



(b)

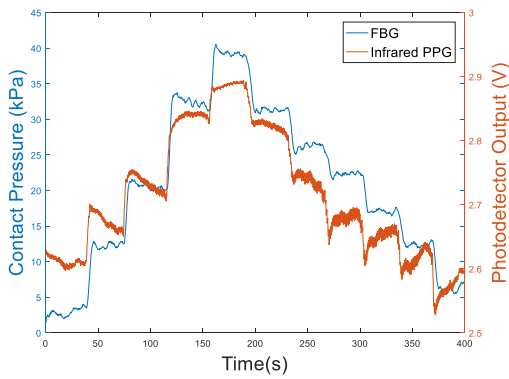


(c)

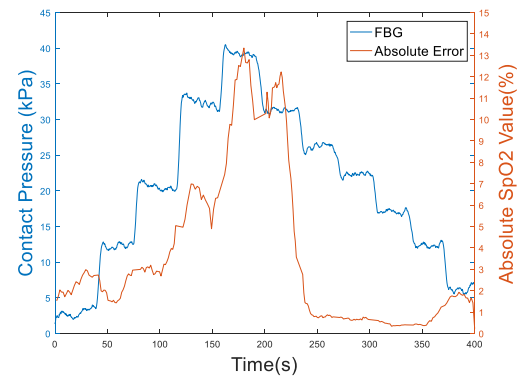


(d)

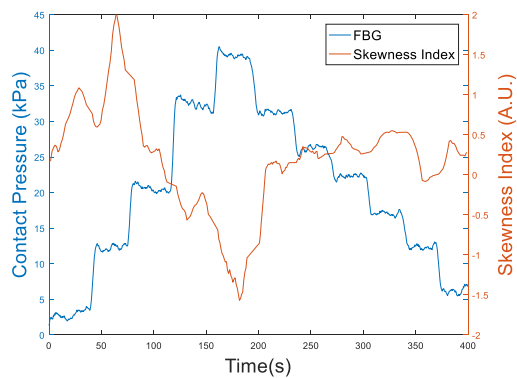
Figure C.54. Volunteer 6-3. (a) FBG VS. Infrared PPG signals. (b) FBG VS. Absolute S_{pO_2} error. (c) FBG VS. Skewness index. (d) FBG VS. Perfusion index.



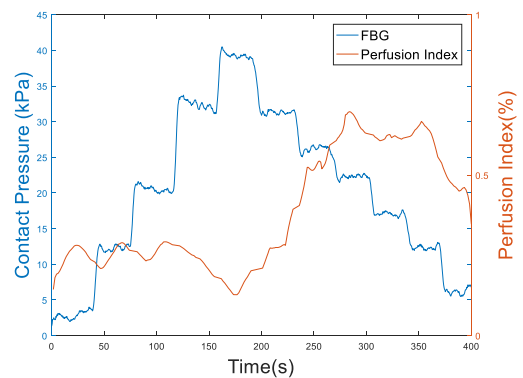
(a)



(b)

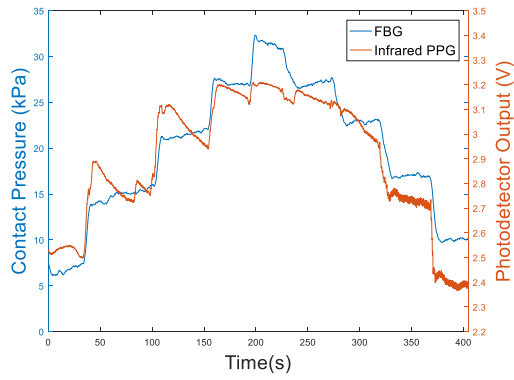


(c)

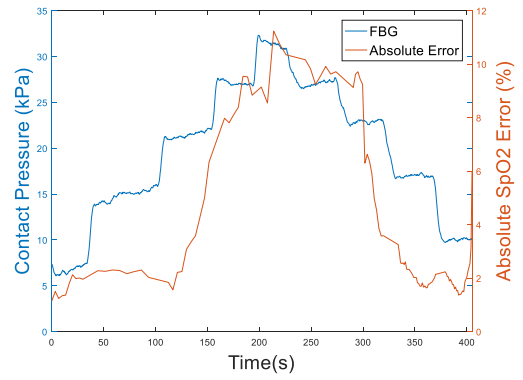


(d)

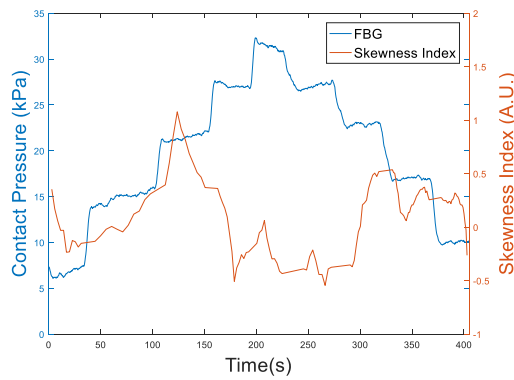
Figure C55. Volunteer 7-1. (a) FBG VS. Infrared PPG signals. (b) FBG VS. Absolute S_{pO_2} error. (c) FBG VS. Skewness index. (d) FBG VS. Perfusion index.



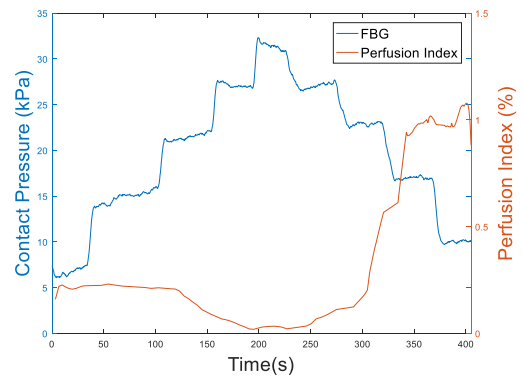
(a)



(b)

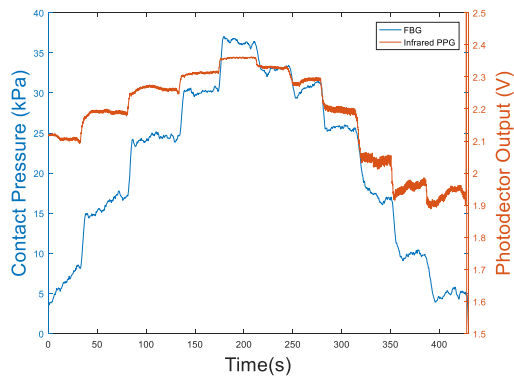


(c)

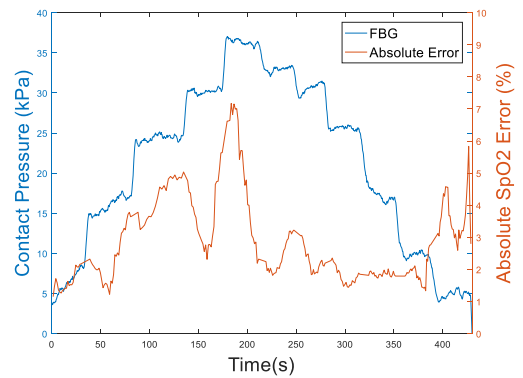


(d)

Figure C.56. Volunteer 7-2. (a) FBG VS. Infrared PPG signals. (b) FBG VS. Absolute SpO₂ error. (c) FBG VS. Skewness index. (d) FBG VS. Perfusion index.



(a)



(b)

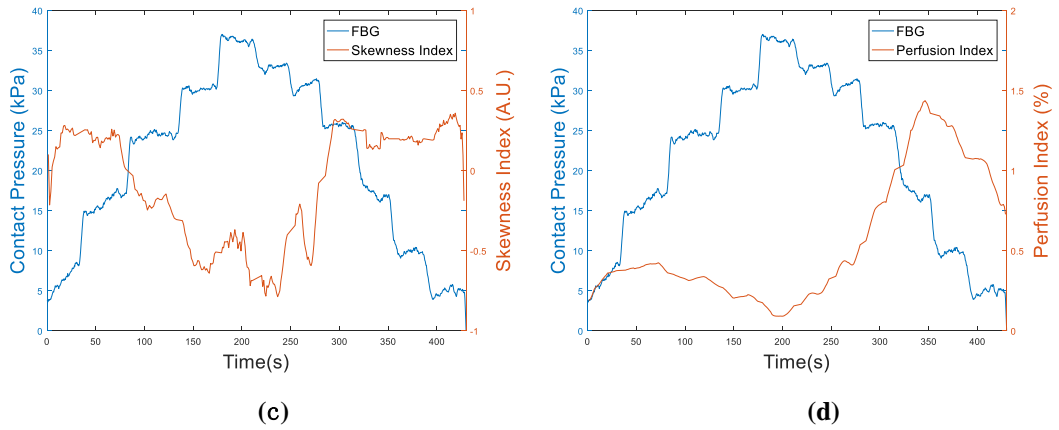


Figure C.57. Volunteer 7-3. (a) FBG VS. Infrared PPG signals. (b) FBG VS. Absolute S_{pO_2} error. (c) FBG VS. Skewness index. (d) FBG VS. Perfusion index.

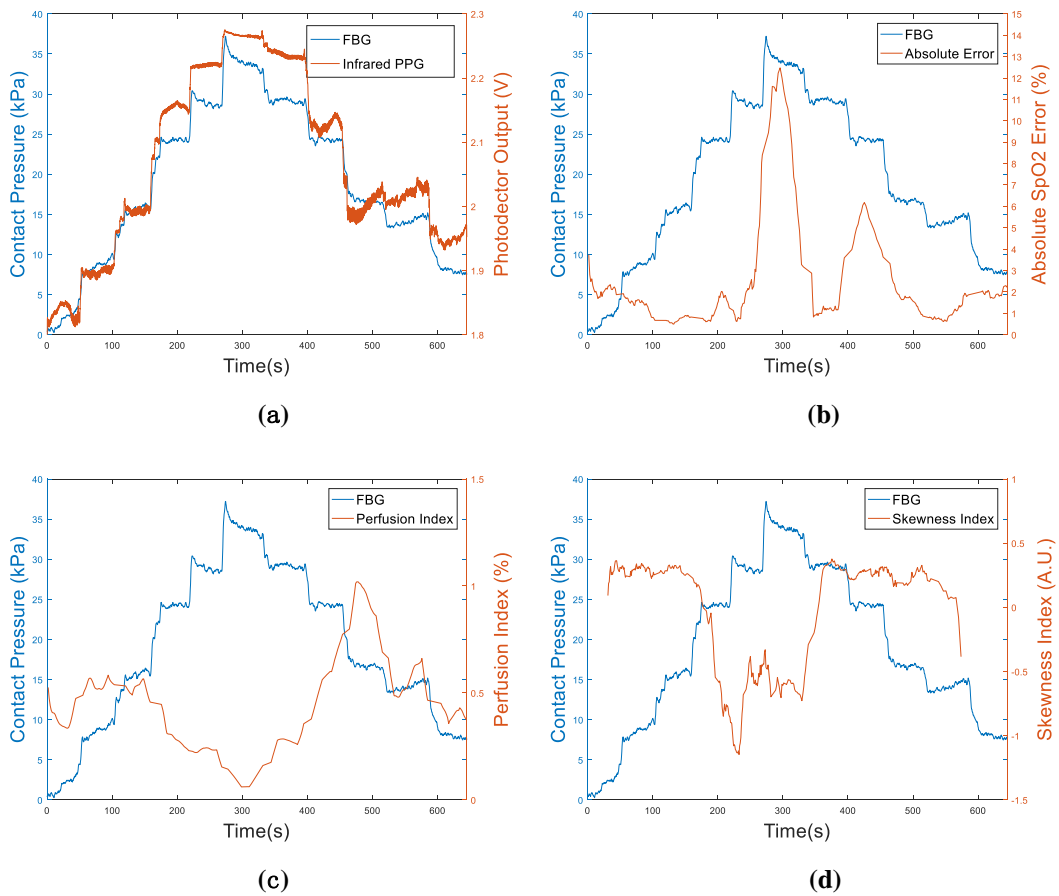
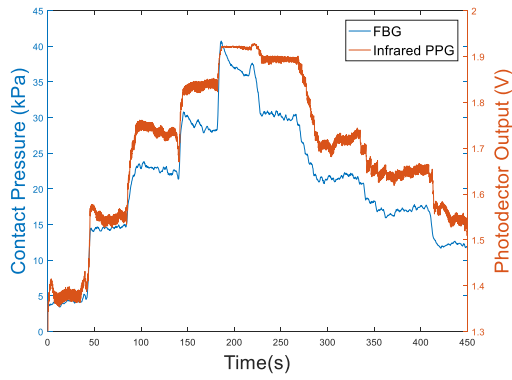
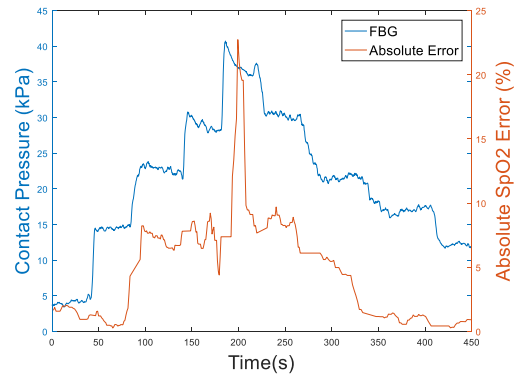


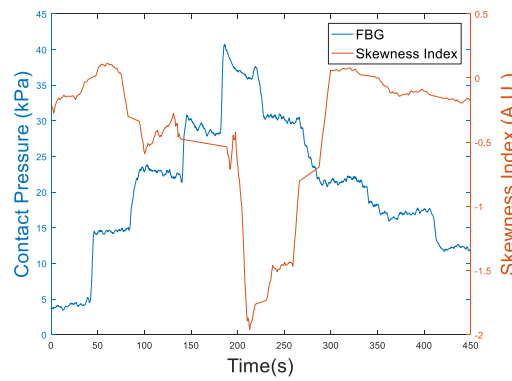
Figure C.58. Volunteer 8-1. (a) FBG VS. Infrared PPG signals. (b) FBG VS. Absolute S_{pO_2} error. (c) FBG VS. Skewness index. (d) FBG VS. Perfusion index.



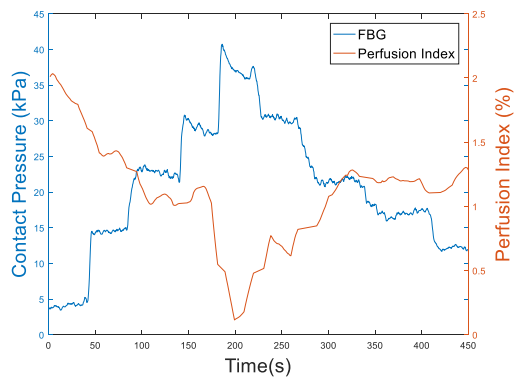
(a)



(b)

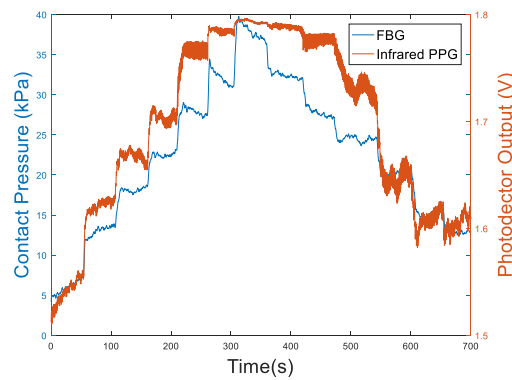


(c)

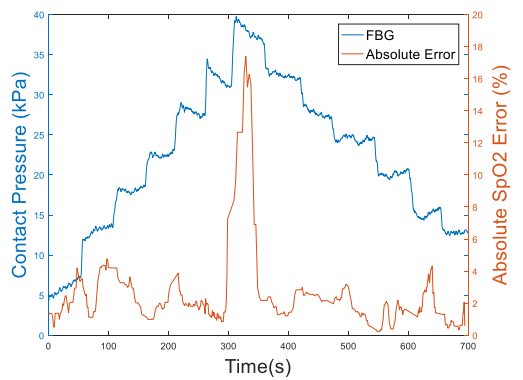


(d)

Figure C.59. Volunteer 8-2. (a) FBG VS. Infrared PPG signals. (b) FBG VS. Absolute SpO₂ error. (c) FBG VS. Skewness index. (d) FBG VS. Perfusion index.



(a)



(b)

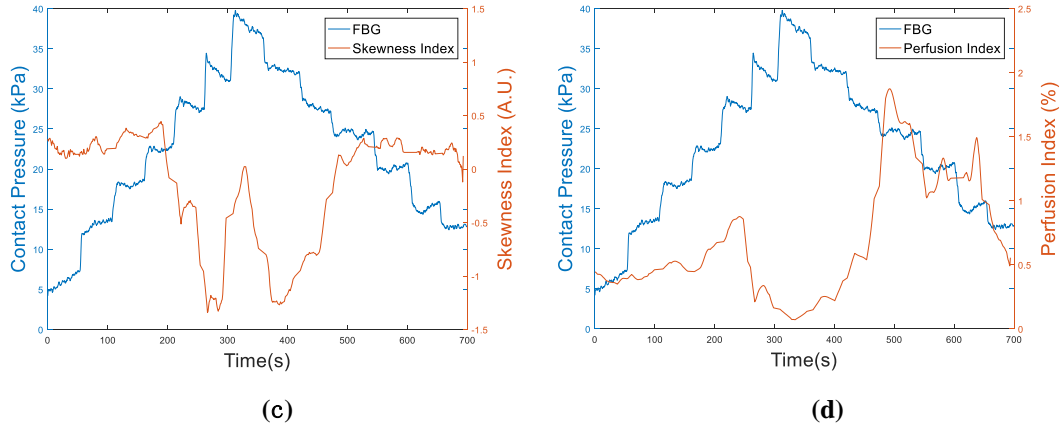


Figure C.60. Volunteer 8-3. (a) FBG VS. Infrared PPG signals. (b) FBG VS. Absolute S_{pO_2} error. (c) FBG VS. Skewness index. (d) FBG VS. Perfusion index.

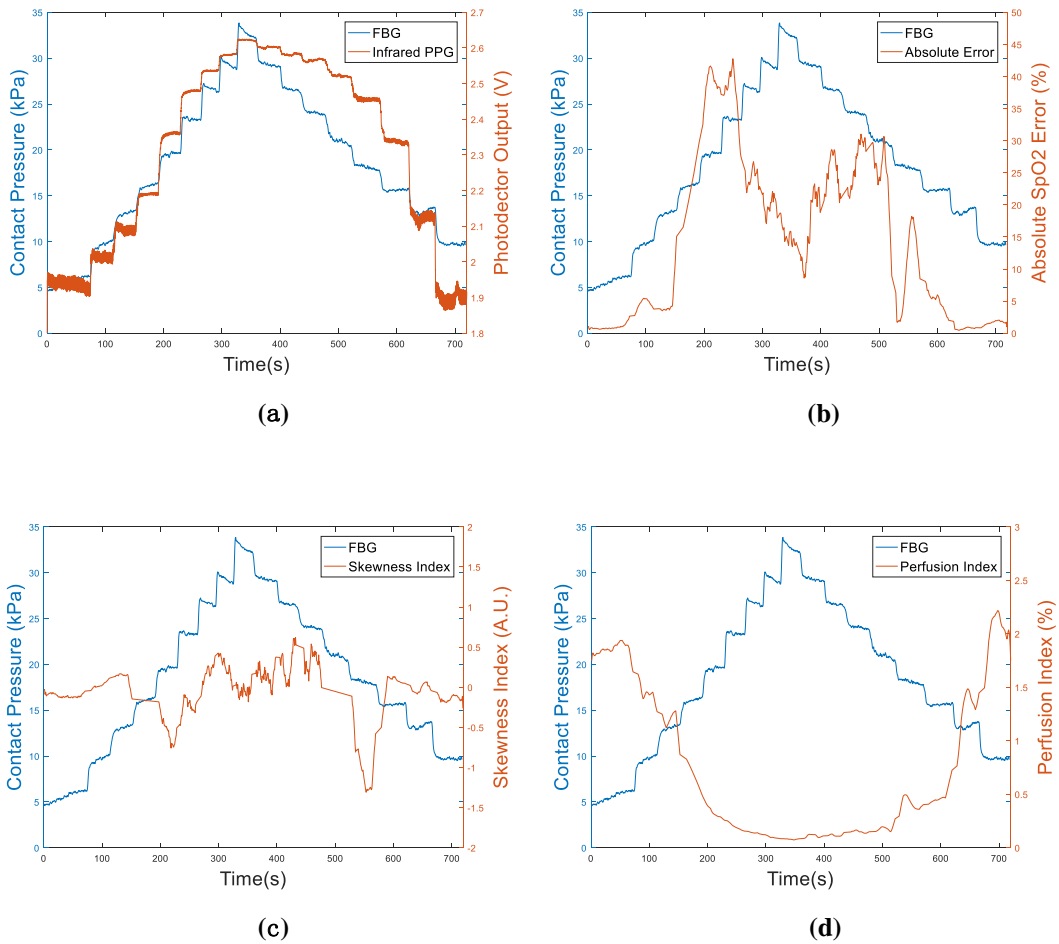
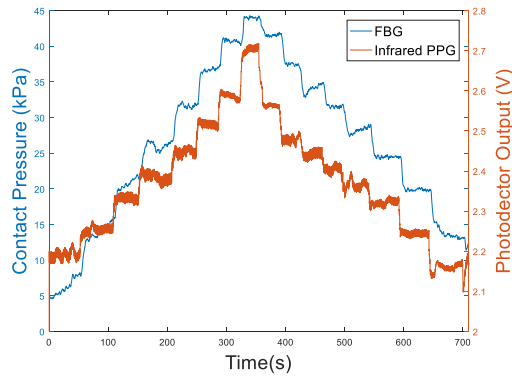
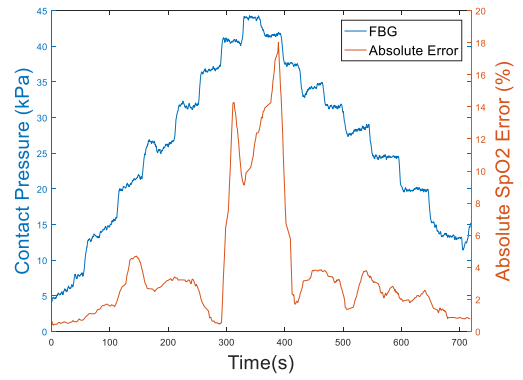


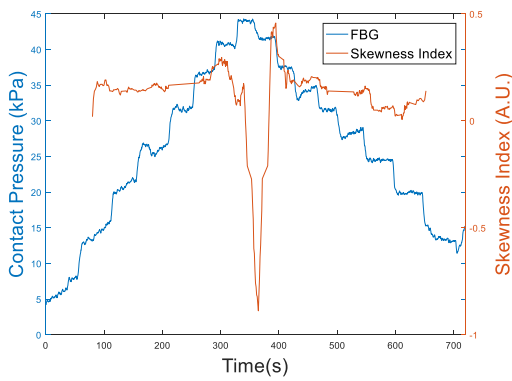
Figure C.61. Volunteer 9-1. (a) FBG VS. Infrared PPG signals. (b) FBG VS. Absolute S_{pO_2} error. (c) FBG VS. Skewness index. (d) FBG VS. Perfusion index.



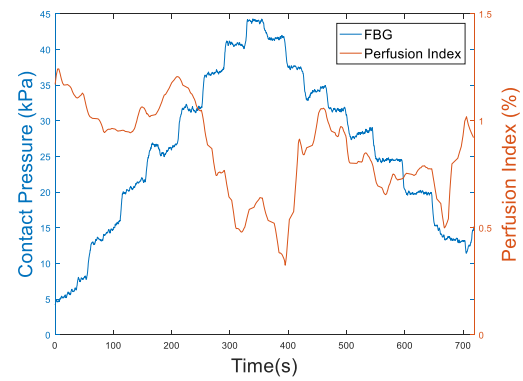
(a)



(b)

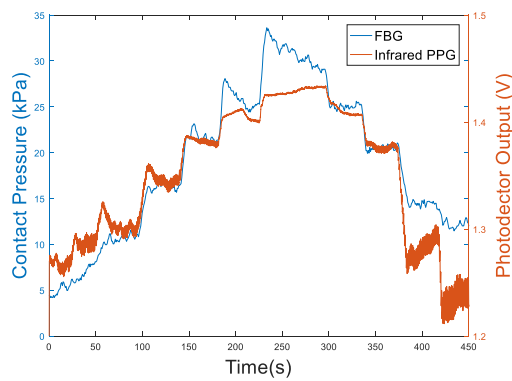


(c)

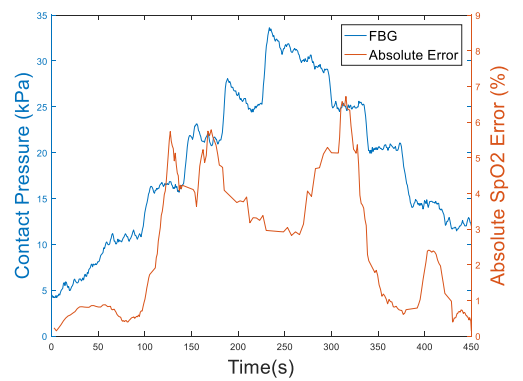


(d)

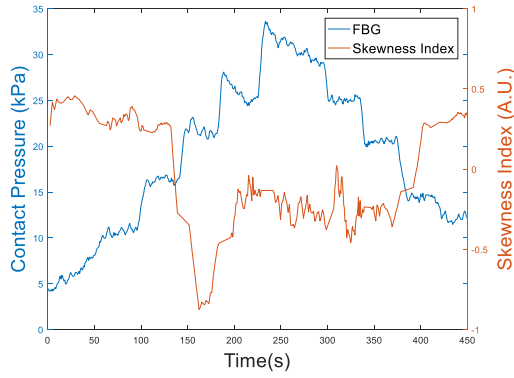
Figure C.62. Volunteer 9-2. (a) FBG VS. Infrared PPG signals. (b) FBG VS. Absolute S_{pO_2} error. (c) FBG VS. Skewness index. (d) FBG VS. Perfusion index.



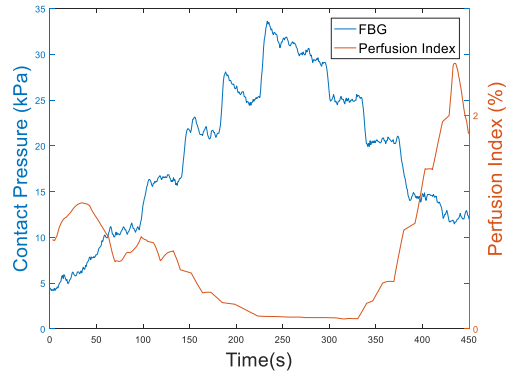
(a)



(b)

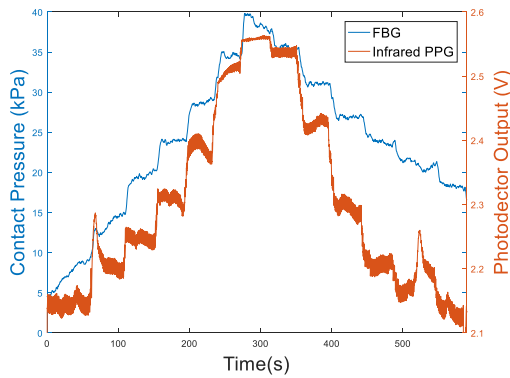


(c)

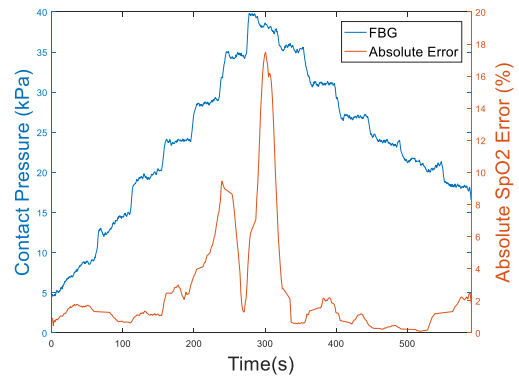


(d)

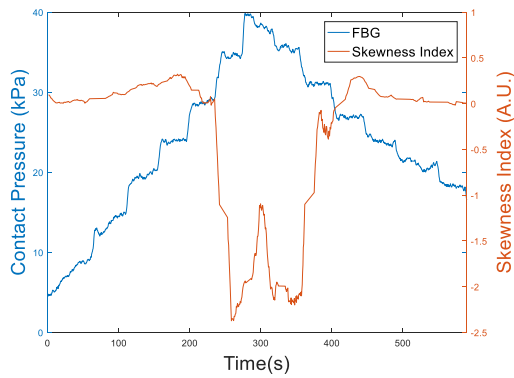
Figure C.63. Volunteer 9-3. (a) FBG VS. Infrared PPG signals. (b) FBG VS. Absolute S_{pO_2} error. (c) FBG VS. Skewness index. (d) FBG VS. Perfusion index.



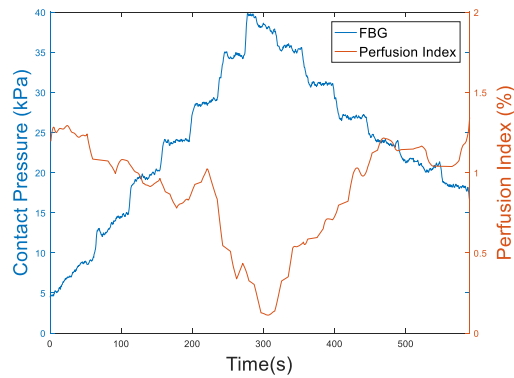
(a)



(b)



(c)



(d)

Figure C.64. Volunteer 10-1. (a) FBG VS. Infrared PPG signals. (b) FBG VS. Absolute S_{pO_2} error. (c) FBG VS. Skewness index. (d) FBG VS. Perfusion index.

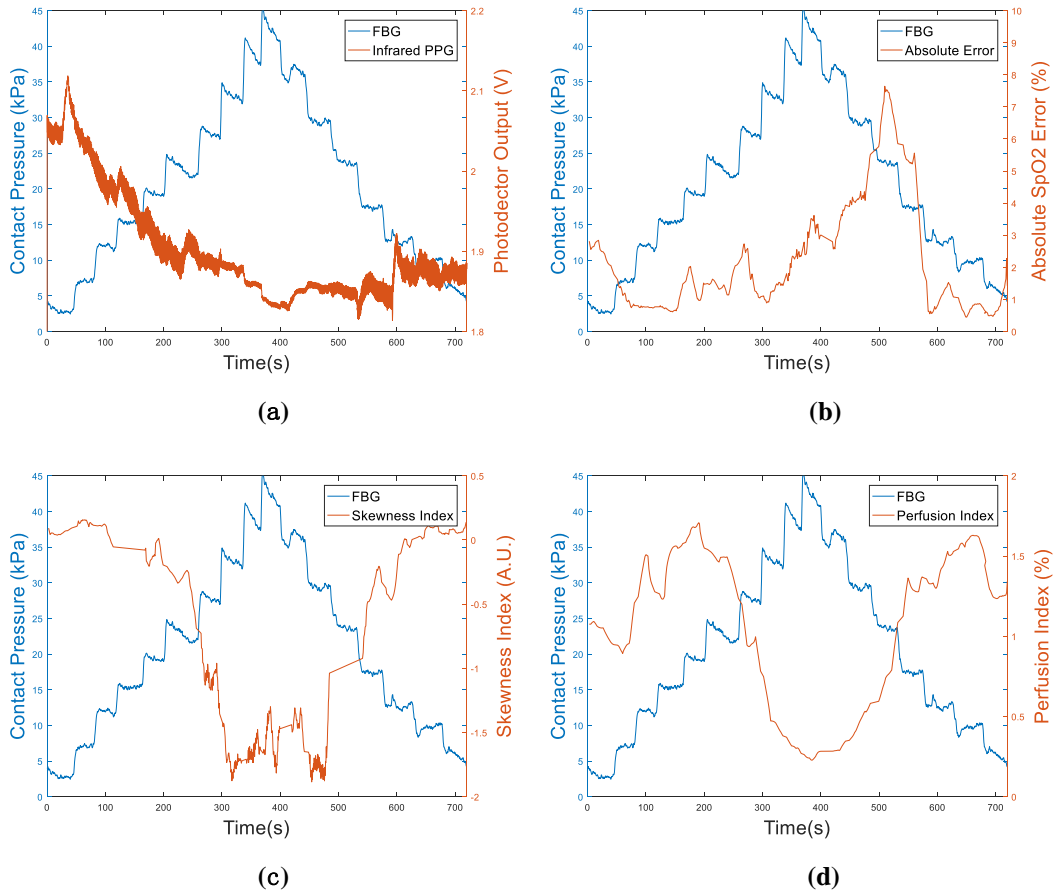
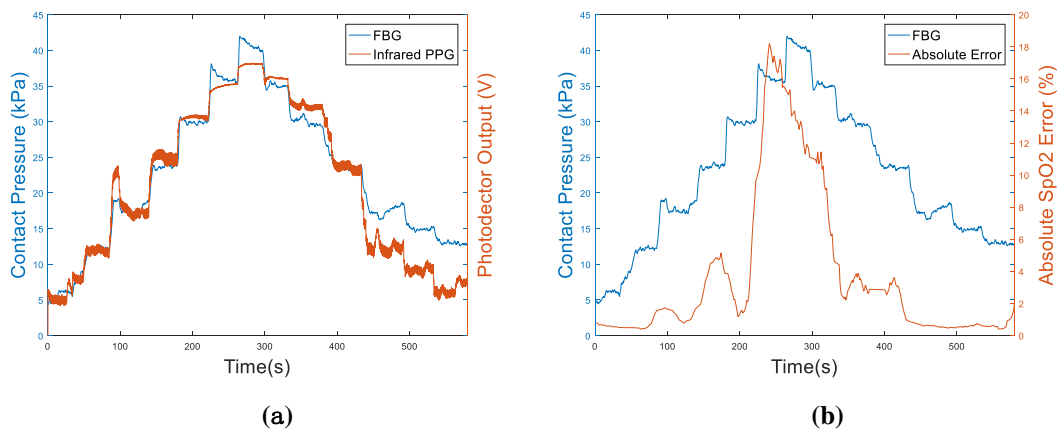


Figure C.65. Volunteer 10-2. (a) FBG VS. Infrared PPG signals. (b) FBG VS. Absolute SpO₂ error. (c) FBG VS. Skewness index. (d) FBG VS. Perfusion index.



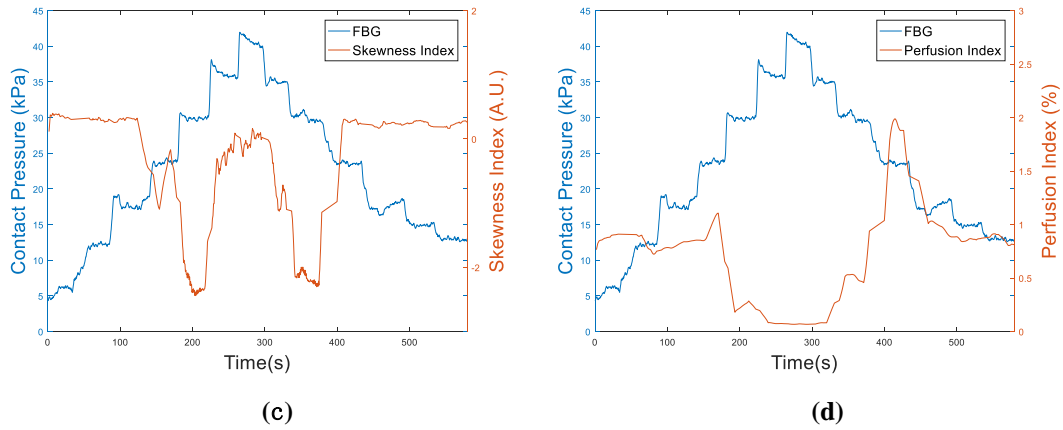


Figure C.66. Volunteer 10-3. (a) FBG VS. Infrared PPG signals. (b) FBG VS. Absolute S_{PO_2} error. (c) FBG VS. Skewness index. (d) FBG VS. Perfusion index.

C.4 10 CRT Experiments Results

In this study, the designed pulse oximetry sensor was applied to measure CRT of 10 volunteers from their index fingers which are shown from C43 to C52. Blue trace in each figure is the output of the FBG pressure sensor whilst red trace in each figure is the photonic power of reflected light signals. For each volunteer, the experiment required them to repeat the blanching-refilling process for at least ten times. Therefore, in each figure, the diagram contains at least 10 refilling signals.

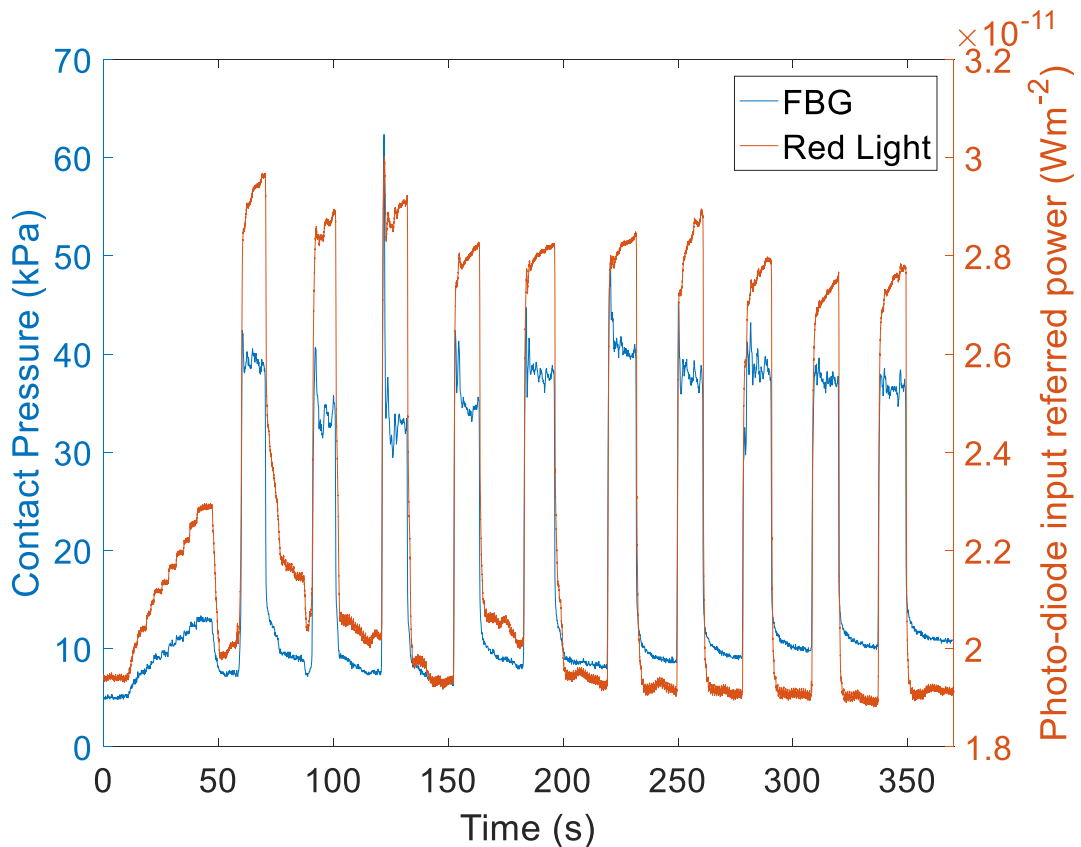


Figure C.67. Reflected light intensity measured by the designed sensor. Blue curve is the output of the FBG patch which recorded the pressure changes during the experiment. (Volunteer 1)

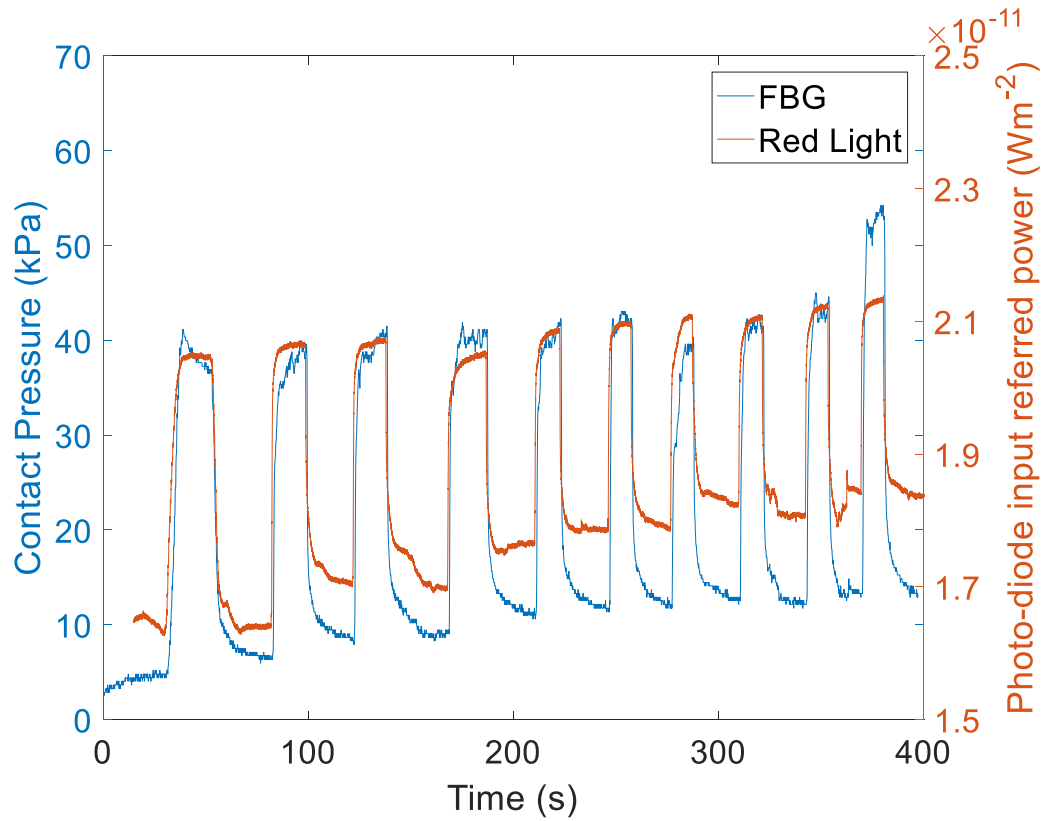


Figure C.68. Reflected light intensity measured by the designed sensor. Blue curve is the output of the FBG patch which recorded the pressure changes during the experiment. (Volunteer 2)

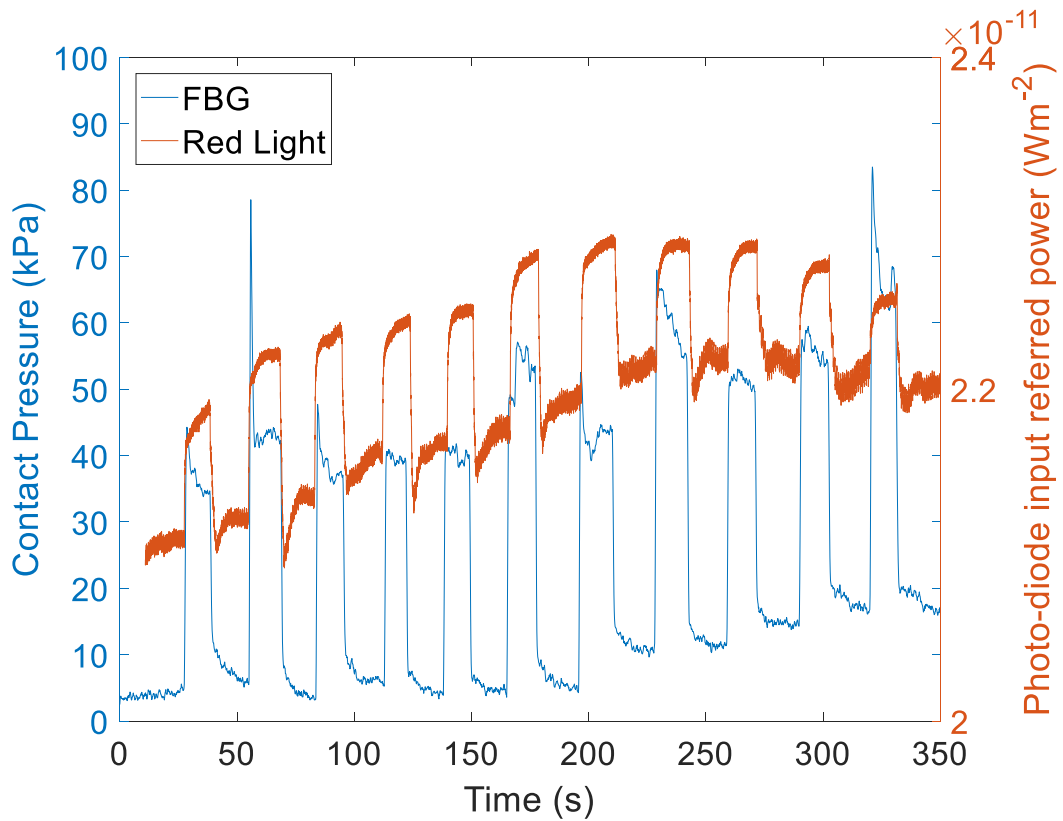


Figure C.69. Reflected light intensity measured by the designed sensor. Blue curve is the output of the FBG patch which recorded the pressure changes during the experiment. (Volunteer 3)

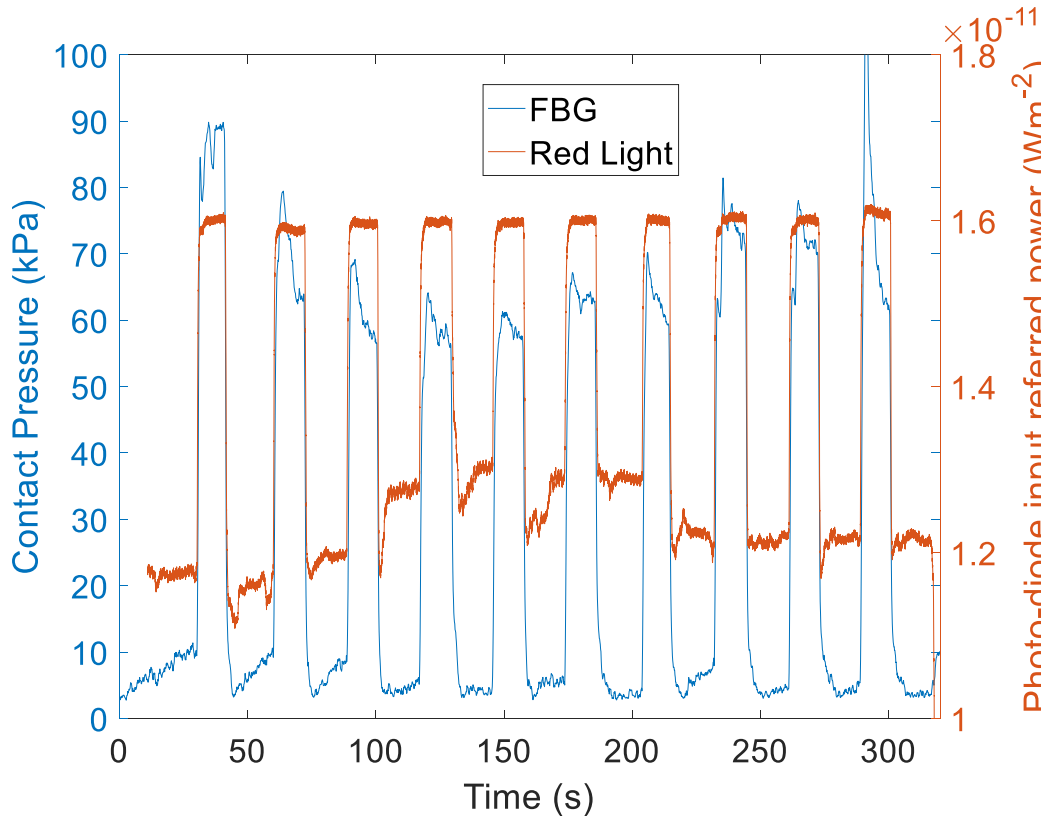


Figure C.70. Reflected light intensity measured by the designed sensor. Blue curve is the output of the FBG patch which recorded the pressure changes during the experiment. (Volunteer 4)

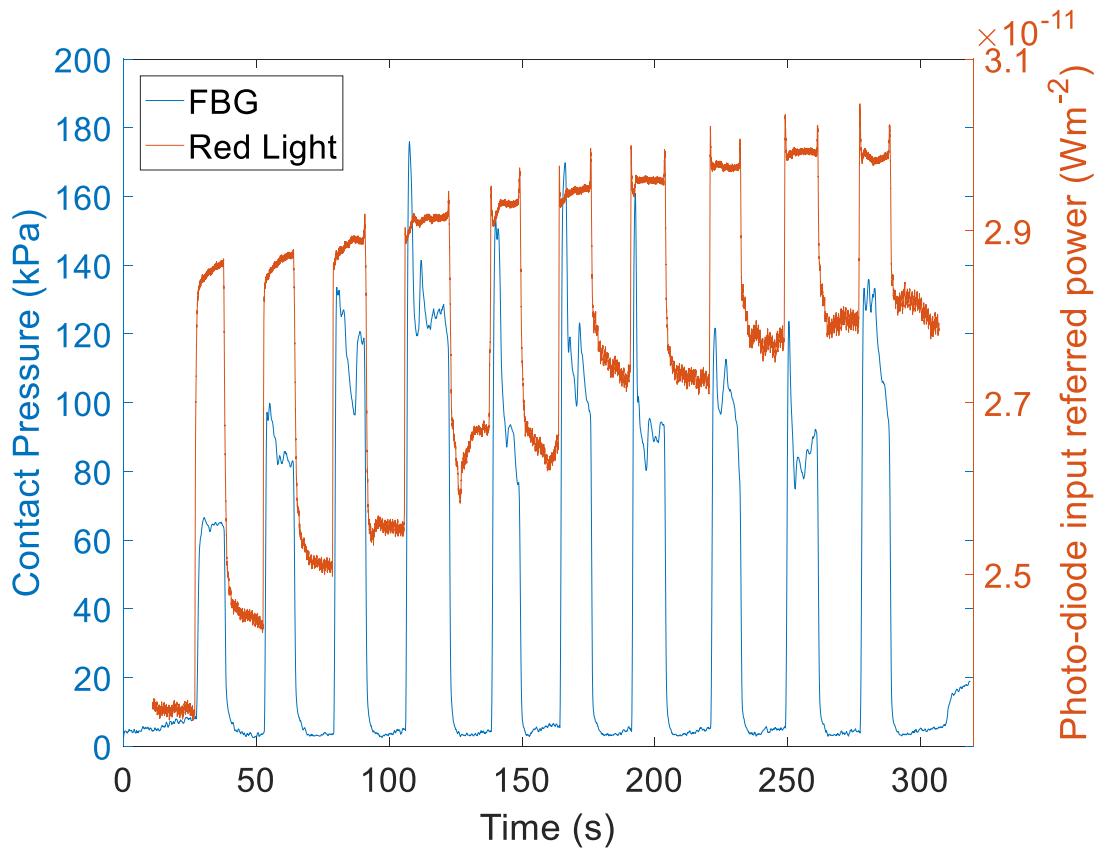


Figure C.71. Reflected light intensity measured by the designed sensor. Blue curve is the output of the FBG patch which recorded the pressure changes during the experiment. (Volunteeer 5)

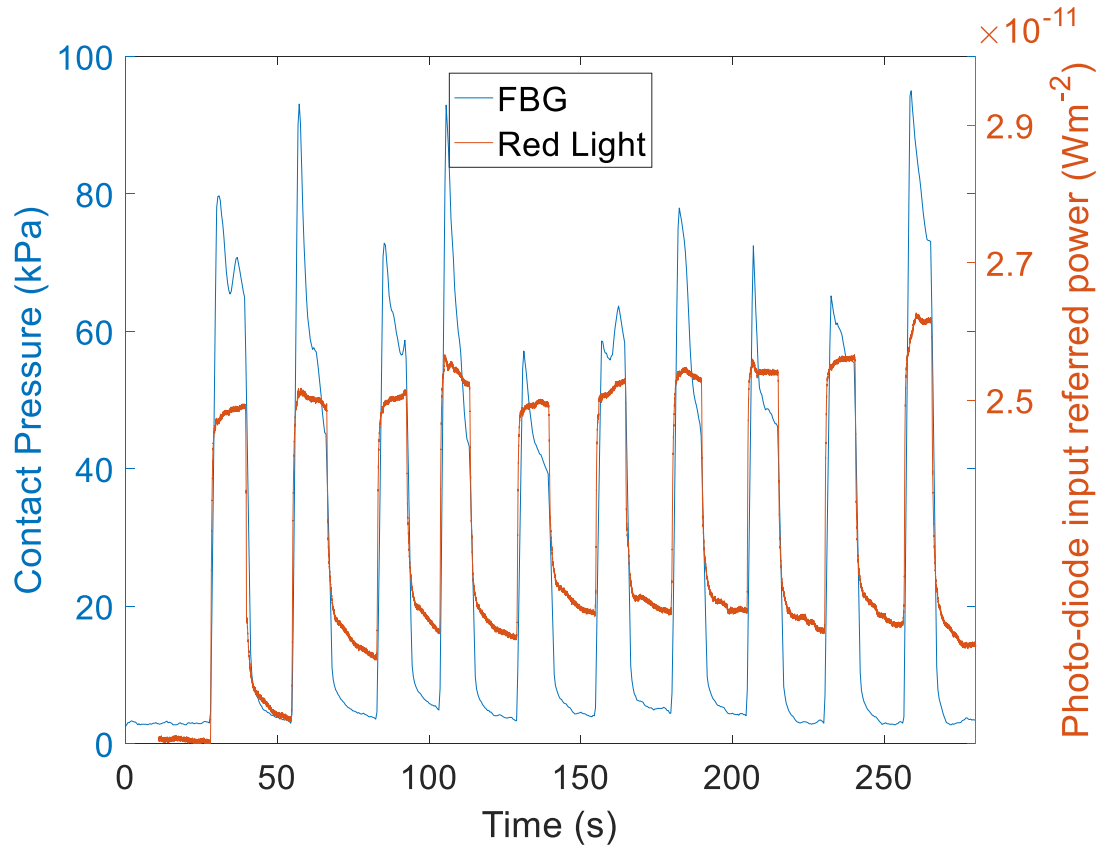


Figure C.72. Reflected light intensity measured by the designed sensor. Blue curve is the output of the FBG patch which recorded the pressure changes during the experiment. (Volunteeer 6)

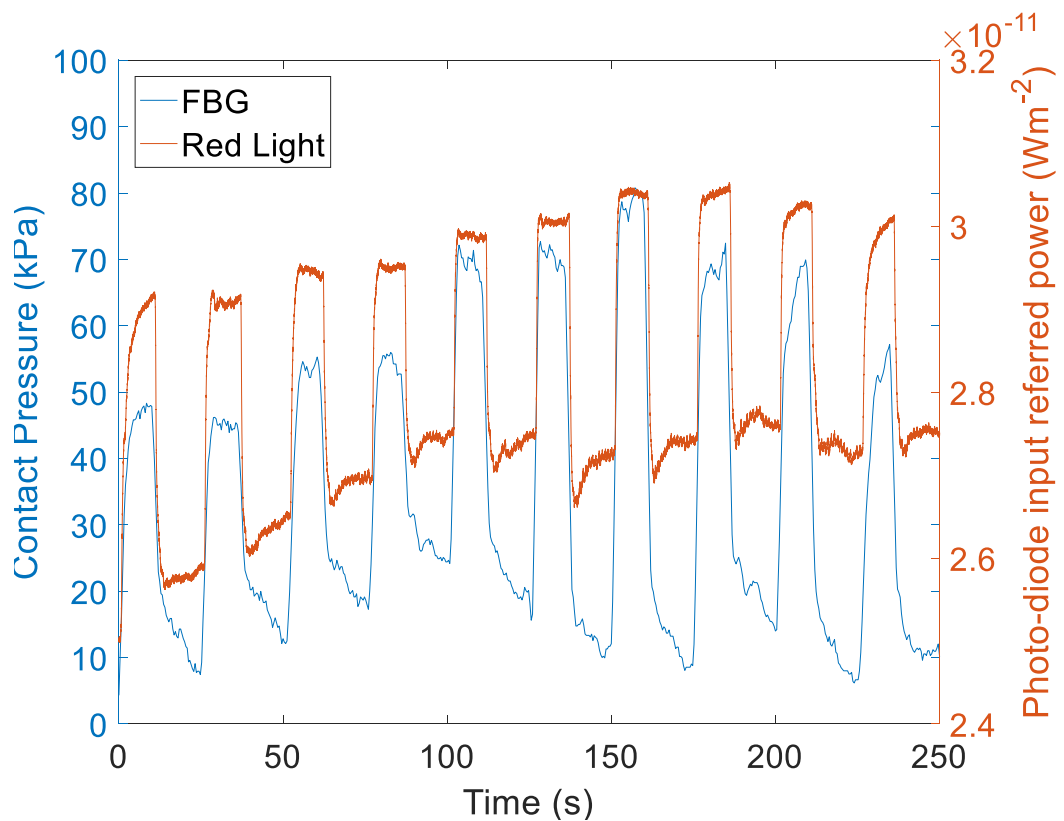


Figure C.73. Reflected light intensity measured by the designed sensor. Blue curve is the output of the FBG patch which recorded the pressure changes during the experiment. (Voluneteer 7)

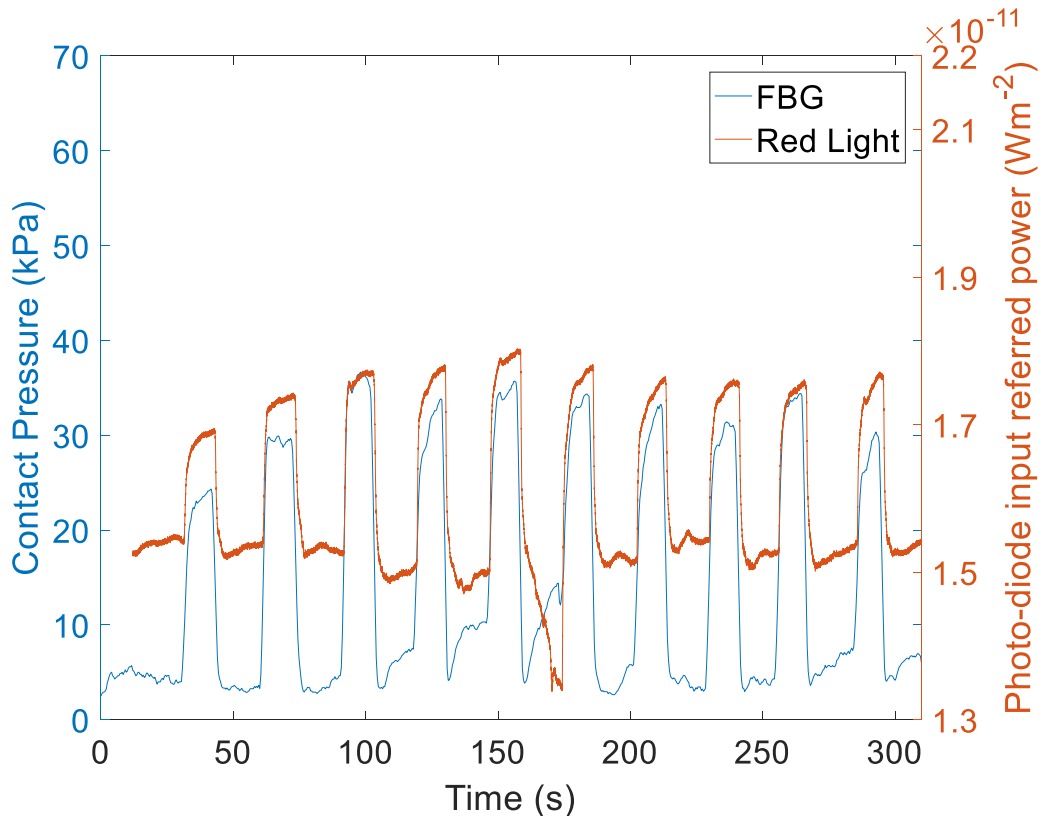


Figure C.74. Reflected light intensity measured by the designed sensor. Blue curve is the output of the FBG patch which recorded the pressure changes during the experiment. (Voluneteer 8)

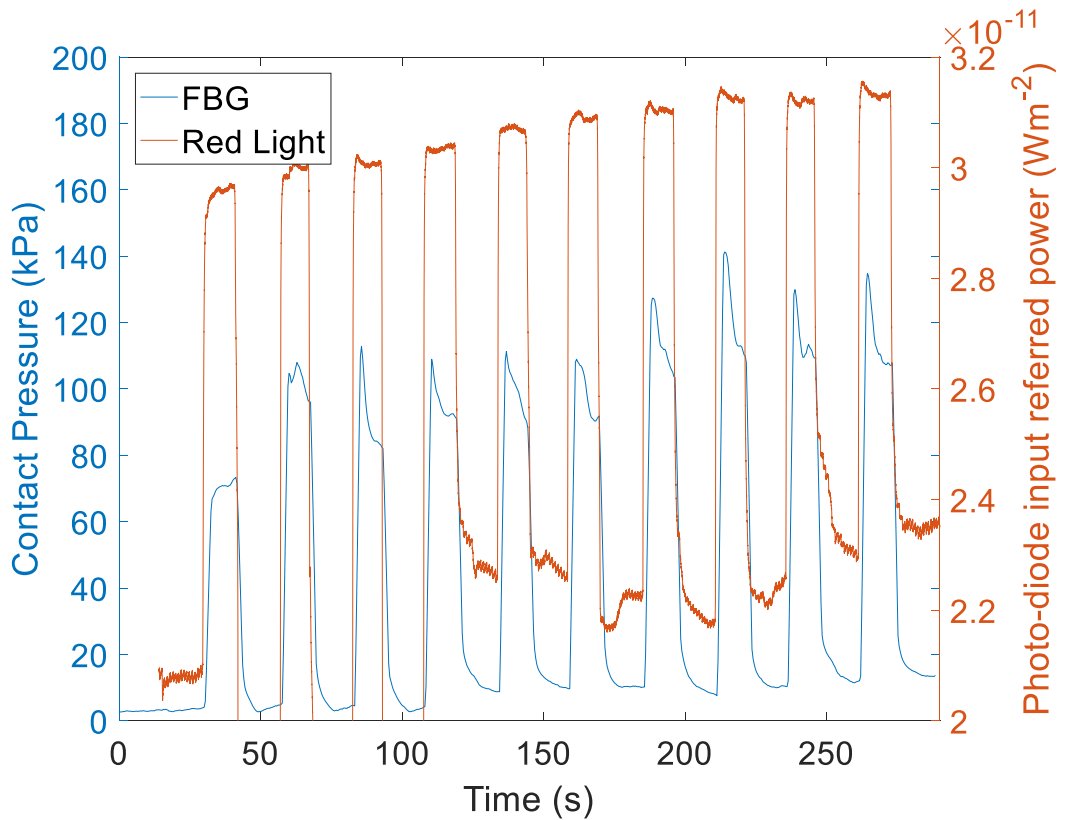


Figure C.75. Reflected light intensity measured by the designed sensor. Blue curve is the output of the FBG patch which recorded the pressure changes during the experiment. (Volunteer 9)

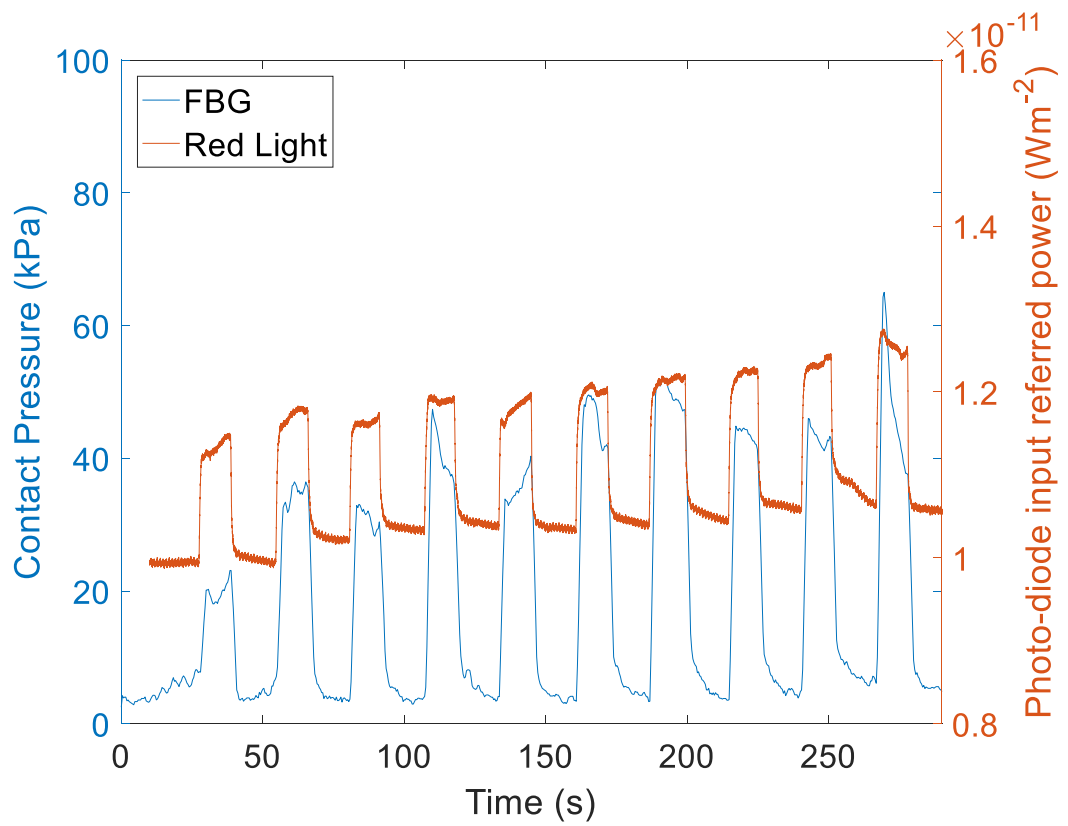


Figure C.76. Reflected light intensity measured by the designed sensor. Blue curve is the output of the FBG patch which recorded the pressure changes during the experiment. (Volunteer 10)

Appendix D

D.1 Axial Loading Strain Interference Compensation

In this research, the designed FBG pressure sensor is embedded into an epoxy patch which increase the sensor's pressure sensitivity. An additional FBG is written on the same fibre adjacent to the pressure sensing FBG, which is pressure immune for compensating the strain interference caused by the thermal extension. The schematic of the sensor is shown in the figure 3.8a. However, the strain interference generated by the external axial loading like occasionally stretches will deteriorate the pressure sensing FBG's output. Figure 6.1 shows how the external strain loading affects the pressure sensing FBG.

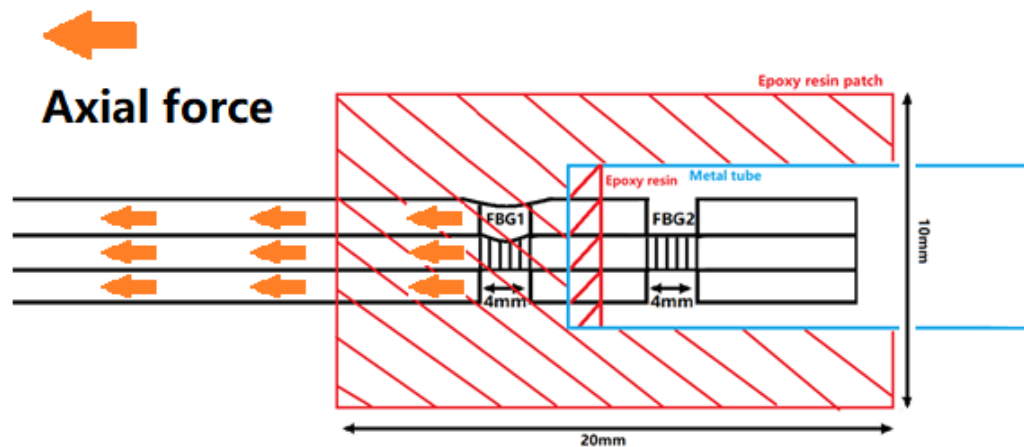


Figure 6.1 External strain loading effect on the pressure sensing FBG.

In order to compensate the external loading interference, the third FBG is added to the same fibre which is sensitive to the axial force but immune to the transversely load. In this case, the output of FBG3 can be used to compensate the axial loading interference on the pressure sensing FBG1.

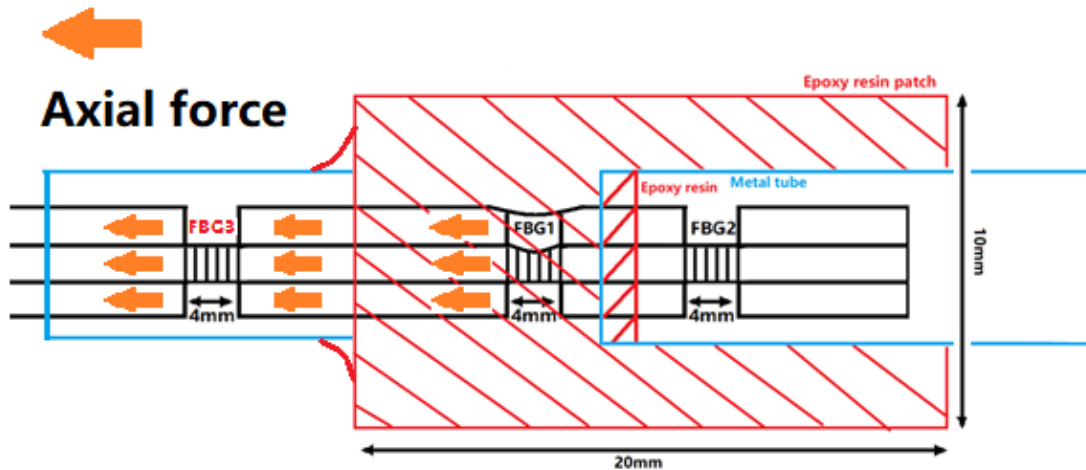


Figure 6.2 The schematic of the FBG sensor with temperature and strain compensating FBGs

D.2 Temperature Caused Low Perfusion Signals Detection

According to the S_{pO_2} test results, the designed sensor performs poorly when the perfusion index of IR or red PPG signals is very low (Section 4.4.2). Under the low peripheral perfusion state, the pulsatile component in the PPG signal is relatively weak and in this case, the performance of the PPG system will be degraded. Thus, it is important to avoid the low peripheral perfusion situation, or remove the low peripheral perfusion during the experiment.

In this research, there are two main causes that give rise to the low peripheral perfusion. The first one is the high contact pressure between the sensor and the skin which generate a sudden embolic event obstructing artery flow. The second one is the low skin temperature as discussed in section 4.4.2. The FBG pressure sensor beneath the POF pulse oximeter can be used to measure the contact force in order to prevent obstruction of arterial flow. However, the low body temperature caused low peripheral perfusion signal cannot be detected by using the designed sensor.

As the FBG sensor is capable of measuring the temperature, it can add a temperature sensing FBG sensor close to the POFs as shown in figure 6.3. In this case, it enables the skin temperature measurement which can be used to indicate the low peripheral perfusion caused by the low body temperature.

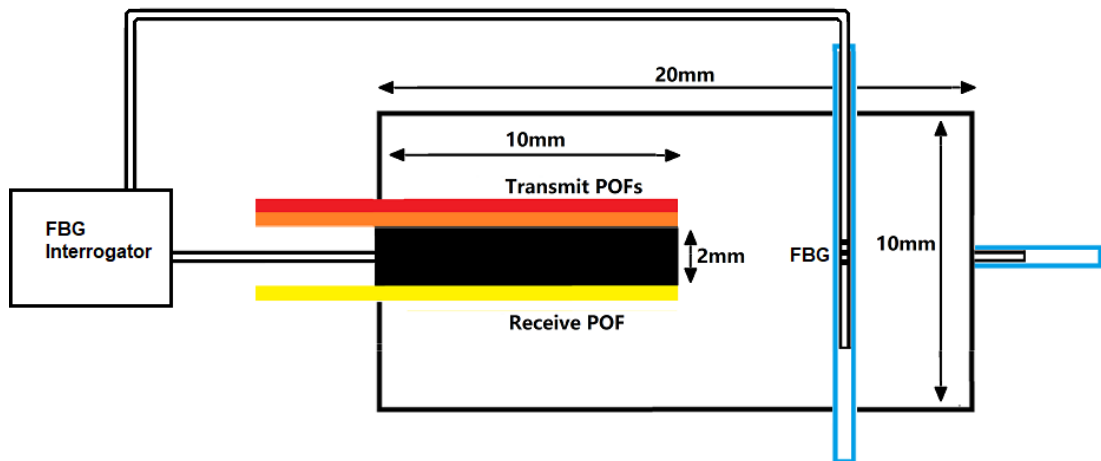


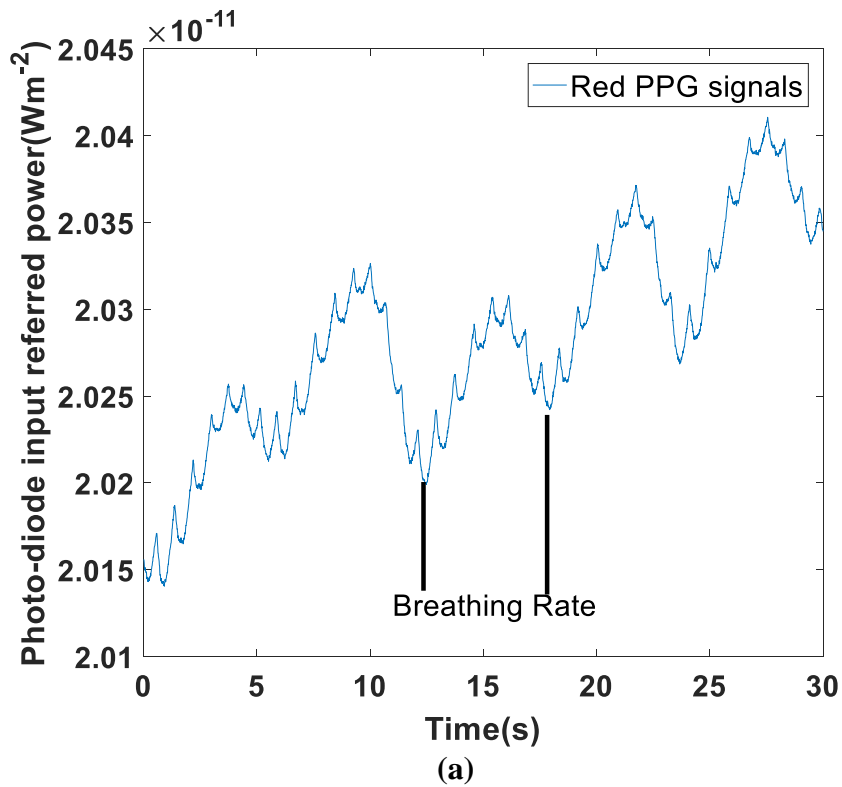
Figure 6.3 The schematic of the POF sensing patch with the FBG temperature sensor. The FBG embedded in the POF sensing patch is used to measure the skin temperature of the subject. The metal tube (blue frame) is applied to protect the FBG against the contact force interference.

D.3 Estimation of Breathing Rate Using Reflectance PPG Signals

As discussed in Section 4.3, breathing rate can be observed from the PPG signal as a low frequency, periodic variation in the baseline drift of the PPG signal [162, 163]. This drift can be extracted by using a certain band pass filter. Vegfors et.al [164] have reported a comparative analysis of different methods for measuring breathing rate including visual observation, capnography, transthoracic impedance plethysmography, an acoustic probe and reflectance PPG, and concluded that reflectance PPG performed well in respiratory measurement [164].

Figure 6.1 shows the reflectance PPG obtained from the index finger by the designed sensor while the subject breathed normally. The low frequency baseline drift caused by normal breathing could be clearly observed in figure 6.4(a). As the normal breathing rate is 12 to 20 breaths per minute [165], it can extract the breathing signal from the PPG signal via band-pass filtering the signal between 0.1 Hz to 0.5 Hz as figure 6.4(b) shown. Figure 6.5 gives the FFT results of filtered PPG signal (shown in

figure 6.4b), which could find the frequency of respiratory rate matched with the manually breathing counted rates. Since the respiratory rate was reported as an important marker of illness and predictor of cardiac arrest [166, 167], it is recommended to use obtained PPG signals to measure the breathing rate of subjects in future study.



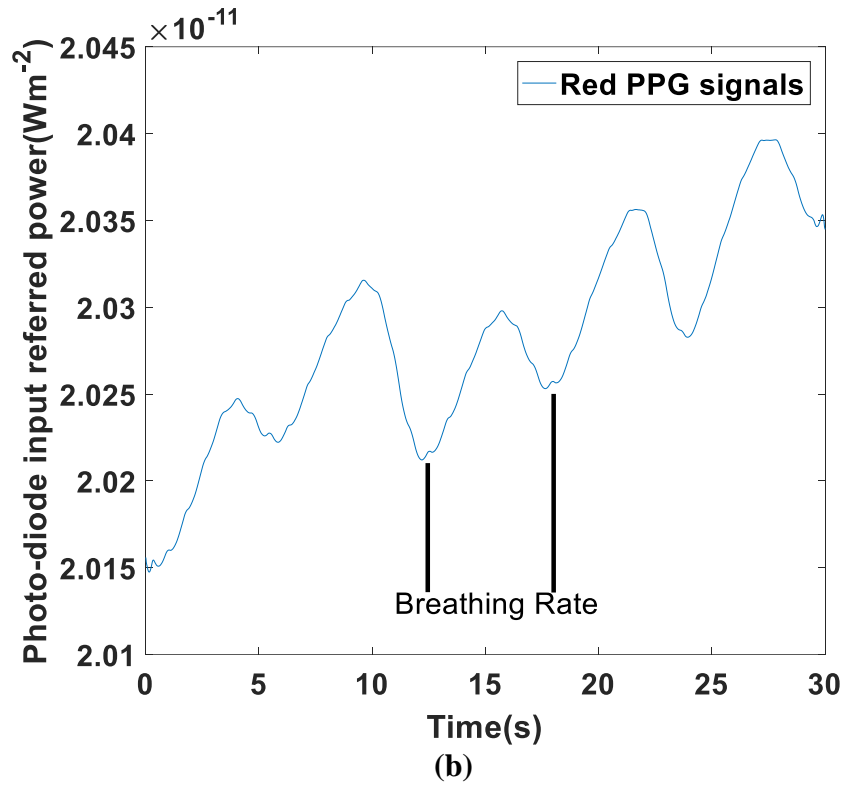


Figure 6.4 (a) Red index finger PPG clearly showing breathing and pulsatile PPG signal. (b) Band pass filtered red index finger PPG showing a breathing signal.

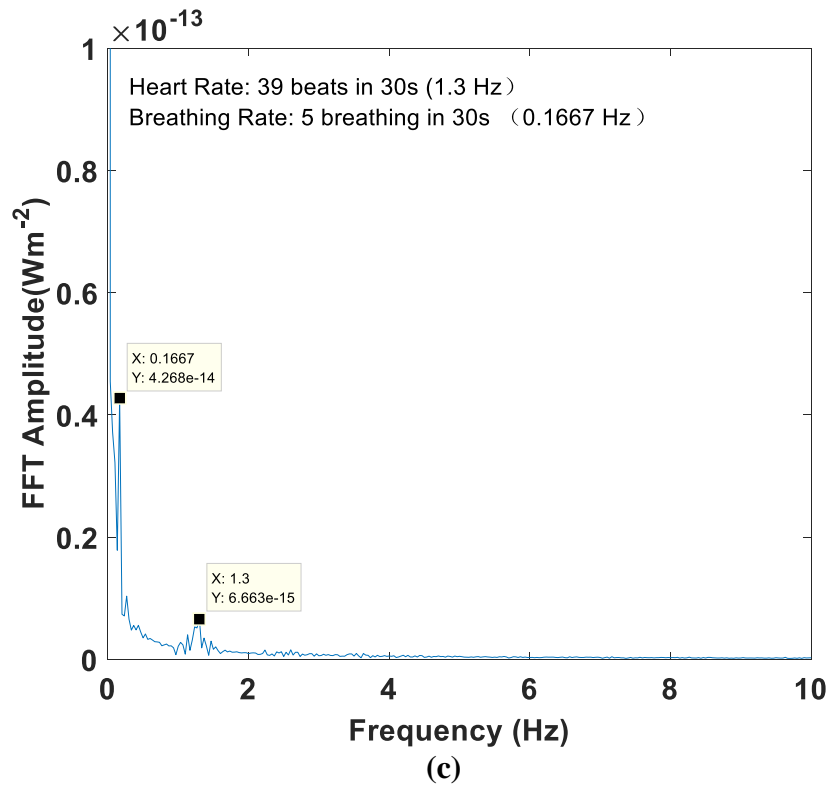


Figure 6.5 FFT analysis of red index PPG signal (shown in figure 6.1) which presents the breathing rate and heart rate.

D.4 Motion Artefact Detection

Motion artefact has been recognised as an intrinsic weakness of PPG signal capture, and has been clinically demonstrated to cause errors in pulse oximeter reading [168, 169]. As section 4.3 presented, the frequency of the AC components of PPG signals was in the 0.5 to 10 Hz while the frequency range of motion artefacts was within the same range [170]. In this case, it is difficult to extract pulsatile PPG signals or motion artefacts signals from the raw data in the frequency or time domain. In most cases, motion artefacts are seen when there is a relative movement between the sensor and the surface of the skin. Fortunately, the designed sensor has the capability to indicate when the device is in contact with the skin as the contract pressure increases. The figure below presents the FBG pressure sensor output (blue curve) with/without the index finger contacted. At the first 70 seconds, the pressure sensor was still without any load. The finger was placed on the sensor at 72 seconds which resulted in a sudden increase in the FBG sensor output. In the following 30 seconds, the finger was sited on the sensor. According to the test result, the sensor can recognise the contact between the skin and the sensor. In this case, the designed sensor has a direct way of measuring the displacement between the sensor and the skin.

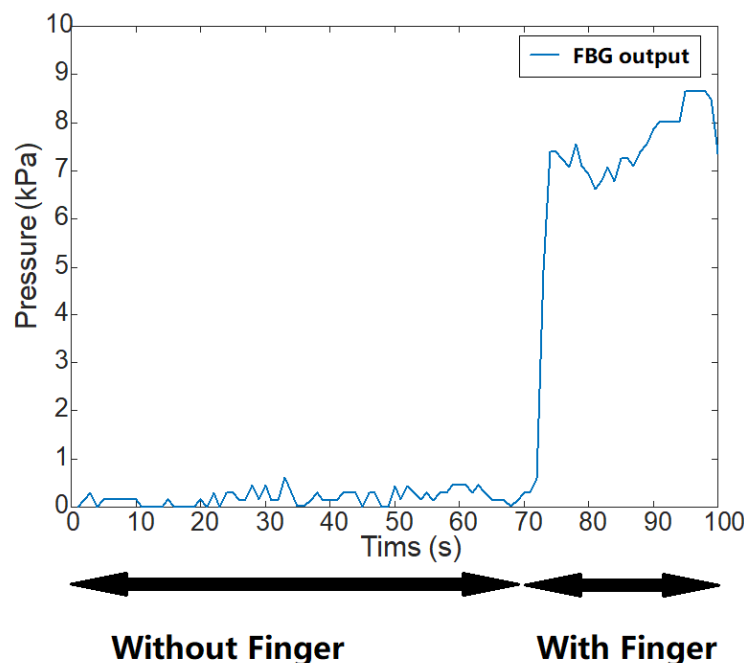


Figure 6.6 The pressure output of the FBG sensor with/without the finger contacted.

In the future work, an experiment to validate the capability of the designed sensor for measuring the motion artefacts can be designed. The figure below shows the schematic

of the control system which is used to move the sensor relative to skin in a controlled way. The rod on the top of the nail is applied to fix the finger on the sensor whilst the electrical linear actuator beneath moves the sensor.

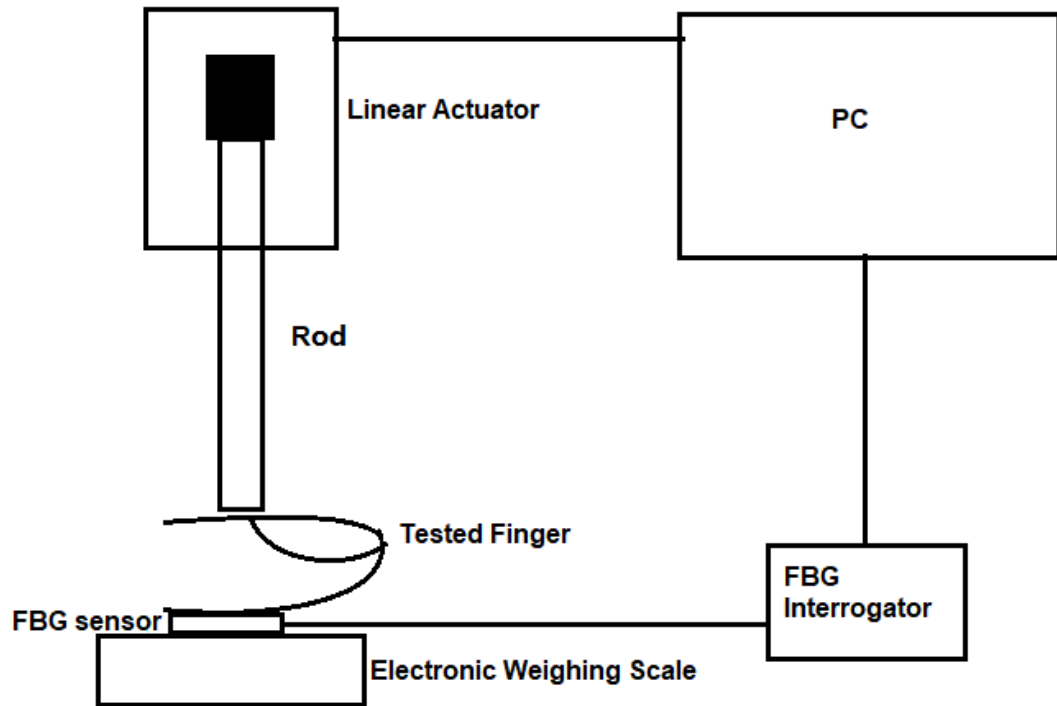


Figure 6.7 The schematic of the pressure control system. The electronic linear actuator is driven by the PC which lifts and lowers a rod. By controlling the position of the rod, the system can control the pressure applied on the finger. The weighing scale beneath the FBG sensor is used to record the transversely loading force which is used to calibrate the FBG pressure sensor.

With the exception of the hardware design, investigation of how to improve the algorithm for eliminating motion artefacts in PPG such as using the least mean squares (LMS) adaptive filter or periodic moving average filter [171-173] is required.

D.5 Plethysmography Using an FBG Pressure Sensor

In photoplethysmography, the reflected light intensity changes with blood volume. This blood volume changes in arteries and veins could also be detected via the contact pressure changes. In previous research, the FBG sensors were attached to the skin to detect the radial artery pulse waveform (plethysmography). The sensor designed in this research also applied the FBG sensor to measure the pressure. Although the FBG sensor was not directly in contact with the skin surface, it can detect the pulsatile signal in the radial artery as well. Figure 6.8 gives the contact pressure changes during the

PPG measurement. It clearly shown that the contact pressure was changing opposite to the intensity of PPG, which shown the potential of using FBG pressure sensor to count HR of subjects. In this case, the FBG sensor output could be used to remove PPG and simplify instrumentation, which is recommended to be investigated in the future study.

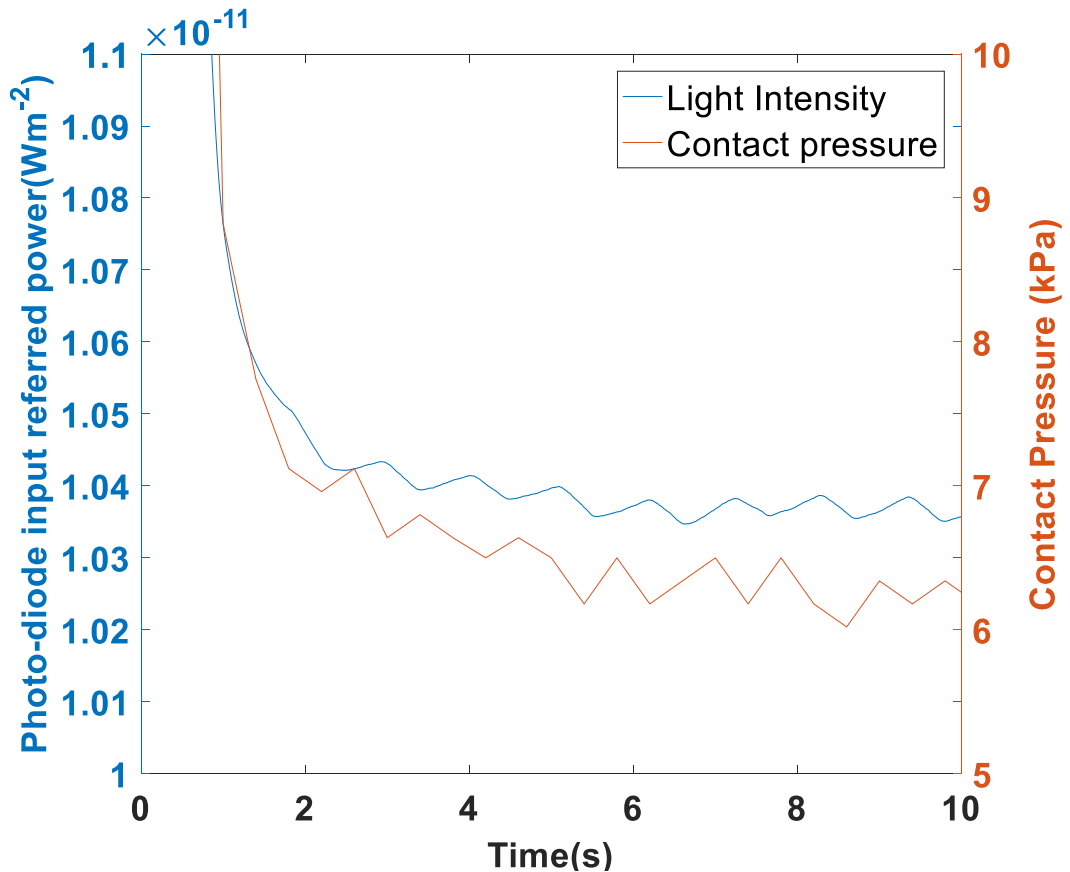


Figure 6.8 Index finger contact pressure showing the pulsatile signal which has opposite trends to the PPG signal.

D.6 Lock-in detection with quadrature demodulation

In this research, the signal processing part did not consider flicker noise. According to equation 4.10, it clearly shown that the flicker noise is inversely proportional to the frequency of the signal. Since the frequency of the PPG signal for a healthy adult is about 1 Hz, the flicker noise should not be ignored. Thus, the future work of this research is recommended to filter the flicker noise.

The channel access method applied in this research is TDMA which cannot separate the flicker noise and the target signal. Therefore, a lock-in amplifier could be applied in order to detect target signals in the presence of noise. Lock-in amplifier is a type of

amplifier which combines a band-pass filter, amplifier and a multiplier to demodulate the detected signal. In this case, the lock-in amplifier can extract the signal with a known carrier wave from a noisy environment. Figure 6.9 shows the schematic of the lock-in amplifier with quadrature demodulator based on the PhD thesis of Grubb [126]. The light source is driven at a carrier frequency away from the flicker noise and then subsequently demodulated back to base band.

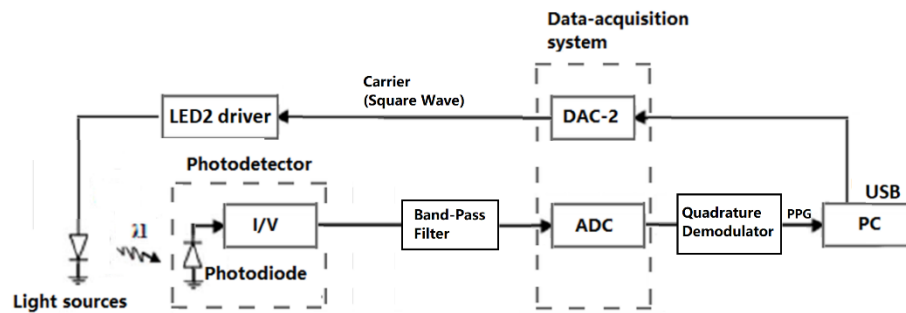


Figure 6.9 Lock-in Amplifier with the quadrature demodulator

D.7 CRT Simulation System

In section 2.4, it has mentioned that the predominant method of measuring CRT is to manually count the time using a stop-watch. Obviously, this method is highly observer dependent, and vulnerable to the background interference. In this case, it is hard to validate the CRT device such as the sensor designed in this research project. In order to prove the accuracy and reproducibility of the CRT sensor designed with the quantitative evidence, a flexible CRT simulation system is recommended.

One method to simulate the CRT is to modulate a light source. In section 5.2, the test results show that the capillary refilling process could be fitted by an exponential curve with a certain baseline. In this way, it demonstrates that the capillary refilling process could be simulated with known properties. Therefore, it could calibrate the designed CRT sensor by exposing the sensor to the modulated light.

D.8 The Photonic Sensing Sock

This research has combined a POF based PPG sensor with an FBG based pressure sensor. The integrated sensor has achieved the CRT measurement on the finger, however, this CRT sensor has two limitations. One is that the sensor is only compatible

for the finger CRT measurements. The other is that the sensor requires the subject or clinician to load and release the external pressure to complete the blanching process.

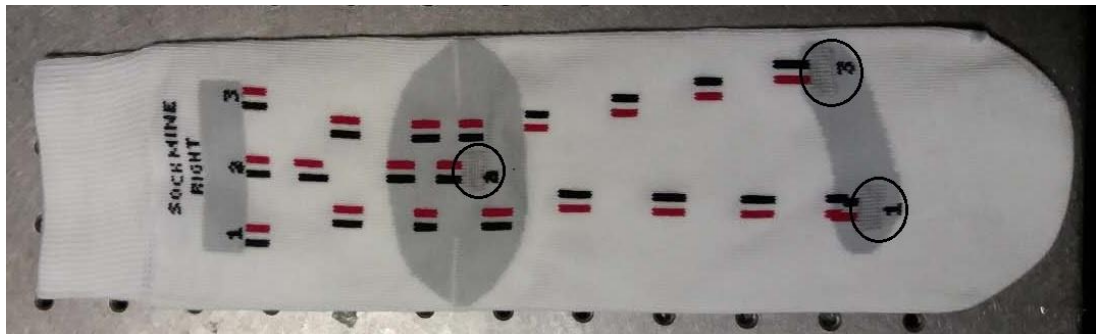
As described in section 1.1, CRT has potential in predicting diabetic foot ulcers. Foot ulcers are a common complication of diabetes as the cumulative lifetime incidence can reach up to 25%. Hence, a sensing sock measuring the CRT on the sole of the foot is worthy of further investigation by clinical researchers. What's more, for measuring the CRT on the sole of the foot, the blanching pressure can be naturally generated during the walking process as every walking step results in a natural blanching pressure under the foot. People usually have a constant gait cycle (stance phase and swing phase) which gives rise to a relatively constant pressure in terms of the duration and the magnitude. In this case, the blanching pressure arising from the walking step is beneficial for high accuracy CRT measurement.

Therefore, it could design a photonic sock to measure the walking CRT from the sole of the foot. In walking CRT measurement experiments, the reflected light could be detected by POF based sensors of which were composed of two 45° cleaved POFs. However, for recording pressures, the FBG pressure sensor was not reliable due to two reasons. The first was the value of exerted blanching pressures were beyond the range of the FBG pressure sensor. The peak pressure under normal feet in standing and walking is ranged from about one hundred to one thousand kilopascal at different positions on the sole of the foot [174-176], and the FBG pressure sensor was designed for low level pressure detection. The second reason was the additional strain interference problem of the FBG fibre. As described in section 3.3, the designed FBG pressure sensor was not immune to the strain. During the experiment, the strain generated on the fibre arising from the walking was not easily preventable. Therefore, a pressure sensing sock made of a conductive was introduced to observe the walking pressure under feet. It could replace the conductive yarn pressure sensor with the FBG pressure sensor in the future to improve the performance of the sensing sock. As the monolithic integrated optic microchip technology was reported as a method to produce miniature interrogators [177-179], the monolithic integrated optic microchip is recommended to be used in the future version of the sensor as well.

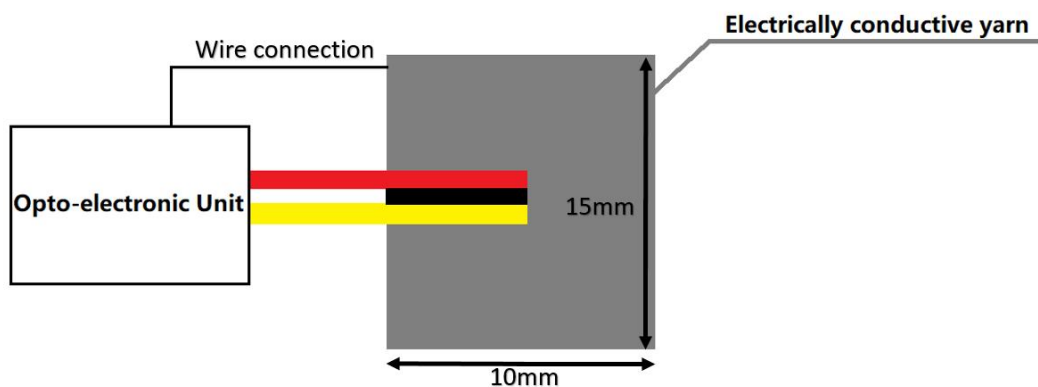
Appendix D.8.1 introduced the configuration of the sensing sock and the incorporated opto-electronic unit. Appendix D.8.2 describes the experiments and presents test results.

D.8.1 Photonic Sensing Sock

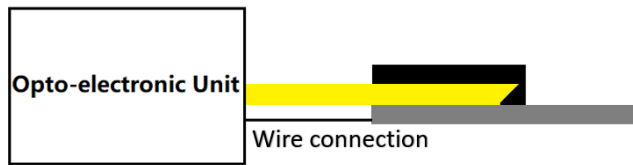
The sock shown in figure D1 integrates three sensors each consisting of a pair of 45° cleaved POF (as described in section 4.1.1) into the textile structure at three different positions (circled in figure D1). Electrically conductive yarn is situated at the same positions as the POF sensors sited (in black circles). The textile sensors were developed by Footfalls and Heartbeats (UK) Ltd. The yarn is a spun staple fibre yarn which is composed of 80% low pill PES (polyester) and 20% Inox steel fibre AISI 316L. The knitted structure changes arise from the loading pressure changes that alters the electrical impedance [180, 181]. Thus, the sensing sock is capable of detecting reflected light signals and pressure changes at three positions on the sole of the foot. Figure D2 shows the plan view and side view of the integrated POF sensor with the electrically conductive yarn sensor.



D1 Photonic sensing sock. Three black circles highlight the positions of the POF sensors. The grey regions are pressure sensors comprised of electrically conducting yarn.



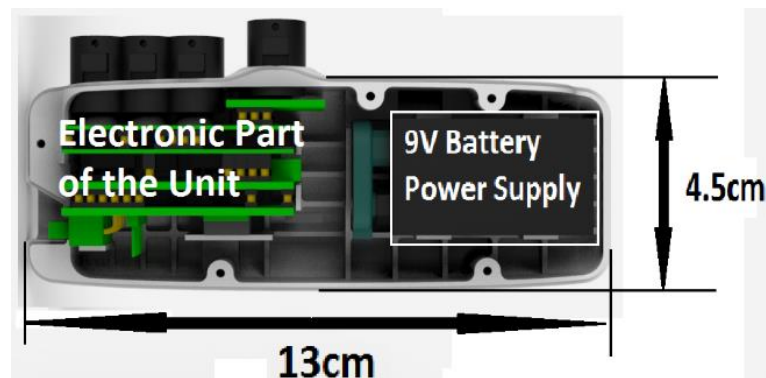
(a)



(b)

Figure D2 (a) Plan view of the integrated POF sensor with conductive yarn beneath. Grey square presents the conductive yarn textile. Red and yellow bars present the light illuminating POF and the light receiving POF. The black bar sited between red and yellow bars is rubber used to avoid light directly coupling from light source to detector without entering the skin. (b) Side view of the integrated POF sensor with conductive yarn beneath.

Figure D3a is the cross-sectional diagram of the opto-electronic unit incorporating the sensing sock, and figure D3b is the schematic of the electronic part of the unit. This unit consisted of one green LED (LXML-PM01-0080, 530nm) mounted on the left top PCB board to transfer light via three illuminating POFs (one for each sensor) to test areas. Three photo-diodes (VISHAY-BPW21R, 565nm) with three front-end circuits respectively were mounted on second PCB board to read the reflected light collected by three receiving POFs (one for each sensor). On the same layer PCB board (second layer), three negative feedback amplifiers were embedded to measure the electrical resistance of three conductive yarn pressure sensors. The third PCB board consisted of six ADC converters (ADC1252U-IC, 24bit) for converting analogue outputs from the second PCB board. The electronic system shown in figure D3b was controlled by a commercial FPGA board (XuLa-200 board) which was configured in the fourth layer. The bottom layer (power board) supplied a constant 5V to the system and the Bluetooth (HC-06) board using a 9V battery. The system transferred data to PC wirelessly via the Bluetooth.



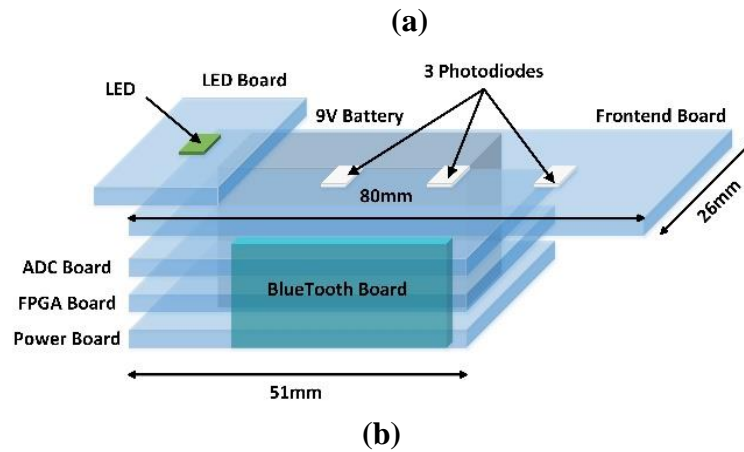


Figure D3 (a) Cross sectional diagram of the opto-electronic unit (b) schematic of the electronic part of the unit.

D.8.2 Walking CRT Measurement Results

Before proceeding to test the CRT on the sole of the foot of a subject, the finger CRT experiment was repeated to verify the performance of the sensing sock. Figure D4 shows the intensity and pressure changes during the test. The volunteer pressed the index finger on the sensing sock from 28.5s to 32s (shown in figure D4) which caused an increase in intensity data (blue line) and pressure recorded (green line). Consequently, the volunteer was asked to hold the pressure for 6 seconds. During this 6 seconds, both light intensity and pressure output remained stable. Then, the volunteer released the pressure which leads to the blood refilling. In this case, the output of pressure (green curve) declined significantly to a stable level whilst the light intensity (blue curve) dropped to a stable baseline with a slower downtrend.

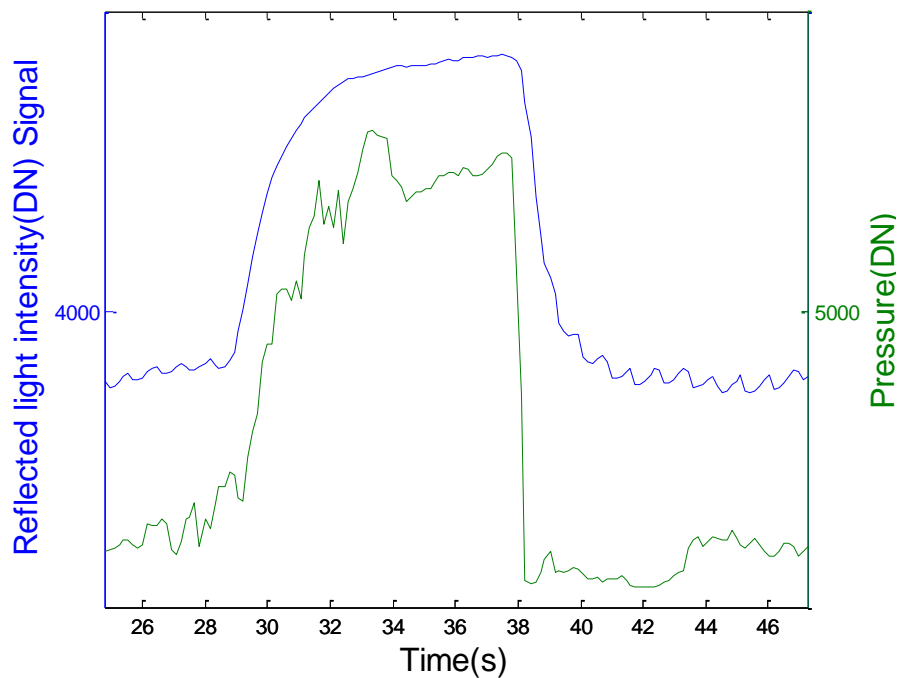


Figure D4 Finger CRT measurement using the sensing sock. The blue trace is the intensity of the reflected light, and the green trace is the pressure recording.

For walking CRT experiments, the volunteer wearing the sensing sock was continuously walking in the lab for 20s. In figure D5a, three test positions were shown in the diagram of the sole of the foot. Figure D5b shows the intensity (blue line) and pressure data (green line) collected during the 20s walking experiment. For position one and three (the top and bottom trace), the optical signal has followed the pressure changes which is similar to the finger experiment.

However, the pressure and reflected light intensity outputs detected at position two (the mid trace) are not clear enough to show the subject's physiological factors, which illustrates two limitations of the designed sensing sock. The unclear pressure output from the sensing sock is due to that the pressure response of the conductive yarn applied in this research is not stable. The noisy light signal at the position two is caused by motion artefacts. This is the other limitation of the sensing sock as the system is not designed to reduce the motion artefacts on S_{pO_2} measurement. In the future work, it is recommended to replace the conductive yarn with a material with more stable pressure response, and improve the design of the sensing sock to reduce the motion artefacts effects.

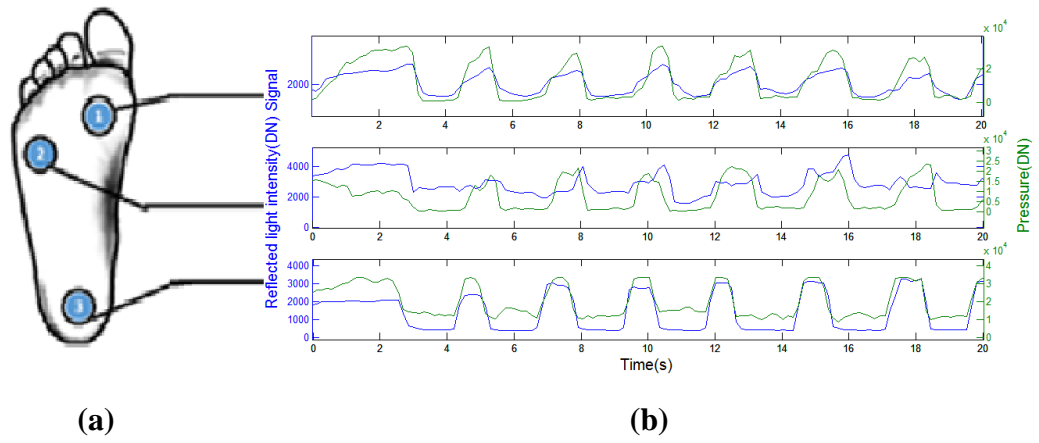


Figure D5 Walking CRT measurement using the sensing sock. (a) Foot positions selected for CRT measurement. (b) Reflected light intensity (blue trace) and pressure output (green trace) of three selected test positions.